Morphological, Cellular and Proteomic Features of Canine Myxomatous Mitral Valve Disease

by

Richard I-Ming Han
BSc BSc(Med)(Hons) MSc(Med) *Cape Town*

Thesis presented for the degree of

Doctor of Philosophy

in the

Division of Veterinary Clinical Studies
Royal (Dick) School of Veterinary Sciences
College of Medicine and Veterinary Medicine
University of Edinburgh

Submitted January 2009
Corrected July 2009

Supervisors
Professor Brendan M Corcoran
Dr Alan D Pemberton

Declaration

I hereby declare that all the work included in this thesis, submitted for the degree of Doctorate of Philosophy at the University of Edinburgh, is my own original work and no part of of this work has been, or will be, submitted for any other degree of qualification.

Richard I-Ming Han
January 2009

Acknowledgements

Undertaking this doctoral research project was a life changing decision. I have abandoned my comfortable life in South Africa and came to study and living in a foreign land. The whole process has been a challenging and often overwhelming experience. Sometimes it is hard to know whether it has been grappling with enough money to survive after paying the totally rip-off £12,000 annual tuition fees, or stay on track of the erratic Lothian bus timetable, or grappling with how to write articulately, squatting in other people's lab, embarking on a new experiment, trying to understand bioinformatics, battling with computer software, and… stay motivated.

I would like to thank the following people, without whose support the completion of this project would not have been made possible:

My utmost gratitude goes to my principal supervisor Prof Brendan Corcoran for his excellent guidance, wonderful support and always needed encouragement. I have been very privileged to have a smart and easy-going supervisor anyone could ask for. I have been stimulated and excited by his good ideas. At the same time, I was allowed the freedom to develop my own thinking and pursuing own research interests. Brendan has the unique ability to grasp the key concepts of complicated matters that I always admire, I learned a great deal of how to present my results clearly from him. His brilliant leadership has been the driving force in this project. His dedication and enthusiasm in heart valve research has inspired me in this project.

Throughout my doctoral study period, the Kennel Club and the Cavalier King Charles Club, through the generosity of my supervisor Brendan, supported the project.

My second supervisor Dr Alan Pemberton for introduced me to proteomics. Alan was very kind to provided me with his equipments to perform all the necessary experiments. He was always patiently listen to my problems and guiding me to the right directions. His most valued comments and suggestions were vital in this project. His input has contributed greatly to success of my project.

Dr Andy Cronshaw for taught me the skill of using mass spec. Andy has relentlessly showed me each step of the process plus the trick of the trade. His

expertise in protein analysis and his knowledge on bioinformatics contributed enormously in the analysis. I really appreciated that Andy has looked after me while I was working in King's Building. I enjoyed the coffee time chatting with him on the top floor of Swann Building looking over the Edinburgh skyline.

Mr Craig Devine and Mr Geoffrey Culshaw for assisted me in animal surgery and tissue collection.

Mr Alex Black, Brendan's collaborator at National University of Ireland, Galway. Alex has contributed in the early formatting of this project and his comments were really welcome.

Wendy of Edinburgh Dog & Cat Home for her support and coordination.

Ms Jean Samuel for helping me in the preparation of histology stains and showed me the fun side of histological staining.

Dr Pam Knight was generously provided me with her protocol and a bench space in her lab to enable me to perform molecular biology experiments.

Dr Jeremy Brown taught me how to perform immunohistochemistry, Jeremy is a gold mine of knowledge, and he was always the first one I came to for trouble-shooting. His advice and suggestion have been most valuable.

Dr Cali Ingham was very kind to allow me to use her special microscope to capture some images. Ms Ann Wright and Ms Lasani Wijetunge gave me good guidance on microscope operations.

Dr Gaetano Impoco was very generous to send me a copy of his microstructure analysis software. We had numerous email discussions; I really appreciate his prompt replies to all my questions.

Mr Steven Mitchell for helping me a lot with the electron microscopy work and all the technical support. I admired his never say die attitude when he facing the uphill battle against the aging machines.

Dr Anne French for her support and interest shown in my work.

Dr Darren Shaw for giving me advice on statistics.

Drs Raanan Tal, Jacqui Ross and Toby Cornish replied to my pleadings for help and gave me very useful tips on colour imaging.

Ms Liz Thorton, Mr Steven Wright and Ms Judith Pate for their constant assistance in the lab.

Everyone in the Hospital for Small Animals, for his or her assistance, encouragement and friendship.

"Have you your stethoscope? Might I ask you-would you have the kindness? I have grave doubts as to my mitral valve, if you would be so good. The aortic I may rely upon, but I should value your opinion upon the mitral." I listened to his heart, as requested, but was unable to find anything amiss, save, indeed that he was in an ecstasy of fear, for he shivered from head to foot… Sir Arthur Conan Doyle, The Sign of Four

Contents

DECLARATION .... **II**

ACKNOWLEDGEMENTS .... **III**

LIST OF FIGURES .... **X**

LIST OF TABLES .... **XVIII**

ABBREVIATIONS .... **XX**

ABSTRACT **1**

1 CHAPTER 1 BACKGROUND INFORMATION ON MITRAL VALVE DISEASE **2**

1.1 INTRODUCTION 2
  1.1.1 *Mitral valve anatomy* *3*
  1.1.2 *Annulus* *3*
  1.1.3 *Leaflets* *4*
  1.1.4 *Tendinous chords* *5*
  1.1.5 *Papillary muscles* *7*
  1.1.6 *Pathology of myxomatous mitral valve disease* *7*
  1.1.7 *Epidemiology* *8*
  1.1.8 *Lesion grades* *8*
  1.1.9 *Diagnosis* *10*
  1.1.10 *Valvular interstitial cells (VIC)* *10*
  1.1.11 *Valvular endothelial cells (VEC)* *11*
  1.1.12 *Extracellular matrix (ECM)* *11*
  1.1.13 *Matrix metalloproteinases (MMP)* *11*
  1.1.14 *Main objectives of this thesis* *11*

2 CHAPTER 2 MORPHOLGICAL ASSESSMENT OF THE CHANGES IN MYXOMATOUS MITRAL VALVE DISEASE **13**

2.1 INTRODUCTION 13
2.2 MATERIALS AND METHODS 14
  2.2.1 *Mitral valve procurement* *14*
  2.2.2 *Tissue dissection* *14*
  2.2.3 *Histology* *14*
  2.2.4 *Microscopy and photography* *15*
  2.2.5 *Image analysis* *15*
  2.2.6 *Leaflet length* *15*
  2.2.7 *Leaflet thickness* *16*
  2.2.8 *Cell density* *16*
  2.2.9 *Cell circularity* *16*
  2.2.10 *Connective tissue* *16*
  2.2.11 *Glycosaminoglycan (GAG)* *17*
  2.2.12 *Statistical analysis* *18*
  2.2.13 *Transmission electron microscopy (TEM)* *20*
  2.2.14 *Quantitative stereology* *22*
  2.2.15 *Circularity of endothelium and valvular interstitial cell* *22*
  2.2.16 *Scanning electron microscopy (SEM)* *22*
  2.2.17 *Image analysis of cell-macerated connective tissue using SEM imagery* *23*
2.3 RESULTS 25
  2.3.1 *Breed* *25*
  2.3.2 *Age* *25*
  2.3.3 *Murmur* *27*
  2.3.4 *Gross pathology* *27*
  2.3.5 *Light Microscopy Study* *28*
  2.3.6 *Leaflet length* *31*
  2.3.7 *Leaflet thickness ratio* *32*
  2.3.8 *Cell density* *34*
  2.3.9 *Circularity* *36*

2.3.10 Connective tissue *37*
2.3.11 Glycosaminoglycan *39*
2.3.12 Transmission electron microscopy (TEM) *48*
2.3.13 Quantitative Stereology *61*
2.3.14 Scanning electron microscopy of cell macerated samples *68*
2.3.15 Quantitative connective tissue micro-structural analysis *74*
2.4 DISCUSSION 80

3 CHAPTER 3 IMMUNOHISTOCHEMISTRY AND IMMUNOPHENOTYPING OF MYXOMATOUS MITRAL VALVE DISEASE IN THE DOG 96

3.1 INTRODUCTION 96
3.2 MATERIALS AND METHODS 97
3.2.1 Mitral valve procurement *97*
3.2.2 Tissue dissection *97*
3.2.3 Immunohistochemistry *97*
3.2.4 Statistical analysis *100*
3.3 RESULTS 101
3.3.1 Vimentin *101*
3.3.2 Adipocyte *109*
3.3.3 α-Smooth muscle actin (α-SMA) *111*
3.3.4 Desmin *120*
3.3.5 Smooth muscle myosin *127*
3.3.6 Fibrillin *130*
3.3.7 MMP-2 .... *132*
3.3.8 MMP-9 .... *132*
3.3.9 MMP-13 .... *134*
3.3.10 Fibronectin *136*
3.3.11 Macrophage *136*
3.3.12 Mast cells *141*
3.3.13 CD34 .... *145*
3.3.14 Von Willebrand factor *147*
3.4 DISCUSSION 148

4 CHAPTER 4 PROTEOMICS 158

4.1 INTRODUCTION 158
4.2 MATERIALS AND METHODS 159
4.2.1 Protein Extraction *159*
4.2.2 1-D SDS-PAGE *159*
4.2.3 2-D SDS-PAGE *159*
4.2.4 2D Gel Staining *160*
4.2.5 Image Analysis *161*
4.2.6 Trypsin Digestion *161*
4.2.7 MALDI-TOF MS Analysis *162*
4.2.8 LC-MS/MS Analysis *163*
4.3 RESULTS 165
4.3.1 1-D SDS-PAGE LS-MS/MS and MALDI-ToF-MS *165*
4.3.2 2-D SDS-PAGE and MALDI-MS *171*
4.4 DISCUSSION 179

5 CHAPTER 5 POLYMERASE CHAIN REACTION 191

5.1 INTRODUCTION 191
5.2 MATERIALS AND METHODS 192
5.2.1 Total RNA isolation *192*
5.2.2 RNA quantification *193*
5.2.3 Reverse transcription of RNA *193*
5.2.4 Primer design *193*
5.2.5 Polymerase chain reaction (PCR) *194*
5.2.6 PCR analysis by electrophoresis *195*
5.2.7 Semi-quantitative PCR by densitometry *195*
5.2.8 Statistical analysis *195*

5.3 RESULTS 197
5.3.1 *RNA quantification* *197*
5.3.2 *Glyceraldehyde 3-phosphate dehydrogenase (GAPDH)* *197*
5.3.3 *Ribosomal protein L19* *197*
5.3.4 *18S ribosomal RNA* *198*
5.3.5 *Vimentin* *199*
5.3.6 *Smooth muscle α-actin (α-SMA)* *200*
5.3.7 *Tropomyosin (TPM)* *201*
5.3.8 *Myosin light polypeptide 4 (MYL-4)* *202*
5.3.9 *Biglycan* *203*
5.3.10 *Fibronectin (FN)* *204*
5.3.11 *Fibrillin (FBN)* *205*
5.3.12 *MMP-13* *206*
5.4 DISCUSSION 207
6 CONCLUSION 209
7 REFERENCES 213
8 APPENDIX 234
8.1 PUBLICATIONS 234
8.1.1 *Journal Articles* *234*
8.1.2 *Proceedings* *234*

List of figures

FIGURE 1.1. DIAGRAM TO SHOW THE ANATOMY OF THE HEART AND LOCATION OF THE MITRAL VALVE. 3
FIGURE 2.1. A SCHEMATIC DIAGRAM SHOWS HOW THE CENTRAL AXIS IS PLOTTED FOR LEAFLET LENGTH MEASUREMENT. 15
FIGURE 2.2. A SCHEMATIC DIAGRAM SHOWS THE POSITIONS OF THE THREE CROSS-SECTIONAL THICKNESS ARE TAKEN FOR LEAFLET THICKNESS MEASUREMENT. 16
FIGURE 2.3. FEATURES OF THE MEANS DIAMONDS DISPLAY USED IN CHARTS 19
FIGURE 2.4. DIAGRAM OF HOW TO INTERPRET THE SIGNIFICANT DIFFERENCE IN COMPARISON CYCLES. 19
FIGURE 2.5. COMPARISON OF DOG AGE TO MITRAL VALVE LESION GRADE. THE RESULTS FROM ANOVA, T-TEST, AND WILCOXON RANKED TEST ARE PRESENTED. THE AGE IS INCREASED DURING THE PROGRESSION OF THE DISEASE. 26
FIGURE 2.6. THE DISTRIBUTION OF DOG AGE ACCORDING TO THE LESION GRADE. THE BEST LINE FIT INTERCEPTS WITH THE AGE ON THE Y-AXIS AT 4.08 YEAR OF AGE. 27
FIGURE 2.7. COMPARISON OF MURMUR TO MITRAL VALVE LESION GRADE. THE BEST LINE FIT INTERCEPTS WITH THE LESION GRADE X-AXIS AT 0.9. 27
FIGURE 2.8. PHOTOGRAPHS OF MITRAL VALVES AT NECROPSY SHOWING LESION GRADES 1-4. 28
FIGURE 2.9. REPRESENTATIVE OF HEMOTOXYLIN AND EOSIN STAINED CROSS-SECTIONAL MITRAL VALVE LEAFLET TISSUES. BAR = 1MM. 29
FIGURE 2.10. H&E STAINED SECTION OF A NORMAL MITRAL VALVE LEAFLET SHOWN CRIMPS ON THE ATRIALIS SURFACE. BAR = 50µM. 30
FIGURE 2.11. H&E STAINED SECTION OF A NORMAL MITRAL VALVE LEAFLET SHOWN THE MUSCLE AT THE BASE. BAR = 50µM. 30
FIGURE 2.12. H&E STAINED SECTION OF A DISEASED MITRAL VALVE LEAFLET SHOWN THE VESSEL IN THE LEAFLET. BAR = 20 µM. 31
FIGURE 2.13. H&E STAINED SECTION OF A DISEASED MITRAL VALVE LEAFLET SHOWN THE FAT CELL LAYER. BAR = 100 µM. 31
FIGURE 2.14. THE COMPARISON OF SEPTAL/MURAL RATIO BETWEEN MITRAL VALVE LESION GRADE. THE RESULTS FROM ANOVA, T-TEST, AND WILCOXON RANKED TEST ARE PRESENTED. 32
FIGURE 2.15. COMPARISON OF SEPTAL LEAFLET THICKNESS RATIO BETWEEN MITRAL VALVE LESION GRADE. THE RESULTS FROM ANOVA, T-TEST, AND WILCOXON RANKED TEST ARE PRESENTED. 33
FIGURE 2.16. COMPARISON OF MURAL LEAFLET THICKNESS RATIO BETWEEN MITRAL VALVE LESION GRADE. THE RESULTS FROM ANOVA, T-TEST, AND WILCOXON RANKED TEST ARE PRESENTED. 33
FIGURE 2.17. AN H&E HISTOLOGICAL SECTION OF A MYXOMATOUS MITRAL VALVE TISSUE SHOWS THE VARIATION IN CELL DENSITY. THE AREA PERIPHERY (P) TO MYXOMATOUS AREA (M) CONTAINS HIGHER CELL DENSITY. BAR = 50 µM. 34
FIGURE 2.18. COMPARISON OF CELL DENSITY IN SEPTAL LEAFLET MYXOMATOUS AREA BETWEEN MITRAL VALVE LESION GRADE. THE RESULTS FROM ANOVA, T-TEST, AND WILCOXON RANKED TEST ARE PRESENTED. 35
FIGURE 2.19. COMPARISON OF CELL DENSITY IN MURAL LEAFLET MYXOMATOUS AREA BETWEEN MITRAL VALVE LESION GRADE. THE RESULTS FROM ANOVA, T-TEST, AND WILCOXON RANKED TEST ARE PRESENTED. 36
FIGURE 2.20. COMPARISON OF CIRCULARITY IN SEPTAL AND MURAL LEAFLETS MYXOMATOUS AREA BETWEEN MITRAL VALVE LESION GRADE. THE CIRCULARITY MEANS ARE PRESENTED. 37
FIGURE 2.21. MASSON'S TRICHROME STAINING OF A DISEASED MITRAL VALVE LEAFLET. MYXOMATOUS AREA SHOWS DESTRUCTION OF COLLAGEN (GREEN) AND ELASTIN (DARK BLUE). BAR = 100 µM. 38
FIGURE 2.22. COMPARISON OF CONNECTIVE TISSUE IN SEPTAL LEAFLET MYXOMATOUS AREA BETWEEN MITRAL VALVE LESION GRADE. THE RESULTS

FROM ANOVA, WILCOXON RANKED TEST AND STUDENT'S T-TEST ARE PRESENTED. 39
FIGURE 2.23. COMPARISON OF CONNECTIVE TISSUE IN MURAL LEAFLET MYXOMATOUS AREA BETWEEN MITRAL VALVE LESION GRADE. THE RESULTS FROM ANOVA, WILCOXON RANKED TEST AND STUDENT'S T-TEST ARE PRESENTED. 39
FIGURE 2.24. ALCIAN BLUE GAG STAINING OF A GRADE 0 NORMAL MITRAL VALVE SEPTAL LEAFLET. 40
FIGURE 2.25. ALCIAN BLUE GAG STAINING OF A GRADE 4 DISEASED MITRAL VALVE SEPTAL LEAFLET. 40
FIGURE 2.26. COMPARISON OF THE PERCENTAGE OF BLUE AREA OF GAG IN LEAFLET BETWEEN MITRAL VALVE LESION GRADE USING K-MEANS CLUSTERING METHOD. SEPTAL LEAFLET IS ON THE LEFT AND THE MURAL LEAFLET IS ON THE RIGHT. 41
FIGURE 2.27. COMPARISON OF THE PERCENTAGE OF BLUE AREA OF GAG IN LEAFLET BETWEEN MITRAL VALVE LESION GRADE USING RGB SPLIT METHOD. SEPTAL LEAFLET IS ON THE LEFT AND THE MURAL LEAFLET IS ON THE RIGHT. 41
FIGURE 2.28. COMPARISON OF THE PERCENTAGE OF BLUE AREA OF GAG IN LEAFLET BETWEEN MITRAL VALVE LESION GRADE USING DECONVOLUTION METHOD. SEPTAL LEAFLET IS ON THE LEFT AND THE MURAL LEAFLET IS ON THE RIGHT. 42
FIGURE 2.29. COMPARISON OF THE PERCENTAGE OF BLUE AREA OF GAG IN LEAFLET BETWEEN MITRAL VALVE LESION GRADE USING THRESHOLD COLOUR METHOD. SEPTAL LEAFLET IS ON THE LEFT AND THE MURAL LEAFLET IS ON THE RIGHT. 43
FIGURE 2.30. COMPARISON OF THE PERCENTAGE OF BLUE AREA OF GAG IN LEAFLET BETWEEN MITRAL VALVE LESION GRADE SHOW IN MEAN ERROR BAR WITH (CLOCKWISE FROM TOP LEFT) BLUE CLUSTER OF K-MEAN CLUSTERING, BLUE CHANNEL OF RGB SPLIT, BLUE DECONVOLUTION AND THRESHOLD OF HSB 140-200. THE BLUE AREA OF GAG ARE ALL BETWEEN THE RANGE OF 20-44%. 44
FIGURE 2.31. COMPARISON OF THE STANDARDISED MEAN BLUE VALUE IN LEAFLET BETWEEN MITRAL VALVE LESION GRADE. THE SEPTAL LEAFLET IS ON THE LEFT AND THE MURAL LEAFLET IS ON THE RIGHT. 45
FIGURE 2.32. CONTINGENCY TABLES SHOW THE COMPARISON OF MEAN BLUE RANKING BETWEEN MITRAL VALVE LESION GRADE. SEPTAL LEAFLET IS ON THE LEFT AND THE MURAL LEAFLET IS ON THE RIGHT. 46
FIGURE 2.33. COMPARISON OF STANDARDISED MEDIAN BLUE VALUE BETWEEN MITRAL VALVE LESION GRADE. THE SEPTAL LEAFLET IS ON THE LEFT AND THE MURAL LEAFLET IS ON THE RIGHT. 46
FIGURE 2.34. COMPARISON OF STANDARDISED MODAL BLUE VALUE BETWEEN MITRAL VALVE LESION GRADE. THE SEPTAL LEAFLET IS ON THE LEFT AND THE MURAL LEAFLET IS ON THE RIGHT. 47
FIGURE 2.35. COMPARISON OF INTEGRATED BLUE INTENSITY BETWEEN MITRAL VALVE LESION GRADE. THE SEPTAL LEAFLET IS ON THE LEFT AND THE MURAL LEAFLET IS ON THE RIGHT. 48
FIGURE 2.36. TRANSMISSION ELECTRON MICROGRAPH OF AN ENDOTHELIAL CELL (E) FROM NORMAL MITRAL VALVE. BASEMENT MEMBRANE (BM), COLLAGEN (CO), EXTRACELLULAR MATRIX (ECM), DESMOSOME JUNCTION (D). BAR = 2 μM. 49
FIGURE 2.37. TRANSMISSION ELECTRON MICROGRAPH SHOWS AN ENDOTHELIAL CELL (E2) UNDERGOING APOPTOSIS NEAR THE SURFACE AND IS WITH BULGE NUCLEUS (NU) AND LARGE VACUOLE (VA). A HEALTHY ENDOTHELIAL CELL (E1) IS UNDERNEATH IT. THE SUB-ENDOTHELIAL TISSUE IS FILLED WITH COLLAGEN (CO). BAR = 4μM. 50
FIGURE 2.38. TRANSMISSION ELECTRON MICROGRAPH SHOWS A MULTI-NUCLEATED INTERSTITIAL CELL (IC) SITUATED VERY CLOSE TO AN ENDOTHELIAL CELL (E). SMALL CYTOPLASMIC PROCESSES ARE SEEN ON THE INTERSTITIAL CELL. THE SUB-ENDOTHELIAL SPACE IS FILLED WITH GROUND SUBSTANCE AND COLLAGEN BUNDLES (CO). BAR = 4μM. 51
FIGURE 2.39. TRANSMISSION ELECTRON MICROGRAPH SHOWING AN ENDOTHELIAL CELL WITH A LARGE FLOCCULATED NUCLEUS (NU) HAS STARTED TO DETACH FROM THE TISSUE. THE CYTOPLASMIC MATERIAL HAS BEEN DEGRADED, BUT

THE MITOCHONDRIA (M) ARE VISIBLE. THE NEIGHBOURING ENDOTHELIAL CELLS (E) LAY FLAT ON THE SURFACE. BAR = 4 μM. 52
FIGURE 2.40. TRANSMISSION ELECTRON MICROGRAPH SHOWS TWO ENDOTHELIAL CELLS SIDE BY SIDE AT THE SURFACE OF THE TISSUE, THEIR NUCLEI (NU) LABELLED. THE ATTACHMENT BETWEEN THEM IS BREAKING DOWN; THERE ARE NOW LARGE INTERCELLULAR SPACES (IS) AND THE CELLS ARE JOINED ONLY BY DESMOSOMES (D). THE LOWER CELL HAS ALSO LOST ITS ATTACHMENT TO ITS OTHER NEIGHBOUR, LEAVING A GAP (G) IN THE ENDOTHELIAL SURFACE. BENEATH THE CELLS IS AN EXPANDED EXTRACELLULAR MATRIX (ECM) AND A FEW SPARSE COLLAGEN BUNDLES (CO) IN BETWEEN. BAR = 3 μM. 53
FIGURE 2.41. TRANSMISSION ELECTRON MICROGRAPH SHOWS THE DISCONTINUATION OF ENDOTHELIUM (E), A LARGE GAP IS SEEN. THE BASEMENT MEMBRANE (BM) HAS BROKEN DOWN, ALLOWING EXTRACELLULAR MATRIX (ECM) MATERIAL TO ESCAPE THROUGH THE GAP. BAR = 1 μM. 54
FIGURE 2.42. TRANSMISSION ELECTRON MICROGRAPH SHOWS AN ENDOTHELIAL CELL (E) UNDERGOING DEGENERATIVE PROCESS IN A DISEASED VALVE. MANY CYTOPLASMIC BUDS (CB) CREATED A RAGGED APICAL SURFACE. THE NUCLEUS (NU) AND VESICLES (VE) CAN BE SEEN WITHIN THE CELL. UNDERNEATH, AN INTERSTITIAL CELL (IC) IS IN CLOSE PROXIMITY TO THE ENDOTHELIUM. THE INTERSTITIAL CELL HAS CYTOPLASMIC PROCESSES THAT EXTEND TOWARDS THE ENDOTHELIUM. BAR = 3μM. 55
FIGURE 2.43. TRANSMISSION ELECTRON MICROGRAPH SHOWS AN ENDOTHELIAL CELL (E) IS DETACHING ITSELF FROM THE BASEMENT MEMBRANE (BM). A GAP (G) BETWEEN THE CELL MEMBRANE AND BASEMENT MEMBRANE CAN BE SEEN. THE EXTRACELLULAR MATRIX (ECM) CONTAINS ABUNDANT GROUND SUBSTANCE AND SPARSE COLLAGEN BUNDLES (CO). BAR = 3 μM. 56
FIGURE 2.44. TRANSMISSION ELECTRON MICROGRAPH SHOWS AN ENDOTHELIAL CELL (E) IN A DISEASED VALVE IS DETACHING ITSELF FROM THE SURFACE OF THE TISSUE. BAR = 3 μM. 56
FIGURE 2.45. TRANSMISSION ELECTRON MICROGRAPH SHOWS BASEMENT MEMBRANE (BM) HAS BECOME DOUBLE LAYERED. THERE IS A GAP (G) BETWEEN THE ENDOTHELIAL CELL (E) AND THE BASEMENT MEMBRANE. THE EXTRACELLULAR MATRIX (ECM) CONTAINS COLLAGEN BUNDLES (CO). BAR = 1μM. 57
FIGURE 2.46. TRANSMISSION ELECTRON MICROGRAPH SHOWS AN INTERSTITIAL CELL (IC) IS SQUEEZING BETWEEN TWO ENDOTHELIAL CELLS (E). THE EXTRACELLULAR MATRIX (ECM) CONTAINS SPARSE COLLAGEN. BAR = 2 μM. .. 58
FIGURE 2.47. TRANSMISSION ELECTRON MICROGRAPH SHOWS THE COLLAGEN (CO) IN THE DISEASED VALVE ARE BENT. THE COLLAGEN ARE ASSOCIATED WITH FILAMENTOUS PROTEOGLYCANS (F). BAR = 0.5 μM. 59
FIGURE 2.48. TRANSMISSION ELECTRON MICROGRAPH SHOWS A TWIN NUCLEATED (NU) INTERSTITIAL CELL WITH AN ELONGATED SHAPE SECRETING VESICLES. BAR = 2 μM. 60
FIGURE 2.49. TRANSMISSION ELECTRON MICROGRAPH SHOWS A ROUND SHAPED INTERSTITIAL CELL IS IN CLOSE CONTACT WITH COLLAGEN (CO). THE CYTOPLASMIC VESICLES CONTAIN PRO-COLLAGEN. BAR = 2 μM. 61
FIGURE 2.50. COMPARISON OF ENDOTHELILUM AS ASSESSED BY QUANTITATIVE STEREOLOGY BETWEEN NORMAL AND DISEASED MITRAL VALVE. 62
FIGURE 2.51. COMPARISON OF VALVULAR INTERSTITIAL CELL AS ASSESSED BY QUANTITATIVE STEREOLOGY BETWEEN NORMAL AND DISEASED MITRAL VALVE. 63
FIGURE 2.52. COMPARISON OF COLLAGEN AS ASSESSED BY QUANTITATIVE STEREOLOGY BETWEEN NORMAL AND DISEASED MITRAL VALVE. 63
FIGURE 2.53. COMPARISON OF EXTRACELLULAR MATRIX AS ASSESSED BY QUANTITATIVE STEREOLOGY BETWEEN NORMAL AND DISEASED MITRAL VALVE. 64
FIGURE 2.54. COMPARISON OF CICULARITY BETWEEN ENDOTHELIUM AND INTERSTITIAL CELL IN NORMAL MITRAL VALVE. 66

FIGURE 2.55. COMPARISON OF CICULARITY BETWEEN ENDOTHELIUM AND INTERSTITIAL CELL IN DISEASED MITRAL VALVE. 67
FIGURE 2.56. COMPARISON OF ENDOTHELIUM CICULARITY BETWEEN NORMAL AND DISEASED MITRAL VALVE. 68
FIGURE 2.57. COMPARISON OF VALVULAR INTERSTITIAL CELL CICULARITY BETWEEN NORMAL AND DISEASED MITRAL VALVE. 68
FIGURE 2.58. SCANNING ELECTRON MICROGRAPH OF A NORMAL MITRAL VALVE SEPTAL LEAFLET AT THE MID ZONE. THE THREE LAYERS ATRIALIS (A), SPONGIOSA (S) AND FIBROSA (F) ARE DISTINGUISHABLE. BAR = 0.1 MM. 69
FIGURE 2.59. SCANNING ELECTRON MICROGRAPH OF A NORMAL MITRAL VALVE SEPTAL LEAFLET AT THE DISTAL ZONE. ATRIALIS SURFACE (A) AND VENTRICULARIS SURFACE (V). BAR = 0.1 MM. 70
FIGURE 2.60. SCANNING ELECTRON MICROGRAPH OF A NORMAL MITRAL VALVE SEPTAL LEAFLET AT THE DISTAL ZONE IN CLOSE UP. THE COLLAGEN FIBRIL (CO), LATERAL STRUTS (*) AND PROTEOGLYCAN NETWORK (PG) ARE VISIBLE. BAR = 10 μM. 70
FIGURE 2.61. SCANNING ELECTRON MICROGRAPH OF A NORMAL MITRAL VALVE SEPTAL LEAFLET AT THE FREE EDGE SURFACE. BAR = 5 μM. 71
FIGURE 2.62. SCANNING ELECTRON MICROGRAPHS OF DISEASED MITRAL VALVE SEPTAL LEAFLETS AT THE MID ZONE. DISRUPTION OF THE CONNECTIVE STRUCTURE DURING THE DISEASE PROGRESSION IS EVIDENT. THE THREE LAYERS ATRIALIS (A), SPONGIOSA (S) AND FIBROSA (F) ARE LABELLED. BAR = 0.1 MM. 72
FIGURE 2.63. SCANNING ELECTRON MICROGRAPHS OF DISEASED MITRAL VALVE SEPTAL LEAFLETS AT THE DISTAL ZONE. THERE WERE DEEP GROOVE LINES DIVIDING THE AREAS INTO “LOBE-LIKE” STRUCTURES. SOME LOBES HAD VEIN LIKE CRACK LINES, ATRIAL SIDE (A) AND VENTRICULAR SIDE (V). BAR = 1 MM.72
FIGURE 2.64. SCANNING ELECTRON MICROGRAPHS OF DISEASED MITRAL VALVE SEPTAL LEAFLETS AT THE DISTAL ZONE IN CLOSE UP. THE COLLAGEN FIBRES ARE THICKEN, AND SOME WITH FRAYED ENDS. BAR = 10 μM. 73
FIGURE 2.65. SCANNING ELECTRON MICROGRAPHS OF A DISEASE MITRAL VALVE SEPTAL LEAFLET SHOWS AMASSED COLLAGEN FIBRES IN DISTAL ZONE. BAR = 5 μM. 73
FIGURE 2.66. SCANNING ELECTRON MICROGRAPHS SHOWS A DISEASED MITRAL VALVE SEPTAL LEAFLET AT THE FREE EDGE SURFACE. THE MESH-LIKE APPEARANCE OF COLLAGEN FIBRES WAS NOT EVENLY SPACED, WITH VOIDS OF IN DIFFERENT SIZES VISIBLE. BAR = 0.5 μM. 74
FIGURE 2.67. QUANTITATIVE CONNECTIVE TISSUE MICRO-STRUCTURAL ANALYSIS DISTRIBUTION CHARTS. FROM TOP, BINARISED IMAGES, PORE AREA, PORE FORM FACTOR, PORE ROUNDNESS, PORE ASPECT RATIO, PORE PERIMETER, PORE DIAMETER, PORE MIN DIAMETER, PORE DIRECTIONALITY AND PORE DIRECTIONALITY ANGLE. 79
FIGURE 3.1. A SCHEMATIC DIAGRAM SHOWS A MITRAL VALVE LEAFLET DIVIDED INTO THREE ZONES BASAL, MID AND DISTAL AND THREE LAYERS ATRIALIS, SPONGIOSA AND FIBROSA FOR IMMUNOHISTOCHEMISTRY SCORING. 99
FIGURE 3.2. VIMENTIN STAINING IN NORMAL VALVE DISTAL ZONE. THE VIMENTIN POSITIVE CELLS ARE MORE ELONGATED IN SHAPE. BAR = 10 μM. 101
FIGURE 3.3. VEIMENTIN POSITIVE CELLS ARE ASSOCIATED WITH CONNECTIVE TISSUE AND VIMENTIN NEGATIVE CELLS ARE ASSOCIATED WITH MYXOMATOUS TISSUE. BAR = 10 μM. 101
FIGURE 3.4. VIMENTIN SCORES IN SEPTAL LEAFLETS. THREE DIFFERENT COLUMNS REPRESENT THE THREE ZONES AND THREE DIFFERENT COLOURS REPRESENT THE THREE LAYERS. EACH ZONE AND EACH LAYER COULD HAVE A MAXIMAL SCORE OF 3, THE COMBINED SCORE FOR A LAYER OR ZONE COULD HAVE A MAXIMAL SCORE OF 9. 103
FIGURE 3.5. VIMENTIN SCORES IN MURAL LEAFLETS. THREE DIFFERENT COLUMNS REPRESENT THE THREE ZONES AND THREE DIFFERENT COLOURS REPRESENT THE THREE LAYERS. EACH ZONE AND EACH LAYER COULD HAVE A MAXIMAL SCORE OF 3, THE COMBINED SCORE FOR A LAYER OR ZONE COULD HAVE A MAXIMAL SCORE OF 9. 104

FIGURE 3.6. THE ADIPOCYTES ARE MODERATELY POSITIVE TO VIMENTIN. BAR = 10 μM. 109
FIGURE 3.7. FAT SCORE IN SEPTAL AND MURAL LEAFLETS. THREE DIFFERENT COLUMNS REPRESENT THE THREE ZONES. EACH ZONE COULD HAVE A MAXIMAL SCORE OF 3, ... 110
FIGURE 3.8. α-SMA POSITIVE CELLS IN LAYERED FORMATION NEAR THE ENDOTHELIUM. BAR = 50 μM. 112
FIGURE 3.9. A CLUSTER OF α-SMA POSITIVE CELLS ASSOCIATED WITH CONNECTIVE TISSUE. BAR = 10 μM. 112
FIGURE 3.10. α-SMOOTH MUSCLE ACTIN SCORES IN SEPTAL LEAFLETS. THREE DIFFERENT COLUMNS REPRESENT THE THREE ZONES AND THREE DIFFERENT COLOURS REPRESENT THE THREE LAYERS. EACH ZONE AND EACH LAYER COULD HAVE A MAXIMAL SCORE OF 3, THE COMBINED SCORE FOR A LAYER OR ZONE COULD HAVE A MAXIMAL SCORE OF 9. 114
FIGURE 3.11. α-SMOOTH MUSCLE ACTIN SCORES IN MURAL LEAFLETS. THREE DIFFERENT COLUMNS REPRESENT THE THREE ZONES AND THREE DIFFERENT COLOURS REPRESENT THE THREE LAYERS. EACH ZONE AND EACH LAYER COULD HAVE A MAXIMAL SCORE OF 3, THE COMBINED SCORE FOR A LAYER OR ZONE COULD HAVE A MAXIMAL SCORE OF 9. 115
FIGURE 3.12. DESMIN POSITIVE CARDIC MYOCYTE SHOWS FILAMENTOUS BANDING. BAR = 10 μM. 120
FIGURE 3.13. DESMIN POSITIVE CHONDROCYTES IN THE FIBROSA LAYER. BAR = 10 μM. 120
FIGURE 3.14. DESMIN SCORES IN SEPTAL LEAFLETS. THREE DIFFERENT COLUMNS REPRESENT THE THREE ZONES AND THREE DIFFERENT COLOURS REPRESENT THE THREE LAYERS. EACH ZONE AND EACH LAYER COULD HAVE A MAXIMAL SCORE OF 3, THE COMBINED SCORE FOR A LAYER OR ZONE COULD HAVE A MAXIMAL SCORE OF 9. 121
FIGURE 3.15. DESMIN SCORES IN MURAL LEAFLETS. THREE DIFFERENT COLUMNS REPRESENT THE THREE ZONES AND THREE DIFFERENT COLOURS REPRESENT THE THREE LAYERS. EACH ZONE AND EACH LAYER COULD HAVE A MAXIMAL SCORE OF 3, THE COMBINED SCORE FOR A LAYER OR ZONE COULD HAVE A MAXIMAL SCORE OF 9. 122
FIGURE 3.16. MICROPHOTOGRAPH SHOWING THE ARTERIOLE WALL STAINED POSITIVE FOR SMOOTH MUSCLE MYOSIN. BAR = 10 μM. 127
FIGURE 3.17. MICROPHOTOGRAPH SHOWING A VESSEL WALL STAINED POSITIVE FOR SMOOTH MUSCLE MYOSIN. BAR = 10 μM. 127
FIGURE 3.18. SMOOTH MUSCLE MYOSIN SCORE IN SEPTAL LEAFLETS. THREE DIFFERENT COLUMNS REPRESENT THE THREE ZONES AND THREE DIFFERENT COLOURS REPRESENT THE THREE LAYERS. EACH ZONE AND EACH LAYER COULD HAVE A MAXIMAL SCORE OF 3, THE COMBINED SCORE FOR A LAYER OR ZONE COULD HAVE A MAXIMAL SCORE OF 9. 128
FIGURE 3.19. SMOOTH MUSCLE MYOSIN SCORE IN MURAL LEAFLETS. THREE DIFFERENT COLUMNS REPRESENT THE THREE ZONES AND THREE DIFFERENT COLOURS REPRESENT THE THREE LAYERS. EACH ZONE AND EACH LAYER COULD HAVE A MAXIMAL SCORE OF 3, THE COMBINED SCORE FOR A LAYER OR ZONE COULD HAVE A MAXIMAL SCORE OF 9. 129
FIGURE 3.20. FIBRILLIN SCORES IN SEPTAL AND MURAL LEAFLETS. THREE DIFFERENT COLUMNS REPRESENT THE THREE ZONES AND THREE DIFFERENT COLOURS REPRESENT THE THREE LAYERS. EACH ZONE AND EACH LAYER COULD HAVE A MAXIMAL SCORE OF 3, THE COMBINED SCORE FOR A LAYER OR ZONE COULD HAVE A MAXIMAL SCORE OF 9. 131
FIGURE 3.21. ENDOTHELIAL CELLS LINING THE VESSEL AND THE PARA-LUMIN SPACE ARE POSITIVE FOR MMP-9. BAR = 10 μM. 132
FIGURE 3.22. THE INTERCELLULAR SPACE NEAR THE POLAR ENDS OF INTERSTITIAL CELLS ARE MMP-9 POSITIVE. BAR = 10 μM. 132
FIGURE 3.23. MMP-9 SCORES IN SEPTAL AND MURAL LEAFLETS. THREE DIFFERENT COLUMNS REPRESENT THE THREE ZONES AND THREE DIFFERENT COLOURS REPRESENT THE THREE LAYERS. EACH ZONE AND EACH LAYER COULD HAVE A

MAXIMAL SCORE OF 3, THE COMBINED SCORE FOR A LAYER OR ZONE COULD HAVE A MAXIMAL SCORE OF 9. 133
FIGURE 3.24. MMP-13 POSITIVE IN SUB-ENDOTHELIAL SPACE. BAR = 10 μM. 134
FIGURE 3.25. MMP-13 POSITIVE AREA ASSOCIATED WITH A NODULE. BAR = 10 μM. .. 134
FIGURE 3.26. MMP-13 SCORES IN SEPTAL AND MURAL LEAFLETS. THREE DIFFERENT COLUMNS REPRESENT THE THREE ZONES AND THREE DIFFERENT COLOURS REPRESENT THE THREE LAYERS. EACH ZONE AND EACH LAYER COULD HAVE A MAXIMAL SCORE OF 3, THE COMBINED SCORE FOR A LAYER OR ZONE COULD HAVE A MAXIMAL SCORE OF 9. 135
FIGURE 3.27. MAC-387 POSITIVE MACROPHAGES ASSOCIATED WITH LUMINAL SIDE OF A VESSEL. BAR = 10 μM. 136
FIGURE 3.28. MAC-387 POSITIVE MACROPHAGES ASSOCIATED WITH TISSUE. BAR = 10 μM. 136
FIGURE 3.29. COMPARISON OF MACROPHAGE NUMBER IN MITRAL VALVE BETWEEN MITRAL VALVE LESION GRADE. THE RESULTS FROM ANOVA, WILCOXON RANKED TEST, STUDENT'S T-TEST, AND LSN ARE PRESENTED. 137
FIGURE 3.30. COMPARISON OF MACROPHAGE NUMBER IN SEPTAL LEAFLET (LEFT) AND MURAL LEAFLET (RIGHT) BETWEEN MITRAL VALVE LESION GRADE. THE RESULTS FROM ANOVA, WILCOXON RANKED TEST, STUDENT'S T-TEST, AND LSN ARE PRESENTED. 138
FIGURE 3.31. COMPARISON OF MACROPHAGE NUMBER PER MM^2 AREA BETWEEN MITRAL VALVE LESION GRADE. THE RESULTS FROM ANOVA, WILCOXON RANKED TEST, STUDENT'S T-TEST, AND LSN ARE PRESENTED. 138
FIGURE 3.32. COMPARISON OF MACROPHAGE NUMBER PER AREA IN SEPTAL LEAFLET (LEFT) AND MURAL LEAFLET (RIGHT) BETWEEN MITRAL VALVE LESION GRADE. THE RESULTS FROM ANOVA, WILCOXON RANKED TEST, STUDENT'S T-TEST, AND LSN ARE PRESENTED. 139
FIGURE 3.33. DISTRIBUTION OF MACROPHAGE AS A PERCENTAGE IN SEPTAL LEAFLET (LEFT PANEL) AND MURAL LEAFLET (RIGHT PANEL). THREE DIFFERENT COLUMNS REPRESENT THE THREE ZONES AND THREE DIFFERENT COLOURS REPRESENT THE THREE LAYERS. 140
FIGURE 3.34. MAST CELL WITH PUNCTUATED DENSE ORGANELLES BY TOLUIDINE BLUE STAIN. BAR = 10 μM. 141
FIGURE 3.35. COMPARISON OF MAST CELL NUMBER IN MITRAL VALVE BETWEEN MITRAL VALVE LESION GRADE. THE RESULTS FROM ANOVA, WILCOXON RANKED TEST, STUDENT'S T-TEST, AND LSN ARE PRESENTED. 141
FIGURE 3.36. COMPARISON OF MAST CELL NUMBER IN SEPTAL LEAFLET (LEFT) AND MURAL LEAFLET (RIGHT) BETWEEN MITRAL VALVE LESION GRADE. THE RESULTS FROM ANOVA, WILCOXON RANKED TEST, STUDENT'S T-TEST, AND LSN ARE PRESENTED. 142
FIGURE 3.37. COMPARISON OF MAST CELL NUMBER PER AREA BETWEEN MITRAL VALVE LESION GRADE. THE RESULTS FROM ANOVA, WILCOXON RANKED TEST, STUDENT'S T-TEST, AND LSN ARE PRESENTED. 142
FIGURE 3.38. COMPARISON OF MAST CELL NUMBER PER AREA IN SEPTAL LEAFLET (LEFT) AND MURAL LEAFLET (RIGHT) BETWEEN MITRAL VALVE LESION GRADE. THE RESULTS FROM ANOVA, WILCOXON RANKED TEST, STUDENT'S T-TEST, AND LSN ARE PRESENTED. 143
FIGURE 3.39. DISTRIBUTION OF MAST CELL AS A PERCENTAGE IN SEPTAL LEAFLET (LEFT PANEL) AND MURAL LEAFLET (RIGHT PANEL). THREE DIFFERENT COLUMNS REPRESENT THE THREE ZONES AND THREE DIFFERENT COLOURS REPRESENT THE THREE LAYERS. 144
FIGURE 3.40. NUMBER OF SEPTAL LEAFLETS (LEFT) AND MURAL LEAFLETS (RIGHT) FOUND WITH AND WITHOUT CD34+ CELLS. 145
FIGURE 3.41. COMPARISON OF CD34+ CELL NUMBER IN MITRAL VALVE BETWEEN MITRAL VALVE LESION GRADE. THE RESULTS FROM ANOVA, WILCOXON RANKED TEST, STUDENT'S T-TEST, AND LSN ARE PRESENTED. 146
FIGURE 3.42. COMPARISON OF CD34+ NUMBER IN SEPTAL LEAFLET (LEFT) AND MURAL LEAFLET (RIGHT) BETWEEN MITRAL VALVE LESION GRADE. THE RESULTS FROM ANOVA, WILCOXON RANKED TEST, STUDENT'S T-TEST, AND LSN ARE PRESENTED. 146

FIGURE 4.1. REPRESENTATIVE 1D SDS-PAGE GEL FROM THE NORMAL GROUP WHICH WAS DIVIDED INTO 5 STRIPS OF EQUAL THICKNESS FOR LC-MS/MS. THE MOLECULAR WEIGHT (MW) MARKERS ARE INDICATED ON THE LEFT. 165
FIGURE 4.2. REPRESENTATIVE MASCOT SEARCH RESULTS SHOWING THE PROBABILITY BASED MOWSE SCORE. THE RED BARS OUTSIDE THE GREEN AREA INDICATES THE MATCHES WERE SIGNIFICANT. 165
FIGURE 4.3. REPRESENTATIVE OF A MALDI-MS PEAKS CHART FROM A STRIP OF TRYPSIN DIGESTED 1D SDS-PAGE. 166
FIGURE 4.4. THE DISTRIBUTION OF PROTEIN SPOTS FOUND TO BE SIGNIFICANTLY DIFFERENT BETWEEN NORMAL AND MODERATE GROUPS. THE PLOT SHOWS THE FOLD CHANGE OF PROTEIN SPOTS FROM NORMAL GROUP TO MODERATE GROUP. THE X-AXIS IS THE FOLD CHANGE IN DENSITY VOLUME AND Y-AXIS IS THE NUMBER OF COUNTS (N=25). 171
FIGURE 4.5. THE DISTRIBUTION OF PROTEIN SPOTS FOUND TO BE SIGNIFICANTLY DIFFERENT BETWEEN MODERATE AND SEVERE GROUPS. THE PLOT SHOWS THE FOLD CHANGE OF PROTEIN SPOTS FROM MODERATE TO SEVERE GROUP. THE X-AXIS IS THE FOLD CHANGE IN DENSITY VOLUME AND Y-AXIS IS THE NUMBER OF COUNTS (N=25). 172
FIGURE 4.6. THE DISTRIBUTION OF PROTEIN SPOTS FOUND TO BE SIGNIFICANTLY DIFFERENT BETWEEN NORMAL AND SEVERE GROUPS. THE PLOT SHOWS THE FOLD CHANGE OF PROTEIN SPOTS FROM NORMAL TO SEVERE GROUP. THE X-AXIS IS THE FOLD CHANGE IN DENSITY VOLUME AND Y-AXIS IS THE NUMBER OF COUNTS (N=37). 172
FIGURE 4.7. TWO-DIMENSIONAL ELECTROPHORETIC MAP FOR NORMAL CANINE MITRAL VALVE. FIRST-DIMENSIONAL SEPARATION WITH IMMOBILIZED PH GRADIENT STRIPS (18 CM, PH RANGE: 3–10); SECOND DIMENSION WAS BY SDS-PAGE (10% ACRYLAMIDE; 16 × 20 CM GELS); PROTEINS WERE VISUALIZED BY SILVER STAINING. PROTEIN SPOTS WERE IDENTIFIED BY TRYPTIC PEPTIDE MAPPING FROM MATCHED COOMASSIE BLUE-STAINED AND SILVERQUEST STAINED GELS. IDENTIFIED PROTEINS ARE LABELED IN WITH THE CORRESPONDING SWISSPROT GENE NAME: SEE TABLE 4.2 BELOW FOR KEY. ... 173
FIGURE 4.8. TWO-DIMENSIONAL ELECTROPHORETIC MAP FOR MODERATELY DISEASED MITRAL VALVE. FIRST-DIMENSIONAL SEPARATION WITH IMMOBILIZED PH GRADIENT STRIPS (18 CM, PH RANGE: 3–10); SECOND DIMENSION WAS BY SDS-PAGE (10% ACRYLAMIDE; 16 × 20 CM GELS); PROTEINS WERE VISUALIZED BY SILVER STAINING... 175
FIGURE 4.9. TWO-DIMENSIONAL ELECTROPHORETIC MAP FOR SEVERELY DISEASED MITRAL VALVE. FIRST-DIMENSIONAL SEPARATION WITH IMMOBILIZED PH GRADIENT STRIPS (18 CM, PH RANGE: 3–10); SECOND DIMENSION WAS BY SDS-PAGE (10% ACRYLAMIDE; 16 × 20 CM GELS); PROTEINS WERE VISUALIZED BY SILVER STAINING. PROTEIN SPOTS WERE IDENTIFIED BY TRYPTIC PEPTIDE MAPPING FROM MATCHED SILVERQUEST STAINED GELS. IDENTIFIED PROTEINS FROM CANINE GENOME SEQUENCE ARE LABELED IN WITH THE CORRESPONDING SWISSPROT GENE NAME: SEE TABLE BELOW FOR KEY. 176
FIGURE 4.10. DYMENSION SOFTWARE GENERATED 2-D PROTEIN SPOT PATTERN FROM SUPERIMPOSED AVERAGE SPOTS IN NORMAL AND SEVERELY DISEASED GROUPS. THE GREEN COLOUR SHOWS THE SPOTS INCREASED IN INTENSITY, THE RED COLOUR SHOWS THE SPOTS IN DECREASED IN INTENSITY, AND THE BLACK REPRESENTS UNCHANGED SPOTS... 177
FIGURE 4.11. PANEL SHOWING HOW THE TROPOMYSIN SPOT WAS PRESENT IN THE NORMAL, DOWN REGULATED IN THE MODERATE AND ABSENT IN THE SEVERELY DISEASED.. 178
FIGURE 4.12. PANEL SHOWING HOW THE MYOSIN REGULATORY LIGHT CHAIN 2 SPOT WAS PRESENT IN THE NORMAL, DOWN REGULATED IN THE MODERATE AND ABSENT IN THE SEVERELY DISEASED. 178
FIGURE 5.1. THE GEL ELECTROPHORESIS PICTURE SHOWS THE RT-PCR PRODUCTS FOR THE HOUSEKEEPING GENE GAPDH (464 BP) AFTER 29 CYCLES. THE VARIABLE EXPRESSION OF GAPDH BETWEEN SAMPLES WAS VISIBLE; ONE SAMPLE IN THE SEVERE GROUP HAS VIRTUALLY NO VISIBLE MRNA. 197

FIGURE 5.2. THE GEL ELECTROPHORESIS PICTURE SHOWS THE RT-PCR PRODUCTS FOR THE HOUSEKEEPING GENE RPL19 (479 BP) AFTER 32 CYCLES. THE BANDS ON THE GEL SHOW A CONSISTENT RPL19 EXPRESSION ACROSS ALL SAMPLES. 198
FIGURE 5.3. DENSITOMETRIC ANALYSIS OF THE RPL19 GENE EXPRESSION. THE RESULTS FROM ANOVA, T-TEST, WILCOXON RANKED TEST AND LSN ARE PRESENTED. 198
FIGURE 5.4. THE GEL ELECTROPHORESIS PICTURE SHOWS THE RT-PCR PRODUCTS FOR THE HOUSEKEEPING GENE 18S RRNA (273 BP) AFTER 22 CYCLES. THE BANDS ON THE GEL SHOW A CONSISTENT 18S RRNA EXPRESSION ACROSS ALL SAMPLES.199
FIGURE 5.5. DENSITOMETRIC ANALYSIS OF THE 18S RRNA GENE EXPRESSION. THE RESULTS FROM ANOVA, T-TEST, WILCOXON RANKED TEST AND LSN ARE PRESENTED. 199
FIGURE 5.6. THE GEL ELECTROPHORESIS PICTURE SHOWS THE RT-PCR PRODUCTS FOR THE VIMENTIN GENE (490 BP) AFTER 28 CYCLES. 200
FIGURE 5.7. DENSITOMETRIC ANALYSIS OF THE NORMALIZED VIMENTIN GENE EXPRESSION. THE RESULTS FROM ANOVA, T-TEST, WILCOXON RANKED TEST AND LSN ARE PRESENTED. 200
FIGURE 5.8. THE GEL ELECTROPHORESIS PICTURE SHOWS THE RT-PCR PRODUCTS FOR THE α-SMA GENE (449 BP) AFTER 28 CYCLES. 200
FIGURE 5.9. DENSITOMETRIC ANALYSIS OF THE NORMALIZED SMOOTH MUSCLE α-ACTIN GENE EXPRESSION. THE RESULTS FROM ANOVA, T-TEST, WILCOXON RANKED TEST AND LSN ARE PRESENTED. 201
FIGURE 5.10. THE GEL ELECTROPHORESIS PICTURE SHOWS THE RT-PCR PRODUCTS FOR THE TROPOMYOSIN GENE (279 BP) AFTER 30 CYCLES. 201
FIGURE 5.11. DENSITOMETRIC ANALYSIS OF THE NORMALIZED TROPOMYOSIN GENE EXPRESSION. THE RESULTS FROM ANOVA, T-TEST, WILCOXON RANKED TEST AND LSN ARE PRESENTED. 202
FIGURE 5.12. THE GEL ELECTROPHORESIS PICTURE SHOWS THE RT-PCR PRODUCTS FOR THE MYOSIN LIGHT POLYPEPTIDE 4 GENE (426 BP) AFTER 28 CYCLES......... 202
FIGURE 5.13. DENSITOMETRIC ANALYSIS OF THE NORMALIZED MYOSIN LIGHT POLYPEPTIDE-4 GENE EXPRESSION. THE RESULTS FROM ANOVA, T-TEST, WILCOXON RANKED TEST AND LSN ARE PRESENTED. 203
FIGURE 5.14. THE GEL ELECTROPHORESIS PICTURE SHOWS THE RT-PCR PRODUCTS FOR THE BIGLYCAN GENE (486 BP) AFTER 31 CYCLES. 203
FIGURE 5.15. DENSITOMETRIC ANALYSIS OF THE NORMALIZED BIGLYCAN GENE EXPRESSION. THE RESULTS FROM ANOVA, T-TEST, WILCOXON RANKED TEST AND LSN ARE PRESENTED. 204
FIGURE 5.16. THE GEL ELECTROPHORESIS PICTURE SHOWS THE RT-PCR PRODUCTS FOR THE FIBRONECTIN GENE (307 BP) AFTER 28 CYCLES. 204
FIGURE 5.17. DENSITOMETRIC ANALYSIS OF THE NORMALIZED FIBRONECTIN GENE EXPRESSION. THE RESULTS FROM ANOVA, T-TEST, WILCOXON RANKED TEST AND LSN ARE PRESENTED. 205
FIGURE 5.18. THE GEL ELECTROPHORESIS PICTURE SHOWS THE RT-PCR PRODUCTS FOR THE FIBRILLIN GENE (318 BP) AFTER 31 CYCLES. 205
FIGURE 5.19. DENSITOMETRIC ANALYSIS OF THE NORMALIZED FIBRILLIN GENE EXPRESSION. THE RESULTS FROM ANOVA, T-TEST, WILCOXON RANKED TEST AND LSN ARE PRESENTED. 206
FIGURE 5.20. THE GEL ELECTROPHORESIS PICTURE SHOWS THE RT-PCR PRODUCTS FOR THE MMP-13 GENE AFTER 55 CYCLES. THE NORMAL (N) CONTAINS TWO BANDS, THE EXPECTED 496 BP AND A FRAGMENT ABOUT 310 BP. THE MODERATELY DISEASED LACKING THE EXPECTED 496 BP FRAGMENT BUT PRODUCED A 310 BP FRAGMENT INSTEAD. THE SEVERELY DISEASE ALSO LACKING THE EXPECTED 496 BP FRAGMENT BUT IT PRODUCED A UNIQUE FRAGMENT ABOUT 600 BP. 206

List of tables

TABLE 2.1. BACKGROUND INFORMATION ABOUT THE DOGS THAT SAMPLES WERE OBTAINED FROM. 21
TABLE 2.2: SHAPE QUANTITATIVE DESCRIPTORS. MEANINGS OF THE PARAMETERS. A: NET AREA; ACONVEX : AREA OF THE CONVEX HULL; AF ILL AREA OF THE FILLED POLYGON; P: PERIMETER; PCONVEX : PERIMETER OF THE CONVEX HULL; DMAX , DMIN : MAXIMUM AND MINIMUM DIMENSION; DINSCR AND DCIRCUM: DIAMETERS OF THE INSCRIBED AND CIRCUMSCRIBED CIRCLE; L: LENGTH OF THE FEATURE ALONG THE FARTHEST POINTS IN THE CONVEX HULL; LF , WF : FIBER LENGTH AND FIBER WIDTH (MEASURED FROM THE SKELETON OF THE FEATURE). 24
TABLE 2.3. BREED DISTRIBUTION OF DOGS. 25
TABLE 2.4. MEDIANS, MEANS AND QUARTILE VALUES FOR THE QUANTITATIVE STEREOLOGY OF ENDOTHELIUM, INTERSTITIAL CELLS, COLLAGEN AND EXTRACELLULAR MATRIX DATA SETS. 61
TABLE 2.5. MEDIANS, MEANS AND QUARTILE VALUES FOR THE CIRCULARITY OF ENDOTHELIUM AND INTERSTITIAL CELL. 65
TABLE 2.6. PREVIOUS STUDIES INVESTIGATED THE MITRAL VALVE LEAFLETS LENGTH AND THEIR CALCULATED SEPTAL/MURAL RATIO. 89
TABLE 3.1. DETAILS OF ANTIBODIES USED. 97
TABLE 3.2. VIMENTIN POSITIVE CELL DISTRIBUTION PATTERNS IN SEPTAL LEAFLETS. THEY ARE PRESENTED IN A HIERARCHAL ORDER. THE MOST FREQUENTLY OCCURRING DISTRIBUTION PATTERN IS AT THE TOP OF EACH BLOCK. 105
TABLE 3.3. VIMENTIN POSITIVE CELL DISTRIBUTION PATTERNS IN MURAL LEAFLETS. THEY ARE PRESENTED IN A HIERARCHAL ORDER. THE MOST FREQUENTLY OCCURRING DISTRIBUTION PATTERN IS AT THE TOP OF EACH BLOCK. 106
TABLE 3.4. VIMENTIN POSITIVE CELL MORPHOLOGIES IN SEPTAL LEAFLETS. THEY ARE PRESENTED IN A HIERARCHAL ORDER. THE MOST FREQUENTLY OCCURRING CELL SHAPE IS AT THE TOP OF EACH BLOCK. 107
TABLE 3.5. VIMENTIN POSITIVE CELL MORPHOLGIES IN MURAL LEAFLETS. THEY ARE PRESENTED IN A HIERARCHAL ORDER. THE MOST FREQUENTLY OCCURRING CELL SHAPE IS AT THE TOP OF EACH BLOCK. 108
TABLE 3.6. ADIPOCYTE DISTRIBUTION PATTERNS IN SEPTAL LEAFLETS. THEY ARE PRESENTED IN A HIERARCHAL ORDER. THE MOST FREQUENTLY OCCURRING DISTRIBUTION PATTERN IS AT THE TOP OF EACH BLOCK. 111
TABLE 3.7. ADIPOCYTE DISTRIBUTION PATTERNS IN MURAL LEAFLETS. THEY ARE PRESENTED IN A HIERARCHAL ORDER. THE MOST FREQUENTLY OCCURRING DISTRIBUTION PATTERN IS AT THE TOP OF EACH BLOCK. 111
TABLE 3.8. α-SMOOTH MUSCLE ACTIN POSITIVE CELL DISTRIBUTION PATTERNS IN SEPTAL LEAFLETS. THEY ARE PRESENTED IN A HIERARCHAL ORDER. THE MOST FREQUENTLY OCCURRING DISTRIBUTION PATTERN IS AT THE TOP OF EACH BLOCK. 116
TABLE 3.9. α-SMOOTH MUSCLE ACTIN POSITIVE CELL DISTRIBUTION PATTERNS IN MURAL LEAFLETS. THEY ARE PRESENTED IN A HIERARCHAL ORDER. THE MOST FREQUENTLY OCCURRING DISTRIBUTION PATTERN IS AT THE TOP OF EACH BLOCK. 117
TABLE 3.10. α-SMOOTH MUSCLE ACTIN POSITIVE CELL MORPHOLGIES IN SEPTAL LEAFLETS. THEY ARE PRESENTED IN A HIERARCHAL ORDER. THE MOST FREQUENTLY OCCURRING SHAPE IS AT THE TOP OF EACH BLOCK. 118
TABLE 3.11. α-SMOOTH MUSCLE ACTIN POSITIVE CELL MORPHOLGIES IN MURAL LEAFLETS. THEY ARE PRESENTED IN A HIERARCHAL ORDER. THE MOST FREQUENTLY OCCURRING CELL SHAPE IS AT THE TOP OF EACH BLOCK. 119
TABLE 3.12. DESMIN POSITIVE CELL DISTRIBUTION PATTERNS IN SEPTAL LEAFLETS. THEY ARE PRESENTED IN A HIERARCHAL ORDER. THE MOST FREQUENTLY OCCURRING DISTRIBUTION PATTERN IS AT THE TOP OF EACH BLOCK. 123
TABLE 3.13. DESMIN POSITIVE CELL DISTRIBUTION PATTERNS IN MURAL LEAFLETS. THEY ARE PRESENTED IN A HIERARCHAL ORDER. THE MOST FREQUENTLY OCCURRING DISTRIBUTION PATTERN IS AT THE TOP OF EACH BLOCK. 124

TABLE 3.14. DESMIN POSITIVE CELL MORPHOLGIES IN SEPTAL LEAFLETS. THEY ARE PRESENTED IN A HIERARCHAL ORDER. THE MOST FREQUENTLY OCCURRING CELL SHAPE IS AT THE TOP OF EACH BLOCK. 125
TABLE 3.15. DESMIN POSITIVE CELL MORPHOLGIES IN MURAL LEAFLETS. THEY ARE PRESENTED IN A HIERARCHAL ORDER. THE MOST FREQUENTLY OCCURRING CELL SHAPE IS AT THE TOP OF EACH BLOCK. 126
TABLE 3.16. MORPHOLOGICAL FEATURES OF VEC AND ENDOTHELIAL LINING DURING THE DISEASE PROGRESSION........ 147
TABLE 4.1. LIST OF SIGNIFICANT PROTEINS FROM 1-D GELS IDENTIFIED BY LCMS AND MALDI-MS THROUGH MASCOT SEARCH AGAINST SWISSPROT........ 167
TABLE 4.2. PROTEIN IDENTIFICATION FOR NORMAL CANINE MITRAL VALVE. 174
TABLE 4.3. PROTEINS IDENTIFIED VIA SEARCHING AGAINST ENSEMBL CANINE GENOME PREDICTED PROTEIN SEQUENCE. 176

Abbreviations

ABC	ammonium bicarbonate
ANOVA	analysis of variance
BB	blood borne
CAN	acetonitrile
CHCA	a-cyano-4-hydroxy cinnamic acid
D	diseased
Da	dalton
DTT	dithiothreitol
EC	extracellular
ECM	extracellular matrix
FBN	fibrillin
FGF-2	fibroblast growth factor 2
FILIP	filamin A interacting protein
FLN	filamin
FN	fibronectin
GAG	glycosaminoglycan
GAPDH	glyceraldehydes 3-phosphate dehydrogenase
H&E	hematoxylin and eosin
HSP	heat shock protein
IAA	iodoacetamide
IC	intracellular
ID	identifier
IgG	immunoglobulin G
LC	liquid chrmatography
LDL	low-density lipoprotein
Lrp5	low-density lipoprotein receptor
LSN	least significant number
M	mass value
MALDI-TOF	matrix-assisted laser desorption ionisation time of flight
MLC	myosin light chain
MMP	matrix metalloproteinase
MMVD	myxomatous mitral valve disease
MR	mitral regurgitation
MS/MS	tandem mass spectometry
MSDB	Mass Spectrometry Protein Sequence Database
MVP	mitral valve prolapse
MYL-4	Myosin light polypeptide
N	normal
NaOH	sodium hydroxide
NCBInr	National Centre of Biotechnology Information non-redundant
NOS	nitric oxide synthase
OD	optical density
PBS	phosphate buffered saline
RGB	red green blue
RPL19	ribosomal protein L19
RT-PCR	reverse transcription polymerase chain reaction
SDS-PAGE	sodium dodecyl sulphate polyacrylamide gel electrophoresis
SEM	scanning electron microscope
SLRP	small leucine rich proteoglycans
TEM	transmission electron microscope

TGF-b1	transforming growth factor-b1
TIMP	tissue inhibitors of metalloproteinase
TPM	tropomyosin
TRRAP	transformation transcription domain associated protein
VEC	valvular endothelial cell
VIC	valvular interstitial cell
α-SMA	α-smooth muscle actin

Abstract

Myxomatous mitral valve degeneration (MMVD) is the single most common cardiac disease of the dog, and is analogous to Mitral Valve Prolapse in humans. Very little is known about the aetiopathogenesis of this disease or the changes in valvular interstitial cell populations in diseased valves. The aim of this study was to identify morphological, cellular and molecular changes associated with MMVD.

Mitral valve leaflets from both normal and varying grades (Whitney's 1-4) of diseased dogs were subject to image analysis, immunophenotyping, proteomics and RT-PCR.

Image analysis - leaflet thickening due to accumulation of glycosaminoglycan was significant in this disease. MMVD is associated with loss of connective tissue, reduction in cell numbers but no change in cell shape in the overtly myxomatous area. Near the surface, increase in valvular interstitial cells (VIC) towards the damaged endothelium in concert with destruction of collagen and building up of ground substance was manifested during the disease process.

Immunophenotyping - activated myofibroblasts were increased and fibroblast-like VICs were reduced without any change in desmin and myosin expression in MMVD compared to clinical normal dogs. In addition, other cell types like macrophage, adipocyte, chondrocyte, mast cell, and stem cell were identified and their possible role in MMVD is discussed.

Proteomics - a protein expression profile was established, with 64 proteins being positively identified from dog's mitral valve using 1-D SDS PAGE LC/MS. Amongst them 44 proteins were differentially expressed comparing normal and severely diseased. Two actin binding proteins, tropomyosin alpha and myosin light chain-2 were found to be differentially expressed in the normal but down regulated in the diseased.

RT-PCR was used to assess the expression of 8 genes of interest. Their expression was compared with 3 different housekeeping genes.

1 Chapter 1 Background Information on Mitral Valve Disease

1.1 Introduction

Myxomatous Mitral Valve Degeneration (MMVD) is the most common cardiac disease in the dog[1]. It is characterised by myxomatous degeneration of the mitral heart valve. The disease is also referred to as Mitral Valve Endocardiosis (MVE) or Chronic Valvular Disease. The prevalence and severity of the disease was found to be closely age dependent. However, some breeds of dog are more predisposed to the disease than others, suggesting a likely inherited component to the disease in some breeds. The disease is most widely associated worldwide with the Cavalier King Charles spaniel. Pathologically, the disease is recognised by the presence of greyish-white nodules and plaque-like nodules, located in the area of apposition of the mitral valve leaflets[2]. Histological studies have shown that the disease is manifested by excessive destruction and derangement of the valve stroma with loss of the collagen bundle organisation and accumulation of glycosaminoglycans in the leaflets. An increase in the severity of valvular damage corresponds to a worsening of the clinical disability. MMVD leads to regurgitation of blood across the closed mitral valve during ventricular systole. As the disease progresses, the lesions are associated with further valvular incompetence, systolic murmurs and eventually congestive heart failure. The condition demonstrates close similarities to Mitral Valve Prolapse in humans in terms of the pathological change and the clinical outcome[3]. Although in humans, the displacement of mitral valve leaflets into the atrium occurs at a lower frequency[4, 5].

Despite major understanding of the diagnosis and pathology of this disease, very little information is available on the morphological and cellular phenotypic changes. The primary aim of this work is to fill in the gap in the current understanding of MMVD.

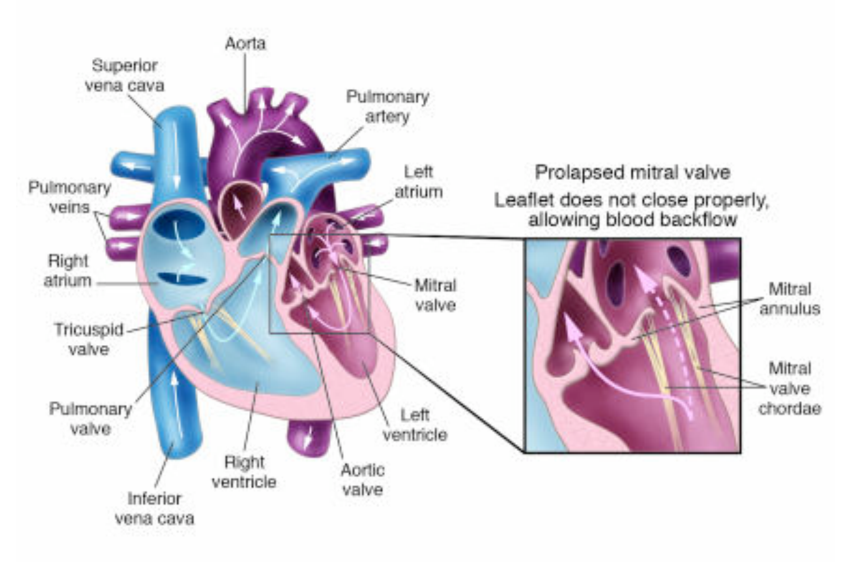

Figure 1.1. Diagram to show the anatomy of the heart and location of the mitral valve.

1.1.1 Mitral valve anatomy

The canine mitral valve complex, similar to humans and other species, consists of the annulus, two leaflets, chordae tendinea and the papillary muscles (Figure 1.1). The mitral valve, separating the atrium and ventricle in the left heart, is open during ventricular diastole and closes during systole and has to withstand the backward pressure during the full force of ventricular contraction[6]. This action requires all its components, together with the adjacent atrial and ventricular muscle, to work in a synchronized fashion in order to direct the blood flow from the left atrium to the left ventricle and finally ejecting it into the aorta[7, 8].

1.1.2 Annulus

The annulus is a complete ring-like fibrous cord that the leaflets are anchored to, although it is more D-shaped than circular. The straight border of the ring incorporates the fibrous continuity between the leaflets of the aortic and mitral valves. The annulus marks the hinge line of the mitral valve leaflets. However, when viewed from the ventricular side, the hinge line is not distinct as the fibrous continuity is an extensive sheet. The annulus also serves as the border separating the atrial and ventricular myocardial muscles. However, the atrial myocardium usually extrudes some distance into the leaflets beyond the level of the annulus.

The flexible nature of the annulus provides a firm origin for the leaflets and acts as a dynamic component during valve motion. Passive contraction of the annulus ensures that at ventricular systole the leaflets co-apt more effectively.

1.1.3 Leaflets

The mitral valve has two leaflets, which are distinctively different in shape and circumferential length. Each leaflet has an atrial and a ventricular surface. The septal leaflet, also known as the anterior or aortic leaflet, can be seen as the fibrous continuity of the aortic valve. It has a semi-circular shape that occupies a third of the annular circumference. The septal leaflet can be divided into two areas. The rough zone, which is slightly thick because of the chordae tendineae attached into it, includes the closure edge and a membranous zone, which is thinner and devoid of chordae tendineae.

The mural leaflet, also known as the posterior ventricular leaflet, is separated from the septal leaflet by two commissures. The mural leaflet is generally scalloped, with a larger central scallop and two smaller lateral scallops described as medial, middle and lateral. A rough zone and a membranous zone can also be identified, but this leaflet also has a basal zone, where the basal chordae tendineae arising, from the left ventricular myocardium end.

The two leaflets meet to form an arc shaped closure line, or zone of apposition. Even though the septal leaflet appears to form the major part of the atrial floor space, it is approximately equal in area to the mural leaflet. The commissures at each end do not reach all the way to the annulus. Strictly speaking there is not a clear commissural line to partition the two leaflets. The mural leaflet also forms slits that allow snug closure of the valve. An argument concerning the number of leaflets within the skirt of the left atrioventricular annulus has been raised; some authors suggesting the mitral valve has more than two leaflets[7, 8].

A single layer of endothelial cells continuous with atrial and ventricular endothelium covers the surfaces of the mitral valve leaflets. At the mid-point of a typical leaflet, there are four cross-sectional layers, namely atrialis, spongiosa, fibrosa and ventricularis. From the atrial side, the atrialis layer is rich in elastin, mixed with scattered collagen fibres and fibroblasts. Smooth muscle cells can also be seen in the atrialis. Underneath the atrialis lies the spongiosa, a loose connective tissue layer composed of loose collagen fibres, scattered collagen bundles and thin elastin fibres embedded in mucopolysaccharide rich ground substance. Within the loosely arranged collagen are scattered fibroblasts and Anitschkov cells (enlarged macrophages). Immediately adjacent to the spongiosa is a dense, well-organised fibrosa layer, which consists of well-defined collagen bundles with scattered entrapped fibroblasts. The fibrosa is continuous with the annulus fibrosus and branch off to form the core of the chordae tendineae. The ventricularis has collagen fibres and scattered elastin, which the chordaes are attached to[1, 6]. Towards the free edge, the junction between spongiosa and fibrosa becomes indistinct, with apparent merging of loose collagen bundles and ground substance of both layers. At the true free edge, this distinction is lost and the free edge appears as almost entirely consisting of spongiosa. Although the designation of the mitral valve leaflet cross-sections into layers is described, nevertheless the leaflet tissue is a continuum of structures from one surface to the other. The designation of segmentation into layers was merely to assist the observer to identify the prevalent segmental variability across the leaflet; the system being somewhat arbitrarily defined.

Based on the electronmicroscopic studies of healthy dogs of various ages, Fenoglio has subdivided the length of the septal leaflet into three zones on the basis of the extent of muscle[9]. The extruding muscle from the atria appears to be sandwiched between the atrialis and fibrosa. The proximal third closest to the annulus contains valvular muscle and appears to be a direct extension from the muscle of the left atrium. At the ultrastructural level, this proximal muscle is identical to atrial myocardium with atrial specific granules. Small nerves and vascular channels are scattered between the muscle fibres. In the middle third of the leaflet, the muscle tissue is progressively thinned leaving individual fibres. The individual muscle cells are surrounded by collagen bundles, fibroblasts and scattered elastic fibres. These loosely arranged constituents are distinctly separated fibrosa and lead to spongiosa. None of the valvular muscle is present in the distal third. In the mural leaflet, the muscle is in similar locations as in the septal leaflet. However, the muscle ends abruptly in the midportion of the leaflet and is immediately replaced by spongiosa and for that reason, Fenoglio divided the mural leaflet into two zones. Small nerves and vascular channels are also present in this leaflet.

1.1.4 Tendinous chords

The chordae tendineae are thin string-like structures that connect the papillary muscles to the mitral valve leaflets. The tendinous chords are attached to two groups of papillary muscles in the ventricular wall. The chordae arise from the apices of the papillary muscles, branch off in a fan-shaped fashion and attach to adjacent ends of both leaflets. The tendinous chords play a crucial role in determining the geometry and hence the performance of the valve. Chordal rupture will result in valve prolapse and regurgitation. The chordea have classically been described as first-, second- and third order chordae. This classification is according to the site of attachment to the leaflets. The first order chords are those attached to the free edge. They are numerous and often form networks near the edge. The second order chordae insert into the ventricular side of the leaflets beyond the free edge, forming the rough zones. Third order chorda attach only to the mural leaflet since they arise from the ventricular wall. They are attached to the basal portion of the mural leaflet. However, third order chordae are seldom found in dogs.

Other authors prefer to divide them into commissural, strut, cleft and basal chordae[10, 11]. The commissural chordae are those inserting into the commissures, and there are normally two. The rough chordae insert into the rough area of the leaflet, and each chordae divides into three before insertion. The strut chordae consist of two rough chordae which can be identified because of their increased thickness and length, and because they insert into the septal leaflet near its free edge. The basal chordae insert into the basal area of the mural mitral leaflet; they tend to be more numerous in the middle or larger scallop. Finally, the cleft chordae are those that insert into the clefts of the mural mitral leaflet, dividing into several small chordae before doing so. The interchordal spaces serve as important pathways for blood flow.

At the ultrastructural level, the cross section of chordae tendineae consists of three distinct layers[9]. An outer layer of flattened endothelial cells is separated by the basal lamina from an area of loosely meshed collagen, elastic fibres and scattered bundles of dense collagen. This is known as the spongiosa layer. Nerves are occasional found in this region. The central core is made up of dense, wavy, tightly packed collagen bundles running in parallel to the axis of the chorda. Scattered fibroblasts are found entrapped in the collagen, but no vessels have been identified[12]. At the point of insertion to the ventricular aspect of the leaflet, the endothelial cells and spongiosa of chordae are continuous with those of the leaflet, but the collagen core divides. The bulk of the collagen is continuous with the fibrosa and courses toward the annulus.

1.1.5 Papillary muscles

The two left ventricular papillary muscles are located in an ideal mechanical position beneath the ends of the zone of apposition or under the commissures between the leaflets; occupying the anterolateral and posteromedial positions in the ventricle. Normally, the papillary muscles arise from the apical and middle third of the left ventricular wall[7]. The anterolateral papillary muscle is generally single, and it receives its blood from the left anterior descending artery. The posteromedial papillary muscle generally consists of two bellies, and receives blood from the right coronary artery. Each muscle gives rise to tendinous chords, which in turn run to support both leaflets of the valve. Microscopic observations reveal the collagen in chordae branching into finger like processes and penetrating between cardiac muscle bundles at the tip of the papillary muscles. At the junction between chordae and papillary muscle, the spongiosa of the chordae expands to form a cushion of loose collagen, together with scattered elastic fibres and large lipid droplets. As the collagen fibres penetrate deeper into the papillary muscle, they divide into smaller and smaller units, eventually forming a network anchoring system much like the roots of a tree. Within the small, wavy collagen bundles, there are numerous small capillaries and nerve fascicles. The collagen fibres appear to terminate in the basal lamina of the muscle cells[9].

1.1.6 Pathology of myxomatous mitral valve disease

The normal healthy mitral valve leaflets are thin, pliable, translucent and soft. Mitral valve MMVD involves a complex connective tissue degenerative process with little or no inflammatory reaction. The pathology is recognized by the presence of greyish-white, smooth, glistening nodules or plaque-like elevations, often situated in the area of apposition on the atrialis surface of the leaflets. The diseased valve leaflets become opaque and thickened; they are more extensible and less stiff than normal leaflets. This compromises the dynamic mechanical properties of the mitral valve[13]. The lesions of MMVD represent a gradual process and may cause no detectable signs during early stage of structural change. However, as the disease progresses it will lead to insufficient co-aptation of the leaflets, increasing regurgitation of blood back into the atria, and in the late stage of the disease dilation of the left ventricle and mitral annulus occurs, and in some cases jet lesions and ruptured chordae. As a consequence, these lesions will lead to mitral systolic murmurs, and in severe cases, congestive heart failure.

Older literature has referred to this disease as a process of 'valvular fibrosis'[14]. However, this concept has been challenged by the observation that the disease process involves thickening of spongiosa and destruction of fibrosa.

1.1.7 Epidemiology

Various papers have reported the occurrence of MMVD in dogs, ranging from 21% to 89% in dogs[1, 15-17]. This huge divergence in these findings might be attributed to the disparate clinical sample selection of the groups of dogs. Apart from the sample pool size, other criteria such as age and breed could influence the reports markedly and these factors should also be take into consideration.

Similar lesions can also appear in tricuspid and aortic valves[18], concomitant with mitral valve lesions, although the incidence of lesions in tricuspid (30%) and aortic valves (3%) occur at much lower frequency. A necropsy survey carried out on 230 dogs with valvular disease at University of Pennsylvania Veterinary Hospital showed the relative incidence of mitral valve lesions involved in 227 dogs at 98.7%. Among the 227 dogs, 143 had lesions affecting the valve alone, the rest had lesions affecting aortic and tricuspid valves as well[1, 2].

1.1.8 Lesion grades

Due to considerable variation in the size of the normal heart valve in different breeds of dogs, direct measurement of the valve lesions offers limited assistance as a gauge of the degree of valve damage. A visual scoring method developed by Whitney[2], is widely used to classify the diseased valve lesions into one of four grades. This scoring method has proved most useful in practice and is robust. A similar classification system is not available for human mitral valve disease. The principal criteria for the classification system are as follows:

Type 1 lesion

A few small oedematous nodules are seen in the area of apposition. There are areas of diffuse opacity in the basal regions of the leaflets. The chordae tendineae themselves are unchanged. There is no sign of valvular incompetence.

Type 2 lesion

Multiple nodules have a tendency to coalesce with their neighbours to form larger nodules in the area of apposition. Some nodules are greyish-white in colour. Areas of diffuse opacity can be observed. The chordae tendineae are unaffected and there is no evidence of valvular incompetence

Type 3 lesion

The nodules are increased in size and some coalesce to form irregular plaque-like deformities in the area of apposition. The chordae tendineae are thickened at the junction with the leaflets. The basal zones of the leaflets have defined areas of opacity. There is evidence that the lesions are associated with valvular incompetence.

Type 4 lesion

The leaflets are grossly distorted with large, greyish-white nodules and plaque-like elevations, predominantly situated in the area of apposition. Along the closure line, the free border may have a rolled edge and ‘ballooning’ overgrowth. The chordae tendineae are thickened. These chordae may be stretched and ruptured in some cases. There is evidence of valvular incompetence in the majority of these cases[2, 4].

The grading system is easy to apply and can provide useful information on the pathogenesis of the disease as each grade represents a stage in the development of the disease process. However, this grading system requires a familiarization with all the manifestations of the disease and may become subjective from person to person.

Whitney found the prevalence and severity of mitral valve lesions correlated with increase in age, based on a post mortem study of 200 dogs subjected to the grading system. When combining all four grades, he found lesions in 37% at 0-4 years of age, 80% at 5-8 years of age, 93% at 9-12 years of age and a staggering 100% at 13-16 years of age. Type 1 lesions (15%) were found predominantly in dogs under 5 years old. Type 2 and 3 lesions (49%) were common in dogs 9-12 years old, while type 3 and 4 lesions (88%) were predominately confined to dogs 13 years and over. The more advanced Types 3 and 4 lesions were found in 24% of the dogs under 9 years old in comparison to 58% in dogs over 9 years old; where the majority showed evidence of congestive heart failure[2].

A modification of the classic Whitney's grading of lesions was proposed by Kogure; instead of 4 types of lesion, Kogure categorised the mitral lesions into 3 groups. Group I corresponded to Whitney's types 1 and 2, whereas Group II is similar to Whitney's type 3 and Group III resembled Whitney's type 4. Among the 64 dogs with mitral valve lesion studied by Kogure, 30 (47%) dogs with a median age of 2 year old were classified into Group I; 22 (34%) dogs with a median age of 4 were in Group II and 12 (19%) dogs with a median age of 10 were in Group III. The result was parallel to Whitney's finding that the severity of lesion increased with age[17]. The term grade 1-4, corresponding to Whitney's Type I-IV are widely used in the veterinary cardiology community and will be adopted as the terms used in this thesis.

1.1.9 Diagnosis

Auscultation examination for cardiac murmur is the common diagnostic method[19]. The systolic murmur is always associated with mitral regurgitation (MR), a complication of MMVD[20]. The murmur sound can be measured in one of the six grades. However, hearing a murmur in a dog with MR is not only dependent on the disease severity, but also on other factors such as the experience of the auscultatory examiner and how difficult the dog is to auscultate[20]. Over the recent years, echocardiography has proven to be the most reliable non-invasive method for the diagnosis of MR[21]. The four-chamber view in echocardiography made visualisation of mitral valve in its nature state is especially useful for diagnosis of MMVD[22].

1.1.10 Valvular interstitial cells (VIC)

Valvular interstitial cells (VIC) are responsible for the maintaining the structural integrity of the valve. The extracellular matrix (ECM) depends on a dynamic balance of synthesis and degradation, which is governed by VIC metabolism. The extracellular matrix (ECM) comprises primarily collagen, elastin and glycosoaminoglycans[23]. VICs also express ECM degradation enzymes such as matrix metalloproteases (MMPs). Fibroblasts of mesenchymal origin are believed to be the most prevalent VIC. Recent studies have suggested a phenotypic change of the valvular interstitial cell from a predominantly fibroblast-like phenotype to a more mixed myofibroblast and/or smooth muscle cell-like phenotype in diseased states[23-

[26]. This phenotypic switching in the disease process is accompanied by dramatic increase in cell numbers and excess secretion of catabolic enzymes[27].

1.1.11 Valvular endothelial cells (VEC)

Denudation of VEC in the mitral valve leaflet in of dogs with myxomatous degeneration was found similar to endothelium damage in human mitral valve prolapse[28-30]. Damage to VEC could influence the synthesis and release of vasoactive substances that in turn interact with matrix tissue. Increased endothelin receptor and NADPH-diphorase activities have been found in canine myxomatous mitral valve leaflets[31, 32]. Therefore, the VEC was suggested to play a role in the pathogenesis of MMVD in dog. Furthermore, the endothelium morphology in diseased mitral valves resemble a response to injury process, a repeat impact model was hypothesed[33].

1.1.12 Extracellular matrix (ECM)

Although the ECM composition in canine mitral valve is not well characterized, its composition is similar to the well-studied human mitral valve. The mitral valve is a complex connective tissue structure, the ECM contains structural proteins like collagen and elastin for mechanical function and proteoglycans and GAG for compliance[34]. It is known that loss of collagen density and changes in fibril alignment accompany canine MMVD[35].

1.1.13 Matrix metalloproteinases (MMP)

Increases in MMP have been linked to MMVD progression in dogs. MMP induced mitral valve regurgitation has been demonstrated in dogs[36, 37]. MMP are a family of Zn^{2+} dependent endopeptidases that participate in tissue remodelling in several physiological and pathological states[38, 39]. At present, 20 MMPs are known, the members of the family share structural homology and each cleaves at least one component of the ECM[39]. The MMPs are secreted as latent zymogens and require catalytic activation by plasmin or other MMPs through conformational change of the active site in the molecule[40], and are inhibited by their specific tissue inhibitors (TIMPs)[38, 40, 41].

1.1.14 Main objectives of this thesis

Much is know about the clinical features of MMVD, its diagnosis and management, but little is know about the aetiopathogenesis. The hypothesis is the alteration in the valvular interstitial cell function that precipitates the myxomatous degeneration characteristic of the disease. The aim of this thesis is to 1) identify the morphological changes associated with MMVD; 2) map out the cellular phenotypic changes and investigate their relationships to ECM during the disease process and 3) identify the proteins associated with MMVD.

2 Chapter 2 Morpholgical Assessment of the Changes in Myxomatous Mitral Valve Disease

2.1 Introduction

Morphological changes are the criteria for the assessment of myxomatous mitral valve disease pathology[2, 42]. While the alteration in cellular phenotypes has been implicated as the determinant of the disease[29, 43, 44], there is little information on morphological change in the valve particularly at the ultrastructural level. Most reports to date have been limited and descriptive.

The aim of this chapter is to give a detailed account of morphological and cellular changes in this disease using a combination of qualitative and quantitative analyses. Microscopic modalities of light microscopy and electron microscopy, in both transmission and scanning mode, were used to assess changes. The light microscopy was applied to histological stained sections using novel parameters, rendering comparisons between samples or even between breeds justifiable. The electron microscopy approach provided insight into detailed ultrastructure that would achieve high resolution and generate meaningful data. Incorporating digital imaging and computer analysis changes that can now be assessed quantitatively makes the analysis of pathological events at a focused level possible. This permits the study of these processes on a measurable basis, not only in cellular phenotypical changes but also in relation to other tissue constituents at microscopic level. ImageJ is a public domain, Java-based image analysis program developed at the National Institutes of Health. ImageJ was designed with an open architecture that provides extensibility via Java plugins and recordable macros. Image analysis allows pictorial information to be improved for qualitative human interpretation and offers the possibility of extracting valuable quantitative data as well.

In this chapter, the results of ad-hoc methods using efficient image processing techniques to analyse morphological changes in myxomatous mitral valve disease quantitatively at micro- and ultrastructural levels are presented.

2.2 *Materials and Methods*

2.2.1 Mitral valve procurement

Hearts were collected from 30 dogs (various pure and mixed breeds, 22 male, 8 female, age range between 1 to 15 year) presented to the Hospital for Small Animals, Easter Bush Veterinary Centre, University of Edinburgh for euthanasia. The background of each dog regarding to age, breed, sex and medical history were carefully scrutinized; these data were entered into a custom designed FileMaker Pro 6 (FileMaker Inc., CA, USA) data bank.

Prior to euthanasia each dog was examined by an experienced veterinary cardiologist. Detectable murmurs were graded on a scale of 1-6[19]. Euthanasia was carried out by intravenous injection of pentobarbital sodium (Merial Animal Health Ltd., Essex, UK) and tissue was collected with full owner consent.

2.2.2 Tissue dissection

The hearts were surgically removed within a few minutes of death and gently flushed with 0.01 M phosphate buffered saline (PBS, Sigma, Dorset, UK) to remove blood. The left ventricle was then filled with PBS to observe the coaptation state of the leaflets and photographed digitally. The left ventricle was opened by carefully cutting between the septal and mural leaflets. The anatomy of the mitral complex was examined. The extent of valvular lesions was assessed by two experienced veterinary cardiologists and a gross pathological grade assigned according to the criteria set out by Whitney (Grade 1-4)[2].

The mitral valves were removed by cutting the annulus base from the myocardium wall. Thin stripes of tissues were excised from the middle of the leaflets (both septal and mural) running from the free edge to the annulus base avoiding major chordae. Following dissection, tissue was preserved in 4% paraformaldehyde (Sigma, Dorset, UK) buffered in 0.01M PBS before embedding in paraffin wax. Serial sections (5µm) of leaflets in transverse position were collected on slides using a rotary microtome.

2.2.3 Histology

Sections were stained with hematoxylin and eosin for general morphological analysis. For the study of connective tissue structures, Masson's trichrome stains were used to stain for elastin, Wiegert's van Gieson stains to stain for collagen and Alcian Blue stain to stain for GAGs.

2.2.4 Microscopy and photography

Microphotographs of low magnification (1.6× objective lens) were acquired using a Leica light microscope linked to a Nurolucida system (Micro Bright Field Inc. VT, USA). Microphotographs of higher magnification (4×, 10×, 20× and 40×) were captured on a Leitz Laborlux microscope (Leica, Germany) fitted with a CCD digital camera (Sony, Japan). To eliminate uneven Kohler illumination across a field, a digitized image of a blank field was taken at exactly the same lighting conditions, then this blank was used to correct other image on a pixel-by-pixel basis by subtracting the background image on Adobe Photoshop CS (Adobe Systems Incorporated, CA, USA).

2.2.5 Image analysis

The morphological analysis was performed on a Macintosh PowerBook G4 (Apple Computer, Cork, Ireland) using the public domain ImageJ software (National Institutes of Health, USA).

2.2.6 Leaflet length

The Hematoxylin and Eosin cross-section slices representing the entire transverse area from annulus to tip of the leaflets were used. Due to the considerable variation in the size of the mitral valve between different breeds of dogs, direct interpretation of the actual sizes offers no meaningful results in helping understanding of the disease process. Therefore, relationships were expressed in terms of ratios to overcome this disparity in breed size. The central axes of the leaflets were best fitted using the segmented line selections (Figure 2.1). The entire length of the leaflet running from the annulus to the tip was measured. The leaflet length ratio for each mitral valve was defined as the length of septal over mural leaflets.

Figure 2.1. A schematic diagram shows how the central axis is plotted for leaflet length measurement.

2.2.7 Leaflet thickness

A thickness index was measured and defined as the ratio of the distal third of the leaflet to the average of two thickness measurements; one taken at the neck of the distal in the junction between middle third and distal third, and one taken at the mid point of the leaflet (Figure 2.2).

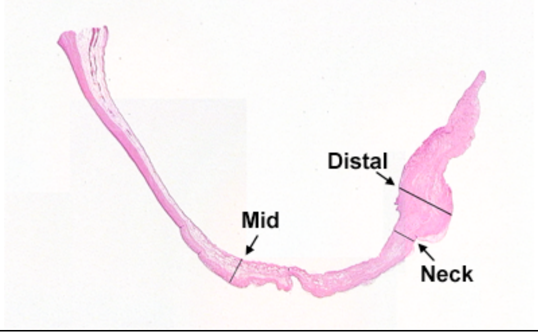

Figure 2.2. A schematic diagram shows the positions of the three cross-sectional thickness are taken for leaflet thickness measurement.

2.2.8 Cell density

From Hematoxylin and Eosin slides, images of the spongiosa layer in the distal third of the leaflet were taken at 100× magnifications. Areas of myxomatous valve were identified and measured using the outline function. Cells were selected based on the density threshold and subjected to watershed segmentation using ImageJ.

2.2.9 Cell circularity

Of the 17,561 cells that were identified in the cell density study, their circularities were measured with the circularity function of ImageJ software. The circularity is defined by the equation $4\pi(\text{area}/\text{perimeter}^2)$, such that the perfect circle has a value of 1 and any value deviating from 1 towards zero indicating alteration in shape from a perfect circle, which can include elongation. The total number of cells and the average circularity were recorded in Excel data sheets.

2.2.10 Connective tissue

From Masson's Trichrome stained slides, images of the distal third of the leaflet were taken at 100× magnifications. Areas of interest, myxomatous in disease and loose connective tissue spongiosa in normal valves, were selected using the outline function of ImageJ. A threshold was applied to pick up the connective tissue in binary (black and white) density. The amount of connective tissue was measured and expressed as a fraction of total selected area.

2.2.11 Glycosaminoglycan (GAG)

From red-green-blue (RGB) microphotographs of Alcian blue (Periodic Acid Shiff pH 2.5) stained slides, the entire cross-sectional area of the mitral valve leaflet was selected and the amount of GAG, represented by the extent of blue stain, was determined using four different methods; k-means Clustering, RGB Split, Threshold Colour and Colour Deconvolution. Each method utilised a separate ImageJ plug-in to perform the task and details are listed as follows.

1. k-means Clustering method: performed pixel-based segmentation of an RGB image. Each cluster was defined by its centroid in colour space. Pixels were grouped by their proximity to a cluster's centroid and the cluster of 'blue' analysed.
2. RBG split method: the image was separated into three 8-bit greyscale images containing the red, green and blue components of the original and the blue channel was analyzed.
3. Threshold Colour method: converted RGB to HSB (hue, saturation and brightness). The hue value from 140 to 200, deemed to cover the complete range of the blue spectrum was used. Selected pixels were put into a binary format and analyzed.
4. Colour Deconvolution method: implemented a stain separation protocol using stain vector. To avoid co-localisation of colours, the previously defined colour values for Alcian Blue and Hematoxylin were used[45, 46]. The detected Alcian Blue stains were also changed to binary and the analyzed.

Finally, the blue pixel of the Alcian Blue stain measured from the above mentioned methods were computed with the Analyze Particles function of ImageJ and the results were expressed as a percentage of the entire cross-sectional mitral valve leaflet area.

From the entire outlined area of the leaflet, the mean, median, modal, integrated density and the forth moment kurtosis values from the blue channel of the RGB image was measured using the Measure RGB plug-in. These values were standardised against their own weighted RGB reference value

(0.299Red+0.587Green+0.114Blue). Furthermore, the means of the green and blue colours in the same area of the RGB image were also calculated. The means of the RGB colours were ranked in a descending order.

2.2.12 Statistical analysis

Data are expressed as means ± standard error of the means. Inferential statistical analysis involved one-way analysis of variance ANOVA testing, a *p*-value less than 0.05 was considered as being statistically significant. Means comparisons between groups were subjected to each pair Student's t-test. Due to the number of samples in this study, the non-parametric Wilcoxon ranked score was applied to validate the significance level and Chi^2 were reported along side the *p*-value.

Explanation of the graphical display used for demonstrating statistical difference in the image analysis study.

1. Chart displaying means diamonds may be interpreted as follows: A means diamond illustrates a sample mean and its 95% confidence interval, as shown by the schematic (Figure 2.3). The centre line across each diamond represents the group mean. The vertical span of each diamond represents the 95% confidence interval for each group. Horizontal overlap marks are drawn above and below the group mean. The width of the diamond is proportional to the sample size of each level of the x variable. It follows that the narrower diamonds are usually the taller ones because fewer data points yield a less precise estimate of the group mean. The grey line across the entire chart is the grand mean. The *p*-value shown with charts represents the overall analysis of variance significance level[47] (JMP version 5.0.1, SAS, NC, USA). The confidence interval computation assumes that variances are equal across observations. Therefore, the height of the confidence interval diamond is proportional to the reciprocal of the square root of the number of observations in the group.

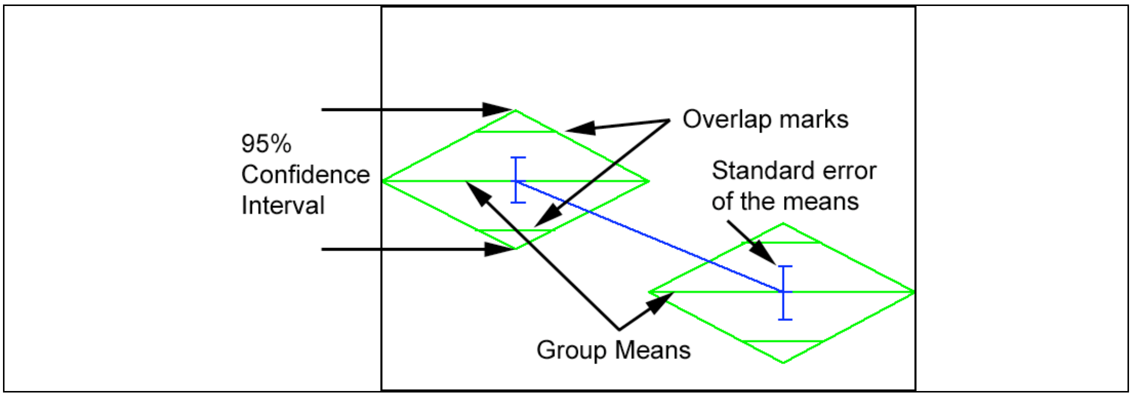

Figure 2.3. Features of the means diamonds display used in charts

2. The plot displays a circle for each group, with the centres lined up vertically. The centre of each circle is aligned with its corresponding group mean. The radius of a circle is the 95% confidence interval for its group mean, comparable to the means diamond. Comparison circles are a graphical technique that allows visual observation of significant separation among means in terms of how circles intersect. The non-overlapping confidence interval shown by the diamonds for groups that are significantly different correspond directly to the case of non-intersecting comparison circles. When the circles intersect, the angle of intersection is the key to determine if the means are significantly different. If the angle of intersection is exactly a right angle at 90°, then the means are on the borderline of being significantly different. If the circles are further apart than the right angle case, then the outside angle is more acute and the means are significantly different. If the circles are closer together, the angle is larger than a right angle; then the means are not significantly different as shown by the schematic (Figure 2.4).

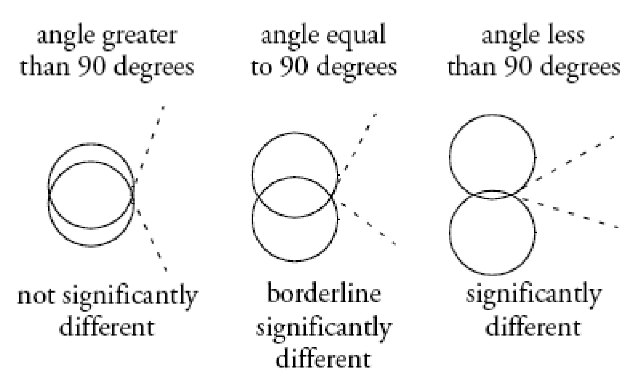

Figure 2.4. Diagram of how to interpret the significant difference in comparison cycles.

3. In the case that ANOVA of group means yields no statistical difference, that is when p>0.05, then the least significant number was calculated to test the sample pool size. The least significant number or LSN is defined as the number of observations needed to drive down the variance of the estimates enough to achieve a significant result with the given values of alpha, sigma, and delta (the significance level, the standard deviation of the error, and the effect size, respectively).
4. Means Comparisons table, which shows all means comparisons with letters denoted for each level are also presented. The groups are listed with the differences sorted in descending order. Levels not connected by same letter are significantly different. Conversely, the levels that share a letter are not significantly different from each other.
5. Analysis of nominal based categorical data is presented in contingency table mosaic plot. A mosaic chart has side-by-side divided bars for each level of its X variable. The bars are divided into segments proportional to each discrete level of the Y variable. The width of each bar is proportional to the sample size. When the lines dividing the bars align horizontally, the response proportions are the same. When the lines are far apart, the response rates of the samples might be statistically different. The hypothesis of marginal homogeneity was tested for independence; the p-values of Chi-square tests from likelihood-ratio and Pearson are reported.

2.2.13 Transmission electron microscopy (TEM)

TEM was employed to study the phenotypic changes at ultrastructural level. Mitral valves from six dogs were used in this study, three from clinical normal Grade 0 dogs and three from dogs diagnosed with severe MMVD Grade 3 or above. Normal valves were from dogs of aged six year old or younger, whilst MMVD affected valves were all from dogs aged eight years or over. Diseased group dogs all had left apical systolic heart murmur, clinical and radiographic signs of congestive heart failure. Details about the dogs are shown (

Table 2.1).

Table 2.1. Background information about the dogs that samples were obtained from.

Mitral Valve	Breed	Sex	Age
Normal	Mixed Breed	Male	3yrs
Normal	Labrador X	Male	2yrs
Normal	Staffie X	Male	6yrs
Diseased	Cavalier King Charles	Male	13yrs
Diseased	Jack Russell Terrier X	Male	16yrs
Diseased	German Shepherd	Female	8yrs

Specimens from valve tissue were taken from the middle strip of the leaflets. The tissues were immediately fixed in 2.5% electron microscope grade glutaraldehyde (Agar Scientific Ltd., Essex, UK) in 0.1M sodium cacodylate (Agar Scientific Ltd., Essex, UK) buffer overnight. The specimens were rinsed excess glutaraldehyde with 0.1M sodium cacodylate buffer (three times for 30 min each) followed by distilled water (three times 2 min each). The specimens were post fixed in 1% osmium tetraoxide OsO_4 (Electron Microscopy Science, Ft. Washington, PA) for 1.5 hours. After removal of excess osmium with distilled water (three times at 2 min each), the specimens were dehydrated in a series of ascending concentrations of ethanol (Fisher Scientific, UK) (50% for 15 min, 70% for 15 min, 90% for 15 min and 100% for 30 min) and eventually twice for 30 min in pure acetone (Fisher Scientific, UK). The specimens were incubated in Spurr™ resin (Agar Scientific Ltd., Essex, UK) and acetone mixture in a 1:2 ratio for an hour followed by Spurr™ resin and acetone in a 1:1 ratio for an hour at room temperature. The specimens were clearly labelled and then cured in a silicone mould with Spurr™ resin at 70°C overnight. The embedded specimen blocks were subsequently trimmed and sections cut using glass knives on a Leica Ultracut™ UCT microtome (Reichert, Vienna, Austria), initially at 1 μm semi-thin, and stained with Toludine Blue. The semi-thin sections were viewed under a Leitz Laborlux light microscope (Leica, Germany) and areas of interest were selected for ultra-thin sectioning. The ultrathin sections of 60nm, with gold inference colour, were collected on Formvar coated single hole copper grids (Agar Scientific Ltd., Essex, UK) and stained with 2% uranyl-acetate (Merck, Darmstadt) for 45 min followed by lead citrate (Electron Microscopy Science, Ft. Washington, PA) for 6 min. The ultra-thin sections were then examined in a Philips CM12 transmission electron microscope (Philips, Netherland) at 75kV beam acceleration voltage and electron micrographs (Kodak Electron Microscope Film 4489, Eastman Kodak, New York) were taken. Ultrastructural identifications were based on cross-reference to published literatures[9, 48, 49].

2.2.14 Quantitative stereology

From each of the six blocks, three ultra-thin sections were cut at assigned points along the length of the septal leaflet, the first one at the tip, the next section was taken 50 μm from the first one towards the base, and the third section was taken a further 50 μm towards the base. Ten images were taken from each of the 18 sections, at random points along the length of the endothelial edge, giving a total of 180 images.

A 1 cm and 1 mm grid were prepared using Macromedia Freehand program (San Francisco, CA USA) and printed on to clear acetate. Electron micrographs were scanned into digital format and viewed using Window Picture and Fax Viewer. Using the 1 cm grid, the number of times collagen lay under a grid intersection was counted. This process was repeated for extracellular matrix. The 1 mm grid was used to count the grid intersections overlying endothelium and interstitial cells. For normalization, the values for collagen and extracellular matrix were multiplied by a factor of 10.

2.2.15 Circularity of endothelium and valvular interstitial cell

From the 180 transmission electron micrographs, non-interrupted endothelium (EH) and valvular interstitial cells (VIC) were identified. The outline of each cell along cell membrane was traced and the circularity was calculated using ImageJ.

2.2.16 Scanning electron microscopy (SEM)

To investigate the connective tissue more closely at ultrastructural level, a modification of the NaOH cell-maceration technique reported by Rossi was used[50]. The value of this technique is that it can dissolve the cellular elements and leave behind the connective tissue matrix intact, allowing for better three-dimensional viewing. Thin strips of tissues were excised in the middle of the septal leaflets running from the free edge to the annulus from one normal and one from each grade of the diseased mitral valves, Following dissection, the tissues were preserved in 4%

paraformaldehyde (Sigma, Dorset, UK). After rinsing in distilled water, the specimens were immersed in 10% NaOH (Sigma, Dorset, UK) solution for 4 days at room temperature. The specimens were rinsed the excessive NaOH until they became transparent, then they were immersed in 1% tannic acid (gift from Scottish Forest Research) for 4 hours at room temperature. Subsequently, the specimens were thoroughly rinsed in distilled water overnight before post fixation in 1% osmium tetroxide OsO_4 (Electron Microscopy Science, Ft. Washington, PA) for 2 hours. After removal of excess of osmium with distilled water (three times for 2 min each), the specimens were dehydrated in a series of ascending concentrations of ethanol (Fisher Scientific, UK) (50% for 15 min, 70% for 15 min, 90% for 15 min and 100% for 30 min) and eventually twice for 30 min in pure acetone (Fisher Scientific, UK). The edges of the specimens were trimmed in the transverse direction with two sharp clean blades in a scissors action under a dissection microscope (Leica, Wetzlar, Germany). Dehydrated specimens were then critical point dried (Polaron, Quorum Technologies, East Sussex, UK), mounted on aluminium stubs (Agar Scientific, Essex, UK), sputter coated with gold palladium (EmScope, Quorum Technologies, East Sussex, UK), and viewed in a Philips SEM 505 (Philips, Netherland). Structural changes were manifested in the mid zone and the distal zone of the leaflets during the degenerative disease process. Areas of interest were photographed on black and white negative film (Kodak Electron Microscope Film 4489, Eastman Kodak, New York). The negatives were scanned on a flat bed film scanner at 300 dpi (Hewlett-Packard, Berkshire, UK).

2.2.17 Image analysis of cell-macerated connective tissue using SEM imagery

One assumption has to made before applying microstructure analysis. That was to distinguish tissue structure and hole or void spaces. SEM imagery of cell-macerated mitral valve connective tissue was analysed using an ImageJ plug-in “SEM microstructure descriptors software”[51]. The images were de-noised by applying a 3×3 median filter to produce accurate results. This software utilizes two commands, namely BinariseSEM and Compustats. BinariseSEM, segments the input grey scale image into pores and structure, where a pore is defined as a patch of contiguous pixels with similar intensity values. Any discontinuity in the pixel intensity is regarded as a discontinuity in the structure of the material. The possible illumination gradient effect due to the acquisition system was taken into account by selecting the Bandpass Filter option; a filter was used to correct the intensity gradient. A threshold value was automatically computed, after visual inspection where any adjustment necessary, the threshold value was used for automatic binarisation. CompuStats performs various statistical analysis on the holes extracted, using the BinariseSEM and the results were presented in histograms and rose plots. The magnification factor in microns of the images was taken into consideration during computation. Examples of feature shape descriptor are shown in Table 2.2.

Table 2.2: Shape quantitative descriptors. Meanings of the parameters. A: net area; Aconvex : area of the convex hull; Afill area of the filled polygon; p: perimeter; pconvex : perimeter of the convex hull; Dmax , Dmin : maximum and minimum dimension; dinscr and dcircum: diameters of the inscribed and circumscribed circle; l: length of the feature along the farthest points in the convex hull; lF , wF : fiber length and fiber width (measured from the skeleton of the feature).

Parameter name	Formula	Parameter name	Formula
Form Factor	$\frac{4\pi \cdot A}{p^2}$	Convexity	$\frac{p_{convex}}{p}$
Roundness	$\frac{4A}{\pi \cdot D_{\max}^2}$	Solidity	$\frac{A}{A_{convex}}$
Aspect Ratio	$\frac{D_{man}}{D_{\min}}$	Hole Fraction	$\frac{A_{fill} - A_{net}}{A_{fill}}$
Elongation	$\frac{l_F}{w_F}$	Radius Ratio	$\frac{d_{inscr}}{d_{circum}}$
Curl	$\frac{l}{l_F}$	Directionality	gradient direct

2.3 **Results**

2.3.1 Breed

The breed distribution of the 30 dogs used in this study is shown in Table 2.3.

Table 2.3. Breed distribution of dogs.

Breed		Number
Beagle		4
Beardie Collie		1
Border Collie		2
Cavalier King Charles Spaniel		2
Collie		1
Collie Cross		4
Collie Terrier		1
German Shepherd Dog		5
Jack Russell Terrier		3
Kerry Blue		1
Labrado		1
Mixed Breed		1
Spaniel		1
Staffie		2
Yorkshire Terrier		1
	Total	30

2.3.2 Age

The disease is known to follow an age dependent process and the results of this study demonstrated the expected progressive nature of this disease. There was a positive correlation between the age and the grade of lesion, as the age increased so did the disease severity before it reached a plateau ($p<0.0001$). The mean ages were as follow, normal Grade 0=2.40, Grade 1=6.83, Grade 2=10.75, Grade 3=12.25 and Grade 4=11.75. Between group comparisons showed that the Grade 0 normal was significantly different to all four Grades of the diseased, the Grade 1 was significantly different to Grade 0 normal as well as to Grade 2, 3 and 4. This is illustrated by the mean age in year plotted against the lesion grade incorporating with Student's t comparison circles in Figure 2.5.

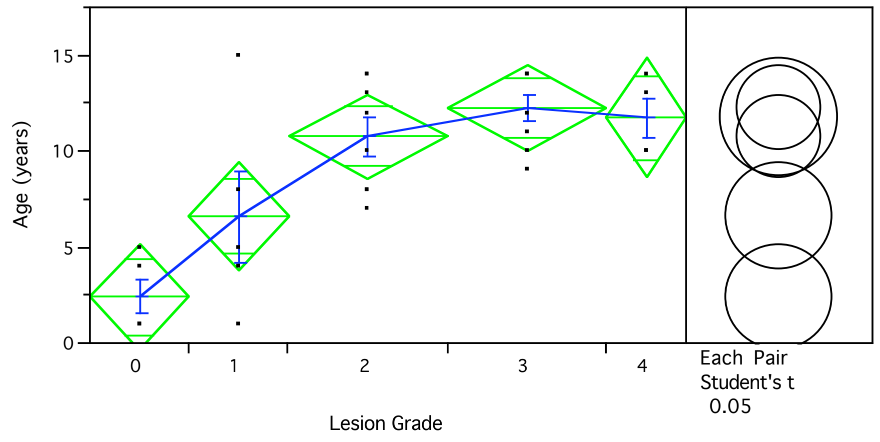

Grade				Mean	p<0.0001
3	A			12.250000	ChiSq=0.0037
4	A			11.750000	
2	A			10.750000	
1		B		6.833333	
0			C	2.400000	

Figure 2.5. Comparison of dog age to mitral valve lesion grade. The results from ANOVA, t-test, and Wilcoxon ranked test are presented. The age is increased during the progression of the disease.

None of the Grade 0 normal dogs were older than 5 years. The distribution of dog age according to the lesion type is shown in Figure 2.6. The dashed blue line joining the means of each group demonstrates the age dependent nature of this disease. With the exception of one dog, no other dogs younger than 9 years had progressed beyond Grade 3. On the other hand, with the exception of one dog, no dogs under the age of 9 had lesion grade 3 or higher. The best linear fit analysis of variance (red line) intercepted with age on the y-axis at 4.08 years and this extrapolated the age of onset. The mean of response is 9.16 year of age at lesion grade 2.54. The difference between different lesion grade groups was significant ($p < 0.0001$).

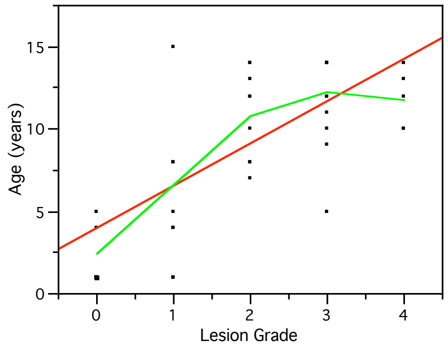

Figure 2.6. The distribution of dog age according to the lesion grade. The best line fit intercepts with the age on the y-axis at 4.08 year of age.

2.3.3 Murmur

For the 28 dogs where auscultation were obtained, the systolic cardiac murmur as assessed by auscultation grade 1-6 was plotted against the lesion grade and is shown in the bivariate scatter plots in Figure 2.7. The intensity of the murmur correlated to the severity of the MMVD ($p<0.0001$). The linear fit intercepted with lesion grade as a measure of disease severity on the x-axis at 0.9.

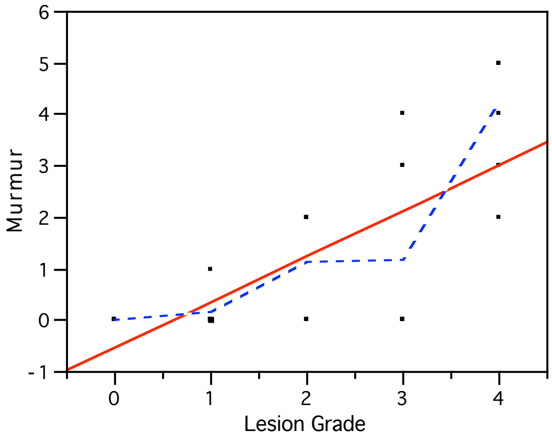

Figure 2.7. Comparison of murmur to mitral valve lesion grade. The best line fit intercepts with the lesion grade x-axis at 0.9.

2.3.4 Gross pathology

The normal healthy mitral valves leaflets were very thin and almost translucent. Valves with grade 1 lesions lost the translucent appearance and became opaque, small nodules budding out from the atrialis surface of the leaflets, notably near the free edges. The nodules seem to fuse with their neighbours to form larger nodules near the area of apposition in the valves with grade 2 lesions. Some nodules were greyish-white in colour. Areas of diffuse opacity could also be observed. In valves with grade 3 lesions, plaque-like thickening were found in the area of valve leaflet apposition. The chordae tendineae were thickened at the junction with the leaflets. In the valves with grade 4 lesions, the leaflet structures were grossly distorted. ‘Ballooning’ or ‘hooding’ types of over growth were found along the thickened free edges. The enlarged chordae were ruptured in some cases (Figure 2.8).

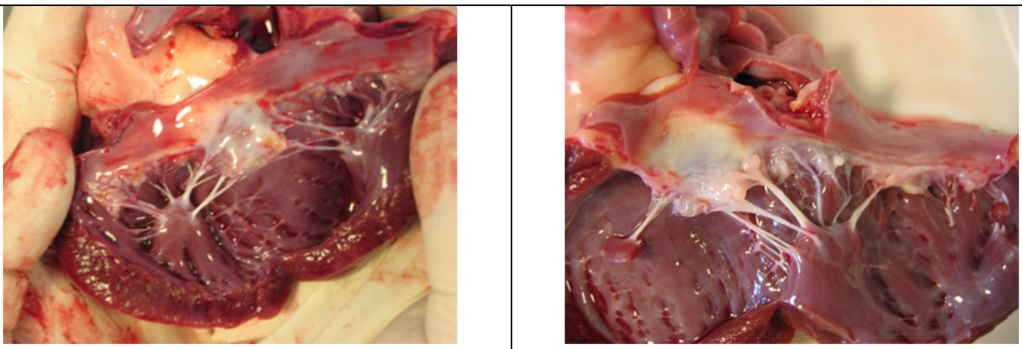

Grade 1

Grade 2

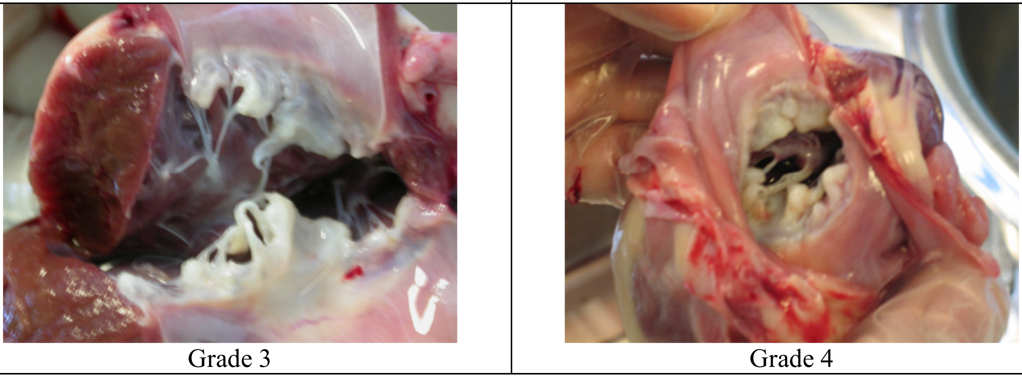

Grade 3

Grade 4

Figure 2.8. Photographs of mitral valves at necropsy showing lesion grades 1-4.

2.3.5 Light Microscopy Study

Representative Hemotoxylin and Eosin stained sections of mitral valve septal leaflets in normal and different diseased states are shown below (Figure 2.9).

Normal Grade 0

Grade 1

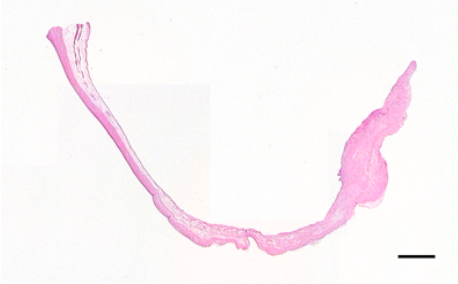

Grade 2

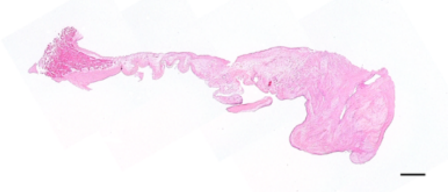

Grade 3

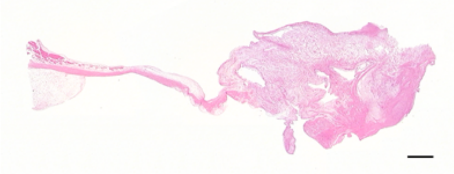

Grade 4

Figure 2.9. Representative of Hemotoxylin and Eosin stained cross-sectional mitral valve leaflet tissues. Bar = 1mm.

In general, in the normal valve the septal leaflet is longer than the mural leaflet. On the atrialis surface, there are many microscopic crimps in the proximal half of the leaflets. Those crimps can stretch out during valve opening, thus increase the atrialis surface area to reduce tension strain (Figure 2.10).

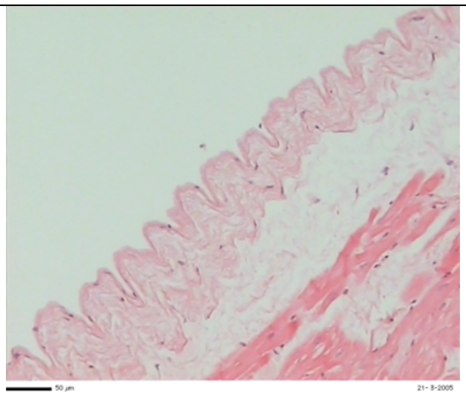

Figure 2.10. H&E stained section of a normal mitral valve leaflet shown crimps on the atrialis surface. Bar = 50μm.

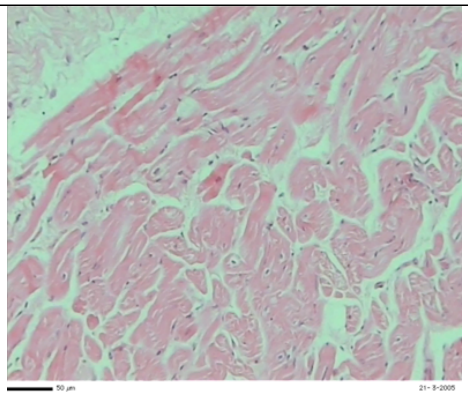

Figure 2.11. H&E stained section of a normal mitral valve leaflet shown the muscle at the base. Bar = 50μm.

Beneath the crimps, the atrialis is rich in elastin. The wavy elastin bands gradually thin out towards the tip of the leaflets. Cardiac muscle extending from the heart wall is sandwiched between the atrialis and spongiosa layers at the base. The mural leaflets have higher muscle content than septal leaflets. The cardiomyocytes in the inner core were rounded in shape and wrapped by the elongated cells, suggesting the muscle is oriented in a circumferential direction and longitudinal direction at the base (Figure 2.11). Cardiomyocytes, along with vessels, and sometimes sparse numbers of fat cells are seen (Figure 2.12). Occasionally, the fat cells form a defined fat tissue layer underneath the atrialis and continue along the axis of the leaflet (Figure 2.13). The spongiosa is composed of a high proportion of ground substance with loose connective tissue and cells. The fibrosa consists of tightly packed collagen fibre bundles scattered with flattened cells. In the diseased valves, areas of metaplasia are identified. Cartilage-like cells are also seen in the fibrosa and/or spongiosa layer. Occasionally, macrophages and monocytes can be observed. The different cell phenotypes and their roles in mitral valve will be discussed in detail in Chapter 3.

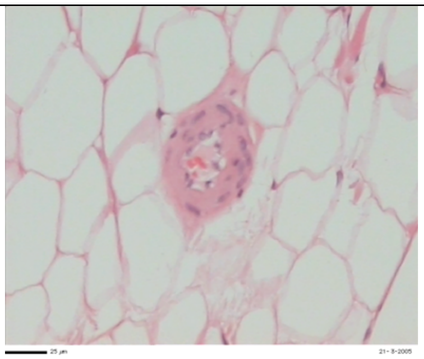

Figure 2.12. H&E stained section of a diseased mitral valve leaflet shown the vessel in the leaflet. Bar = 20 μm.

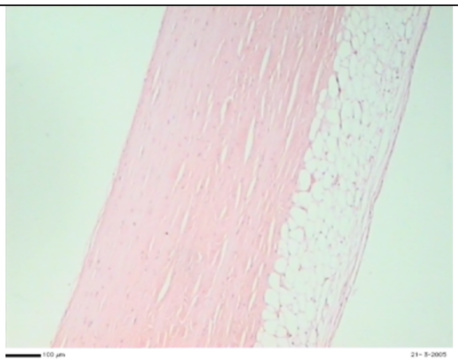

Figure 2.13. H&E stained section of a diseased mitral valve leaflet shown the fat cell layer. Bar = 100 μm.

Towards the free edge, the typical findings are expansion of the spongiosa layer and the destruction of the fibrosa layer in the diseased valve. Histologically, fibro-elastic proliferation in the spongiosa is concomitant with the degeneration of collagen bundles in the fibrosa layer, resulting in areas of myxomatous regions. The junction between spongiosa and fibrosa can be indistinguishable, with apparent accumulation of loose collagen bundles and ground substance in both layers. Together this results in thickening of the leaflets near the free edges.

2.3.6 Leaflet length

The septal/mural length ratio was greater than 1 in all dogs, in both normal and affected, indicating that the septal leaflet was always longer than the mural leaflet within the same valve. The mean length ratio for each grade was as follows; Grade 0=1.812, Grade 1=1.745, Grade 2=1.606, Grade 3=1.484 and Grade 4=1.525. There was a decrease in length ratio as the disease progressed, being most apparent in the more severe forms of the disease (Figure 2.14). However, no significant difference was achieved using ANOVA (p=0.4627) or the t-test. The LSN was predicted to be 80.46.

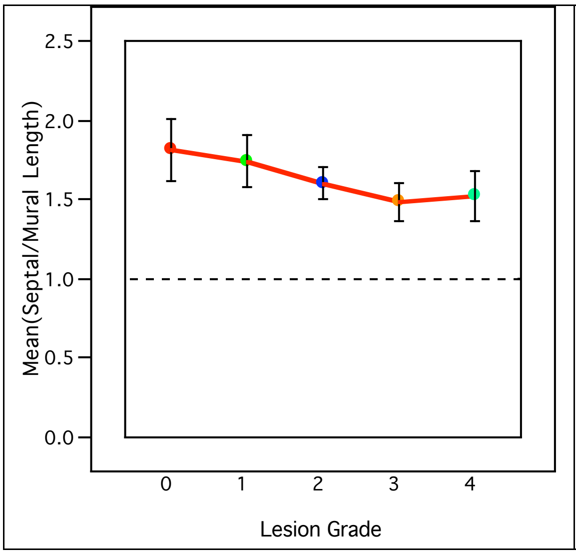

p=0.4627

ChiSq=0.4293

LSN=80.46

Figure 2.14. The comparison of septal/mural ratio between mitral valve lesion grade. The results from ANOVA, t-test, and Wilcoxon ranked test are presented.

2.3.7 Leaflet thickness ratio

Septal and mural leaflets were treated as separate entities as the differences in length between the two leaflets were established in length ratios studies. The results of the leaflet thickness ratio are shown in Figure 2.15 and Figure 2.16. The thickness ratio revealed that there is a trend to progressive thickening at the distal end of leaflets according to the severity of the disease, and this applied to both septal and mural leaflets. In severe Grade 4 stage of the disease, the distal ends of the leaflets were about three times thicker than the Grade 0 valve leaflets. Significant differences were found in both septal leaflets ($p<0.0001$) and mural leaflets ($p=0.0041$) between grades using ANOVA. The mural leaflets consistently had a slightly higher thickness ratio than the septal leaflets at all stages of the disease. Between group comparisons found that septal leaflet Grade 0 normal was significantly different to disease Grade 2, 3 and 4; the Grade 1 was different to grade 3 and 4; and the Grade 4 was significantly different to all others (Figure 2.15). In the mural leaflets, the Grade 0 normal was significantly different to Grade 3 and 4, while the Grade 4 was significantly different to all other grades. The results of the t-test are presented in Figure 2.16.

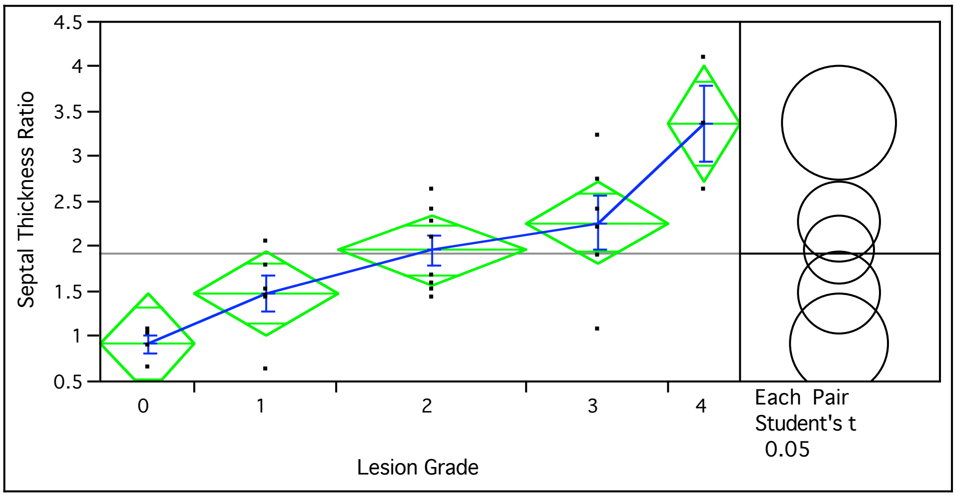

Grade					Mean
4	A				3.3650000
3		B			2.2621667
2		B	C		1.9563750
1			C	D	1.4791667
0				D	0.9185000

p<0.0001

ChiSq=0.0029

Figure 2.15. Comparison of septal leaflet thickness ratio between mitral valve lesion grade. The results from ANOVA, t-test, and Wilcoxon ranked test are presented.

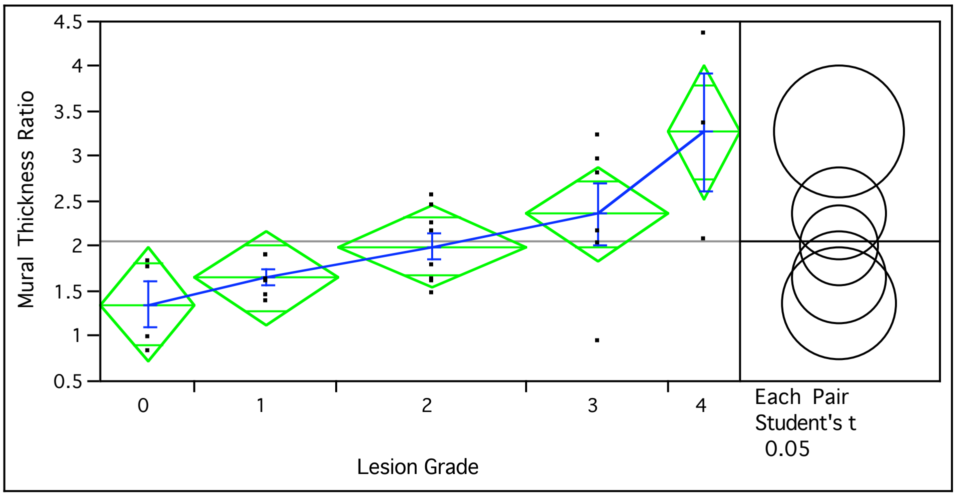

Grade				Mean
4	A			3.2713333
3		B		2.3598333
2		B	C	1.9927500
1		B	C	1.6471667
0			C	1.3545000

p=0.0041

ChiSq=0.0278

Figure 2.16. Comparison of mural leaflet thickness ratio between mitral valve lesion grade. The results from ANOVA, t-test, and Wilcoxon ranked test are presented.

2.3.8 Cell density

In diseased valves, the myxomatous areas were localised to the distal zone of the leaflets. The myxomatous areas were readily identifiable. The “initiation” site was visible in the spongiosa layer, but as the disease progresses the myxomatous area expands to the collagen rich fibrosa layer and to a lesser extent the connective tissue in the atrialis layer. The cells in the myxomatous area often appeared in a whorl like arrangement, but while cell distribution appeared to be relatively uniform across the myxomatous area, cell numbers in the areas adjacent to the myxomatous area varied. Variations in cells numbers were observed in the fibrosa layers in the distal zone. Areas of increased cell numbers were found adjacent to the myxomatous changes near the tip of the leaflets, and there was distinct localisation of cells towards the free edge coinciding with likely leaflet contact points (Figure 2.17).

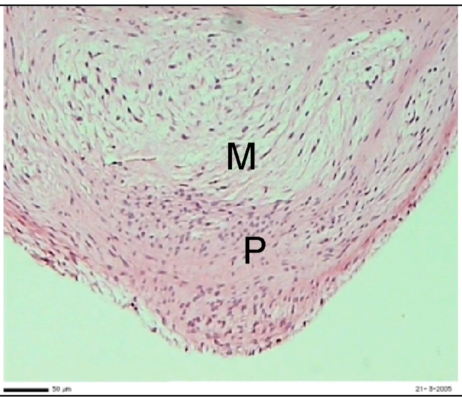

Figure 2.17. An H&E histological section of a myxomatous mitral valve tissue shows the variation in cell density. The area periphery (P) to myxomatous area (M) contains higher cell density. Bar = 50 μm.

Because of this distinct localisation, only in the myxomatous area was cellularity assessed and compared with cell numbers in the corresponding distal zone of the spongiosa layer of the normal valve. A total of 17,561 cells were identified and measured using ImageJ in the 30 valves. Cell density in the myxomatous areas (as a % of area) in the distal zone of the diseased valves was lower than the corresponding spongiosa in normal valve, indicating a decreased cell density associated with disease progression. The mean cell density in myxomatous areas were as follows; Grade 1: septal = 8.54±1.10 cells/0.01mm^2, mural = 8.03±1.10; Grade 2: septal = 7.04±1.02, mural = 7.76±1.02; Grade 3: septal = 7.21±0.96, mural = 5.66±0.95; Grade 4: septal = 7.20±1.56, mural = 5.94±1.55, cells per 0.01mm^2 (Figure 2.18 and Figure 2.19). Comparable corresponding loose spongiosa areas in normal leaflets were found to have higher cell density; septal = 15.04±1.21, mural =

15.42±1.20, cells per 0.01mm^2. Statistically significant reductions in cell density were found comparing the normal and the diseased grades 1 to 4 for both septal (p=0.0002) and mural (p<0.0001) leaflets, but within the four diseased grades no significant difference was found for either septal or mural leaflets. In general, the cell numbers in the spongiosa of the normal valve were two fold higher in comparison to cell numbers in the myxomatous diseased areas.

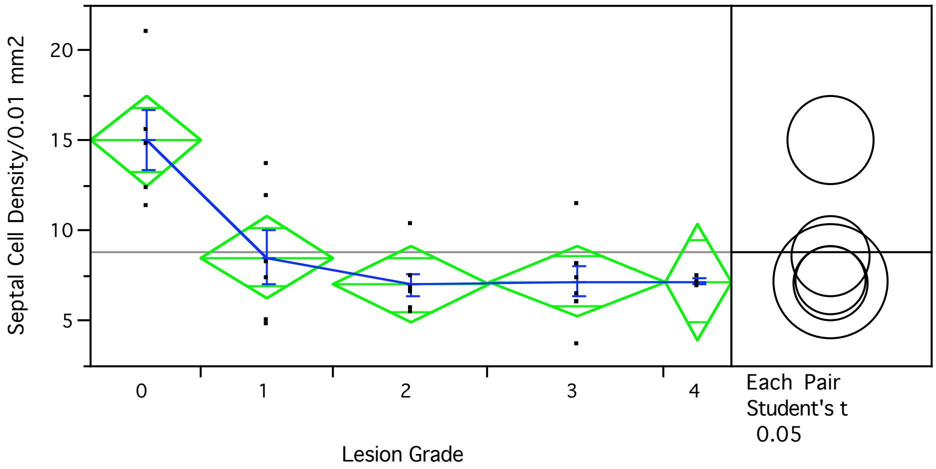

Grade		Mean
0	A	15.042000
1	B	8.543333
3	B	7.206250
4	B	7.196667
2	B	7.038571

p=0.0002

ChiSq=0.0238

Figure 2.18. Comparison of cell density in septal leaflet myxomatous area between mitral valve lesion grade. The results from ANOVA, t-test, and Wilcoxon ranked test are presented.

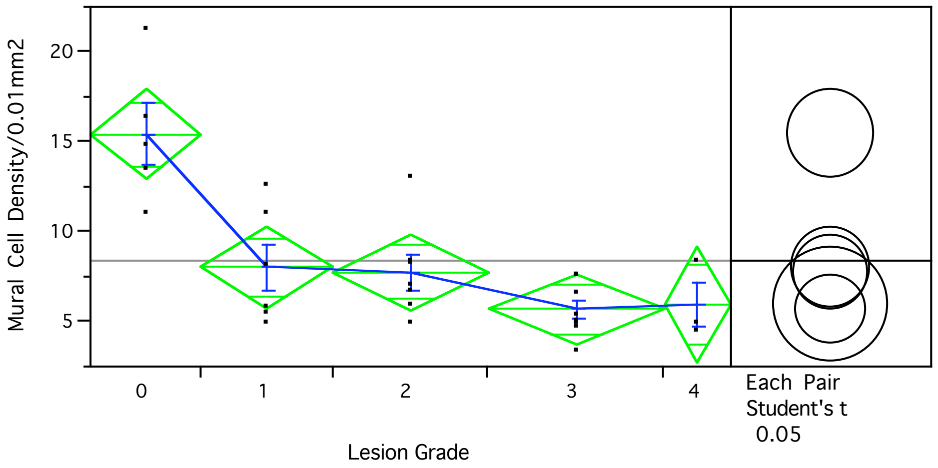

Grade		Mean	p<0.0001
0	A	15.416000	ChiSq=0.0054
1	B	8.028333	
2	B	7.764286	
4	B	5.936667	
3	B	5.668750	

Figure 2.19. Comparison of cell density in mural leaflet myxomatous area between mitral valve lesion grade. The results from ANOVA, t-test, and Wilcoxon ranked test are presented.

2.3.9 Circularity

The circularity score of cells were calculated in the myxomatous area of the diseased and corresponding distal spongiosa area in normal leaflets and are shown in Figure 2.20. No significant differences were found in both septal (p=0.1432, ChiSq=0.2117) and mural (p=0.5276, ChiSq=0.3912) leaflets between grades. The mean circularity values for the septal and mural leaflets within each grade were closely matched as shown in the chart (Figure 2.20). The values of circularity were restricted to a narrow range (between 0.68 to 0.77) indicating cells are spindle shaped. The LSN was 41.68 for septals and 91.19 for murals.

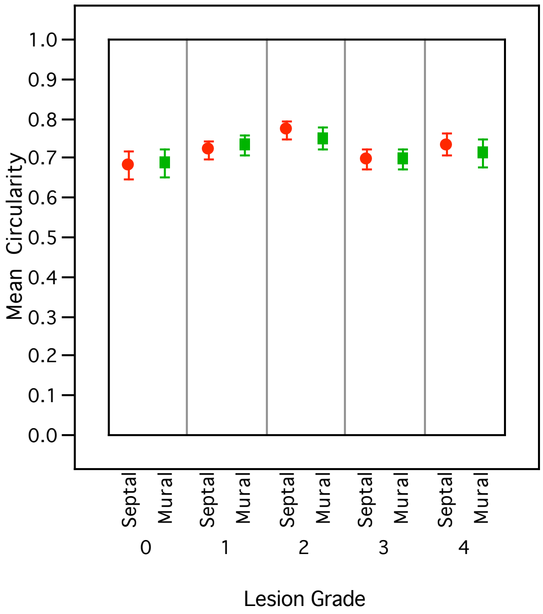

Septal leaflet			Mural leaflet		
Grade	n	Mean	Grade	n	Mean
0	5	0.683072	0	5	0.687085
1	6	0.720720	1	6	0.731160
2	8	0.770210	2	8	0.749940
3	8	0.695754	3	8	0.697158
4	3	0.732988	4	3	0.711650

Figure 2.20. Comparison of circularity in septal and mural leaflets myxomatous area between mitral valve lesion grade. The circularity means are presented.

On closer inspection, the impression was that cells in the higher grade of disease (older dogs) were marginally more elongated, whereas the cells in the normal younger dogs displayed a more polygonal shape in the corresponding spongiosa regions. In contrast, in areas surrounding the myxomatous region some cells tended to be more rounded. This aspect will be discussed in detail in the chapter covering immunohistochemistry. Occasionally, twin or multi-nucleated cells were observed neighbouring the myxomatous region. In other areas, determining the circularity of cells were not possible, due to the range of different cell types.

2.3.10 Connective tissue

As previously stated, MMVD is most pronounced in the distal zone of the spongiosa layer. During disease progression, myxomatous areas can be initiated from more than one site, there is a gradual disarrangement of connective tissue. By analogy it can be best described as tearing a knitted fabric and unravelling of the twisted yarn to expose the fluffy fibres. Furthermore, loss of connective tissue is recognized to be concomitant with accumulation of glycosaminoglycans (GAGs) in the myxomatous areas. However, there are localized areas of high connective tissue density peripheral to the myxomatous areas with intense collagen, elastin and fibronectin staining. However, these locations are patchy and sometimes sandwiched between two neighbouring disease sites (Figure 2.21). This feature will be covered in more detail with in later chapters.

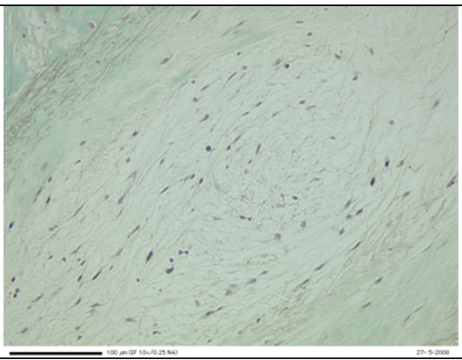

Figure 2.21. Masson's trichrome staining of a diseased mitral valve leaflet. Myxomatous area shows destruction of collagen (green) and elastin (dark blue). Bar = 100 µm.

Using image analysis of stained histological sections, the extent of connective tissue as a fraction of loose spongiosa area in the Grade 0 normal and myxomatous area in the diseased Grade 1 to 4 valves were plotted for septal (Figure 2.22) and mural (Figure 2.23) leaflets. There was a gradual destruction of connective tissue as the disease progressed in both leaflets, with a distinct linear relationship between the decrease in connective tissue and progression of the disease. Significant differences were found in both the septal ($p<0.0001$, ChiSq=0.0011) and mural ($p<0.0001$, ChiSq=0.0009) leaflets between grades. In the septal, the normal Grade 0 and Grade 1 were significantly different from Grade 2, 3 and 4. In the mural, the normal Grade 0 is significantly different from Grade 2, 3 and 4, whereas the Grade 1 was significantly different to Grade 3 and 4.

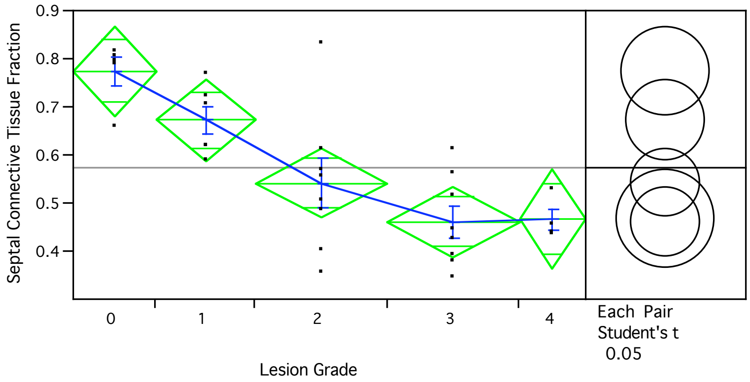

Grade			Mean
0	A		0.77352000
1	A		0.67213333
2		B	0.54148750
4		B	0.46570000
3		B	0.46040000

p<0.0001

ChiSq=0.0011

Figure 2.22. Comparison of connective tissue in septal leaflet myxomatous area between mitral valve lesion grade. The results from ANOVA, Wilcoxon ranked test and Student's t-test are presented.

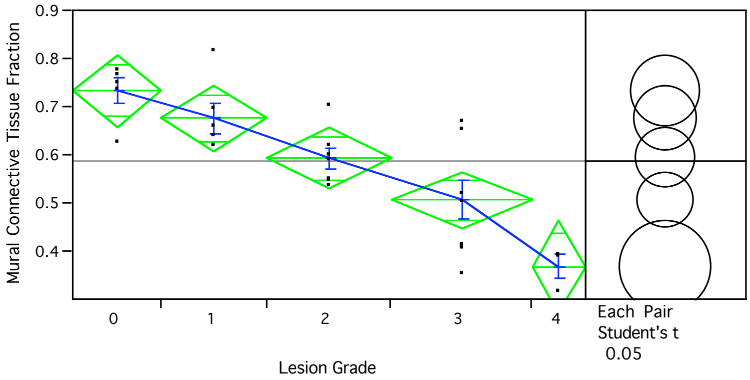

Grade					Mean
0	A				0.73258000
1	A	B			0.67540000
2		B			0.59261429
3			C		0.50537500
4				D	0.36723333

p<0.0001

ChiSq=0.0009

Figure 2.23. Comparison of connective tissue in mural leaflet myxomatous area between mitral valve lesion grade. The results from ANOVA, Wilcoxon ranked test and Student's t-test are presented.

2.3.11 Glycosaminoglycan

The intensity and extent of GAG-specific Alcian blue staining was readily appreciated in the normal and affected valves. In the normal mitral valves, staining had a light shade of blue, was evenly distributed throughout the entire leaflet and had a slightly greater intensity in the spongiosa layer towards the distal end of the leaflet (Figure 2.24).

Figure 2.24. Alcian blue GAG staining of a Grade 0 normal mitral valve septal leaflet.

In the diseased leaflets conspicuous areas of intense blue colour, indicative of GAG accumulation was noted in the spongiosa of the distal part of the leaflet, and the area and the intensity of the blue stained related to the severity of the disease (Figure 2.25).

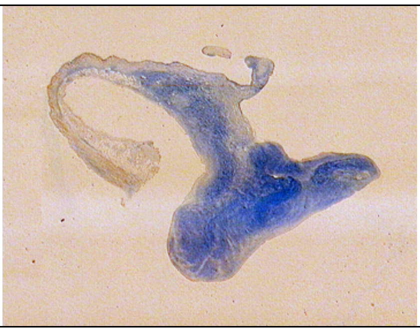

Figure 2.25. Alcian blue GAG staining of a Grade 4 diseased mitral valve septal leaflet.

k-means clustering

From k-means Clustering, although ANOVA found no significant differences existed in both septal (0.2559) and mural ($p=0.1294$) leaflets, between groups comparison the t-test revealed that in the septal leaflets the blue pixels area in normal Grade 0 (44.40%) valves was more than twice as in Grade 4 (20.56%) and this difference was significant. Nonetheless, the large mean error bar in Grade 0 due to sample placements outside the diamond confidence zone was observed. In mural leaflets, a different trend was seen; the Grade 1 (40.0%) was different to Grade 0 (26.83%) and Grade 3 (25.8%). The LSN was 53.99 for septal and 36.11 for mural leaflets (Figure 2.26).

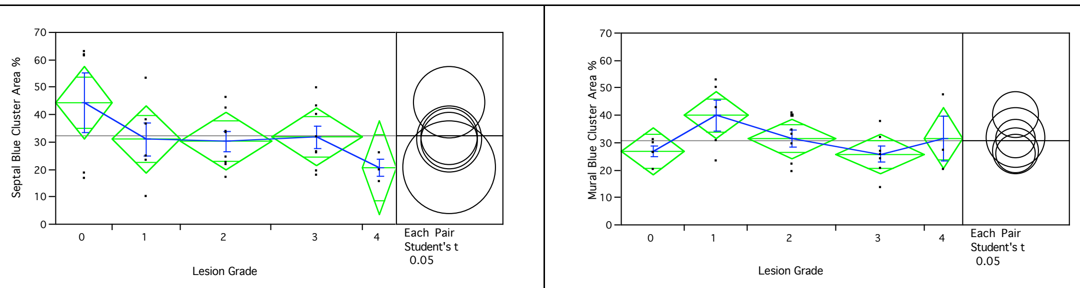

Grade		Mean	
0	A	44.400000	p=0.2559
3	A B	31.825000	ChiSq=0.5442
1	A B	31.000000	LSN=53.99
2	A B	30.262500	
4	B	20.566667	

Grade		Mean	
1	A	40.000000	p=0.1294
4	A B	31.666667	ChiSq=0.2945
2	A B	31.414286	LSN=36.11
0	B	26.820000	
3	B	25.800000	

Figure 2.26. Comparison of the percentage of blue area of GAG in leaflet between mitral valve lesion grade using k-means clustering method. Septal leaflet is on the left and the mural leaflet is on the right.

RGB split

From RGB split, all the group means were similar and fell into a limited range, from 30.62% to 37.05% within less 7% margin in septal leaflets and from 34.55% to 43.36%, within less than 9% margin in mural leaflets. As a result, the ANOVA of means detected no significant differences in both septal (p=0.8145) and mural (p=0.4561) leaflets. Furthermore, no statistical differences were found in between group comparison using Student's t-test in both septal and mural leaflets. The LSN was 192.78 for septal leaflets and 79.46 for mural leaflets (Figure 2.27).

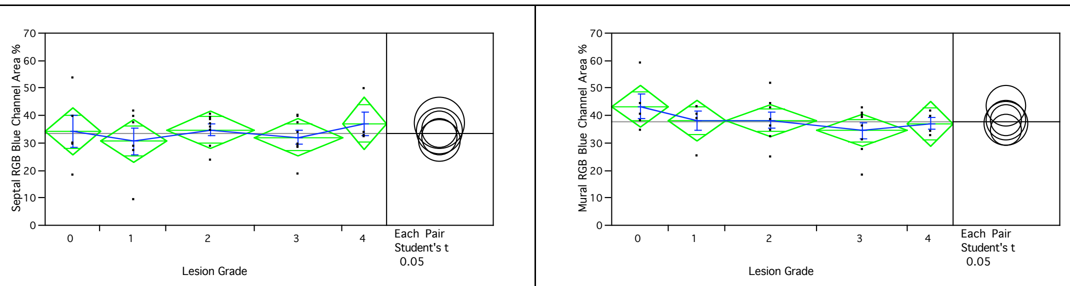

Grade		Mean	
4	A	37.050000	p=0.8145
2	A	34.750000	ChiSq=0.9481
0	A	34.180000	LSN=192.78
3	A	32.000000	
1	A	30.616667	

Grade		Mean	
0	A	43.360000	p=0.4561
2	A	38.162500	ChiSq=0.6142
1	A	38.120000	LSN= 79.46
4	A	37.025000	
3	A	34.550000	

Figure 2.27. Comparison of the percentage of blue area of GAG in leaflet between mitral valve lesion grade using RGB split method. Septal leaflet is on the left and the mural leaflet is on the right.

Deconvolution

The Alcian Blue hematoxylin colour deconvolution method separated the two chromogens while taking the co-localization of colours into consideration. In septal leaflets, the blue stain group means all fell into a narrow range, covered 26.67% to 32.22% within a margin of less than 6% of the total leaflet area, and so one-way analysis shown no statistical significance was achieved. Between groups comparison found no difference between pairs. In the mural leaflets, one-way analysis of group means revealed the p-value was 0.085, and Student's t-test showed Grade 2 (41.65%) was different to Grade 0 of (27.84%) and Grade 4 (25.08%). The LSN was 314.11 for septal leaflets and 30.06 for mural leaflets (Figure 2.28).

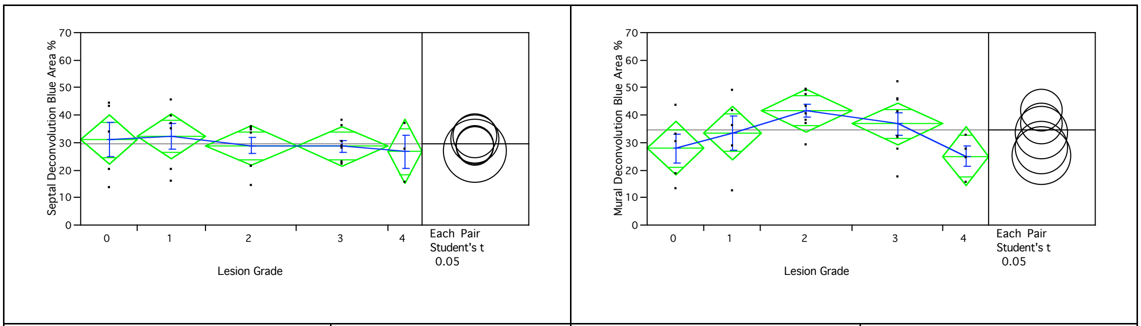

Grade		Mean	p=0.9193
1	A	32.216667	ChiSq=0.8943
0	A	31.040000	LSN=314.11
2	A	28.900000	
3	A	28.650000	
4	A	26.666667	

Grade			Mean	p=0.0850
2	A		41.650000	ChiSq=0.1013
3	A	B	36.750000	LSN=30.06
1	A	B	33.560000	
0		B	27.840000	
4		B	25.075000	

Figure 2.28. Comparison of the percentage of blue area of GAG in leaflet between mitral valve lesion grade using deconvolution method. Septal leaflet is on the left and the mural leaflet is on the right.

Threshold colour

From Threshold HSB method, ANOVA of means found no significant differences in both septal (p=0.7064) and mural (p=0.1542) leaflets. Again, the group means in septal leaflets were fell into a narrow range from 28.28% to 36.14% within a margin of less than 8%, and no differences were found between groups using the Student's t-test. However, in the mural leaflets, the grade 2 (40.81%) was found to be different to normal Grade 0 (26.54%) and Grade 1 (24.8%). The LSN was 135.16 for septal leaflets and 38.6 for mural leaflets (Figure 2.29).

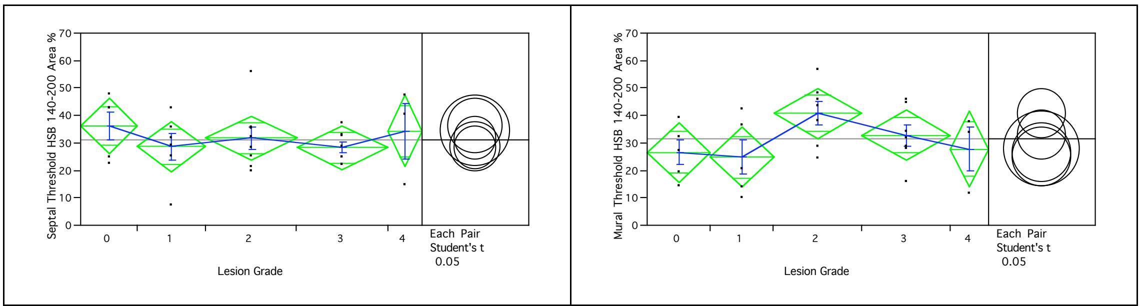

Grade		Mean	p=0.7064
0	A	36.140000	ChiSq=0.7150
4	A	34.266667	
2	A	31.762500	LSN=135.16
1	A	28.650000	
3	A	28.287500	

Grade			Mean	p=0.1542
2	A		40.814286	ChiSq=0.1749
3	A	B	32.757143	
4	A	B	27.766667	LSN=38.6
0		B	26.540000	
1		B	24.800000	

Figure 2.29. Comparison of the percentage of blue area of GAG in leaflet between mitral valve lesion grade using threshold colour method. Septal leaflet is on the left and the mural leaflet is on the right.

Comparing the results calculated by the four different colour measuring techniques, all the group means including both septal and mural leaflets lie between 20% to 44% of total area, with no more than 24% margin of difference in area. The results computed from Decovolution and Threshold Colour HSB methods were noticeably similar. When presented in bar charts side by side, the close resemblance in patterns was obvious (Figure 2.30). This could be interpreted that regardless of the severity of MMVD there are no significant differences in GAG expression, that the GAG occupy between 20% to 44% of the cross-sectional area of a mitral valve leaflet, and this applies equally to septal and mural leaflets.

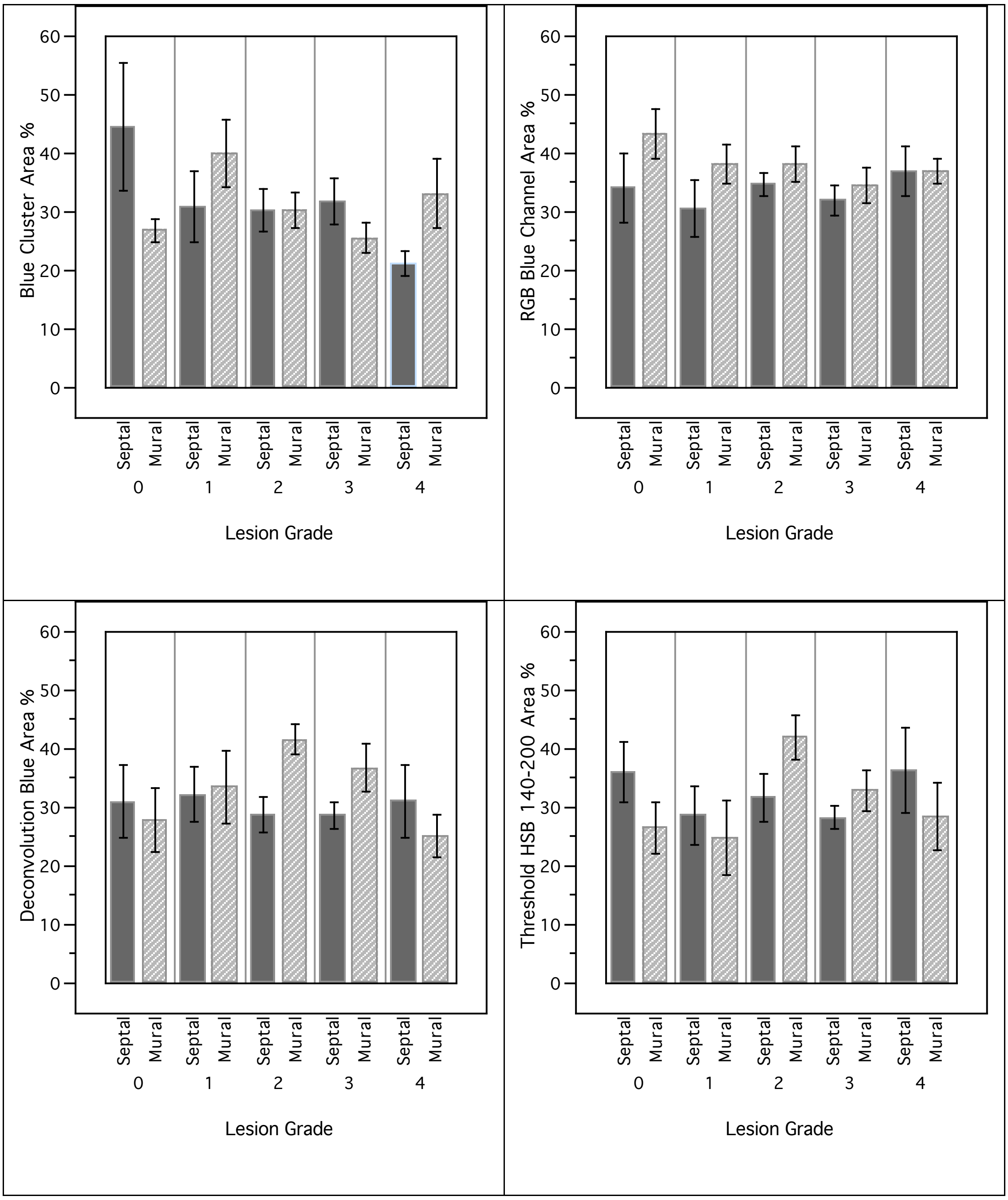

Figure 2.30. Comparison of the percentage of blue area of GAG in leaflet between mitral valve lesion grade show in mean error bar with (clockwise from top left) blue cluster of k-mean clustering, blue channel of RGB split, blue deconvolution and threshold of HSB 140-200. The blue area of GAG are all between the range of 20-44%.

Mean blue

From standardised mean blue values, ANOVA of group means found no significant difference in the septal leaflets (p=0.5364). However, in the mural leaflets, the p-value of 0.0959 is closer to the borderline of significance. Between groups t-test showed there was no difference in the septal leaflets, even though a slightly higher blue value found in grade 1 normal and grade 4 diseased. In mural leaflets, the mean blue in grade 2 was different to grade 1. The LSN for septal was 95.83, whereas the LSN for mural was only 36.19 (Figure 2.31).

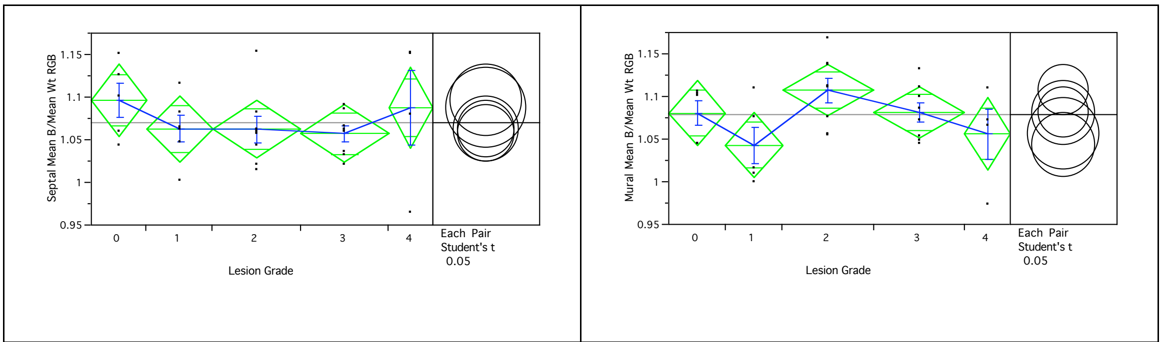

Grade		Mean	
0	A	1.0964645	p=0.5364
4	A	1.0874295	ChiSq=0.5686
1	A	1.0627591	LSN=95.83
2	A	1.0620499	
3	A	1.0569395	

Level		Mean	
2	A	1.1070690	p=0.0959
3	A B	1.0814645	ChiSq=0.1368
0	A B	1.0805401	LSN=36.19
4	A B	1.0557790	
1	B	1.0426062	

Figure 2.31. Comparison of the standardised mean blue value in leaflet between mitral valve lesion grade. The septal leaflet is on the left and the mural leaflet is on the right.

Mean blue ranking

The ranking orders of the mean values for each of the three RGB colours were expressed as frequency counts, each type of ranking order was represented in a different colour in the contingency table (Figure 2.32). In the septal leaflets, the general trend was that the B>G>R type (pink) never surpassed B>R>G (lime) in probability, provided that the B>R>G (lime) was always equal to or higher than the others in probability. The R>B>G type (blue) contained the least probability and it did not exceed more than 25% in any situations. The grade 4 stood out as the odd one, it was similar to grade 3 with B>G>R (pink) at 25% and B>R>G (lime) at 50%, but instead of R>B>G (blue) as in grade 3, the grade 4 contained the unique R>G>B type (orange) at probability of 25%. As a whole, the blue colour in the septal leaflets consistently achieved the highest mean value in ranking at no less than 75% in probability. However, likelihood and Pearson tests found no statistical differences.

In the mural leaflets, both the Grade 0 normal and Grade 1 were at the same level of B>G>R (pink) at 20% probability, but compared with the 60% B>R>G (lime) as in Grade 0, there was only 20% probability in Grade 1, the lowest B>R>G (lime) counts in all groups, whereas the R>B>G in Grade 1 was at 60% probability, the highest in all groups. The Grade 2 and the Grade 3 both achieved a same B>G>R (pink) probability at 50%, but instead of 12.5% R>B>G (blue) as found in

Grade 3, there was no R>B>G (blue) in Grade 2. The Grade 4 composed of 70% B>R>G (lime) and 30% R>B>G (blue) was distinctly different to others, as no B>G>R (pink) was found. Overall, in the mural leaflets with the exception of the Grade 2, the mean values of the blue colour achieved the highest rank at 75% or more in all other cases. Nevertheless, likelihood and Pearson tests found no statistical differences.

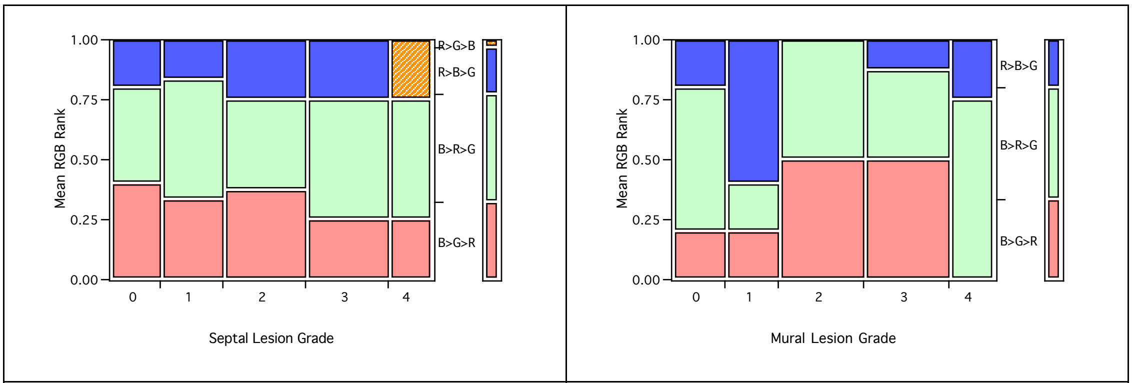

Test	ChiSq	Test	ChiSq
Likelihood Ratio	p=0.8884	Likelihood Ratio	p=0.1325
Pearson	p=0.7534	Pearson	p=0.2087

Figure 2.32. Contingency tables show the comparison of mean blue ranking between mitral valve lesion grade. Septal leaflet is on the left and the mural leaflet is on the right.

Median blue

From standardised median blue values, ANOVA found no significant differences in both septal (p=0.2003) and mural (p=0.1993) leaflets. Between groups t-test shown the normal Grade 0 was different to Grade 2 in the septals and the Grade 2 was different to Grade 4 in the murals. The LSN for septal leaflets and mural leaflets were 49.53 and 47.83 respectively (Figure 2.33).

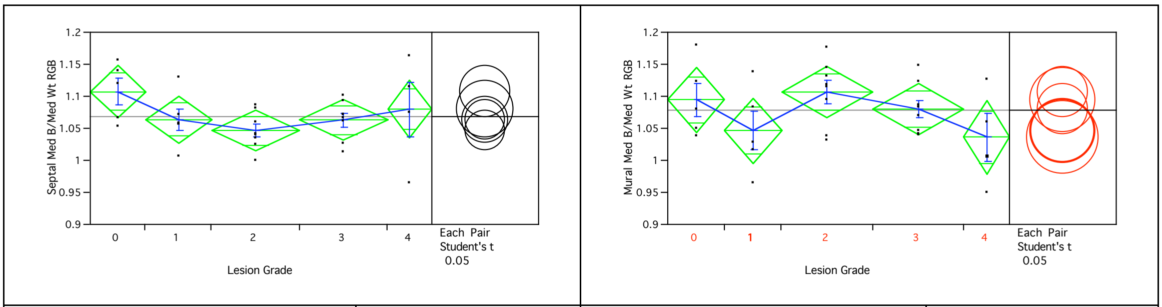

Grade		Mean	p=0.2003	Grade		Mean	p=0.1993
0	A	1.1073757	ChiSq=0.2256	2	A	1.1065784	ChiSq=0.3297
4	A B	1.0796149		0	A B	1.0943961	
1	A B	1.0634958	LSN=49.53	3	A B	1.0800046	LSN=47.83
3	A B	1.0631357		1	A B	1.0463567	
2	B	1.0462290		4	B	1.0358673	

Figure 2.33. Comparison of standardised median blue value between mitral valve lesion grade. The septal leaflet is on the left and the mural leaflet is on the right.

Modal blue

The standardised modal blue represents the most frequently occurring blue value. The group means of modal appeared to conform to a certain pattern when comparing the septal leaflets and mural leaflets, with the Grade 0 normal taken the highest level and the severely diseased grade 4 at the lowest level. Nevertheless, no significant differences were detected in ANOVA in both septal and mural leaflets. Between group comparison showed no difference in septals, but in the murals the Grade 0 was different to the Grade 4 (Figure 2.34).

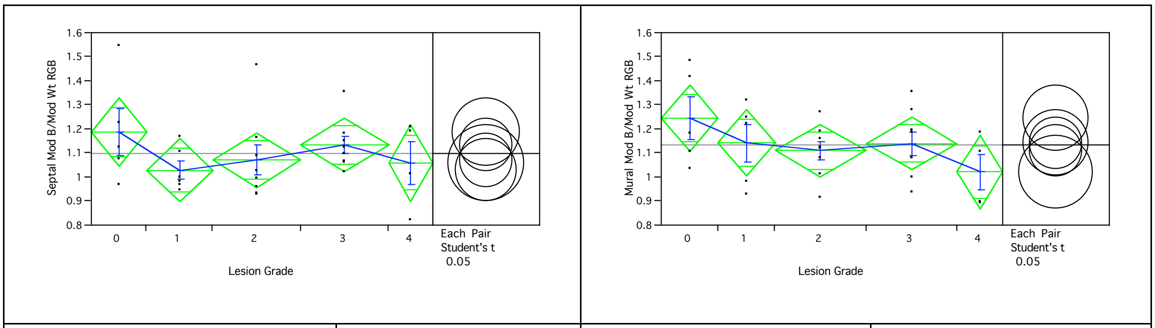

Grade		Mean	p=0.4555
0	A	1.1875711	ChiSq=0.3246
3	A	1.1332640	
2	A	1.0704085	LSN=81.97
4	A	1.0586940	
1	A	1.0283645	

Grade		Mean	p=0.2946
0	A	1.2443046	ChiSq=0.4837
1	A B	1.1403321	
3	A B	1.1387645	LSN=58.42
2	A B	1.1091423	
4	B	1.0207316	

Figure 2.34. Comparison of standardised modal blue value between mitral valve lesion grade. The septal leaflet is on the left and the mural leaflet is on the right.

Integrated blue intensity

From the standardised integrated intensity, even though no statistical differences were found in ANOVA in both septal (p=0.5363) and mural (p=0.0959) leaflets, the p-value for mural leaflets was relatively low. Between groups t-test shown the Grade 2 and the Grade 1 in mural were different to each other (Figure 2.35).

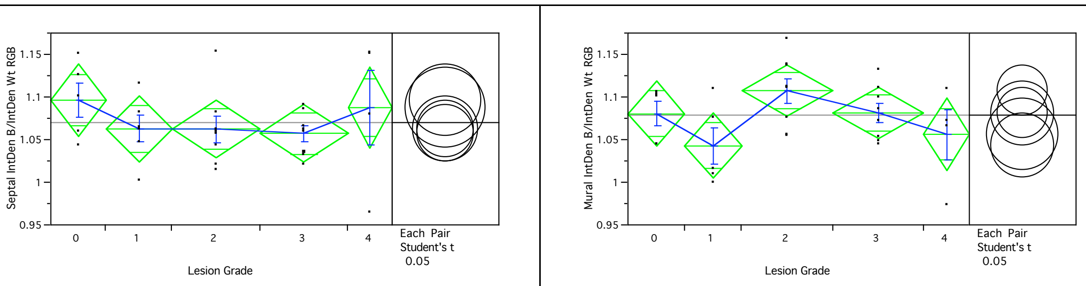

Grade		Mean	
0	A	1.0964633	p=0.5363
4	A	1.0874305	ChiSq=0.5686
1	A	1.0627582	LSN=95.82
2	A	1.0620494	
3	A	1.0569385	

Grade			Mean	
2	A		1.1070698	p=0.0959
3	A	B	1.0814662	ChiSq=0.1368
0	A	B	1.0805401	LSN=36.20
4	A	B	1.0557796	
1		B	1.0426075	

Figure 2.35. Comparison of integrated blue intensity between mitral valve lesion grade. The septal leaflet is on the left and the mural leaflet is on the right.

2.3.12 Transmission electron microscopy (TEM)

2.3.12.1 Endothelium: normal samples

In the normal samples, the endothelium was found to cover the tissue forming a continuous single-cell thick outer layer. The cells were flat and joined tightly together. The apical side of the cell membrane was quite smooth, forming an even surface. The basal side of the cell was attached to the basement membrane of the tissue. The basement membrane can be seen as an unbroken grey line underneath the endothelium marking the border with ECM (Figure 2.36). In between cells, desmosomal type cell junctions were observed. The nucleus was the most prominent organelle in the endothelial cells, occupied the majority of the cytosolic space and often appeared as flattened rod-like in shape. The granulated nuclear chromatin was particularly apparent, but unlike the typical nuclear morphology of actively expressed genes with light euchromatin in the centre and the dormant genes of the dark heterochromatin located near the periphery, the dense heterochromatin of the endothelial cell with their tightly bound histones appeared as black speckles in juxtaposition with the lighter granulated euchromatin throughout the nuclear space. The cell nucleoli were not readily visible. Other organelles like mitochondrion and vacuoles could be seen in small numbers, often sparsely located in the two polar ends of the perinuclear area in the cytoplasm. Occasionally, tiny round vesicles were recognized near the sub-surface in the apical side, indicating endocytosis and/or exocytosis activity. However, the endothelial cells in the normal valve lacked the well-defined endoplasmic reticulum and Golgi apparatus.

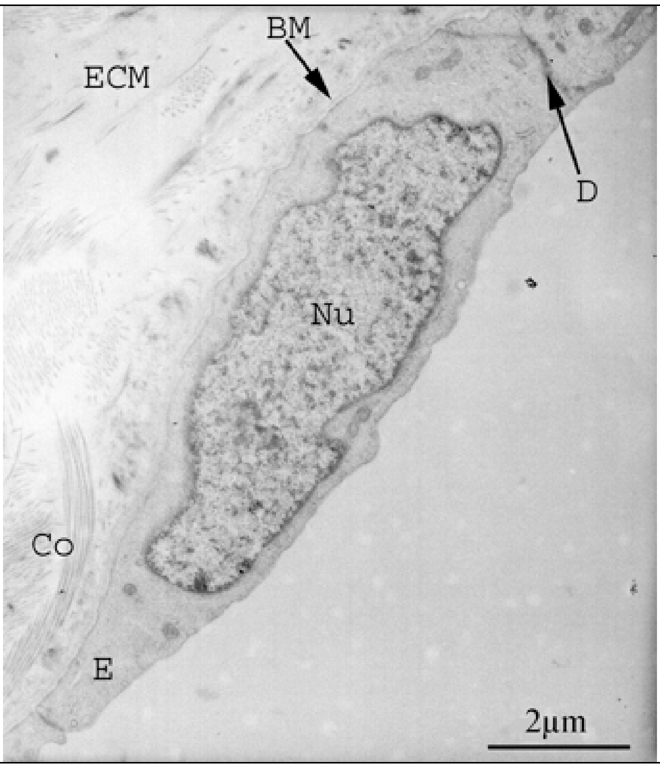

Figure 2.36. Transmission electron micrograph of an endothelial cell (E) from normal mitral valve. Basement membrane (BM), Collagen (Co), extracellular matrix (ECM), desmosome junction (D). Bar = 2 μm.

In some areas, apoptotic and cycling processes of endothelium were observed, where healthy normal looking endothelial cells were found lying below another endothelial cell undergoing apoptosis. Apoptotic cells demonstrated a nucleus that was swollen and caused the cell to bulge outwards towards the apical side. The nuclear contents were flocculated with no distinguishable chromatic structures visible. Degradation in the cytoplasm produced large vacuoles and many small vesicles, while the granular electron dense cytoplasmic contents disappeared (Figure 2.37). Often the cell membrane was no longer intact and cytoplasmic matter leaked into the surrounding space.

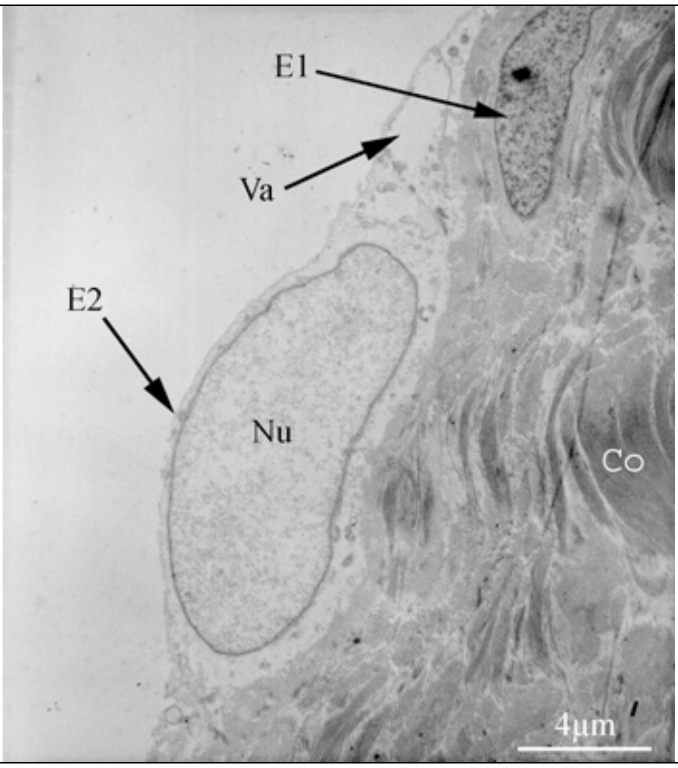

Figure 2.37. Transmission electron micrograph shows an endothelial cell (E2) undergoing apoptosis near the surface and is with bulge nucleus (Nu) and large vacuole (Va). A healthy endothelial cell (E1) is underneath it. The sub-endothelial tissue is filled with collagen (Co). Bar = 4μm.

2.3.12.2 Sub-endothelial layer: normal samples

Immediately beneath the basement membrane, there was a narrow band of extracellular matrix separating the endothelium and the underlying collagen rich connective tissue. This band consisted of isolated individual collagen fibres together with proteoglycan ground substance. Valvular interstitial cells were occasionally found in this zone, some in close proximity to the endothelium and others in direct contact with the endothelial cells through extended cytoplasmic processes or pseudopodia (Figure 2.38). Different types of cells were recognized in this zone just beneath the endothelium, including multi-nucleated neutrophils, lysosome-carrying macrophages, polymorphic fibroblasts and collagen associated smooth muscle cells. Deeper into the tissue, organised collagen bundles running in different directions were observed. Typical banding pattern of the collagen was visible at high power. In some areas, collagen extended out towards the surface endothelium and was in close association with endothelial cells.

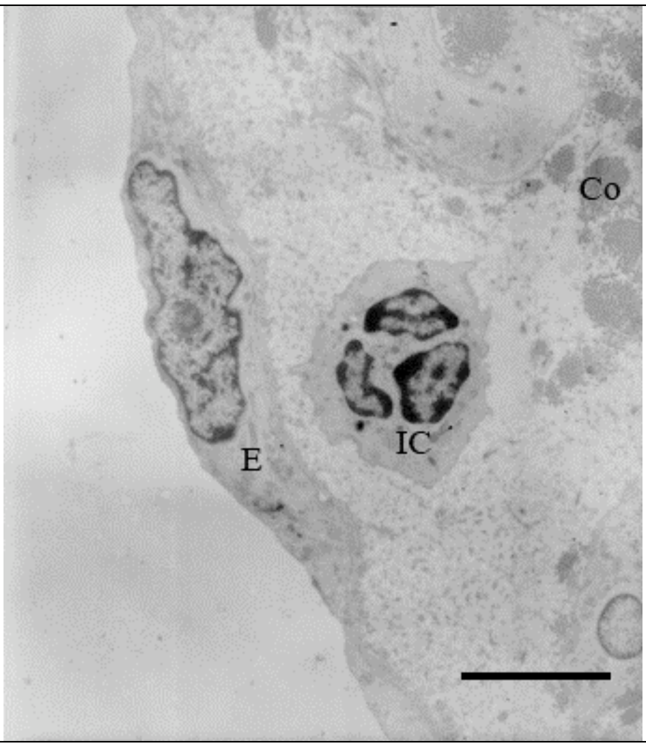

Figure 2.38. Transmission electron micrograph shows a multi-nucleated interstitial cell (IC) situated very close to an endothelial cell (E). Small cytoplasmic processes are seen on the interstitial cell. The sub-endothelial space is filled with ground substance and collagen bundles (Co). Bar = 4μm.

2.3.12.3 Abnormality in clinical normal valve

Throughout one of the samples classified as clinically normal, there was some evidence of sub-clinical disease. Abnormalities were evident in the endothelium, basement membrane and sub-endothelial tissues. Although the endothelium had areas that were normal, with features as those described above, other areas were denuded of endothelium, with just fragments of cells left. These cell fragments had a variable shapes. In some areas the endothelium was still present, the cells were frequently degenerating or dying. Many vacuoles and small vesicles were observed in these cells. The nuclei were swollen, and the cytoplasmic contents rose above the endothelium lining towards the apical side cause the cell to appear dome-shaped. Some of these cells had lost their attachment to the tissue (Figure 2.39).

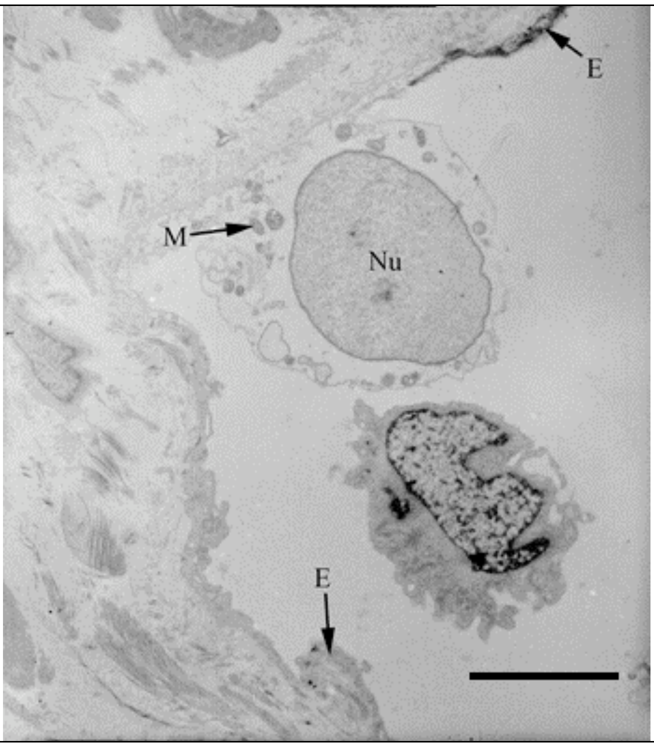

Figure 2.39. Transmission electron micrograph showing an endothelial cell with a large flocculated nucleus (Nu) has started to detach from the tissue. The cytoplasmic material has been degraded, but the mitochondria (M) are visible. The neighbouring endothelial cells (E) lay flat on the surface. Bar = 4 μm.

Changes to the basement were also seen. In some areas where the endothelial cells were degenerating, breaks in the basement membrane were observed at high power. In other areas the basement membrane was thickened, but also included gaps. Where there were interruptions to the basement membrane, the junctional spaces between the cells were increased, and were joined together only by the desmosomal attachments (Figure 2.40).

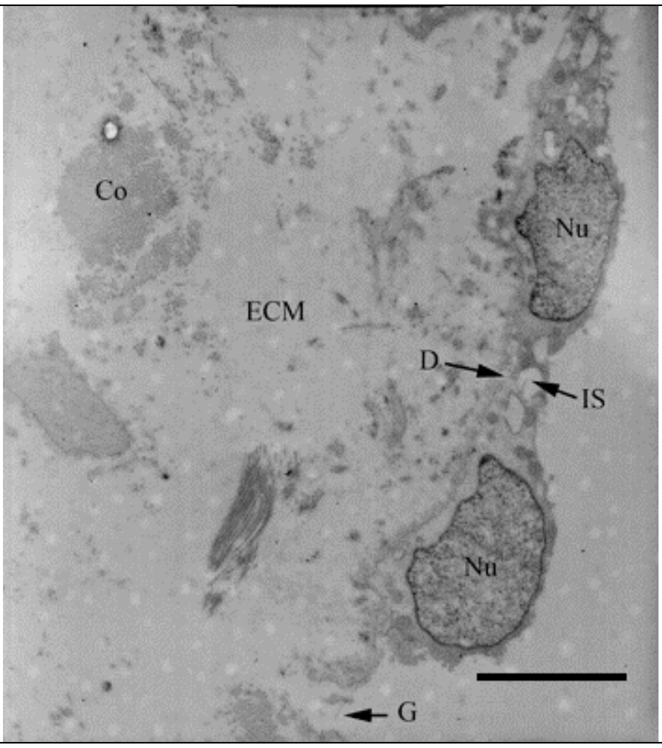

Figure 2.40. Transmission electron micrograph shows two endothelial cells side by side at the surface of the tissue, their nuclei (Nu) labelled. The attachment between them is breaking down; there are now large intercellular spaces (IS) and the cells are joined only by desmosomes (D). The lower cell has also lost its attachment to its other neighbour, leaving a gap (G) in the endothelial surface. Beneath the cells is an expanded extracellular matrix (ECM) and a few sparse collagen bundles (Co) in between. Bar = 3 μm.

The tissue underneath the disrupted basement membrane was also marked by change. At high magnification, amorphous ECM material was seen leaking out through the broken basement membrane (Figure 2.41).

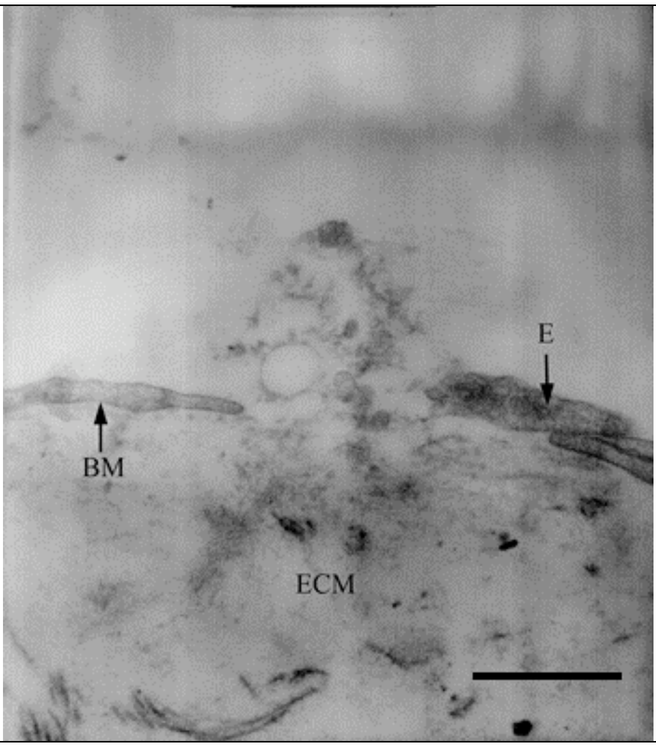

Figure 2.41. Transmission electron micrograph shows the discontinuation of endothelium (E), a large gap is seen. The basement membrane (BM) has broken down, allowing extracellular matrix (ECM) material to escape through the gap. Bar = 1 μm.

2.3.12.4 Endothelium: MMVD diseased samples

In the diseased samples, the denudation of endothelium was much more extensive. Although isolated cells were often present on the surface, the continuity of the endothelium was lost. The remaining cells underwent transformations from a flattened profile with an even outer surface to cells with a protuberant dome shaped out growth and ragged outer surface. The ragged and often crenated outer surface revealed micro-appendages or short cytoplasmic processes (Figure 2.42).

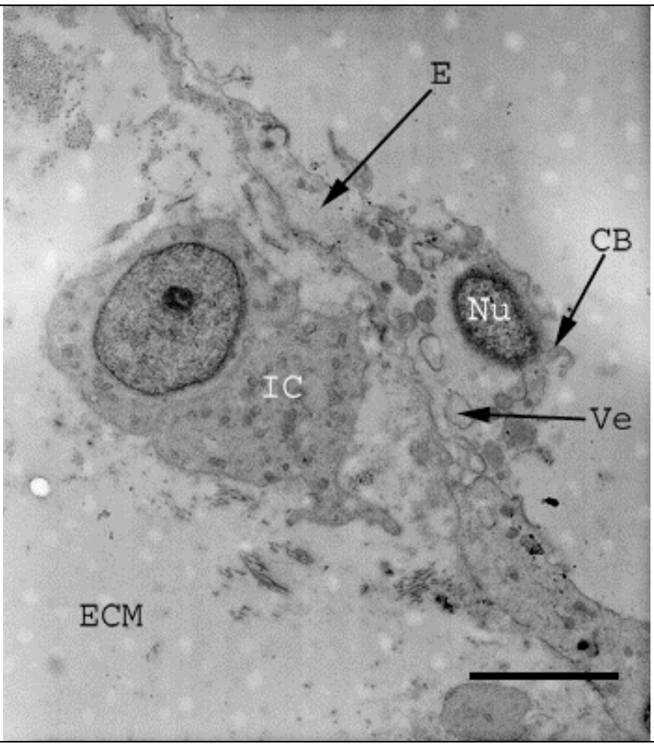

Figure 2.42. Transmission electron micrograph shows an endothelial cell (E) undergoing degenerative process in a diseased valve. Many cytoplasmic buds (CB) created a ragged apical surface. The nucleus (Nu) and vesicles (Ve) can be seen within the cell. Underneath, an interstitial cell (IC) is in close proximity to the endothelium. The interstitial cell has cytoplasmic processes that extend towards the endothelium. Bar = 3μm.

Similar to the apoptotic cells in the normal samples described earlier, cells in the diseased valve also had swollen nuclei with increasing numbers of small vacuoles, some appeared as dense storage vacuoles. However, unlike the typical cell going through the apoptotic process, it seemed these cells were actively detaching from the basement membrane and migrating towards void space on the apical side. The definition between euchromatin and heterochromatin structures in the nuclei became apparent. As the cell protruded the shape changed from a dome to mushroom-like (Figure 2.43). Finally, the cells totally detached themselves and separated from the basement membrane (Figure 2.44).

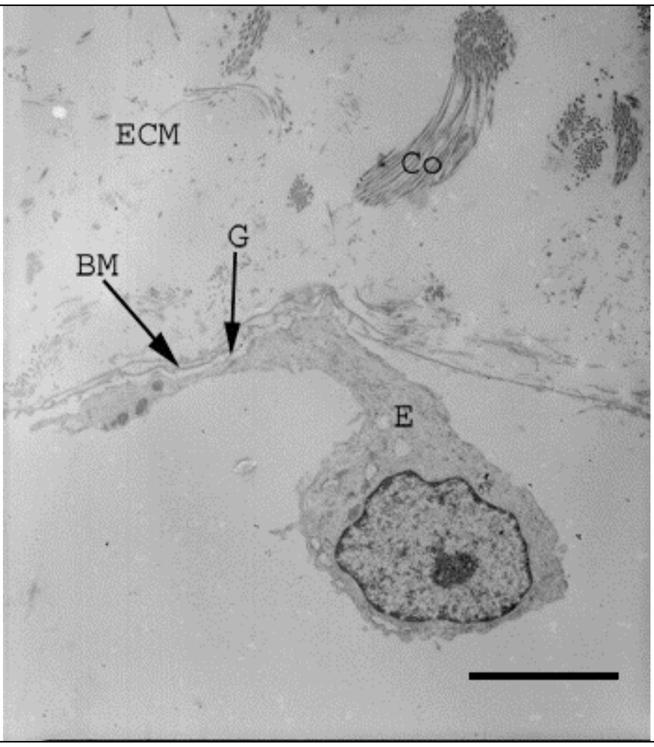

Figure 2.43. Transmission electron micrograph shows an endothelial cell (E) is detaching itself from the basement membrane (BM). A gap (G) between the cell membrane and basement membrane can be seen. The extracellular matrix (ECM) contains abundant ground substance and sparse collagen bundles (Co). Bar = 3 μm.

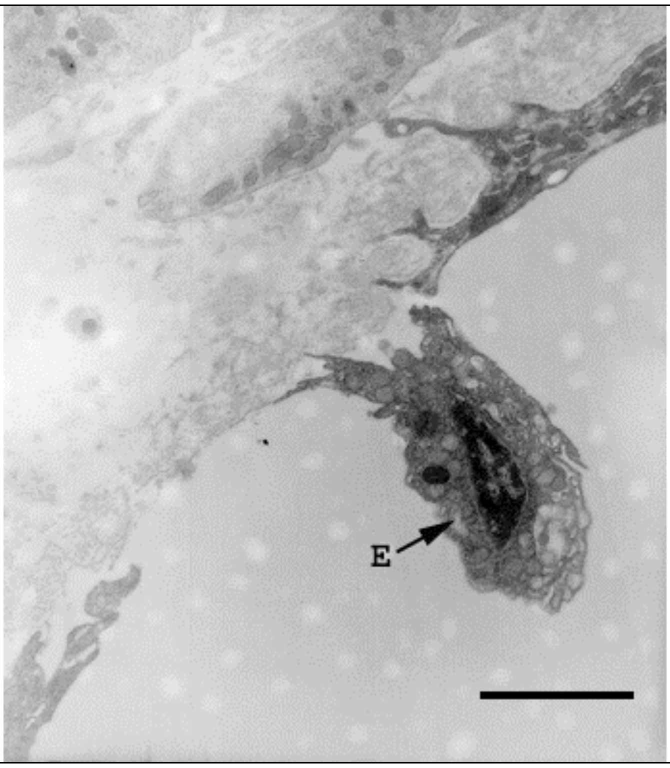

Figure 2.44. Transmission electron micrograph shows an endothelial cell (E) in a diseased valve is detaching itself from the surface of the tissue. Bar = 3 μm.

2.3.12.5 Sub-endothelial layer: MMVD diseased samples

The damage to the basement membrane was present at different degrees of severity. In some areas, where endothelial cells were still present, the basement membrane was disrupted with small gaps in it exposing the underlying ECM. As with "sub-clinically" affected areas in normal valves, the basement membrane became thickened and in other areas a definite two-layered membrane structure was observed (Figure 2.45). There were areas where the basement membrane appeared intact despite desquamation of overlying endothelial cells. Remnants of cells under advanced flocculation were found nearby. However, at higher magnification small gaps were discovered on the membrane. In severe changes, there was obliteration of the basement membrane, exposing the underlying ECM. The degraded ECM often appeared as an amorphous mixture of grey and translucent matter, and some small matrix vesicles.

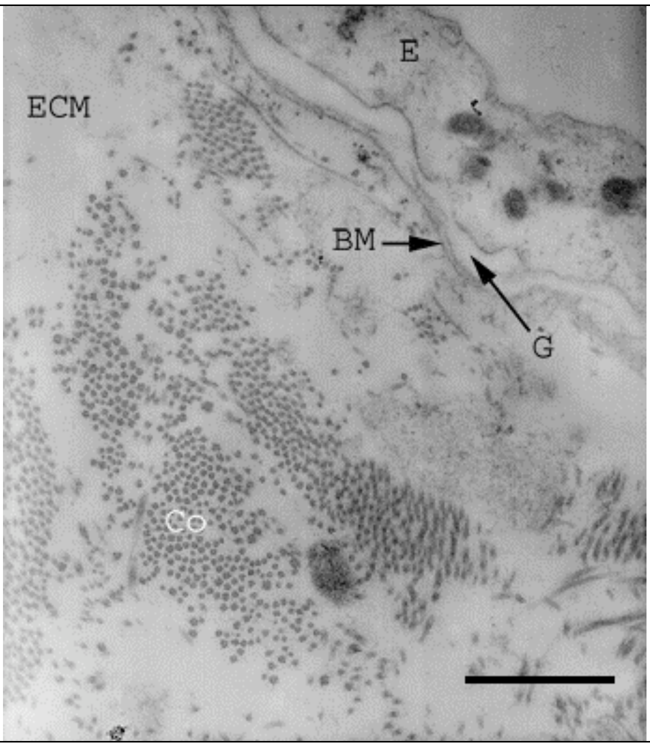

Figure 2.45. Transmission electron micrograph shows basement membrane (BM) has become double layered. There is a gap (G) between the endothelial cell (E) and the basement membrane. The extracellular matrix (ECM) contains collagen bundles (Co). Bar = 1 μm.

Interstitial cells were seen congregated towards the damaged endothelial cells in the diseased valves. More interstitial cells were found in the zone just beneath the basement membrane compared to normals. Whether the interstitial cells play a direct role in the transformation or degeneration of the endothelial cells is hard to elucidate in this study, but there was strong evidence to demonstrate that some interstitial cells were in contact with endothelial cells through their micro-appendages. Another interesting observation was that interstitial cells could squeeze between two endothelial cells and escape from the ECM (Figure 2.46).

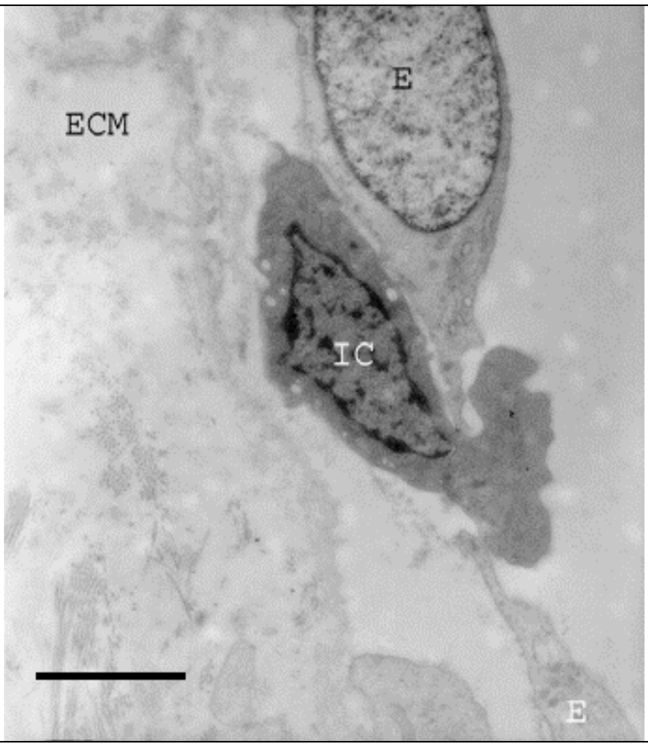

Figure 2.46. Transmission electron micrograph shows an interstitial cell (IC) is squeezing between two endothelial cells (E). The extracellular matrix (ECM) contains sparse collagen. Bar = 2 μm.

In the sub-endothelial level, the collagen fibre bundles appeared in disarray. The disorganized collagen bundles were sparsely arranged in the abundant ground substance. The typical banding patterns of densely packed collagen fibre were no longer readily visible. Some collagen bundles showed signs that they had been splintered. Close inspection revealed that some individual collagen fibrils were bent at various angles rather than being straight. There was an increase in inter-collagen fibril space. At higher magnification, some collagen fibres were associated with thread like filamentous proteoglycans (Figure 2.47).

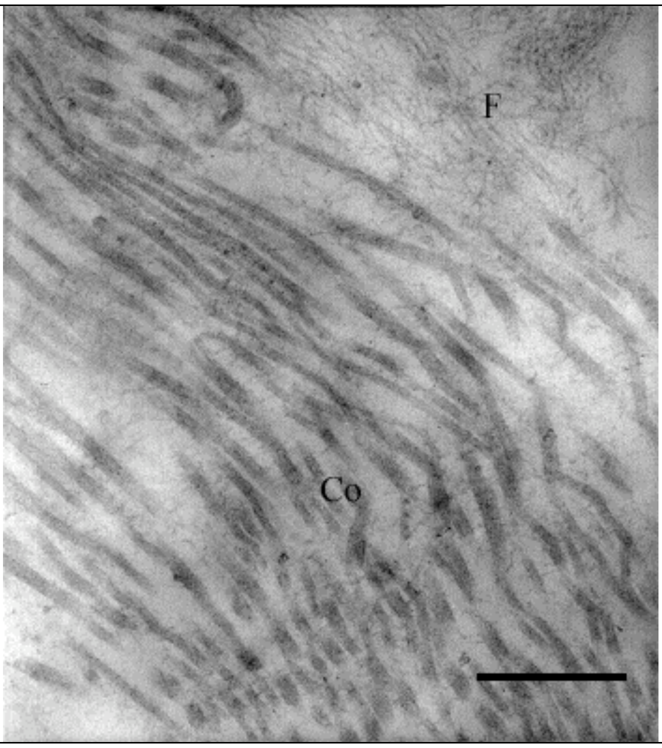

Figure 2.47. Transmission electron micrograph shows the collagen (Co) in the diseased valve are bent. The collagen are associated with filamentous proteoglycans (F). Bar = 0.5 μm.

The interstitial cells presented in the tissue were truly pleomorphic. Cells of disparate morphology were co-localised side by side in the tissue. More than one phenotype was observed at any one time. The fibroblast-like cells were usually elongated in shape. These cells contained numerous vacuoles and vesicles. Some of the vacuoles were filled with lipid. Twin nucleated cells were commonly seen (Figure 2.48). They were initially thought to be cells of high proliferation undergoing cell division, but there was no evidence of spindle formation, a characteristic feature of cell division. In spite of their abnormal morphology, these cells were seen to be involved with the ECM. The majority of the fibroblast-like cells were actively engaged in secreting. Matrix vesicles of various sizes could be seen next to cells. These cells contained nuclei that consisted of central light granulated euchromatin surrounded by dark heterochromatin, typical of mature viable cells.

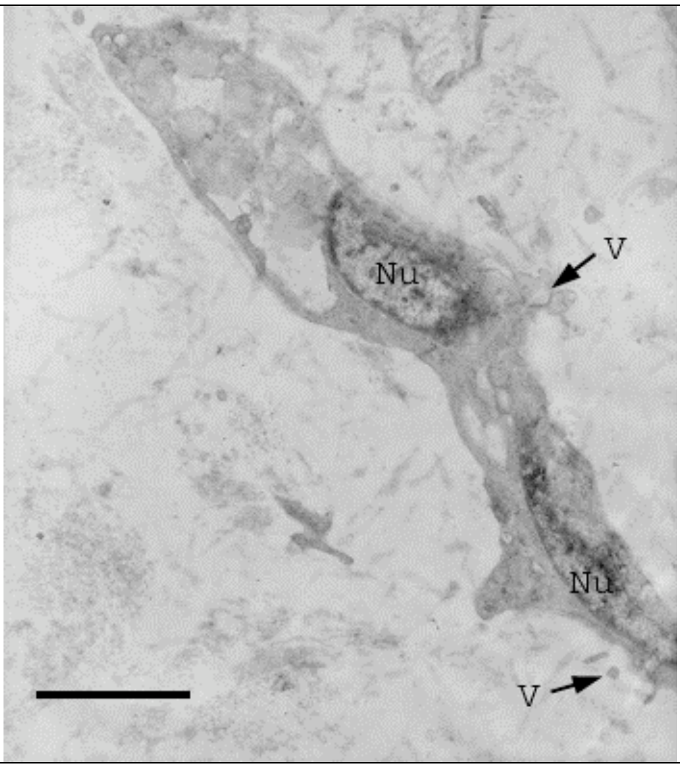

Figure 2.48. Transmission electron micrograph shows a twin nucleated (Nu) interstitial cell with an elongated shape secreting vesicles. Bar = 2 μm.

Other cells identified were more rounded and had a more smooth muscle like phenotype. The cytoplasm was more granular, indicative of a more rigid cytoskeleton. The cells were viewed regularly in association with collagen, and sometimes pro-collagen fibres could be seen in the vacuoles (Figure 2.49).

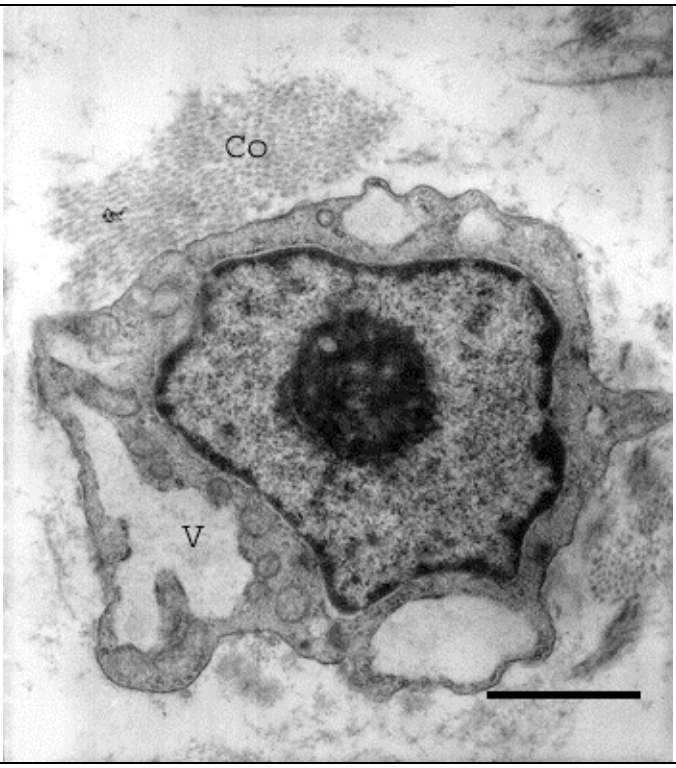

Figure 2.49. Transmission electron micrograph shows a round shaped interstitial cell is in close contact with collagen (Co). The cytoplasmic vesicles contain pro-collagen. Bar = 2 μm.

2.3.13 Quantitative Stereology

The data obtained from stereology grid count was analysed using ANOVA. The four data sets included endothelium, interstitial cells, collagen and extracellular matrix. The features of the data sets are presented (Table 2.4).

Table 2.4. Medians, means and quartile values for the quantitative stereology of endothelium, interstitial cells, collagen and extracellular matrix data sets.

	Endothelium		Interstitial cells		Collagen		Extracellular matrix	
	Normal	Diseased	Normal	Diseased	Normal	Diseased	Normal	Diseased
75% Q	3796.0	2551.2	2696.8	4006.0	16425.0	9525.0	14050.0	17425.0
Median	2439.5	1667.0	1775.5	2146.0	12700.0	5650.0	9500.0	14600.0
25% Q	1339.0	263.8	696.2	1159.0	8200.0	3375.0	5575.0	10250.0
Mean	2669.7	1639.2	2018.8	2862.9	12404.4	6876.7	9808.9	13958.2

Dramatic differences in medians and means in each data pair between normal and diseased were identified.

2.3.13.1 Endothelium

Results from the sterology study shown there was less endothelium in the diseased valves. The median and both the upper and lower quartile values were lower in the diseased valves in comparison with their counterparts in normal valves. There was a slight skew in the distribution of data in the diseased, where more data had values at the lower end of the range. This was due to the lower frequency of endothelium presented in the diseased. ANOVA showed the difference in endothelium between normal and diseased valves was highly significant (p<0.0001) (Figure 2.50).

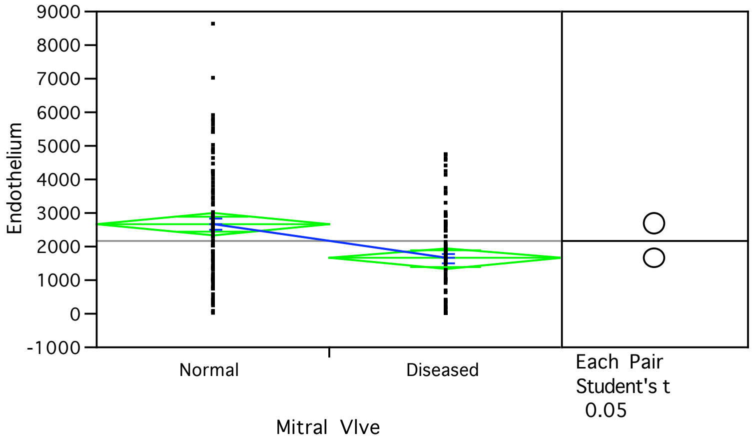

Group			Mean	
Normal	A		2669.6889	p<0.0001
Diseased		B	1639.2444	

Figure 2.50. Comparison of endothelilum as assessed by quantitative stereology between normal and diseased mitral valve.

2.3.13.2 Valvular interstitial cells

The data sets for interstitial cells in both normal and diseased valves showed deviation from the standard normal distribution. The distributions were similar to an exponential distribution that skewed to one side. The lower tails were shallow but dense. Nonetheless, results showed more interstitial cells in the diseased state (Figure 2.51). The difference between normal and diseased achieved statistical significance (p=0.0084).

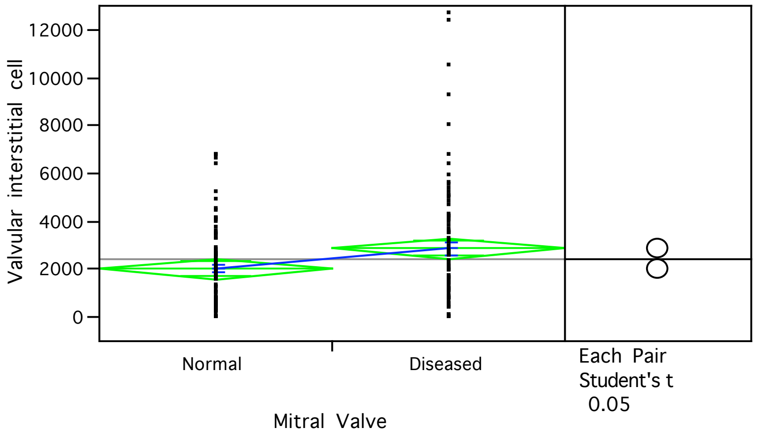

Group			Mean	p=0.0084
Diseased	A		2862.9000	
Normal		B	2018.7778	

Figure 2.51. Comparison of valvular interstitial cell as assessed by quantitative stereology between normal and diseased mitral valve.

2.3.13.3 Collagen

The data sets for collagen for both normal and diseased resembled the standard normal distribution of a unimodal data set. There was a dramatic decrease in collagen quantity in the diseased valves that almost two fold less than the normal (Figure 2.52). This difference was found to be highly significant in ANOVA, as the $p<0.0001$.

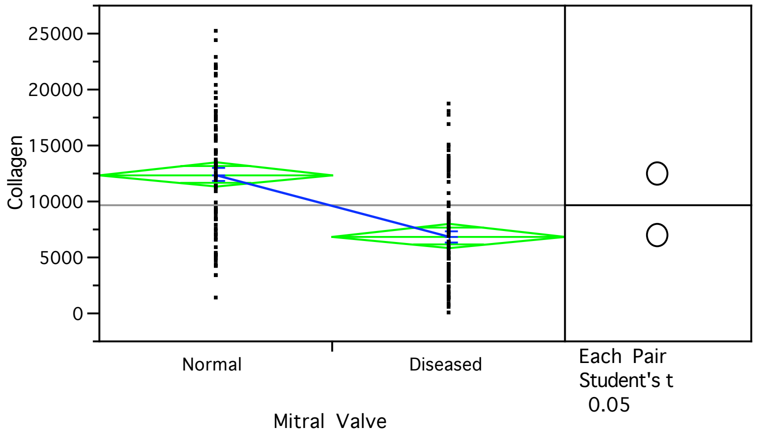

Group			Mean	p<0.0001
Normal	A		12404.444	
Diseased		B	6876.667	

Figure 2.52. Comparison of collagen as assessed by quantitative stereology between normal and diseased mitral valve.

2.3.13.4 Extracellular matrix

Both the data sets for normal and diseased valves showed the classic standard normal distribution with unimodal peaks. There was a marked increase in the amount extracellular matrix in the diseased valves (Figure 2.53). ANOVA revealed this difference was highly significant (p<0.0001).

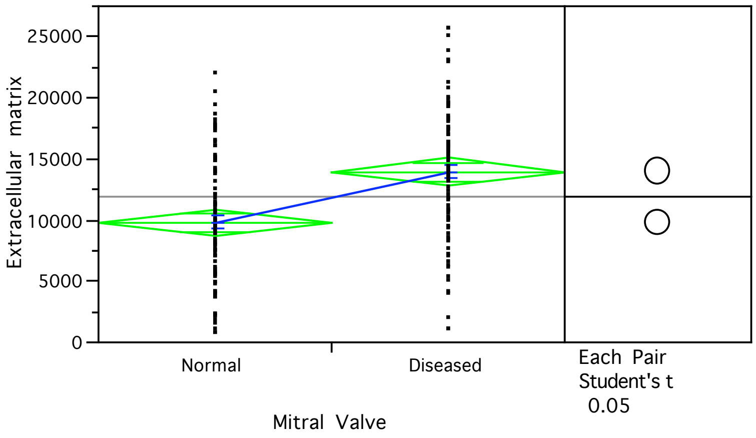

Group			Mean	p<0.0001
Diseased	A		13958.222	
Normal		B	9808.889	

Figure 2.53. Comparison of extracellular matrix as assessed by quantitative stereology between normal and diseased mitral valve.

2.3.13.5 Circularity

All the data sets obtained for circularity analysis exhibited the normal distribution paradigms of a bell curve. Some features of the data sets are presented (

Table 2.5). By comparing the number of cells in each category between normal and diseased, the data confirmed the observations made under TEM and confirmed the change in cell numbers previously reported. Out of the 180 micrographs analysed there was a decrease in the number of endothelial cells, but an increase in the number of interstitial cells found in the diseased in compared to normal valves.

Table 2.5. Medians, means and quartile values for the circularity of endothelium and interstitial cell.

	Endothelium		Interstitial cell	
	Normal	Diseased	Normal	Diseased
n	52	44	37	42
75% Q	0.34500	0.51375	0.74050	0.81725
Median	0.28100	0.42700	0.64100	0.67400
25% Q	0.21675	0.36900	0.51800	0.53375
Mean	0.309096	0.443795	0.62354	0.656547

2.3.13.5.1 Endothelium vs. interstitial cells: Normal valve

In the normal valves, the mean circularity value for endothelial cells was low typical of their flattened and elongated shape. In contrast, the interstitial cells were much circular and had a higher mean circularity; more than two fold higher than the endothelium. This difference was highly significant ($p<0.0001$). There were a few outliers in circularity score in the endothelium at the top tail end, due to cells undergoing apoptosis and becoming plumper. The sample distribution covered a wide range in the interstitial cells as a result of the multi type of polymorphic interstitial cells. The outliers at the lower tail end in the interstitial cells were probably due to the development of irregular micro-appendage in certain cells (Figure 2.54).

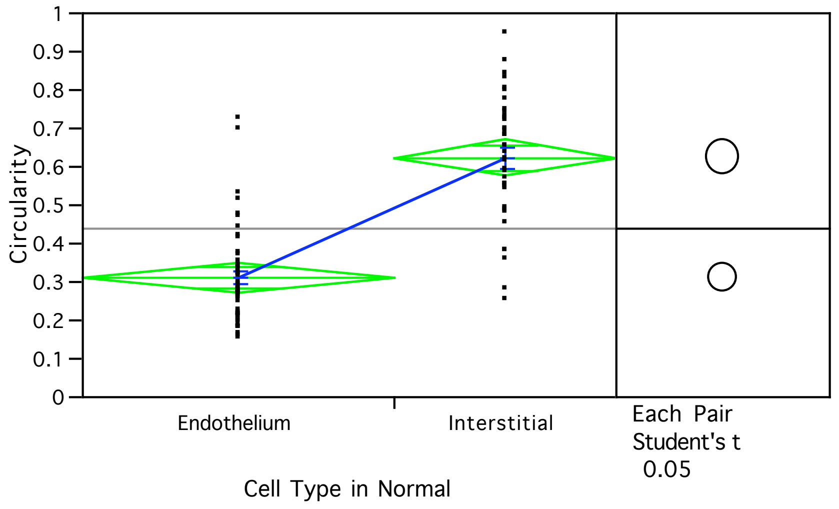

Group			Mean	p<0.0001
Interstitial	A		0.62354054	
Endothelium		B	0.30909615	

Figure 2.54. Comparison of cicularity between endothelium and interstitial cell in normal mitral valve.

2.3.13.5.2 Endothelium vs. interstitial cells: Diseased valve

In the diseased valves, although the degree of difference in circularity between endothelial and interstitial cells was smaller, owing to the presence the endothelial protuberances. The mean circularity score of the interstitial cells was higher than the endothelial cells. The difference was highly statistically significant ($p<0.0001$). Again, the samples distribution covered a wide range due to the polymorphic nature of interstitial cells (Figure 2.55).

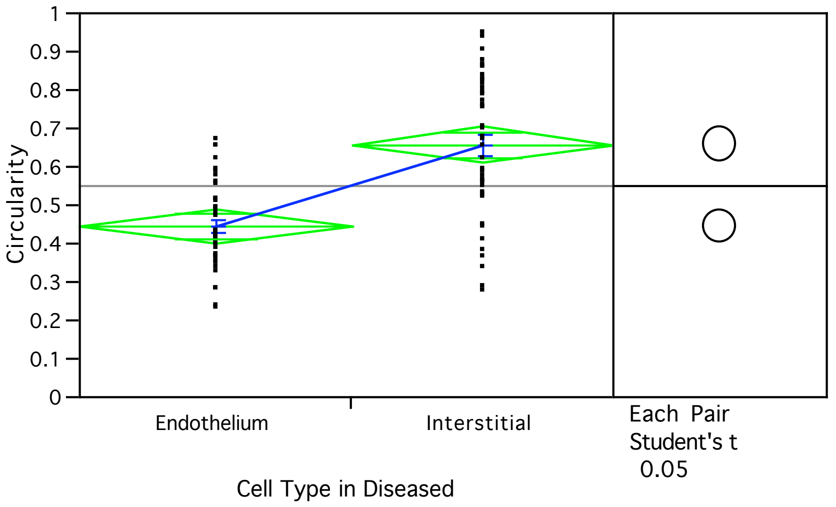

Level			Mean	p<0.0001
Interstitial	A		0.65654762	
Endothelium		B	0.44379545	

Figure 2.55. Comparison of cicularity between endothelium and interstitial cell in diseased mitral valve.

2.3.13.5.3 Endothelial cells: normal vs. diseased

The mean circularity of endothelial cells was higher in the diseased valve as a consequence of pathological transformation in which the endothelial cells bulged out compared to the normal flattened state. A highly significant difference in circularity of the endothelial cells between normal and diseased was formed. Any outliers at the upper tail of the normal range were due to swelling during apoptosis (Figure 2.56).

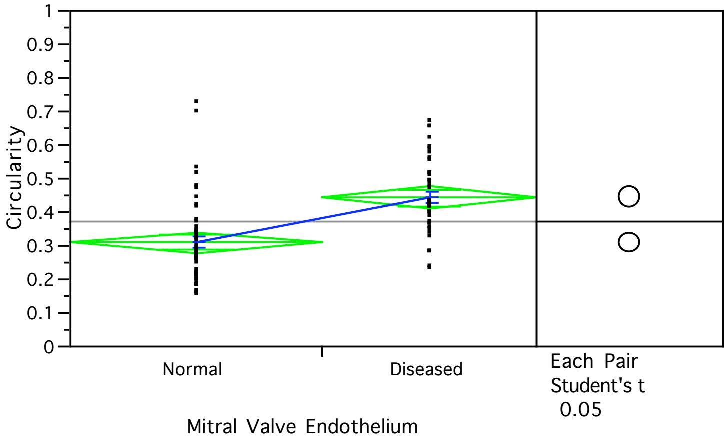

Group		Mean	p<0.0001
Diseased	A	0.44379545	

Normal	B	0.30909615	

Figure 2.56. Comparison of endothelium cicularity between normal and diseased mitral valve.

2.3.13.5.4 Interstitial cells: normal vs diseased

In both normal and diseased the circularity values for interstitial cells exhibited more variation than for endothelial cells. This attribute was due to the polymorphic nature of the interstitial cells. Cells of different phenotypes often coexisted in close proximity. The data distribution patterns were at similar levels in both normal and diseased. Even though a slight increase in circularity in the disease was noticed, this difference did not reach statistical significance. The postulated LSN was calculated at 443. The circularity values for the interstitial cells showed no statistical difference between normal and diseased valve and were not much different from the circularity values calculated in myxomatous regions using ImageJ light microscopic study (Figure 2.57).

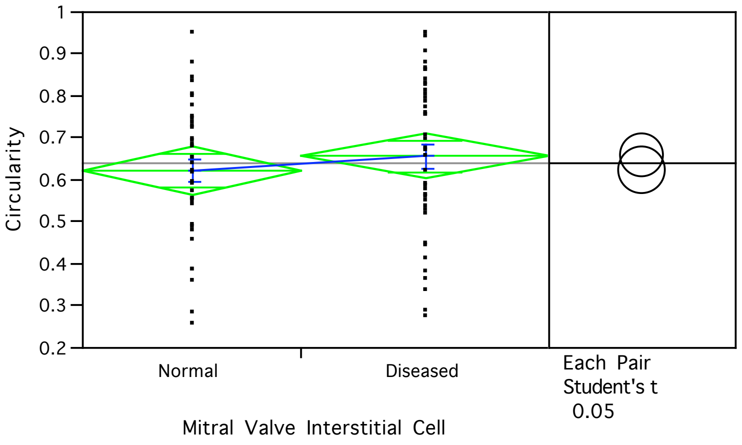

Group		Mean	
Diseased	A	0.65654762	p=0.4056
Normal	A	0.62354054	LSN=443.38

Figure 2.57. Comparison of valvular interstitial cell cicularity between normal and diseased mitral valve.

2.3.14 Scanning electron microscopy of cell macerated samples

2.3.14.1 Normal

At the mid zone of the leaflet, the layered structure of the connective tissue skeleton structure was distinctly visible. The atrialis layer consisted of interwoven fibres forming a fine mesh network. The middle spongiosa layer was loosely constructed. Its organisation had a honeycomb appearance with many matrix empty voids. On close examination, collagen struts could be seen to make up the framework structure. The fibrosa layer was compacted with dense collagen and formed a continuous band. There were numerous tiny gaps evenly spaced in the band of collagen. The void gaps had a spindle shape which closely resembled the outlines of interstitial cells. To delineate the ventricularis layer used by other researchers was slightly tricky. Surprisingly there was no clear line distinguishing the ventricularis from the fibrosa. The ventricularis could be arbitrarily identified as a very thin dense layer on the outer rim of the fibrosa (Figure 2.58).

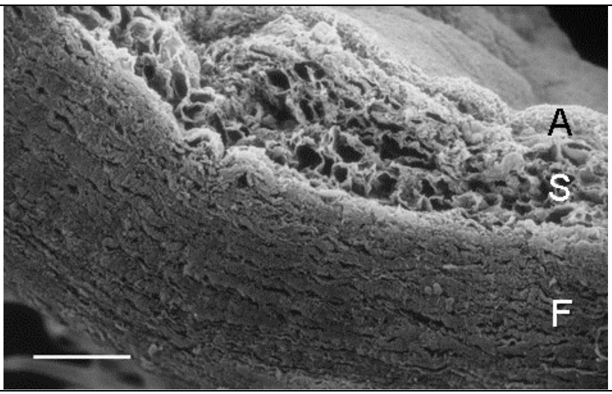

Figure 2.58. Scanning electron micrograph of a normal mitral valve septal leaflet at the mid zone. The three layers atrialis (A), spongiosa (S) and fibrosa (F) are distinguishable. Bar = 0.1 mm.

At the distal end, the leaflet showed a sponge or cork-like connective tissue architecture. The cross section views exhibited a craquelure like texture made of lignified connective tissue juxtaposed with tiny gaps. The layered structure was vaguely distinguishable, although the spongiosa in the middle appeared loosely arranged compared to the more tightly structured atrialis and fibrosa (Figure 2.59).

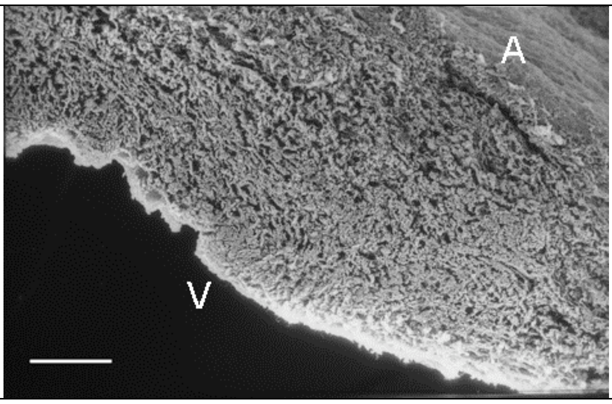

Figure 2.59. Scanning electron micrograph of a normal mitral valve septal leaflet at the distal zone. Atrialis surface (A) and ventricularis surface (V). Bar = 0.1 mm.

At higher magnification, the spongiosa in the distal zone appeared trabecular in organisation. The collagen fibres inter-twined to form an extensive network. Some collagen fibres twisted together to form thicker collagen bundles. Lateral struts were found connecting between bundles for support (Figure 2.60).

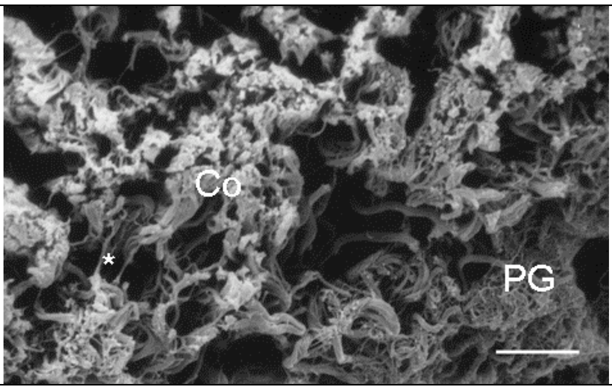

Figure 2.60. Scanning electron micrograph of a normal mitral valve septal leaflet at the distal zone in close up. The collagen fibril (Co), lateral struts (*) and proteoglycan network (PG) are visible. Bar = 10 μm.

At the free edge, the surface was made of an interweaving network of collagen fibres. There were slightly thicker main fibres aligned in the same direction as the axis of the leaflet. The main fibres were joined together by the aborisation of thin fibre networks (Figure 2.61).

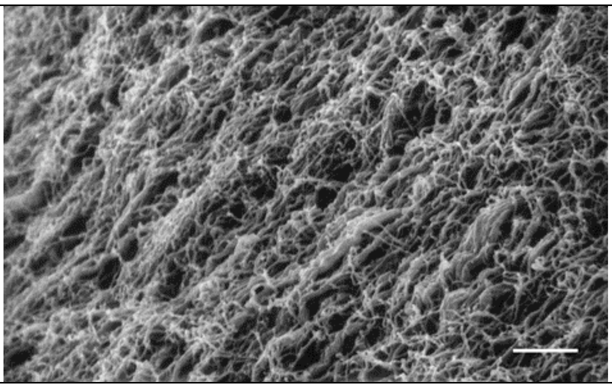

Figure 2.61. Scanning electron micrograph of a normal mitral valve septal leaflet at the free edge surface. Bar = 5 μm.

2.3.14.2 Diseased Grade 1 to 4

In the diseased samples, disruption of the connective tissue structure was evident at the mid zone, notably in the collagen rich fibrosa layer. The degree of the destruction was proportional to the severity of the disease. In the Grade 1 diseased, the honeycomb pocket structure in the spongiosa layer was collapsed. The normal collagen struts supporting the framework could not be seen, leaving a distorted structure with large void spaces. However, the fibrosa in Grade 1 was intact and comparable to that seen in the normal. In the Grade 2 diseased, distortion of the pocket structure in spongiosa was observed as well as small cracks in the fibrosa layer. In the Grade 3 disease, disintegration could be seen in all three layers. The atrialis was frayed looking, a departure from its normal wavy structure. The compartmental arrangement in spongiosa architecture was barely recognisable. Instead the spongiosa was filled with large void gaps. There were numerous crevasses and cracks in the fibrosa layer, a sign of major collagen disintegration. In the Grade 4 disease, there was a marked destruction of the connective tissue structure of the valve stroma. The tissue skeleton seemed as been torn apart. There were only remnants of the trabecular structure still visible in the spongiosa and collagen in the fibrosa became totally fragmented leaving deep crevasses (Figure 2.62).

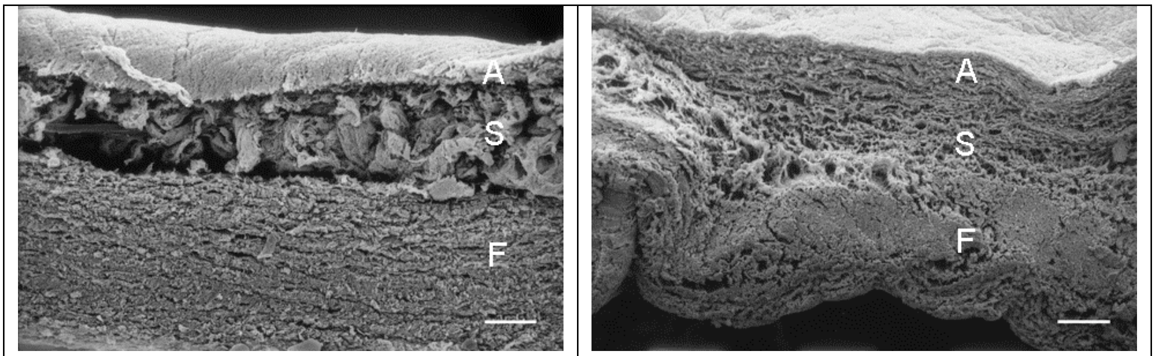

Grade 1

Grade 2

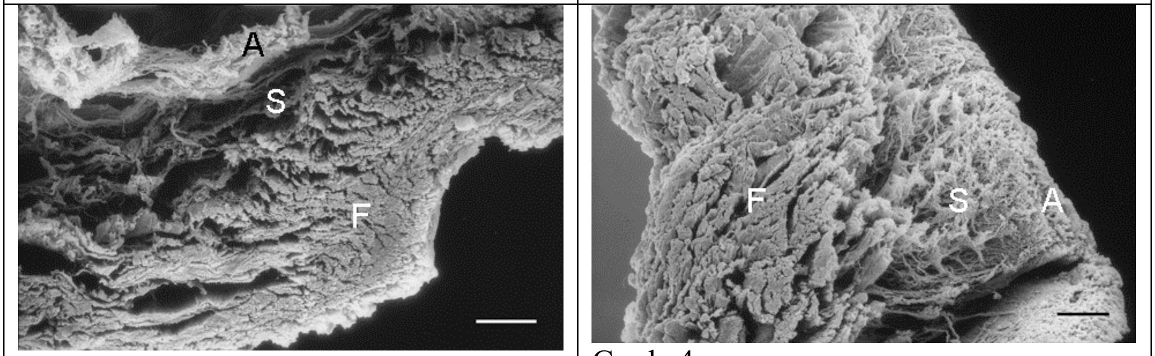

Grade 3

Grade 4

Figure 2.62. Scanning electron micrographs of diseased mitral valve septal leaflets at the mid zone. Disruption of the connective structure during the disease progression is evident. The three layers atrialis (A), spongiosa (S) and fibrosa (F) are labelled. Bar = 0.1 mm.

At the distal end, increase in thickness of the leaflet during disease progression was apparent and the overall structure had a bizarre looking appearance. There were deep groove lines dividing the areas into “lobe-like” structures. Some lobes had vein like crack lines. Others had crinkled lines and resembled brain gyri and sulci (Figure 2.63).

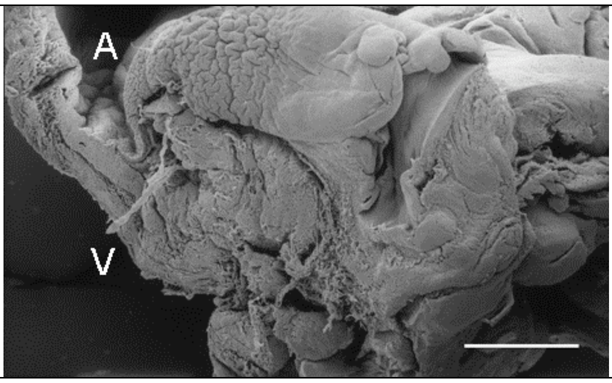

Figure 2.63. Scanning electron micrographs of diseased mitral valve septal leaflets at the distal zone. There were deep groove lines dividing the areas into “lobe-like” structures. Some lobes had vein like crack lines, atrial side (A) and ventricular side (V). Bar = 1 mm.

At high magnification the distal end spongiosa layer, the major site of myxomatous changes, showed much thicker fibres separate from each other. Each thick fibre was made of very thin thread-like fibre, and many fibres exhibited frayed ends. The fine collagen network structure seen in normal valve was lost (Figure 2.64).

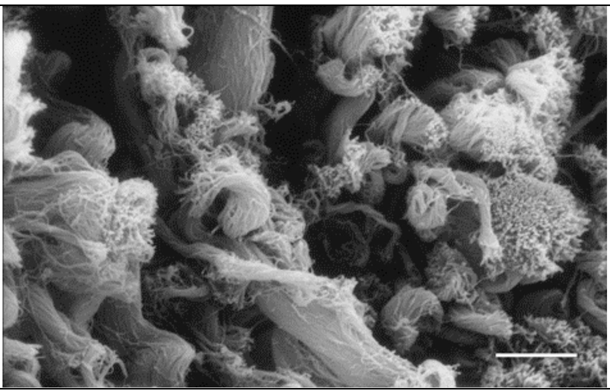

Figure 2.64. Scanning electron micrographs of diseased mitral valve septal leaflets at the distal zone in close up. The collagen fibres are thicken, and some with frayed ends. Bar = 10 μm.

At some discrete locations in the distal zone, thin collagen fibres in a highly compacted arrangement were found. These collagen fibres did not seem to be part of any recognizable structure arrangement or network (Figure 2.65).

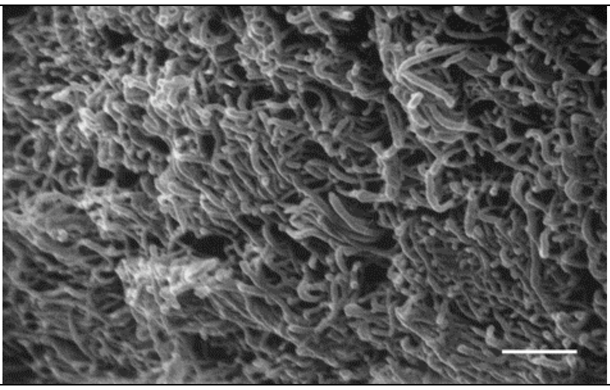

Figure 2.65. Scanning electron micrographs of a disease mitral valve septal leaflet shows amassed collagen fibres in distal zone. Bar = 5 μm.

At the atrialis surface near the free edge, some of the thin collagen fibres were tangled into lumps. The mesh-like appearance of collagen fibres was not evenly spaced, with voids of in different sizes visible (Figure 2.66).

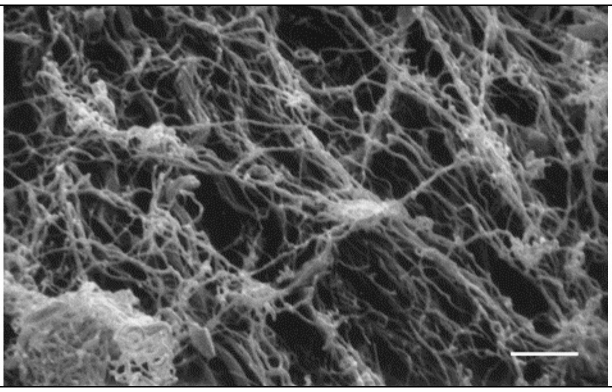

Figure 2.66. Scanning electron micrographs shows a diseased mitral valve septal leaflet at the free edge surface. The mesh-like appearance of collagen fibres was not evenly spaced, with voids of in different sizes visible. Bar = 0.5 μm.

2.3.15 Quantitative connective tissue micro-structural analysis

The BinariseSEM method was found capable of dealing with this problem. The software was fully automated after the initial stage of calibration and image segmentation and was capable of calculating a large data set and generating numerous different structural distribution profile data charts. To overcome the problem of data overload, the determination of the difference between normal and diseased only used micrographs taken at the distal zone spongiosa layer in Grade 0 normal valve and Grade 3 diseased valve. The micrographs were captured at the same magnification of ×1690, the same viewing angle and the same orientation relative to the surface. The different quantitative shape descriptors were applied as parameters to determine the difference in connective tissue structure between normal and diseased mitral valves.

Pore Area

Pore area is a measure of pore size. The computed results shown the mean pore area in the diseased valve was 0.301 μ^2, and was more the twice as large as the pore area in normal valve at 0.127 μ^2. Furthermore, the maximum pore area in the diseased valve was 6.190 μ^2 compared to 0.777 μ^2 in the normal valve. Many smaller pores clustered at the left hand side of the x-axis on the distribution chart were seen in both normal and diseased, even though their respective x-axes were at vastly different scales (Figure 2.67).

Pore form factor

Pore form factor is a shape descriptor. The distribution patterns of pore form factor were markedly different between the two samples. However, the mean pore form factors were similar; 1.064 in the normal and 0.928 in the diseased. Moreover, the min, max and mode values of the two samples were also similar.

Pore roundness

Pore roundness is a measure of pore circularity. The pore roundness distribution in the normal valve showed some resemblance of a normal distribution curve with unimodal peak in the middle. The counts in the normal sample occurred at regular intervals, but only up to 0.003, whereas the roundness distribution in the diseased was scattered across a wider range up to 0.007. The pore roundness distribution in the diseased valve exhibited a twin peak distribution curve deviation from the normal distribution. Furthermore, the mean and maximum roundness values were also higher respectively in the diseased valve.

Pore aspect ratio

Pore aspect ratio is a ratio of the maximum to minimum dimensions. There were certain common features in the pore aspect ratio distribution patterns in both normal and diseased valve. Both distribution patterns resembled a normal distribution despite of counts weighted slightly more on the left hand side of the charts. Additionally, the means were almost the same plus the minimun, maximum and mode values were also similar.

Pore perimeter

Pore perimeter is a measure of the pore boundary. Increase in crevasses in the diseased had resulted in numerous pore counts with large perimeters. Although the means between the two samples (normal=1.018, diseased=1.484) were very close, the maximum value in the diseased valve was 14, more than four times bigger than the 3.434 in normal valve. The two distribution charts consequently had varying in scale on the x-axis, but if the chart for normal is resized to match the diseased, the two distribution patterns would match each other quite well, the majority of pore perimeters were on the smaller side of the scale in both samples.

Pore max diameter

The pore max diameter is a measure of the longest line that can fit into a pore. The mean pore max diameter at 9.836 μ in normal was actually bigger than the diseased at 7.830 μ. The lower end values of the two samples were the same at 1.1414 μ, but the upper end value range extended to 75.432 μ in the diseased valve, more than twice as large as the 34.132 μ in the normal valve. If the distribution charts were standardised, the distribution patterns of pore max diameter in normal valve was quite similar to the pore max diameter in diseased valve.

Pore min diameter

The pore min diameter is a measure of the shortest line that can fit into a pore. This was similar to the distributions in the pore max diameters. The lower end minimum diameters were the same again at 1.414 μ in both samples. The two means were close, but the top minimum diameter in diseased valve was up to 27.019 μ and up to 17.088 μ in the normal valve. The distribution pattern profiles were similar between the two samples. The trend was an exponential increase in counts when moving towards the lower end on the left.

Pore directionality

Pore directionality is a measure of the gradient direction. The pore directionality distribution profiles in both samples were similar. However, the normal valve had more freedoms of choice in directionality than the diseased. One striking feature was the gaps seen in the middle of distribution charts in both. It could be interpreted, that there was a limited range of pore directionality in both normal and diseased valves.

Pore directionality angle

The pore directionality angle diagrams corresponded to the patterns in pore directionality distribution charts. In the normal, there were more degrees of freedoms found in the directionality angle, although there were a few preferred directions found. The orientations of the pores in the diseased valve were restricted to certain angles. The remaining directionality angles in the disease valve were similar to the directionality found in normal.

Overall, there was an increase in pore area and pore perimeter as the disease progressed, but there was no change in pore aspect ratio. The change found in pore form factor was so small it could be considered as negligible. There was an alteration in pore roundness and the diseased covered a wider range than the normal. Both the pore maximum and minimum values increased and the range extended in the diseased valve while their mean values remained comparable to the normal. The pore directionality was more restricted in the diseased but the preferred directionality was similar to the normal.

Grade 0 Normal binarised	Grade 3 diseased binarised
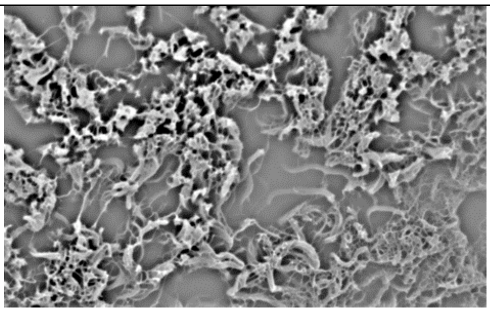	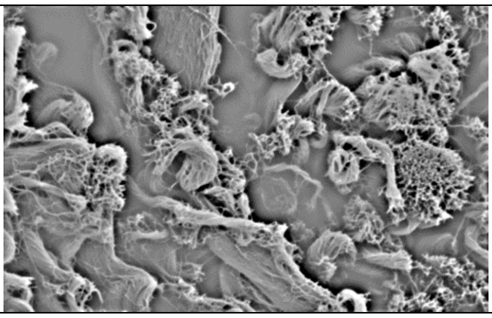
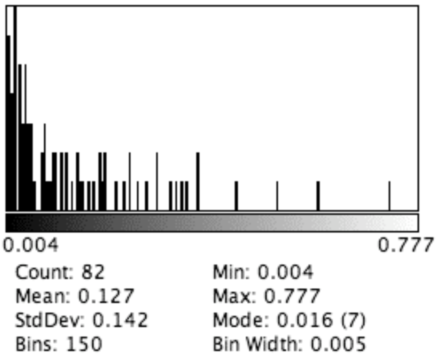 Count: 82 Mean: 0.127 StdDev: 0.142 Bins: 150 Min: 0.004 Max: 0.777 Mode: 0.016 (7) Bin Width: 0.005 Grade 0 Pore Area (μ^2)	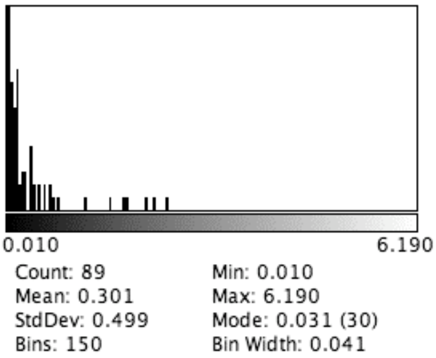 Count: 89 Mean: 0.301 StdDev: 0.499 Bins: 150 Min: 0.010 Max: 6.190 Mode: 0.031 (30) Bin Width: 0.041 Grade 3 Pore Area (μ^2)
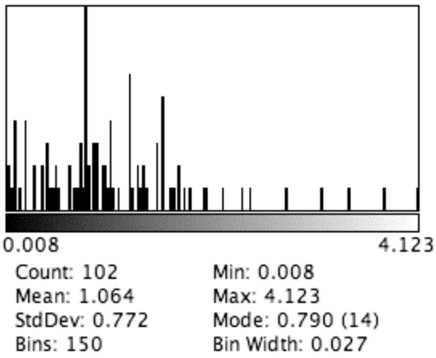 Count: 102 Mean: 1.064 StdDev: 0.772 Bins: 150 Min: 0.008 Max: 4.123 Mode: 0.790 (14) Bin Width: 0.027 Grade 0 Pore Form Factor	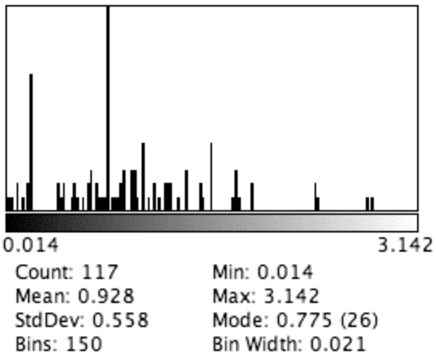 Count: 117 Mean: 0.928 StdDev: 0.558 Bins: 150 Min: 0.014 Max: 3.142 Mode: 0.775 (26) Bin Width: 0.021 Grade 3 Pore Form Factor

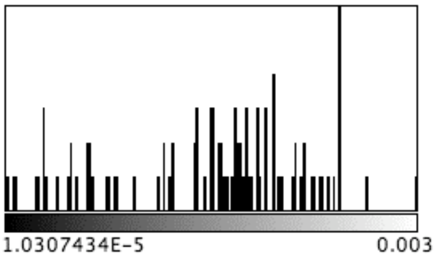

```
Count: 101            Min: 1.0307434E-5
Mean: 0.001           Max: 0.003
StdDev: 6.53695E-4    Mode: 0.002 (12)
Bins: 150             Bin Width: 1.8220373E-5
```

Grade 0 Pore Roundness

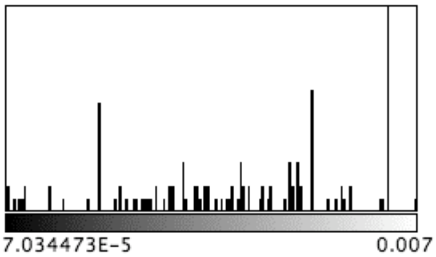

```
Count: 122            Min: 7.034473E-5
Mean: 0.004           Max: 0.007
StdDev: 0.002         Mode: 0.006 (17)
Bins: 150             Bin Width: 4.523707E-5
```

Grade 3 Pore Roundness

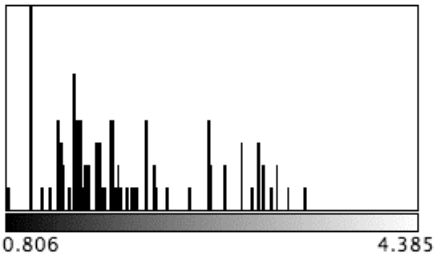

```
Count: 101            Min: 0.806
Mean: 1.787           Max: 4.385
StdDev: 0.669         Mode: 1.009 (14)
Bins: 150             Bin Width: 0.024
```

Grade 0 Pore Aspect Ratio

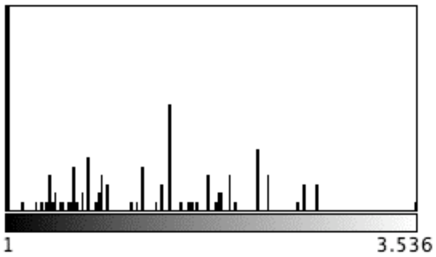

```
Count: 122            Min: 1
Mean: 1.768           Max: 3.536
StdDev: 0.598         Mode: 1.008 (23)
Bins: 150             Bin Width: 0.017
```

Grade 3 Pore Aspect Ratio

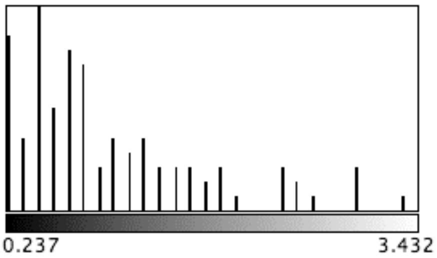

```
Count: 101            Min: 0.237
Mean: 1.018           Max: 3.432
StdDev: 0.726         Mode: 0.482 (14)
Bins: 150             Bin Width: 0.021
```

Grade 0 Pore Perimeter (μ)

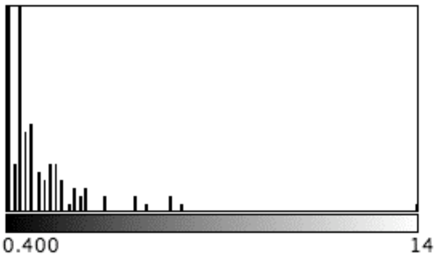

```
Count: 122            Min: 0.400
Mean: 1.484           Max: 14
StdDev: 1.643         Mode: 0.445 (26)
Bins: 150             Bin Width: 0.091
```

Grade 3 Pore Perimeter (μ)

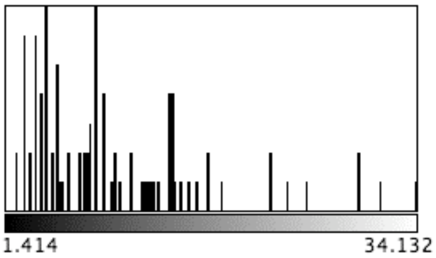

```
Count: 93             Min: 1.414
Mean: 9.836           Max: 34.132
StdDev: 6.941         Mode: 4.577 (7)
Bins: 150             Bin Width: 0.218
```

Grade 0 Pore Max Diameter (μ)

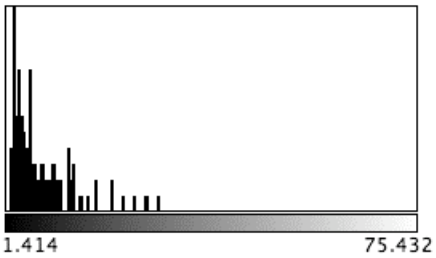

```
Count: 105            Min: 1.414
Mean: 7.830           Max: 75.432
StdDev: 5.830         Mode: 2.648 (13)
Bins: 150             Bin Width: 0.493
```

Grade 3 Pore Max Diameter (μ)

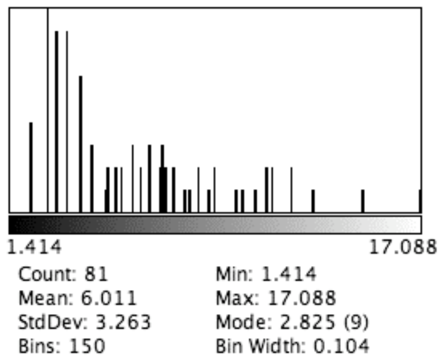

Grade 0 Pore Min Diameter (μ)

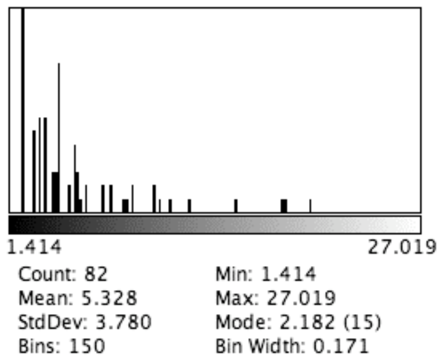

Grade 3 Pore Min Diameter (μ)

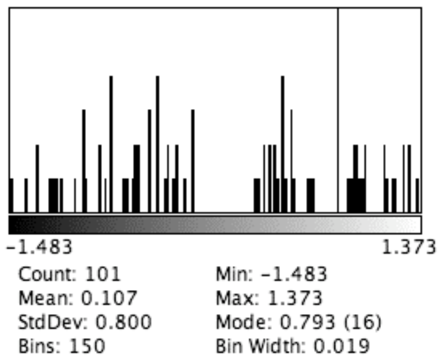

Grade 0 Pore Directionality

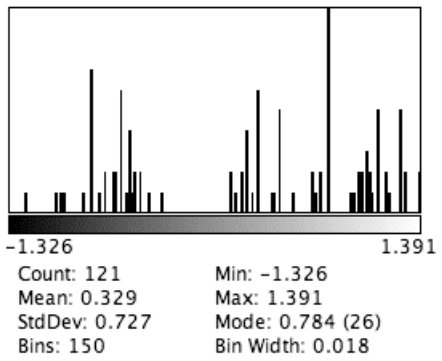

Grade 3 Pore Directionality

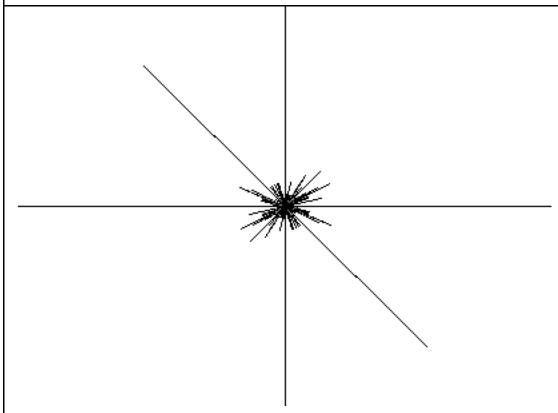

Grade 0 Pore Directionality Angle

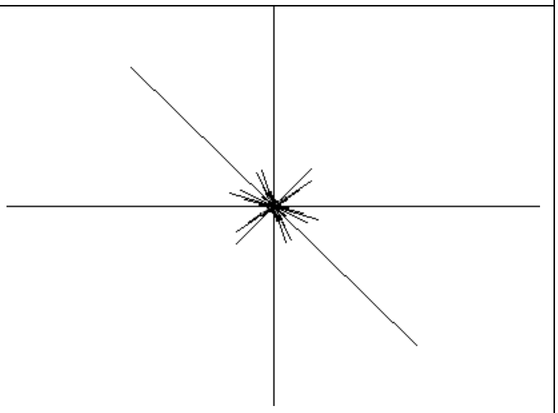

Grade 3 Pore Directionality Angle

Figure 2.67. Quantitative connective tissue micro-structural analysis distribution charts. From top, binarised images, pore area, pore form factor, pore roundness, pore aspect ratio, pore perimeter, pore diameter, pore min diameter, pore directionality and pore directionality angle.

2.4 Discussion

The mitral valve complex is a complicated anatomical structure whose function requires all its components to work in a precise synchronised fashion to allow adequate left ventricular filling and emptying[6, 7]. Alteration in tissue structure will result in deformation and compromised performance of the valve. In this study image analysis methods were applied to investigate different aspects of the morphological and cellular changes that occur with myxomatous mitral valve disease in the dog. Qualitative visual evaluations as well as quantitative analyses were conducted at macro-structural and ultra-structural levels. Using a novel set of parameters, this study has shown that with disease progression there are quantifiable changes in leaflet length, leaflet edge thickness, connective tissue content and cell numbers in the valve leaflet. A subjective change in GAG expression was found but could not be quantified using different colour measuring techniques. In the myxomatous area, there was no change in cell shape associated with disease and cells were typically spindle-shaped, consistent with an interstitial cell phenotype. However, the morphological changes in endothelial cells noted with disease were found to be significant. The study also showed the public domain image analysis software ImageJ can be used to assess morphogenesis, but should be used with caution when applied to measure changes in colour intensity.

The age dependent nature of MMVD[52] was highlighted once again in this study. The age distributions of the dogs according to lesion grades are in line with previously published data[1, 2, 22, 53, 54]. All the normal dogs were five years or younger and all dogs over the age of nine were affected by this disease. At the extreme end of the scale, it seemed the Grade 4 disease has reached the upper limit set by age. This observation was likely due to mortality kicked in as an antagonist to survival. Although there is no comparable grading system in human medicine the dog age distribution is comparable with human patients. Most reported human patients requiring mitral valve repair surgery or replacement tend to be middle-aged. It is likely such intervention occurs before the more severe form of the disease seen in aged dogs becomes apparent[55-57]. The exact prevalence of MVP in the human population is still a matter of debate. Compiling the data from 17 population-based studies, the prevalence commonly ranges from 2 to 10 percent, but up to 35 percent in studies[56, 58]. The prevalence of MVP is low in young children, but increases from childhood to adolescence, and this change is concomitant with the growth spurt of adolescence[59]. The conflicting data from human medicine is clearly shown by two separate papers published by Framingham heart study where the prevalence of MVP and MR were determined using echocardiography. The prevalence of MVP was found at to be as low as 2.4%, whereas the MR normally regarded as a complication of MVP, was found in a surprising 19.0% of patients[60, 61]. The sample selection, the diagnostic tool used and the criteria of selection used could all have influenced the outcome of these studies, and the issue of a standardised method of diagnosis and measurement criteria has been raised[62].

Using the data from the current study, the onset of the disease in the dog can be extrapolated to be just shortly after the age of four years. However, this onset could only be applied to a heterogeneous group of mixed breed dogs, as in this instance, and it is well documented that certain highly predisposed breeds like the Cavalier King Charles spaniel (CKCS) shown signs of MMVD at very early age[53, 54]. Because of this breed association it has long been thought the disease is inherited. The parent to offspring inheritable relationship was established in an echocardiographic study of MR in CKCS and Dachshounds[32]. The disease, in affected breeds, is believed to be an autosomal dominant complex polygenic trait with variable penetrance[63]. Increase in plasma platelets response and fibrinogen have already been put forward as useful biomarkers in CKCS[64-66]. An inherited form of the disease is seen in human Marfan syndrome patients who develop myxomatous mitral degeneration at an early age. However, Marfan Synfrome is caused by the mutation a single gene encoding for the extracellular structural protein fibrillin[67-69].

There may be a gender predisposition to MMVD. Although the gender issue was beyond the scope of this study, there were more male dogs in the sample group. However, a proportion of the samples available were from male dogs with a history of behavioural problems (reason for euthanasia). A higher incidence in male dogs has been found in some studies, which might point to a possible hormonal factor[1, 70]. In human MVP, higher prevalence among lean young women in some cases raised the question about life style choice[58].

The auscultatory findings for the dogs in this study were highly dependent on the progression of the disease. The extrapolated data has shown the earliest murmur detected intercepted with Grade at 0.9, thus auscultation was only sensitive for detection of murmur from Grade 1. Pedersen has pointed out the auscultation finding was related to stage of the disease, the early stage mild systolic murmur has low intensity therefore very hard to detect even for experienced cardiologist[71].

In normal valve closure, the two leaflets meet each other snugly with the free edges in apposition but at an angle to the smooth zone of the leaflet[7]. The leaflet itself is a multilayer structure covered by a single cell thick endothelial lining along each surface. On cross section the mitral valve leaflet can be seen to consist of an elastic atrialis layer, a loose spongiosa layer, a dense connective tissue fibrosa layer and a ventricularis layer to which the chordae tendinae attach. Nevertheless, the leaflet is a continuous structure with each constituent element performing specialized functions. Although the designation of mitral valve leaflet cross-sections into layers was somehow arbitrarily defined in the distal zone of diseased valves, the layering across the leaflet was otherwise distinct. The structural changes due to myxomatous degeneration in the leaflets are not always uniformly distributed, but have long been identified as the most important factors contributing to mitral valve dysfunction in dogs[1, 2, 17, 43, 72]. The rough zone of the leaflet on the ventricle side where the tedinous chords attach is particularly prone to myxomatous degeneration. The chordal insertion areas were usually the most severely affected[73]. At later stages of this disease, gross distortion of the apposition line of the leaflets was caused by the development of interchordal hoodings[7, 71]. The middle section of the leaflet is less susceptible to myxomatous degeneration and at the same time withstands the strongest pressure loading during the cardiac cycle[74]. In mitral valve prolapse in people, the mid section of the leaflets is involved, especially the middle scallop of the mural leaflet with changes seen in 88% of patients[55, 75]. Considering the changes noted in dogs, the current study focused on the tissue in the central line from free edge to annulus.

The mean diamonds incorporating comparison circles method was chosen to graphically represent the final statistical analysis. This allows a view of the large amount of information embedded in the chart graph, and appreciation of the spread of variance, the sample group size, the distribution of sample, the confidence level, the standard error and the distance in significance between each group.

Various techniques have been used over the years to investigate morphological and structural changes in human and canine MMVD. These techniques have concentrated mainly on biochemical methods to assess ECM expression[76-78]. Gross, histological and ultrastructural descriptions have also been reported[17, 29, 43]. The current study is the first to use image analysis for this purpose in the dog. A similar methodology has been used in normal human valves, but not in human diseased leaflets[79]. In that study age-related reduction in valve area, increase in GAGs and elastin and a decrease in collagen, all as a function of total valve area, were reported. Using Movat's pentachrome staining and Image Pro Plus the "area" of GAGs was measured and not the intensity of staining. Bearing in mind canine MMVD is an age-related condition, it is possible that in that study by McDonald and co-workers (2002)[79] their aged "normal" subjects would be classified as abnormal in a veterinary context and that the changes noted matched those found in dogs with MMVD. Indeed, the authors refer to thickening of the leaflets with age, a feature common in canine MMVD, and the potential problem this would cause with echocardiograph assessment of mitral valves in aged human subjects. It could be argued that the valve thickening and ECM changes noted is in fact evidence of disease and the report by Murata (1981) that GAG content decreases with age in humans would support that view[76].

Myxomatous degeneration is associated with valve interstitial cell (VIC) phenotypic alteration, and this has been demonstrated in both dogs and humans, and there is a degree of reasonable assumption that this change in VIC from a quiescent fibroblast (vimentin-positive) to an activated myofibroblast (α-smooth muscle actin-positive (α-SMA) phenotype contributes to the pathology of the disease[27, 43, 80-82]. What is not clear is whether or not this process involves changes in cell numbers in diseased areas. Studies in human mitral valve disease have documented an increase, in one study of 3.5 times, in activated myofibroblasts in myxomatous areas, and that many of these cells are also CD-34 positive[27, 83]. However, in the dog α-SMA positive cells congregated toward the valve edge have been demonstrated, while there is a concurrent reduction in vimentin positive cells in myxomatous areas[80]. Furthermore, it can be seen in myxomatous lesions there are concentrations of cells at the edge of such lesions towards the tip of the leaflet, and it is likely that counting those cells alone would suggest an apparent increase in cell numbers. Using a computerised imaging tool it could now in this study be shown that, compared to normal spongiosa, there is a reduction in cell density in myxomatous areas in all grades of disease in the dog. While this contrasts with previous reports for human valves the present data is more robust since as many of the cells if not all the cells in definite diseased areas were counted using a computerised imaging tool[26, 27, 83]. However, there is no difference in the cell density when comparing myxomatous areas between different grades of disease, suggesting no cell recruitment or cell proliferation. The increased numbers of CD-34 positive cells reported in myxomatous areas of human mitral valves might be due to cell recruitment from the blood pool[83]. Immunohistochemistry studies have failed to shown a marked increase in CD34+ cells, suggesting such recruitment of CD-34 cells does not occur in the dog.

The exact phenotype of cells in the myxomatous areas of leaflets is likely to be complex, and there is a reasonable presumption that they are predominantly mesenchymal interstitial cells. There is evidence from immunohistochemical and ultrastructural morphology studies in dogs and humans that this is the case, and the majority of cells are either quiescent vimentin-positive fibroblasts or activated α-smooth muscle actin-positive myofibroblasts[26, 43, 82-84]. Since fibroblast-like cells have an elongated spindle shape, it was interesting to see if analysis of cell shape would support this view. A measurement of cell circularity indeed demonstrates a tendency towards an elongated spindle shape in myxomatous areas leaflets. However, some cells in myxomatous areas that are vimentin and α-SMA negative, that tend be more rounded in shape were reported, but their exact phenotype has not yet been fully identified[80].

Scanning Electron Microscopy has previously documented denudation of the endothelium in some areas of the diseased valves of dogs with regional pleomorphism in adjacent intact endothelial areas. The significance of these observations was not known[29]. The TEM data from the current study clearly shows the denudation of endothelium is linked to the MMVD. Furthermore, the denudation of endothelium was concomitant with destruction of collagen and build up of extracellular ground substance in the presence of congregation of VIC near the distal surface. One consideration is that since the Whitney's grading is a gross classification only, and was used to classify the dogs into different grades, and that only a small area of the relatively large valve is observed with TEM, it is problematic to accurately correlate changes seen with disease severity. In the study by Corcoran et al (2004) abnormally diseased and normal endothelium were found adjacent to each other. An additional confounding factor is that the orientation of the TEM sections were not discerned after the point of ultrathin section collection, However, images were taken at random intervals along the length of the endothelium on each sample in an attempt to get better association with disease severity. The labour intensive nature of TEM sample preparation did not allow cross-sectional surface-to-surface examination of samples. Since the main use of TEM is to study a very small area at high magnification, the TEM study was focused on the endothelium and its immediate microenvironment. The observation area did not extend deep into the stroma where myxomatous areas are mainly located.

A favoured hypothesis at present is that the MMVD is a response to repeated impact of the leaflet edges[71]. Myxomatous deformation alters the valve motion resulting in abnormal closure and further damage and the changing in hemodynamic force due to regurgitation may cause endothelial damage[30]. The location and the histology of the thickened foci on leaflet edges supports this hypothesis, but the sequence of events and the time course is unknown[4]. Damage to valve endothelial cells (VEC) could influence the synthesis and release of vasoactive mediators that in turn interact with subendothelial matrix tissue. Endothelin is a potent vasoconstrictor, but also has the potential of stimulating proliferation of fibroblasts and increasing collagen production, and is a possible candidate. An increase in endothelin receptor density has been found in the distal end of canine mitral leaflet with myxomatous changes[31]. However, the actual level of the endothelin was not measured; so direct involvement of endothelin could not be substantiated. Alternatively, endothelium derived nitric oxide might be important and nitric oxide synthase (NOS) has been shown to be increased in the presence of collagen degradation[32]. The clear-cut alteration in the sub-endothelial space shown by TEM favours the idea of involvement of mechanisms of endothelial derived vasoactive substances. However, damage and denudation to endothelial is not restricted to the valve free edge; but can be seen in other areas of the leaflet including the chordae tendineae [29, 85]. Even the endothelium in the normal valve leaflet exhibited a pleomorphic surface feature under SEM[86]. This suggests repeated impact from opening and closing of the valve might not account for the injury to the endothelium alone. The altered turbulence and shear stress during MMVD could also be assumed to exert a detrimental effect on the endothelium. In vitro porcine aortic valve endothelial cells (PAVEC) respond to steady shear stress by aligning perpendicular to flow[87]. Steady shear stress also induced alteration in transcriptional profile of PAVEC on collagen I in culture by up regulating genes associated with chondrogenesis[88]. Co-culture models have also shown that endothelial cells hinder VIC proliferation with hemodynamic shear stress[89] and VIC have been shown to migrate to and proliferate at the site of endothelial denudation and damage in a mitral valve explant organ culture system[84]. Evidence from in vitro experiments suggests that VECs respond dynamically to environmental stimuli and at the same time modulate the VIC activities. Ex-vivo studies have demonstrated that wound healing in the mitral valve is a slow process and involves VEC migration and incorporation into damaged endothelium. Only the VECs at the margin of an injury appear to participate in the regenerative response. At eight weeks post denudation injury round shaped VEC covered the cut edge and the VEC became more flattened only after 12 weeks. This healing process is also associated with phenotypic modulation of interstitial cells from fibroblast to myofibroblast[90]. In the current study, the phenotype of the VICs seen on TEM could not ascertained by their morphology, but there was distinctive VIC polymorphism.

It can be presumed the morphological changes in the VEC and VIC populations are part of the mitral valve response to injury and it is reasonable to speculate it is the response of the mitral valve to injury that determines the clinical and pathological features of MMVD. Using the valve injury model, a reasonable hypothesis is that up-regulation of fibroblast growth factor 2 (FGF-2) contributes by promoting mitral VIC migration and proliferation in response to injury[91]. The mitogenic effect of FGF-2 in conjunction with TGF-β1 induces fibroblast to myofibroblast transformation this can be elegantly demonstrated by TEM[92-94]. The fibroblast-like VICs express matrix metalloproteinases that degrade extracellular matrix and so facilitating migration towards damaged endothelium and transform into myofibroblasts to participate in valve repair and remodelling[82]. Lastly, another consideration is that the damaged endothelium would no longer form a barrier on the surface and the underlying valvular tissue will be exposed to blood borne factors. However, these mechanisms, while useful in explaining changes at the valve surface, are less able explain the processes observed in the overtly myxomatous areas of the inner spongiosa layer. The current study has clearly identified destruction of structural connective tissue in these areas concomitant with accumulation of GAGs but without cellular phenotypic change in numbers or shapes. Much of the current knowledge of the biochemical mechanism in MMVD is derived from experimental work in cell culture. The intricate spatial and temporal relationship in native mitral valve could not be demonstrated in vitro. The possibility of another pathobiological mechanism being involved in the ectopic myxomatous degeneration needs to be considered. Currently there is no feasible mechanical pathway that could adequately be applied to explain the changes in the myxomatous areas, but an understanding of valve development and embryogenesis might be useful. During the early stage of valve development, the GAG rich cardiac cushion is the site that initiates ECM remodeling that transforms later into valve leaflets. However, the cells responsible are believed to be VECs delaminated from endothelium that migrate into the cardiac cushion through a process referred to as endothelial-mesenchymal transformation (EMT)[95-97]. The mechanisms governing the EMT are complex, with many pathways implicated, including VEGF, TGF-β, Notch and Wnt/β-catenin[96]. Some of the mature aortic VECs retain their ability to trans-differentiate in vitro to a mesenchymal phenotype[98]. The question is, is it possible the endothelial cells are also responsible for maintaining the VIC in the mature valve? The hypothesis would be that once the VEC is damaged, signals from the endothelium are diminished and the VICs in the spongiosa, the most remote part of the valve revert to their foetal form and express GAGs for ECM remodeling. A useful model of this effect is seen in the interactions between endothelial and pericyte (smooth muscle cells) in vascular biology. Failure of the interaction between these two cell-types results in severe cardiovascular defects in genetic mouse models[99]. Unfortunately, present knowledge in this field derived from experimental studies on angiogenesis has no parallel implication in MMVD research, but close association between VEC and VIC in both normal and diseased mitral valves is evident, and the functional interaction between these two cells populations needs further examination.

It has generally been presumed that while necessary to maintain normal physiological valve structure and function, the normal valve VECs and VICs are relatively quiescent. In diseased valve, cellular signals promote cell activation[100]. Nuclear bulges and micro-appendages on endothelial cells have been reported in the diseased dog mitral valve on SEM[28]. It is assumed these changes reflect cell derangement or activation but what causes this change or what the functional consequences might be are unknown. Nuclear bulging might be a response to surface tension changes due to myocardial stretching, and surface micro-appendages might participate in phagocytotic sampling the blood pool. Circulating endothelium derived micro particles have been shown to inhibit mitral VEC function; possibly by negatively regulating VEC migration and proliferation[101]. In the diseased dog valve one of the most striking findings was the range of VEC and VIC shapes, demonstrating their plasticity and motility capabilities. Motility of VECs is essential in the normal repairing process, and in this role decorin has an important function in promoting VEC adhesion and migration on collagen I through integrin[102]. Considering the wide range of ECM components in the VEC microenvironment and the various mechanisms that are necessary to fine tune the synthesis and remodeling of ECM, it is apparent there is a complex relationship between the ECM and many aspects of VEC migration and survival[103, 104]. In the cell-macerated connective tissue skeletons from diseased valves, the surface mesh-like collagen fibril network, typical of normal valves was lacking and this will hamper the motility of VECs. It is not known precisely how the VECs desquamate from the surface. All the evidence from TEM suggested it was not necessary for VEC to defend its post resolutely until became obliterated by the hemodynamic force. Unlike the VEC under went apoptosis procedure in the normal repair process. Swollen but viable EC could simply detach itself from the surface and escape into the space. It was assumed the basement membrane was also damaged as many were seen either thickened or in double layers with gaps in between them. The fate of these escaping VEC from the endothelium remained a mystery. A few VIC were spotted squeezing through the basement membrane towards the surface. It is conceivable they were also part of the repair process, but to what extent still needs to be elucidated. Cell macerated connective tissue skeleton of diseased revealed void holes on the surface that could well facilitate VIC migration. It is now believed that there is a reservoir of stem cells in mitral valve that could participate in repair. Stem cell trans-differentiate into EC and improve heart function was demonstrated in canine ischemic model[105]. The biochemical changes in VEC and VIC merit further investigation.

This study investigated gross morphological changes in canine valves. The challenge posed in studying the dog is the considerable variation in the size of the mitral valve between different breeds of dogs making comparison of the actual dimensions difficult. This problem has been identified by other investigators[106]. Therefore, in the present study relationships were expressed in terms of ratios to overcome the disparity in breed sizes[106]. This also allowed comparison between individual samples. By expressing the leaflet length as septal/mural ratio, the leaflets themselves acted as their own standard control. What was found was that there was a gradual decrease in anterior/posterior leaflet length ratio from normal to severe grade 3, but no further change at grade 4. The difference was not found to be a statistically significant. However, whether elongation or shrinkage in one or both leaflets plays a detrimental role in mitral valve redundancy is unproven. Previous reports have described the leaflets of MMVD dogs as contracted with a rolled edge border, but also point out the possible contribution of stretching of the mitral valve annulus associated with left ventricular dilation and stretching of the chordae tendinae to distortion of valve geometry[1, 2, 4]. Increasing in mitral leaflet area has been reported in human patients with a floppy valve in combination with MR[56, 107-109].

Previous studies of normal human mitral valves have reported valve leaflet lengths that gave anterior/posterior length ratios of 1.71-1.78 for men and 1.75-1.81 for women[11, 110]. These ratios are comparable to the ratio of 1.81 noted for normal dogs in present study. A review of the literature on this subject is shown in (Table 2.6).

Table 2.6. Previous studies investigated the mitral valve leaflets length and their calculated septal/mural ratio.

			Normal mitral valve			Diseased mitral valve		
Investigators	Year	Species	Septal	Mural	Septal/Mural	Septal	Mural	Septal/Mural
Rusted[110]	1952	Human (50)	2.3 (m)	1.3 (m)	1.78	-	-	-
			2.1 (f)	1.2 (f)	1.75	-	-	-
Ranganthan[11]	1970	Human (50)	2.4 (m)	1.4 (m)	1.71	-	-	-
			2.2 (f)	1.2 (f)	1.83	-	-	-
Kunzelman[106]	1994	Human (18)	2.0	1.2	1.67	-	-	-
		Porcine (10)	2.0	1.2	1.67	-	-	-
Grande-Allen[111]	2005	Human (37)	2.51	1.64	1.53	3.22	2.31	1.39
Timek[112]	2006	Sheep	2.11	1.14	1.85	2.43	1.33	1.83

In human patients with congestive heart failure, Grande-Allen and co-workers reported much longer valve leaflets (ratio 1.39) than normal controls (ratio 1.53), and suggested myxomatous degeneration as the best explanation for this difference[111]. This change in ratio is comparable to our findings in the dog. However, it is not possible to compare absolute length changes because of the marked disparity in size between different breeds of dogs used in this study. Judging by the extrapolated spetal/mural leaflet ratios from two recent studies, seemingly the decrease in septal/mural length ratio appeared to correlated with increasing in leaflet length. Coupled with the change in connective tissue elements in diseased valves, it can be seen how such length changes could contribute to poor leaflet co-aptation and mitral regurgitation during ventricular systole. Furthermore, increased leaflet extensibility and reduced stiffness has been demonstrated in human myxomatous leaflets[13], and this has been in conjunction with a change in length ratio and a progressive thickening of the leaflet, most noticeable towards the leaflet edge. In normal mitral valves the leaflet tapers towards the free edge[34]. The thickening of the leaflets near the free edge apposition is conspicuous in MMVD and MVP and it is suspected that repeated trauma at time of closure might be implicated. The progressive nature of the disease is manifested in the gradual expansion of the spongiosa at distal zone. The thickening noticed in disease is likely to be due to the expansion of the loose connective tissue component of the leaflet and increased GAG production. Such changes will undoubtedly have profound effects on the mechanical competence of the leaflet[34]. Similar to human mitral valve prolase, the mural leaflet in the dogs was found to be more severely affected than the septal, suggesting the mural leaflet in dogs would appear to degenerate at a more accelerated rate than septal leaflet. Interestingly, current mitral valve surgical repair techniques are targeted at the middle scallop of mural leaflets[113]. Despite obvious changes the thickened mitral valve is rarely discussed in the literature[107, 111]. This is despite the principle of Whitney's classification being based largely on mitral valve thickness[2]. With the advancement of echocardiographic technology, the thickening of leaflets has been identified as a 'classic' feature in mitral valve prolapse[61]. The Whitney system provides an easy and reliable grading system and when applied to valves from different breeds of dog the system remains robust as demonstrated in this study. In humans a similar grading system does not exist, and a mixture of clinical terms such as mitral prolapse, mitral incompetence, billowing valve are indiscriminately intermingled with pathological terms such as mitral redundency and mitral fibroelastic deficiency which are used to describe a common pathological pathway[114].

The mechanical properties of the mitral valve leaflets are intrinsically linked to the amount of connective tissue, its organisation and orientation. In this study, a reduction in connective tissue (collagen mainly being assessed) quantity and density was demonstrated. Furthermore, this reduction in connective tissue showed a close relationship with disease progression. Previously, x-ray diffraction studies have shown loss of collagen in visibly diseased area of canine valves, changes in fibril alignment and total tissue volume[35]. Importantly, in the visibly normal areas of diseased leaflets, which often co-exist in close proximity to diseased areas, such changes are not identified.

While using x-ray diffraction has not yet investigated the changes in connective tissue across all grades of disease, the current study has shown that this does indeed occur. There are conflicting reports on changes in collagen content in human MMVD. Using image analysis of histological stained sections, collagen content decreases with age in normal humans with a concomitant increase in GAGs, but biochemical analysis has also shown an increase, no change and a decrease (chordal collagen)[77-79, 115, 116]. The difficulty in interpreting these data includes the problem of disease identity (many patients had rheumatic heart disease), the co-existence of areas of fibrosis, which is seen in discreet areas in canine MMVD, and the measurement of collagen in the entire valve as opposed to distinctly diseased areas. The cell macerated connective tissue skeleton technique used in the current study has shown discreet areas of compressed collagen fibrils near the myxomatous area. X-ray diffraction has previously demonstrated the patchy distribution of collagen loss in canine MMVD and it is likely that the same loss can be seen using image analysis of histologically stained canine and human (age-related) mitral valves[79]. The reported increase collagen in human valves may represent the consequence of reactive fibrosis or increased collagen production in the valve mid and basal zones in response to the mechanical failure of the valve. It would have been interesting to quantify changes in elastin content, but this was not possible using image analysis as elastin staining was diffused. There was an impression in some diseased valves of an increase in elastin, but this change was variable and inconsistent. While elastin makes up a small component of the total connective tissue content of the valve leaflets, its mechanical strength and deformability may give it a role in valve mechanics disproportionate to the quantity in a leaflet. An increase in elastic fibres has been reported in human myxomatous mitral valves, but the fibres are thinner than normal, arranged into more distinct bundles, and the bundles are more widely separated than in normal leaflets[117].

The destruction and fragmentation of collagen as seen in the connective tissue as the disease progresses was particularly striking. The crevasses and cracks observed in collagen rich fibrosa were probably a consequence of the harsh treatments during SEM sample preparations. The tissues were macerated in a strong 10% w/v NaOH, solution, the equivalent of 2.5M NaOH for a considerable period of time. Afterwards, the tissue went through a thorough a dehydration process of ascending concentrations of ethanol and then acetone. Nevertheless, the appearance of crevasses and cracks can be regarded as a sign of weakening of the structural protein collagen. It was known from the TEM studies that the collagen fibres in diseased valves are loosely packed and disorganised, and hence it can be presumed tensile strength was compromised. It was also observed at high power TEM that the collagen was associated with proteoglycans in abundance in the diseased valves. Myxomatous leaflets have been shown to have more water content and higher GAG concentration than normal[118]. Proteoglycans are complex macromolecules, which consist of specialized polysaccharide chains called glycosaminoglycans linked to a core protein via a covalent linkage. Proteoglycan is extremely hydrophilic and has strong tendency to bind to water. With associated water molecules, these components of the extracellular matrix tend to occupy large volumes called domains[119]. This in part explains the increase in distance of the collagen inter-fibril space observed in diseased valves. Once water was extracted from the tissue, the spaces once occupied by water turned into voids and crack formation occurs along weak points of the tissue. The lobe-like configurations of the masses observed in the distal zone of diseased under SEM resemble the myxomatous areas viewed under light microscope. The vein like crack patterns in the lobes match the whirl arrangement of cells in the myxomatous area.

Collagen and elastin are the most important structural connective tissue proteins in the mitral valve. During synthesis and subsequent assembly, collagen and elastin are acted upon by lysyl oxidase, an enzyme that converts the amine side chain of lysine and hydroxylysine residues into an aldehyde for subsequent self cross-linking. In collagen, the telopeptide regions are the established sites of aldehyde formation for self cross-linking. The chemistry of this type of self-cross-linking is complex and not fully understood although it is known that lysyl oxidase catalyses the formation of hydroxy-pyridinium cross-links in collagen and desmosine and isodesmosine in elastin[120, 121]. Mutation in genes coding for collagen I, III and V was not associated with human MVP in segregation analysis[122]. The loose collage arrangement together with disappearance of the trabeculated connective tissue network thus might point to a down stream deficiency in collagen assembly.

Mitral valve disease has serious cardiovascular consequences. The current treatment regimes in human medicine involve surgical repair or at the severe case valve replacement. Unfortunately, even the latest generation of bioprosthetic valves has a major drawback. The bioprosthetic valve tissue undergoes structural degeneration after implantation in the human heart due to calcification process. The cells in bioprosthetic valve tissue are rendered non-viable by chemical fixation are unable to promote growth and tissue modeling[123]. Advancement in tissue engineering has presented new hope in valve therapy. The cell-macerated connective tissue skeleton provided an incredibly useful insight into the architecture of mitral valve, the complicated splendor of the structure projected a blueprint for the frontier in bioengineered valve that will be bioactive to promote cell growth and tissue modeling.

Reduction in connective tissue density in myxomatous mitral valve disease is known to coincide with increased expression of GAGs[77, 116-118]. The relative proportions of the different GAGs also changes with age in normal human subjects[25, 79]. This was subjectively and clearly apparent using Alcian blue staining in the dog, but image analysis was not able to confirm or quantify this finding. The outcome of the results using the four different colour measuring methods to detect the blue staining of GAG was surprising, none of the colour measuring techniques applied was able to detect a significant difference in blue staining comparing normal and different grade of the diseased valves. This finding was not anticipated. This represents a shortcoming of image analysis in colour measurement. The images underwent analysis as 8-bit per channel RGB images such that in any picture the blue component consisted of $2^8=256$ possible shades of blue. In any of the colour measuring techniques used, the colour thresholds covered a wide range of the blue spectrum and all pixels considered blue were taken into account and contributed, irrespective of their corresponding greyscale values, to the total estimation of GAG content. This means that even the light shade of blue throughout the normal valve leaflet occupies more or less the same percentage area as the diseased valves making differences between valves indistinguishable. One other possible explanation is that different dyes were used in Alcian Blue staining. Histological stains behave as "subtractive" colours and it was very likely that they colocalised in some places. Although different structures were visualized as having different colours, they might actually have complex overlapping absorption spectra. When perceived colour was to be separated, the quantification of each stain component could not be determined at any single wavelength because the optical density at such wavelength was determined by the combination of different stains.

GAGs are an important component of the ECM and while their role in the ECM appears complex it is also not completely understood. In human MVP there is an alteration in the respective concentrations of the different GAGs, but the normal age-associated change is a confounding factor in interpreting this change[76, 79]. GAGs are necessary for the proper assembly of the ECM and collagen II shows a greater level of interaction with GAGs than collagen I in human leaflets[124]. GAGs also interact with other important structural proteins such as fibronectin and laminin and may have a role to play in the interaction between VICs and the ECM. They also have a role in elastin fibrogenesis.[37] Hyaluronic acid is the most abundant GAG in mitral valves, but other proteoglycans, particularly the small leucine-rich proteoglycans (SLRP), may have an equally important role in maintaining a healthy ECM[125]. There is increased expression of the SLRP decorin in human myxomatous leaflets. The accumulation of GAGs in MMVD and MVP is a major contributor to valve thickening and undoubtedly contributes to the mechanical failure of the valve[117].

In conclusion, this study has quantified morphological changes in canine myxomatous mitral valve disease and recognised changes in leaflets associated with disease progression. Since disease grade in the dog roughly approximates to the duration of disease, it can be readily appreciated that connective tissue changes are progressive over time. For cell density, there is a reduction in myxomatous diseased areas compared to analogous loose connective tissue areas of normal valves, but cellularity then remains constant throughout the time course of the disease.

Denudation of endothelium in concomitant with destruction of collagen and increasing ECM in the presence of congregation of VICs near the surface is associated with MMVD.

3 Chapter 3 Immunohistochemistry and immunophenotyping of myxomatous mitral valve disease in the dog

3.1 Introduction

Myxomatous mitral valve disease is the single most common acquired cardiovascular disease of dogs and is a major cause of morbidity and early death in this species[53, 81]. The disease is of substantial veterinary importance but is also of comparative interest as bears close similarity to mitral valve prolapse in humans[4, 71]. The underlying cause of this degenerative process is unknown but appears to be associated with phenotypic alteration in the valvular interstitial cell population[26, 27, 43]. Previous studies suggested that this phenotypic alteration is crucial to the development of myxomatous degeneration, accompanied by alteration to the valve endocardial endothelium[29, 32]. With respect to the valvular interstitial cell population, transformation from an inactive fibroblast phenotype to a more active myofibroblast has been documented for dogs[43] and human[27]. This is suspected to result in a derangement of dynamic valve matrix remodeling, which may be the result of over expression of a range of matrix metalloproteinases (MMPs) and other catabolic enzymes[27, 82].

To date, the only data illustrating valvular interstitial cell phenotypic alteration in dogs with MMVD have been at the ultrastructural level and this has been found only in small localized, obviously diseased areas of affected valve leaflets[43]. This is also the case in humans with MMVD, where no data exist on regional development of pathologic changes. The purpose of this study was to map the cellular distribution and phenotypic alteration of the predominant cell population throughout the entire valve length of dogs with MMVD. In addition, the role of MMPs in matrix remodeling during the disease process was explored. These were achieved by use of histological and immunohistochemical techniques to identify phenotype on the basis of expression of standard cell and protein markers. Furthermore, the relationship between disease severity, cell distribution and cell immuno-phenotype was also investigated.

3.2 *Materials and Methods*

3.2.1 Mitral valve procurement

As described in Chapter 2.2.1.

3.2.2 Tissue dissection

As described in Chapter 2.2.2.

3.2.3 Immunohistochemistry

In order to distinguish valvular interstitial cells phenotypes and extracellular structure changes, the following primary antibodies were used (Table 3.1. Antibodies were used at the manufacturer's recommended concentration, or at concentrations previously published.

Table 3.1. Details of antibodies used.

Antibody	**Clone**	**Cat. No.**	**Specie Raised**	**Manufacturer**
Vimentin	V9	V 6630	Monoclonal Mouse	Euro/DPC, Llanberis, UK
α-Smooth muscle actin	1A4	A 2547	Monoclonal Mouse	Sigma, Missouri, USA
Smooth muscle myosin	HSM-V	M 7786	Monoclonal Mouse	Sigma, Missouri, USA
Desmin	DE-U-10	D 1033	Monoclonal Mouse	Sigma, Missouri, USA
Fibrillin	11C1.3	MAB1919	Monoclonal Mouse	Chemicon, Watford, UK
CD34[126]	1H6	MCA2411	Monoclonal Mouse	AbD Serotec, Oxford, UK
Von Willebrand Factor		A0082	Polyclonal Rabbit	DakoCytomation, Denmark
MMP-2[127]	8B4	IM83T	Monoclonal Mouse	Calbiochem/Merck, USA
MMP-9[128]	56-2A4	IM37T	Monoclonal Mouse	Calbiochem/Merck, USA
MMP-13	VIIIA2	IM78T	Monoclonal Mouse	Calbiochem/Merck, USA
Fibronectin	IST-3	F 0791	Monoclonal Mouse	Sigma, Missouri, USA
Myeloid/Histocyte[129]	MAC387	M0747	Monoclonal Mouse	DakoCytomation, Denmark
IgG1κ		M 9269	Monoclonal Mouse	Sigma, Missouri, USA
IgG2a,κ		M 9144	Monoclonal Mouse	Sigma, Missouri, USA

Tissue sections were dewaxed in xylene and rehydrated through descending concentrations of ethanol. Antigen retrieval was carried out where necessary either by heating in 0.01M citric acid pH 6.0 (Fisher Scientific, UK) or 10mM Tris buffer (Sigma, Dorset, UK) with 1mM EDTA (Sigma, Dorset, UK) pH 9.0 by microwave[130-132]. Sections were treated with 1% hydrogen peroxide (Sigma, Dorset, UK) in PBS for 10 min to inhibit endogenous peroxidase activity. Antibody detection procedures were performed in a Sequenza immunostaining centre (Thermo Shandon, Runcorn, UK). Tissue sections were first incubated with primary antibodies diluted in PBS contained 0.5% Tween 80 (Fisher, Leicestershire, UK) and 10% species appropriate normal sera (Sigma, Dorset, UK); this was followed by incubation with biotinylated secondary antibodies (Vector Laboratories, USA) against mouse IgG. An avidin biotin peroxidase system was used according to manufacturer's recommendation (ABC kit, Vector Laboratories, Peterborough, UK). Diaminobenzidine (DAB kit, Vector Laboratories, Peterborough, UK) were added as colour identification substrates for the peroxidase. In some cases, nickel chloride enhancement was employed in the diaminobenzidine step. Finally, sections were lightly counter stained with Mayer's hematoxylin (Sigma, Dorset, UK), dehydrated through ascending concentrations of ethanol, cleared in xylene and mounted on slides in DPX (Fisher, Leicestershire, UK). Histological section from canine lung tissue served as positive control for the identification of fibroblasts, smooth muscle cells, macrophages and MMPs. Bone marrow was used as positive control for CD34+. Immunoglobulin isomers IgG1κ and IgG2a,κ were substituted for primary antibody and applied as negative controls. For the identification of mast cells, sections were stained with acidic toluidine blue and counter stained with eosin orange.

The slides were viewed under an Olympus BH-2 light microscope (Olympus Optical Co., London, UK). Positive cell identifications were based on cross-reference to corresponding negative control (IgG1κ and IgG2a,κ) slides and positive control slides. For morphological analysis of immunohistochemistry slides, a semi-quantitative scoring system was developed to assess the degree of antigen-antibody reaction. Score were defined as 0 absent, 1=weak (less than 33% of cells), 2=moderate (between 33% to 67% of cells) and 3=strong (greater than 67% of cells). A score was given in best estimation to each of the atrialis, spongiosa and fibrosa layers at base, middle and distal third of the leaflets (Figure 3.1). In addition, the prominent distribution patterns of the positive cells were described in each layer of the three zones. The scores and distribution patterns were entered into a custom designed FileMaker Pro 6 (FileMaker Inc., CA, USA) data bank. Similarly, a semi-quantitative scoring scheme was applied to antigens staining for extracellular matrix proteins, 0=absent, 1=weak, 2=moderate and 3=strong. Since each zone and each layer could have a maximal score of 3, the combined score for a layer or zone could have a maximal score of 9. A scoring system was also applied to assess the number of fat cells in each zone of a leaflet using of a lens graticule. The number of fat cells as compared with the surface-to-surface thickness of the leaflet, where 0=absent, 1=mild (up to 15% thickness), 2=moderate (15%-30% thickness) and 3=strong (over 30% thickness). Only a small number of cells stained positive for CD34, MAC387 and toluidine blue, consequently the total number of cells could be counted accurately employing an eyepiece reticle and a manual cell counter. For all of the above, comparisons of total number of positive cells were made between grades.

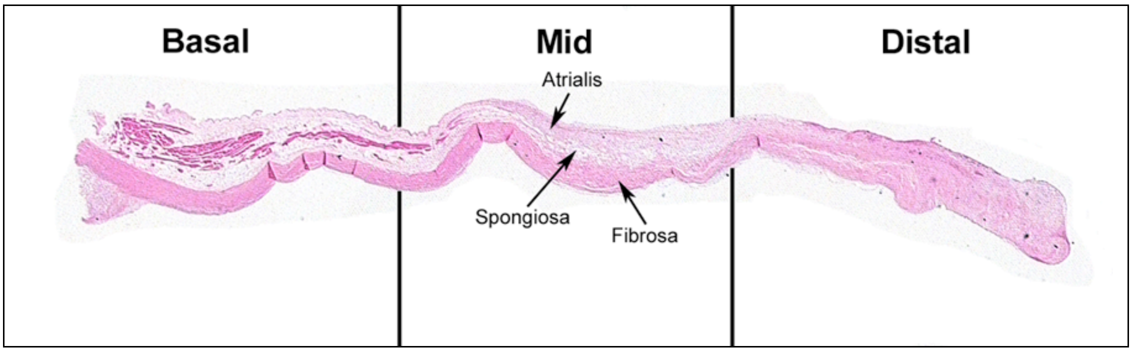

Figure 3.1. A schematic diagram shows a mitral valve leaflet divided into three zones basal, mid and distal and three layers atrialis, spongiosa and fibrosa for immunohistochemistry scoring.

The distribution patterns and morphologies of the positive cells were recorded in a table of hierarchical order.

The descriptors adapted to depict the distribution pattern were:

Pattern	*Definition*
Sparse	cells to cells distance were uniform and cells were evenly distributed
Cluster	conglomerates of cells with minimum cells to cell distances
Whorl	cells forming concentric circles
Layered	cells aligning to each other

The common morphological features of von Willebrand factor positive endothelial cell shapes and the endothelial cell lining were described thereof:

Endothelial cell shape: flat, spindle, dome or round.

Endothelial cell lining	
Attaching	endothelial cell lining is fasten on the valve surface.
Detaching	small intermitted gaps between endothelial cell lining and valve surface.
Lifting	a defined void space between endothelial cell lining and valve surface.
Separating	endothelial cell lining is totally disconnected from valve surface, often the endothelial cell lining is broken up.

3.2.4 Statistical analysis

As described in Chapter 2.2.12.

3.3 Results

3.3.1 Vimentin

In mitral valves of clinically normal dogs, the immunostaining for vimentin was extensive. The vimentin positive cells were visible in all layers, being distributed evenly throughout both septal and mural leaflets. The cardiomyocytes at the basal zone spongiosa layer did not show any reactivity, but a few positive cells were found between muscle bundles. The fat cells in the spongiosa layer were weakly positive. Although the greatest density of vimentin positive cells was in the mid zone of septal leaflet (score 7 out of 9) and distal zone of mural leaflet (7.5 out of 9) (Figure 3.2), fewer positive cells were seen in the fibrosa layer. Vimentin positive cells were in close alignment with the direction of the collagen bundles in the fibrosa layer and were elongated and spindle shaped, whereas vimentin negative cells were more rounded. In the septal leaflet, the density of positive cells in the fibrosa layer increased from mid to distal zone, whereas the proportion of positive cells in the atrialis layer remained the same. On the other hand, densities of vimentin positive cells in distal zone were higher than the mid zone in all three layers. The most commonly observed vimentin positive cells were oval or spindle shaped and distributed throughout the tissue.

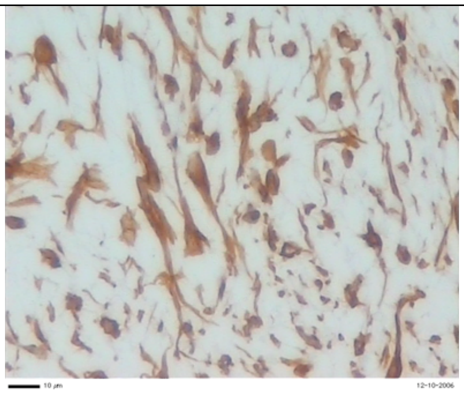

Figure 3.2. Vimentin staining in normal valve distal zone. The vimentin positive cells are more elongated in shape. Bar = 10 µm.

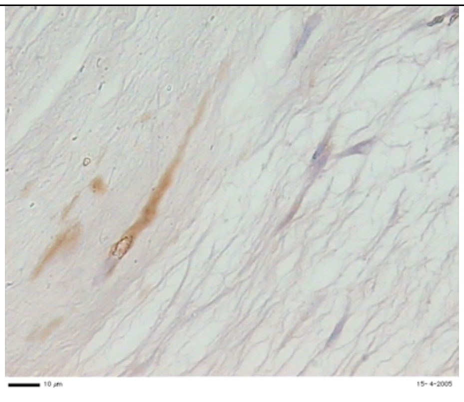

Figure 3.3. Veimentin positive cells are associated with connective tissue and vimentin negative cells are associated with myxomatous tissue. Bar = 10 µm.

In mitral valve leaflets of dogs with MMVD, immunostaining for vimentin was still substantial, but a recognizable decrease in vimentin positive cell density was found with increasing disease severity (Figure 3.3). This reduction was gradual and proportional in all layers in all zones, but somewhat more so in the atrialis and spongiosa layers. The densities of vimentin positive cells were closely matched between septal and mural leaflet in each grade of disease. The rate of reduction in vimentin positive cells was similar between septal and mural leaflets, with a approximately10~15% reduction in vimentin positive cells in each zone from one to the next lesion grade (Figure 3.4 and Figure 3.5). The distribution pattern of positive cells was a predominantly sparse arrangement. As the disease progressed a more clustered and layered pattern emerged in the mid and distal zones and whorl like distribution appearing in the distal zone (Table 3.2 and Table 3.3).

Within the connective tissue in the atrialis and ventricularis layers, some vimentin positive cells were slightly flattened. However, in the myxomatous regions of the valve, elongated spindle shaped vimentin positive cells predominated. Yet, oval or more rounded shaped positive cells could also be seen adjacent to the myxomatous area in the distal zone of the diseased valves. In the severe form of the disease, little evidence of vimentin positive cells was observed in myxomatous areas (Table 3.4 and Table 3.5).

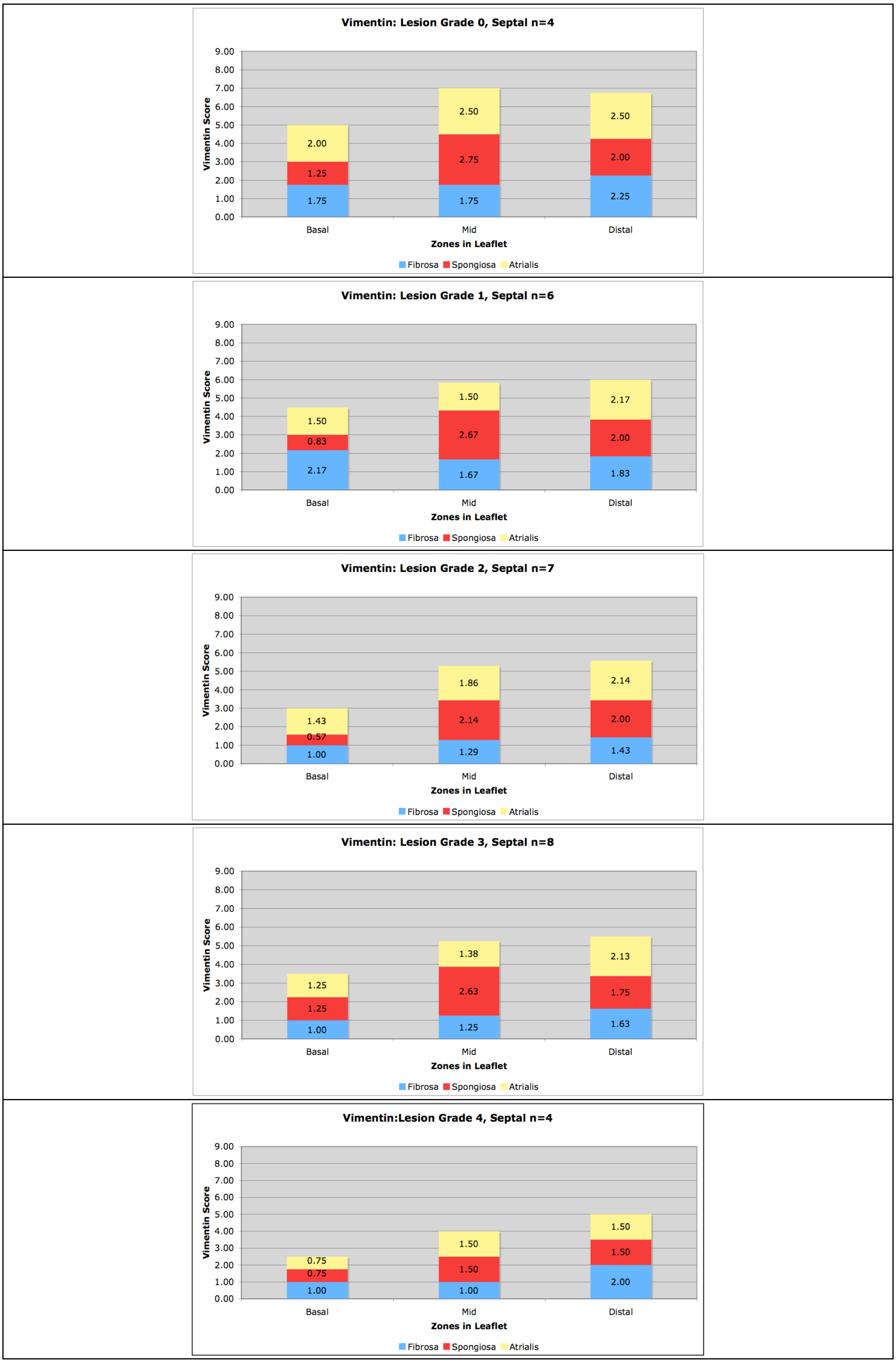

Figure 3.4. Vimentin scores in septal leaflets. Three different columns represent the three zones and three different colours represent the three layers. Each zone and each layer could have a maximal score of 3, the combined score for a layer or zone could have a maximal score of 9.

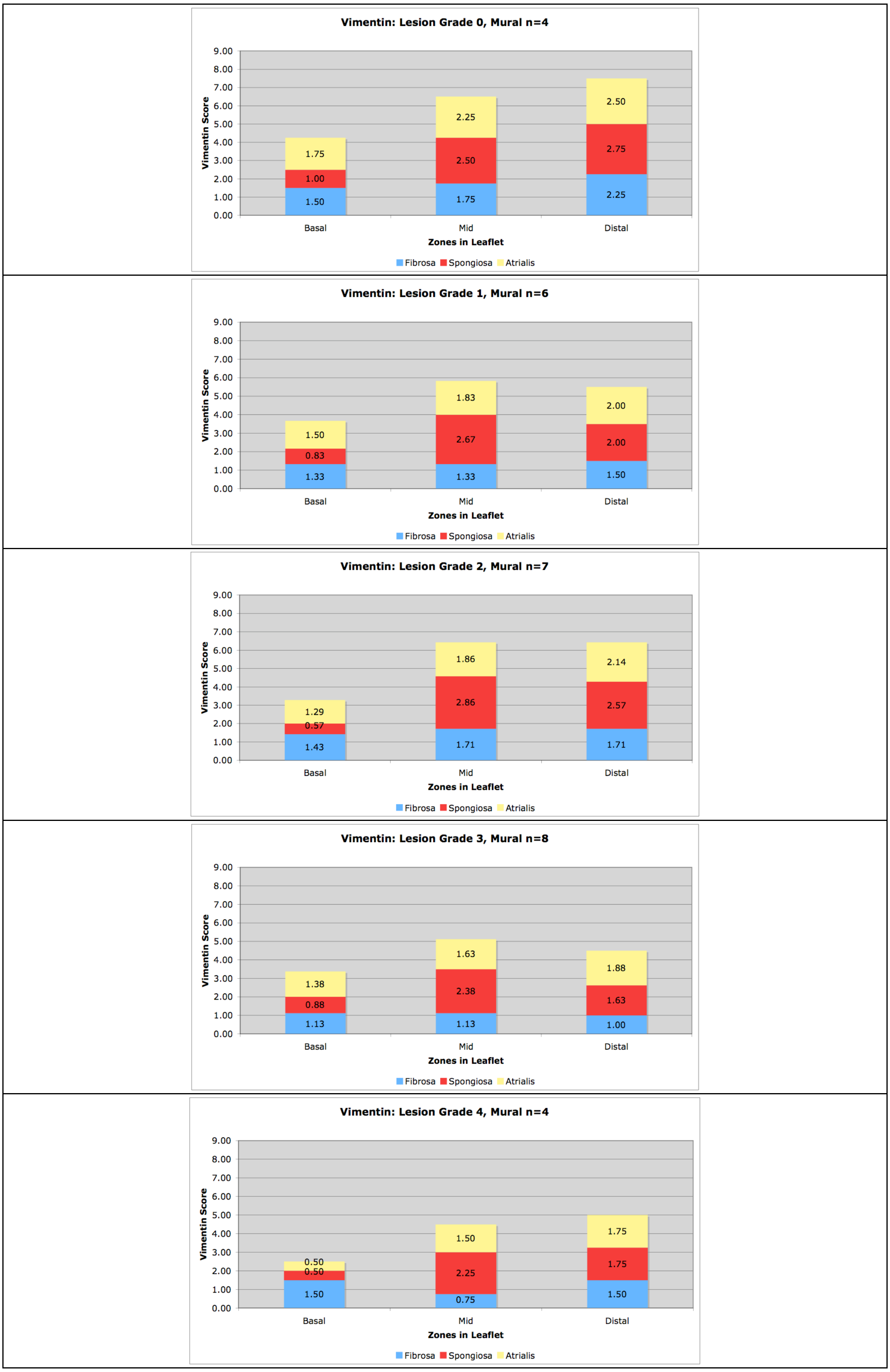

Figure 3.5. Vimentin scores in mural leaflets. Three different columns represent the three zones and three different colours represent the three layers. Each zone and each layer could have a maximal score of 3, the combined score for a layer or zone could have a maximal score of 9.

Table 3.2. Vimentin positive cell distribution patterns in septal leaflets. They are presented in a hierarchal order. The most frequently occurring distribution pattern is at the top of each block.

Grade 0 Septal	*Basal*	*Mid*	*Distal*
Atrialis	Layered=Sparse	Sparse	Sparse Cluster
Spongiosa	Sparse	Cluster=Layered=Sparse	Sparse
Fibrosa	Sparse Layered	Sparse	Sparse Cluster=Layered
Grade 1 Septal	*Basal*	*Mid*	*Distal*
Atrialis	Sparse Layered	Layered Sparse	Cluster=Sparse Layered
Spongiosa	Sparse	Sparse Layered	Whorl Cluster=Sparse
Fibrosa	Sparse	Sparse	Cluster=Sparse
Grade 2 Septal	*Basal*	*Mid*	*Distal*
Atrialis	Sparse Cluster=Layered	Layered=Sparse Cluster	Layered Sparse Cluster
Spongiosa	Sparse	Sparse Layered	Sparse Whorl Layered
Fibrosa	Sparse Cluster=Layered	Sparse Layered	Sparse Layered=Whorl
Grade 3 Septal	*Basal*	*Mid*	*Distal*
Atrialis	Sparse Layered	Sparse	Layered Cluster Sparse
Spongiosa	Sparse Layered	Sparse Cluster=Layered=Whorl	Sparse Layered=Whorl
Fibrosa	Layered Sparse	Sparse Cluster=Layered=Whorl	Sparse Layered
Grade 4 Septal	*Basal*	*Mid*	*Distal*
Atrialis	Sparse Layered	Sparse Cluster	Sparse Cluster
Spongiosa	Cluster=Sparse	Layered=Sparse	Whorl Sparse
Fibrosa	Sparse	Sparse	Sparse Cluster=Layered=Whorl

Table 3.3. Vimentin positive cell distribution patterns in mural leaflets. They are presented in a hierarchal order. The most frequently occurring distribution pattern is at the top of each block.

Grade 0 Mural	*Basal*	*Mid*	*Distal*
Atrialis	Layered Sparse	Sparse=Layered	Sparse
Spongiosa	Sparse Cluster	Layered Whorl	Sparse
Fibrosa	Sparse Layered	Sparse Cluster	Sparse

Grade 1 Mural	*Basal*	*Mid*	*Distal*
Atrialis	Sparse Layered	Sparse Layered Cluster	Sparse Layered
Spongiosa	Sparse	Sparse Layered	Sparse Cluster=Layered=Whorl
Fibrosa	Sparse Layered	Sparse	Sparse Layered

Grade 2 Mural	*Basal*	*Mid*	*Distal*
Atrialis	Sparse=Cluster Layered	Cluster Sparse Layered	Layered=Sparse Cluster
Spongiosa	Sparse	Layered Cluster=Sparse	Sparse Cluster=Whorl
Fibrosa	Sparse Layered	Sparse	Sparse Layered Cluster

Grade 3 Mural	*Basal*	*Mid*	*Distal*
Atrialis	Sparse Cluster=Layered	Sparse Layered Cluster	Cluster=Sparse Layered
Spongiosa	Sparse Layered	Cluster Layered=Sparse	Sparse Whorl Cluster=Layered
Fibrosa	Sparse Cluster	Sparse Cluster	Sparse Layered

Grade 4 Mural	*Basal*	*Mid*	*Distal*
Atrialis	Sparse	Sparse	Sparse Layered
Spongiosa	Sparse	Cluster Layered=Sparse	Sparse=Whorl Layered
Fibrosa	Sparse Layered	Sparse	Cluster Sparse=Whorl

Table 3.4. Vimentin positive cell morphologies in septal leaflets. They are presented in a hierarchal order. The most frequently occurring cell shape is at the top of each block.

Grade 0 Septal	*Basal*	*Mid*	*Distal*
Atrialis	Spindle Oval=Stellate	Stellate Oval=Spindle	Oval Flat=Stellate
Spongiosa	Oval	Oval Spindle=Stellate	Stellate Spindle
Fibrosa	Spindle Round=Stellate	Oval=Spindle	Oval Spindle=Stellate
Grade 1 Septal	*Basal*	*Mid*	*Distal*
Atrialis	Flat=Oval Stellate	Oval Round=Stellate	Oval Flat=Round
Spongiosa	Oval Round=Stellate	Oval Flat Round	Flat=Oval=Stellate
Fibrosa	Oval Flat=Spindle	Oval Spindle	Oval Flat=Stellate
Grade 2 Septal	*Basal*	*Mid*	*Distal*
Atrialis	Stellate Oval Round=Spindle	Flat=Oval=Round Spindle=Stellate	Round Spindle Oval=Stellate
Spongiosa	Oval	Oval Flat=Stellate Round=Spindle	Flat=Oval=Spindle Stellate
Fibrosa	Stellate Flat Oval	Flat=Oval Round=Stellate	Oval Flat=Round=Spindle Stellate
Grade 3 Septal	*Basal*	*Mid*	*Distal*
Atrialis	Oval Spindle	Oval Flat Round=Spindle=Stellate	Oval Round Flat
Spongiosa	Oval Flat	Flat Oval Spindle	Flat Oval=Spindle Stellate
Fibrosa	Spindle Oval Flat	Flat=Oval=Spindle	Oval Flat=Round=Spindle Stellate
Grade 4 Septal	*Basal*	*Mid*	*Distal*
Atrialis	Oval	Oval Round	Round Spindle
Spongiosa	Flat=Oval	Flat=Oval	Flat
Fibrosa	Flat Spindle	Flat=Oval Round=Spindle	Flat Oval=Round

Table 3.5. Vimentin positive cell morpholgies in mural leaflets. They are presented in a hierarchal order. The most frequently occurring cell shape is at the top of each block.

Grade 0 Mural	*Basal*	*Mid*	*Distal*
Atrialis	Oval=Spindle	Oval Spindle=Stellate	Spindle Stellate
Spongiosa	Oval	Spindle Oval	Spindle=Stellate
Fibrosa	Oval=Spindle=Stellate	Oval Spindle=Stellate	Oval=Spindle
Grade 1 Mural	*Basal*	*Mid*	*Distal*
Atrialis	Flat=Oval Spindle=Stellate	Oval Flat Stellate	Flat Oval Spindle
Spongiosa	Oval Flat=Round	Oval Flat=Stellate Spindle	Flat=Oval Round=Stellate
Fibrosa	Flat Oval=Spindle	Flat=Stellate Oval=Spindle	Oval Flat Stellate
Grade 2 Mural	*Basal*	*Mid*	*Distal*
Atrialis	Flat=Oval=Spindle Stellate	Flat=Round=Stellate Oval	Spindle Round=Stellate Flat
Spongiosa	Oval	Stellate Flat=Oval Spindle	Stellate Flat=Oval=Spindle
Fibrosa	Oval Spindle Flat=Stellate	Oval=Round=Spindle Stellate	Oval Stellate Flat
Grade 3 Mural	*Basal*	*Mid*	*Distal*
Atrialis	Oval Flat=Spindle=Stellate	Oval Flat=Spindle	Round Flat=Oval=Spindle
Spongiosa	Oval Flat=Round	Stellate Oval Flat=Round	Flat=Stellate Oval=Spindle
Fibrosa	Oval Spindle Flat	Stellate Flat Oval	Flat Stellate Spindle
Grade 4 Mural	*Basal*	*Mid*	*Distal*
Atrialis	Oval=Round	Oval=Round Flat	Oval Flat=Round
Spongiosa	Round	Oval Flat	Flat Oval=Round=Spindle
Fibrosa	Oval Flat=Spindle	Flat=Oval	Oval Flat=Round=Stellate

3.3.2 Adipocyte

Regardless the lesion grade, the adipocytes in mitral valve leaflets stained moderately positive to vimentin antibody (Figure 3.6). Adipocytes were seen as a “signet ring” structure with unilocular of lipid mass in the centre. The cytoplasm was pushed to the side forming a thin rim around the lipid. The cytoplasm was the site that showed positive staining for vimentin. The nucleus was not always distinct, but when visible was flattened and displaced to the edge by the lipid mass.

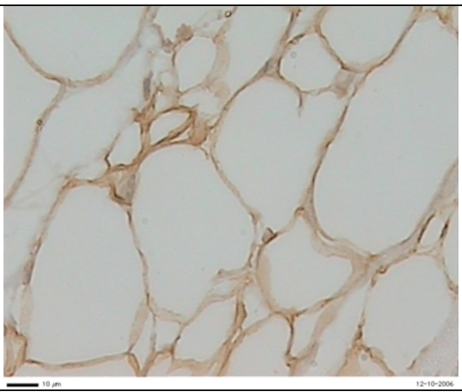

Figure 3.6. The adipocytes are moderately positive to vimentin. Bar = 10 μm.

There were no major differences in fat content between normal and varying grades of the disease, in either septal or mural leaflets. However, the difference in fat content between septal and mural leaflets within the same valve was marked (Figure 3.7). In the septal leaflets, the fat accounted for about a third of the basal zone and about a quarter of the leaflet thickness in the mid zone, except the Grade 4 diseased which contained less fat. Only half of the fat content was found at corresponding zones in the mural leaflets. In both septal and mural leaflets, the adipocyte layer was apposed to the muscle at the base and extended towards the spongiosa layer in the mid zone, but adipocytes were rarely found in the distal zone. Due to the higher fat content in the septal leaflets, the adipocytes conformed into a defined layered structure (Table 3.6). The adipocytes were pushed against each other in the fat layer and seemed to form a mosaic of polygonal cells instead of the usual round or oval shape. In the mural leaflets, the distribution of the adipocytes was sparse by arrangement in the basal zone and became more cluster-like in the mid zone (Table 3.7).

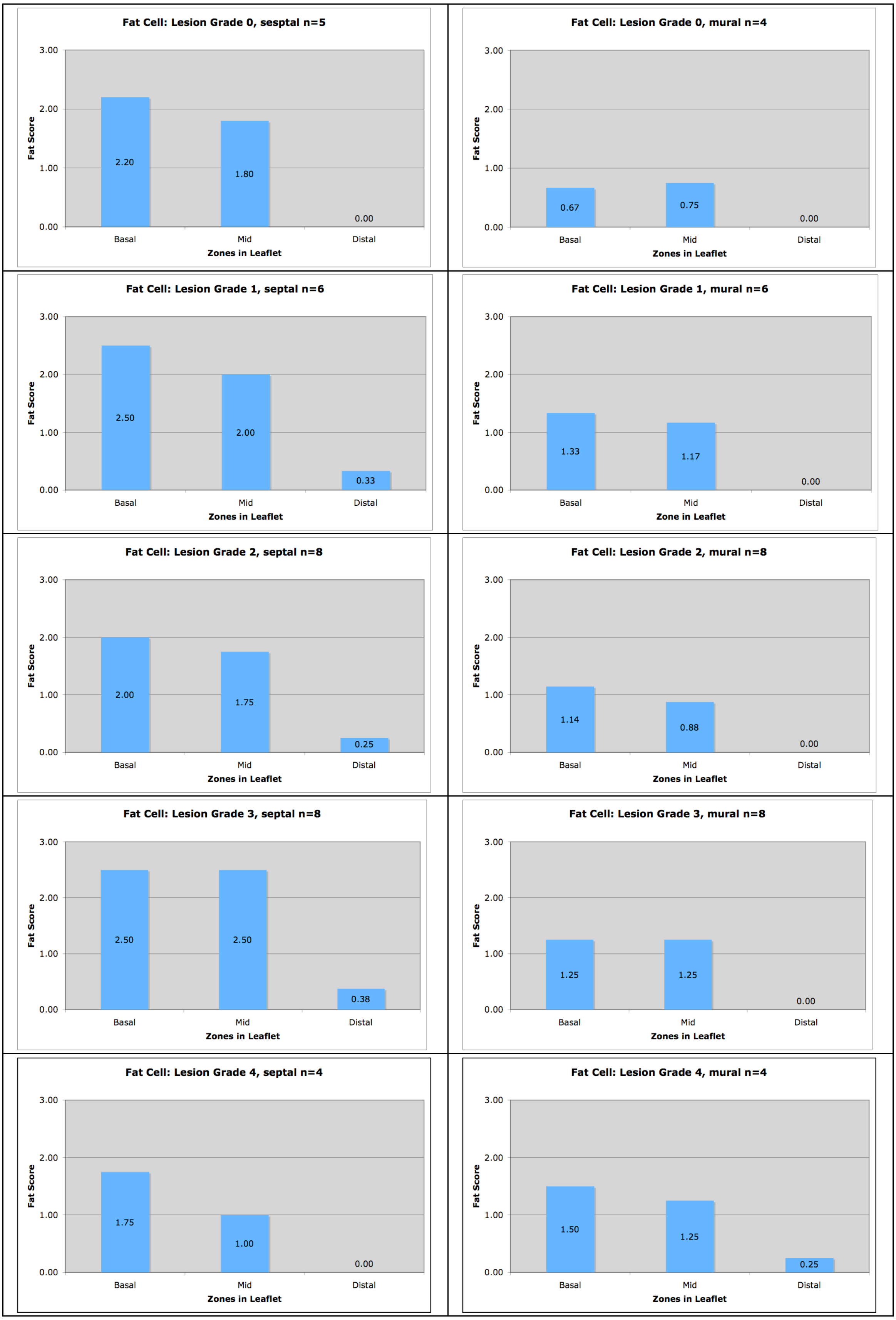

Figure 3.7. Fat score in septal and mural leaflets. Three different columns represent the three zones. Each zone could have a maximal score of 3,

Table 3.6. Adipocyte distribution patterns in septal leaflets. They are presented in a hierarchal order. The most frequently occurring distribution pattern is at the top of each block.

	Basal	*Mid*	*Distal*
Grade 0 Septal	Layered	Cluster=Layered Sparse	-
	Basal	*Mid*	*Distal*
Grade 1 Septal	Layered Sparse	Layered Cluster Sparse	Cluster=Sparse
	Basal	*Mid*	*Distal*
Grade 2 Septal	Layered Cluster Sparse	Layered Cluster=Sparse	Sparse
	Basal	*Mid*	*Distal*
Grade 3 Septal	Layered Cluster	Layered Cluster=Sparse	Cluster Sparse
	Basal	*Mid*	*Distal*
Grade 4 Septal	Layered=Sparse	Sparse Cluster	-

Table 3.7. Adipocyte distribution patterns in mural leaflets. They are presented in a hierarchal order. The most frequently occurring distribution pattern is at the top of each block.

	Basal	*Mid*	*Distal*
Grade 0 Mural	Sparse	Cluster=Sparse	-
	Basal	*Mid*	*Distal*
Grade 1 Mural	Sparse Cluster	Cluster=Sparse Layered	-
	Basal	*Mid*	*Distal*
Grade 2 Mural	Cluster Sparse	Sparse Cluster	-
	Basal	*Mid*	*Distal*
Grade 3 Mural	Sparse Cluster Layered	Cluster Sparse	-
	Basal	*Mid*	*Distal*
Grade 4 Mural	Cluster=Sparse	Cluster=Sparse	Cluster

3.3.3 α-Smooth muscle actin (α-SMA)

Immunostaining for α-SMA was sparse in mitral valve leaflets from clinically normal dogs. In both septal and mural leaflets, among the α-SMA positive cells, larger numbers were located in the atrialis layer just beneath the endothelium, and to a lesser extent in the basal zone of the fibrosa side. α-SMA was differentially expressed in cardiomyocytes at the base of leaflets and displayed a filamentous appearance. Some small arterioles with or without patent intima were α-SMA positive, showing they are vascular smooth muscle cells. Occasionally, a few protruding cells from the endothelial lining were found to be α-SMA positive. Although positive cells were quite sparsely distributed in all zones and all layers, towards the distal ends the pattern became was more clustered or layered in appearance (Table 3.8 and Table 3.9). The cells were predominantly oval or spindle shaped (Table 3.10 and Table 3.11).

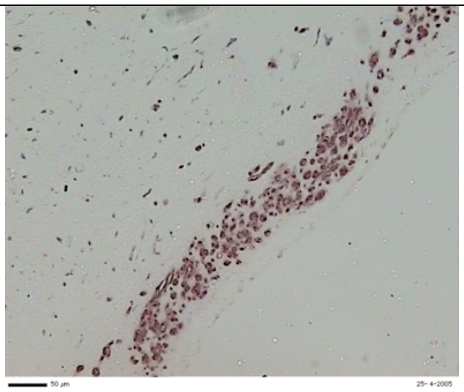

Figure 3.8. α-SMA positive cells in layered formation near the endothelium. Bar = 50 μm.

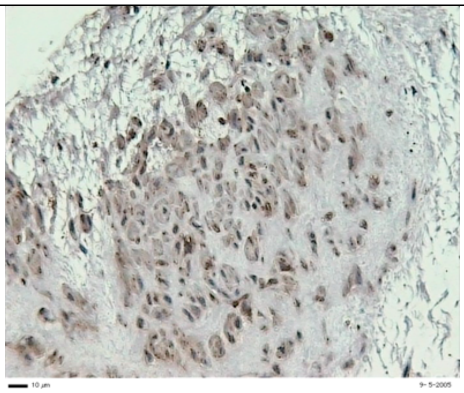

Figure 3.9. A cluster of α-SMA positive cells associated with connective tissue. Bar = 10 μm.

In mitral valve leaflets of dogs with MMVD, the number of α-SMA positive cells increased with an increase in disease severity. The variations in densities of α-SMA positive cells were closely matched between septal and mural leaflet in each grade. The cardiomyocytes in the base were still differentially positive for α-SMA. In Grade 1 diseased valves, α-SMA positive cells were seen under eroded endothelium of the atrialis layer. Towards the distal end, α-SMA positive cells were in juxtaposition with negative cells in the newly developed areas of metaplasia, often in a cluster or layered fashion. Many of the α-SMA positive cells were spindle shaped that resembled the morphology of fibroblasts. In Grade 2 diseased valves, there was a distinct increase in positive cells along the atrialis layers. Aggregations of α-SMA positive cells were found lying underneath the thickened endothelium (Figure 3.8). The positive cells were closely associated with dense fibrous connective tissue. In Grade 3 diseased, an increase in the density of α-SMA positive cells in the distal zone was more apparent, especially in the fibrosa layer. Clusters of α-SMA positive cells were found underneath detached endothelium. However, the cells in the overtly myxomatous area were not readily identified to be α-SMA positive. In Grade 4 diseased, an increase in α-SMA positive cells was notable in the mid zone, with the ventricularis side having a higher concentration of cells (Figure 3.10 and Figure 3.11). Positive cells were embedded in the dense fibrosa connective tissue and were absent from the distinct myxomatous areas (Figure 3.9). Little change in cell morphology comparing normal to the varying grades of diseases was noted and a mixture of oval and rounded shape of cells predominated throughout the disease process.

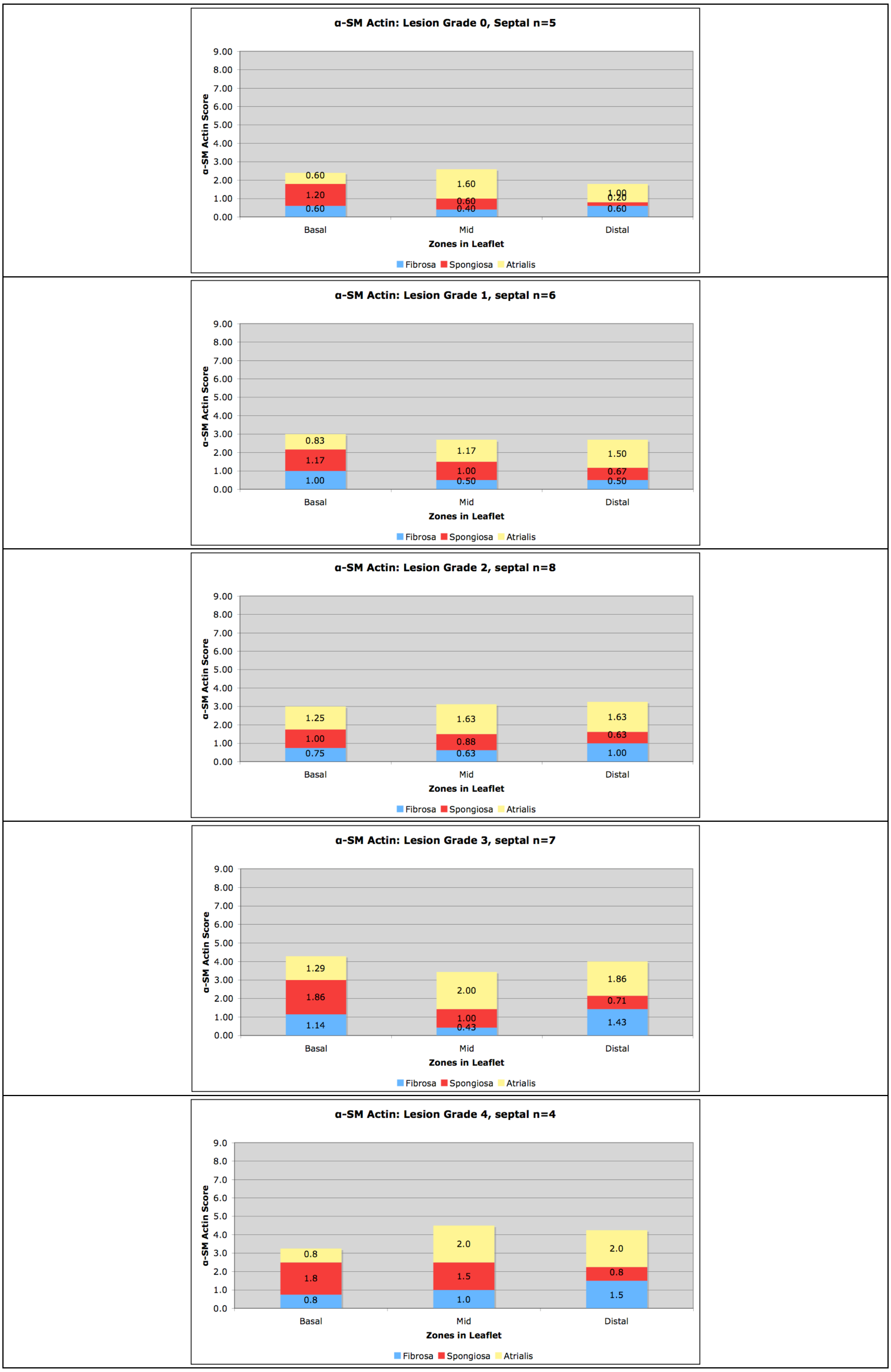

Figure 3.10. α-Smooth muscle actin scores in septal leaflets. Three different columns represent the three zones and three different colours represent the three layers. Each zone and each layer could have a maximal score of 3, the combined score for a layer or zone could have a maximal score of 9.

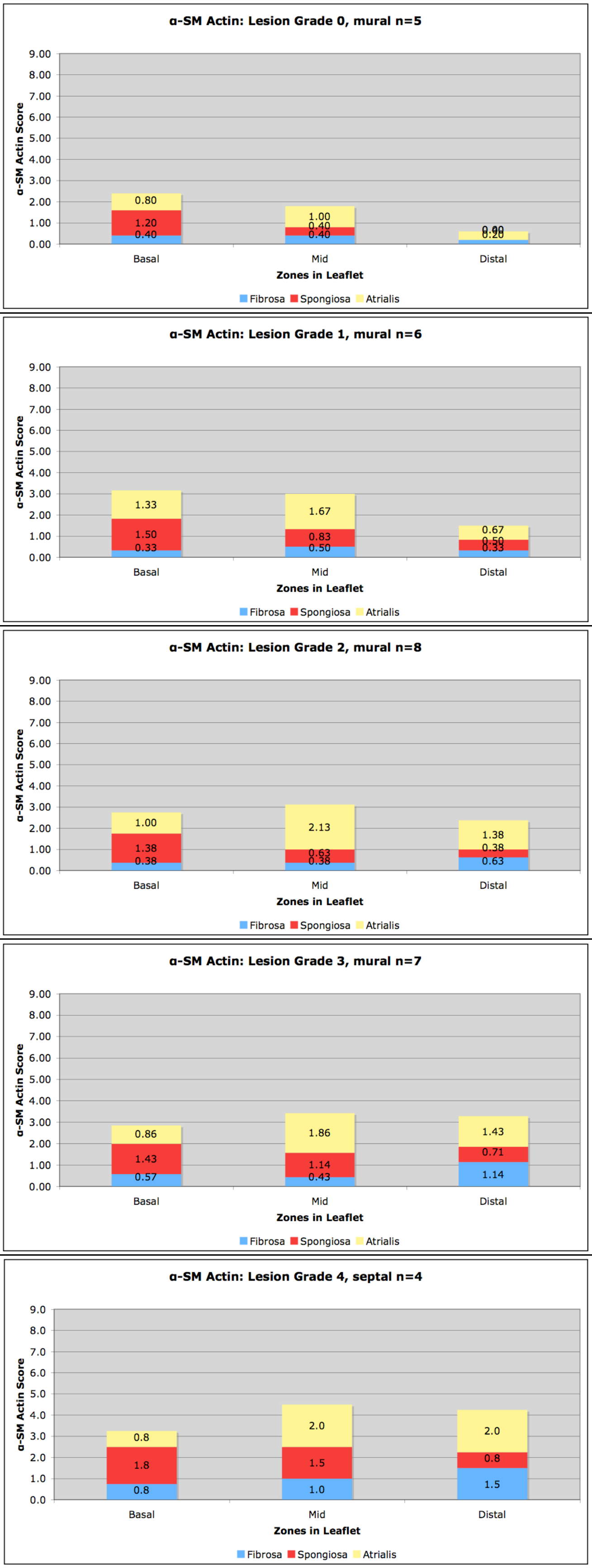

Figure 3.11. α-Smooth muscle actin scores in mural leaflets. Three different columns represent the three zones and three different colours represent the three layers. Each zone and each layer could have a maximal score of 3, the combined score for a layer or zone could have a maximal score of 9.

Table 3.8. α-Smooth muscle actin positive cell distribution patterns in septal leaflets. They are presented in a hierarchal order. The most frequently occurring distribution pattern is at the top of each block.

Grade 0 Septal	*Basal*	*Mid*	*Distal*
Atrialis	Sparse	Sparse Layered	Layered Sparse
Spongiosa	Muscle	Sparse	-
Fibrosa	Sparse Layered	Sparse	Sparse
Grade 1 Septal	*Basal*	*Mid*	*Distal*
Atrialis	Layered Sparse	Sparse Cluster Layered	Layered Cluster=Sparse
Spongiosa	Muscle	Sparse Layered	Sparse=Whirl
Fibrosa	Layered Sparse	Cluster Sparse	Layered=Sparse
Grade 2 Septal	*Basal*	*Mid*	*Distal*
Atrialis	Layered Sparse	Layered Cluster=Sparse	Layered Cluster=Sparse
Spongiosa	Muscle	Sparse Cluster	Sparse Cluster=Whirl
Fibrosa	Layered=Sparse	Sparse Layered	Cluster=Sparse
Grade 3 Septal	*Basal*	*Mid*	*Distal*
Atrialis	Sparse Layered	Cluster Layered=Sparse	Cluster Layered
Spongiosa	Muscle	Sparse Layered	Sparse Whirl
Fibrosa	Layered Sparse	Sparse	Cluster=Layered Sparse
Grade 4 Septal	*Basal*	*Mid*	*Distal*
Atrialis	Layered	Cluster=Layered Sparse	Cluster Layered=Sparse
Spongiosa	Muscle	Layered=Sparse	Whirl
Fibrosa	Sparse Layered	Sparse	Cluster Layered=Sparse

Table 3.9. α-Smooth muscle actin positive cell distribution patterns in mural leaflets. They are presented in a hierarchal order. The most frequently occurring distribution pattern is at the top of each block.

Grade 0 Mural	*Basal*	*Mid*	*Distal*
Atrialis	Sparse	Cluster Layered	Cluster
Spongiosa	Muscle	Sparse	-
Fibrosa	Sparse	Sparse	Cluster
Grade 1 Mural	*Basal*	*Mid*	*Distal*
Atrialis	Sparse Cluster=Layered	Layered Sparse	Sparse Cluster=Layered
Spongiosa	Muscle	Sparse Cluster	Sparse Whirl
Fibrosa	Sparse	Sparse Whirl	Sparse
Grade 2 Mural	*Basal*	*Mid*	*Distal*
Atrialis	Sparse Layered	Cluster Layered	Layered Cluster=Sparse
Spongiosa	Muscle	Sparse Layered	Sparse
Fibrosa	Sparse Cluster	Sparse Cluster	Layered=Sparse
Grade 3 Mural	*Basal*	*Mid*	*Distal*
Atrialis	Sparse Layered	Layered Cluster=Sparse	Cluster=Layered Sparse
Spongiosa	Muscle	Sparse Layered	Whirl Layered=Sparse
Fibrosa	Sparse Cluster	Sparse	Layered Sparse
Grade 4 Mural	*Basal*	*Mid*	*Distal*
Atrialis	Sparse Layered	Layered=Sparse	Layered Cluster=Sparse
Spongiosa	Muscle	Cluster Layered=Sparse	Whirl Cluster
Fibrosa	Sparse Cluster	Sparse Cluster	Cluster Layered

Table 3.10. α-Smooth muscle actin positive cell morpholgies in septal leaflets. They are presented in a hierarchal order. The most frequently occurring shape is at the top of each block.

Grade 0 Septal	*Basal*	*Mid*	*Distal*
Atrialis	Oval=Spindle	Oval	Oval=Spindle
Spongiosa	Filamentous Oval	Oval Stellate	-
Fibrosa	Spindle	Oval	Oval
Grade 1 Septal	*Basal*	*Mid*	*Distal*
Atrialis	Flat Oval=Stellate	Oval Spindle	Oval Flat
Spongiosa	Filamentous Flat	Oval Filamentous	Flat=Oval
Fibrosa	Oval Spindle	Oval	Flat=Round
Grade 2 Septal	*Basal*	*Mid*	*Distal*
Atrialis	Oval Flat=Spindle	Oval Flat Spindle=Stellate	Oval Round
Spongiosa	Filamentous Round	Oval Round	Oval Flat=Round
Fibrosa	Oval=Round=Spindle	Oval	Oval
Grade 3 Septal	*Basal*	*Mid*	*Distal*
Atrialis	Oval Flat=Spindle	Oval Flat Spindle	Oval
Spongiosa	Filamentous	Oval Round Flat=Spindle	Flat Oval
Fibrosa	Flat=Oval Round=Spindle	Round Flat	Oval Flat=Round
Grade 4 Septal	*Basal*	*Mid*	*Distal*
Atrialis	Oval Flat=Spindle	Oval Flat=Spindle	Flat=Oval Spindle
Spongiosa	Filamentous Oval	Oval Flat	Flat
Fibrosa	Flat=Oval=Round	Round Flat	Round Oval=Spindle

Table 3.11. α-Smooth muscle actin positive cell morpholgies in mural leaflets. They are presented in a hierarchal order. The most frequently occurring cell shape is at the top of each block.

Grade 0 Mural	*Basal*	*Mid*	*Distal*
Atrialis	Oval	Oval	Oval
Spongiosa	Filamentous Oval	Oval=Stellate	-
Fibrosa	Round=Spindle	Oval=Stellate	Spindle
Grade 1 Mural	*Basal*	*Mid*	*Distal*
Atrialis	Oval	Oval Round=Spindle	Oval Flat
Spongiosa	Filamentous Oval	Oval Flat	Flat
Fibrosa	Flat=Oval	Oval Flat	Oval
Grade 2 Mural	*Basal*	*Mid*	*Distal*
Atrialis	Oval Flat	Oval Flat=Round=Spindle	Oval=Round Spindle
Spongiosa	Filamentous Oval	Flat=Oval=Spindle	Oval=Round Spindle
Fibrosa	Round=Oval=Spindle	Round	Oval Flat=Round
Grade 3 Mural	*Basal*	*Mid*	*Distal*
Atrialis	Oval Spindle Stellate	Oval Flat=Spindle	Oval Spindle
Spongiosa	Filamentous Oval	Oval Flat	Flat Oval=Round
Fibrosa	Round=Oval=Spindle	Round Oval	Flat
Grade 4 Mural	*Basal*	*Mid*	*Distal*
Atrialis	Oval Flat=Round	Flat=Oval	Oval Flat
Spongiosa	Filamentous Oval	Oval Flat=Round	Flat Spindle
Fibrosa	Round=Oval	Oval Round	Flat=Oval=Round

3.3.4 Desmin

In mitral valve leaflets from clinically normal dogs, the immunostaining for desmin was almost exclusively associated with cardiac myocytes in the basal zone (Figure 3.12). The cardiac myocytes differentially expressing desmin had a distinct filamentous banding pattern (Table 3.12 and Table 3.13). The spindle shaped fibroblast like cells located between the cardiac myocytes were desmin negative (Table 3.14 and Table 3.15). In the mid zone, a few desmin positive cells were sparsely scattered among fat cells. Occasionally, clusters of spindle shaped desmin positive cells were located between atrialis and spongiosa layers in the mural leaflet. Positive cells were rare in the distal zone.

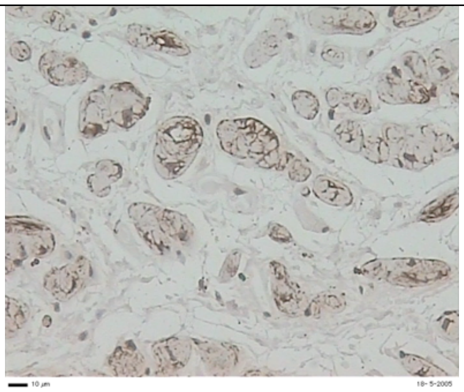

Figure 3.12. Desmin positive cardic myocyte shows filamentous banding. Bar = 10 µm.

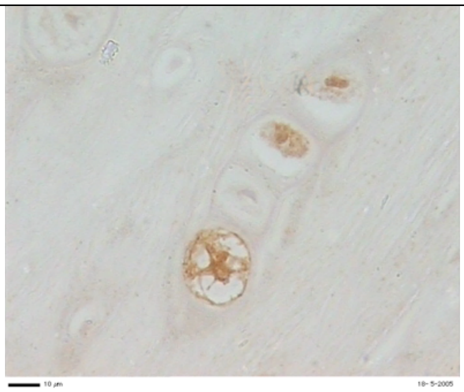

Figure 3.13. Desmin positive chondrocytes in the fibrosa layer. Bar = 10 µm.

There was no apparent change in the density of desmin positive cells between varying grades of disease and in the diseased valve the desmin positive cells were still predominantly associated with cardiac myocytes in the basal zone spongiosa layer. Overall, the desmin positive cells were rare in the distal zone of the diseased leaflets. A slight but almost negligible increase in positive cells occurred in the atrialis layer (Figure 3.14 and Figure 3.15). However, a few clusters of positive cells were observed in the possible mid point stress zone on the atrialis layer, the location coinciding with α-SMA positive cells in connective tissue. Cells that were suggestive of cartilage metaplasia were desmin positive. These cells were conspicuous, often arranged in a row with a distinct morphology of intense desmin staining in the centre and a diffusely speckled staining towards the periphery of the cells (Figure 3.13).

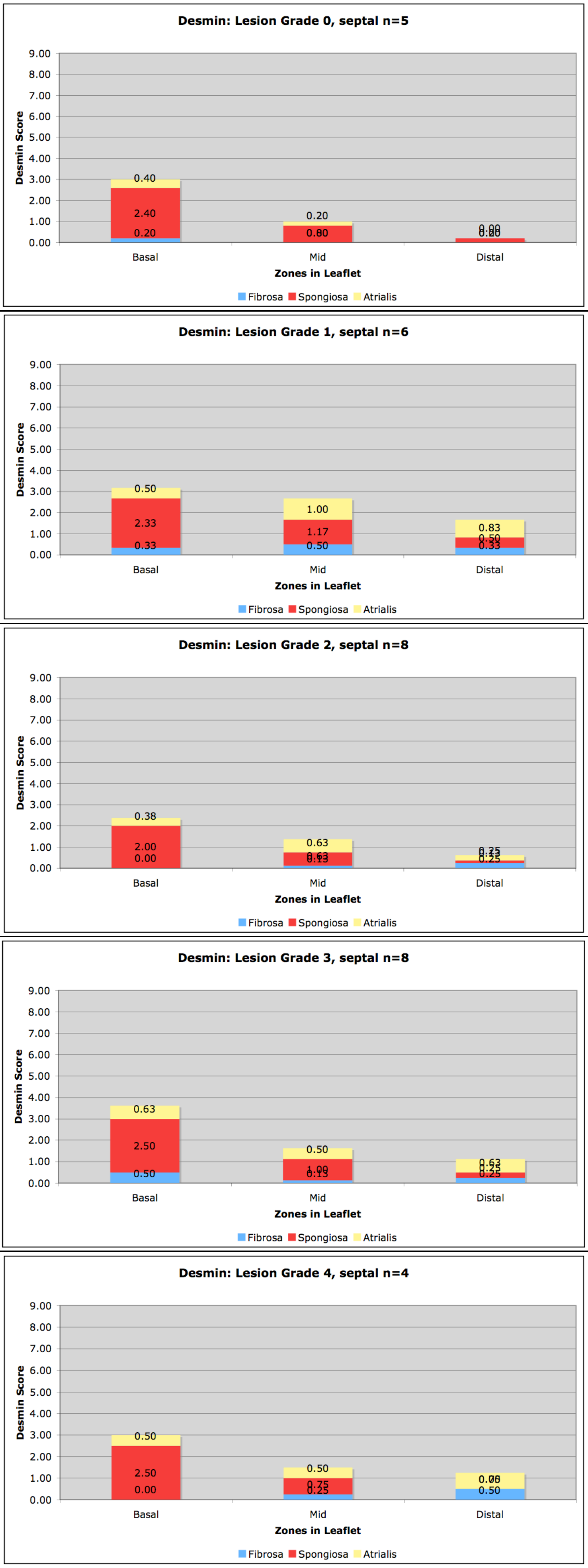

Figure 3.14. Desmin scores in septal leaflets. Three different columns represent the three zones and three different colours represent the three layers. Each zone and each layer could have a maximal score of 3, the combined score for a layer or zone could have a maximal score of 9.

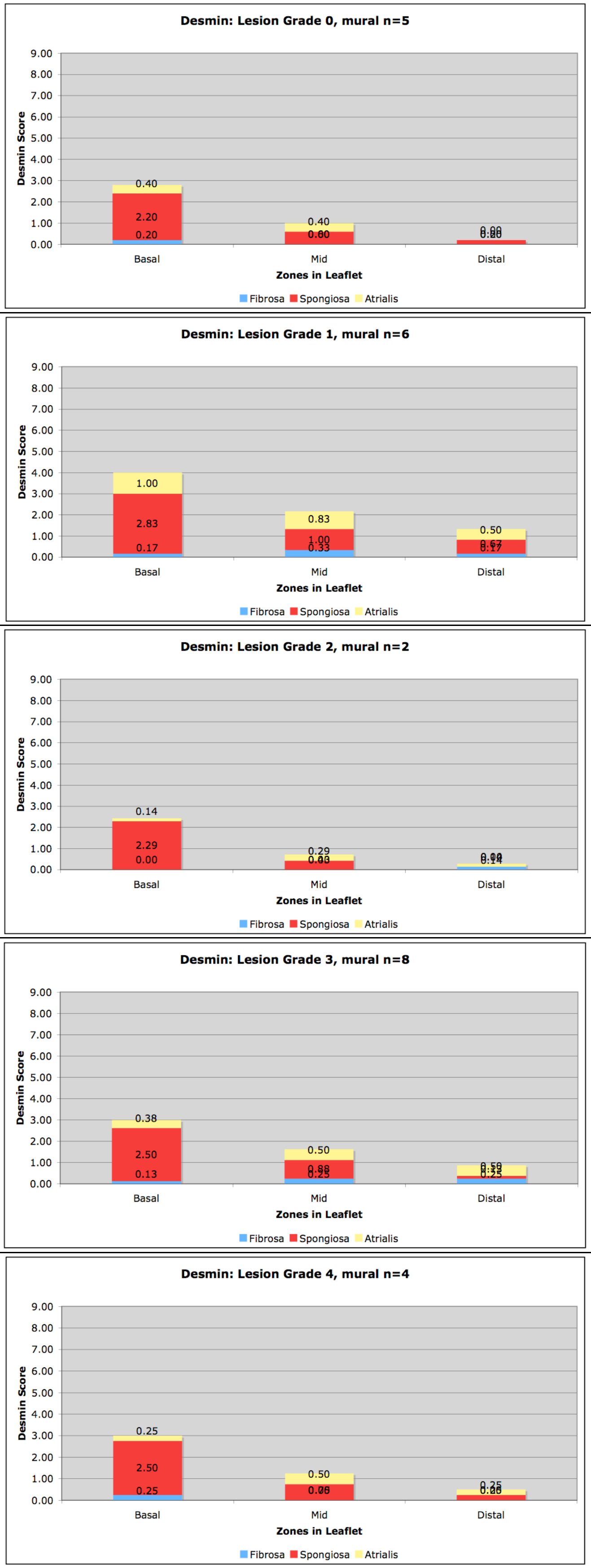

Figure 3.15. Desmin scores in mural leaflets. Three different columns represent the three zones and three different colours represent the three layers. Each zone and each layer could have a maximal score of 3, the combined score for a layer or zone could have a maximal score of 9.

Table 3.12. Desmin positive cell distribution patterns in septal leaflets. They are presented in a hierarchal order. The most frequently occurring distribution pattern is at the top of each block.

Grade 0 Septal	*Basal*	*Mid*	*Distal*
Atrialis	Layered=Sparse	Sparse	Sparse
Spongiosa	Muscle Cluster	Sparse Layered	
Fibrosa	Sparse	-	
Grade 1 Septal	*Basal*	*Mid*	*Distal*
Atrialis	Sparse	Sparse Cluster	Layered Cluster
Spongiosa	Muscle Cluster	Cluster=Layered Sparse	Sparse
Fibrosa	Sparse	Sparse	Cluster
Grade 2 Septal	*Basal*	*Mid*	*Distal*
Atrialis	Cluster=Sparse Layered	Cluster Layered	Cluster
Spongiosa	Muscle Cluster	Cluster=Layered Sparse	Sparse
Fibrosa	-	Sparse	Sparse
Grade 3 Septal	*Basal*	*Mid*	*Distal*
Atrialis	Cluster=Sparse Layered	Layered Sparse	Cluster Sparse
Spongiosa	Muscle Cluster	Cluster Sparse Layered	Sparse
Fibrosa	Sparse Layered	Sparse	
Grade 4 Septal	*Basal*	*Mid*	*Distal*
Atrialis	Sparse	Cluster=Sparse	Cluster Sparse
Spongiosa	Muscle Cluster	Sparse Cluster=Layered	-
Fibrosa	-	Sparse	Cluster=Layered

Table 3.13. Desmin positive cell distribution patterns in mural leaflets. They are presented in a hierarchal order. The most frequently occurring distribution pattern is at the top of each block.

Grade 0 Mural	*Basal*	*Mid*	*Distal*
Atrialis	Layered=Sparse	Cluster=Whirl	-
Spongiosa	Muscle Cluster	Cluster=Sparse Whirl	Sparse
Fibrosa	Sparse	-	-
Grade 1 Mural	*Basal*	*Mid*	*Distal*
Atrialis	Cluster=Sparse Layered	Layered Sparse	Sparse
Spongiosa	Muscle Cluster	Cluster Layered=Sparse	Sparse Cluster=Layered
Fibrosa	Layered	Sparse	Sparse
Grade 2 Mural	*Basal*	*Mid*	*Distal*
Atrialis	Cluster	Cluster=Sparse	Sparse
Spongiosa	Muscle Cluster	Cluster=Sparse Layered	-
Fibrosa	-	-	-
Grade 3 Mural	*Basal*	*Mid*	*Distal*
Atrialis	Cluster=Sparse Layered	Sparse Layered	Cluster Layered=Sparse
Spongiosa	Muscle Cluster	Cluster Sparse Layered	Sparse
Fibrosa	Cluster	Sparse	Sparse
Grade 4 Mural	*Basal*	*Mid*	*Distal*
Atrialis	Cluster	Cluster=Sparse	-
Spongiosa	Muscle Cluster	Sparse Cluster	-
Fibrosa	Sparse	-	-

Table 3.14. Desmin positive cell morpholgies in septal leaflets. They are presented in a hierarchal order. The most frequently occurring cell shape is at the top of each block.

Grade 0 Septal	*Basal*	*Mid*	*Distal*
Atrialis	Crystalline=Spindle	Speckle	-
Spongiosa	Filamentous Flat	Oval Flat=Speckle	Stellate
Fibrosa	Spindle	-	-
Grade 1 Septal	*Basal*	*Mid*	*Distal*
Atrialis	Oval	Oval=Round=Spindle	Spindle Round
Spongiosa	Filamentous Flat=Speckle	Oval Flat=Speckle=Spindle	Oval Spindle
Fibrosa	Oval=Spindle	Sparse	Round
Grade 2 Septal	*Basal*	*Mid*	*Distal*
Atrialis	Oval=Round=Spindle	Oval=Round Speckle	Round
Spongiosa	Flat Filamentous=Speckle	Flat=Spindle Oval=Speckle	Spindle
Fibrosa	-	Sparse	Round
Grade 3 Septal	*Basal*	*Mid*	*Distal*
Atrialis	Spindle Crystalline=Oval	Oval Spindle	Oval Round=Spindle
Spongiosa	Filamentous=Flat	Oval Flat=Crystalline	Oval
Fibrosa	Oval Spindle	Sparse	-
Grade 4 Septal	*Basal*	*Mid*	*Distal*
Atrialis	Oval	Round=Spindle	Round Oval
Spongiosa	Filamentous Oval=Speckle	Oval Speckle=Spindle	-
Fibrosa	-	Sparse	Round

Table 3.15. Desmin positive cell morpholgies in mural leaflets. They are presented in a hierarchal order. The most frequently occurring cell shape is at the top of each block.

Grade 0 Mural	*Basal*	*Mid*	*Distal*
Atrialis	Oval=Speckle	Spindle	-
Spongiosa	Filamentous Flat=Oval	Spindle Oval=Speckle	Spindle
Fibrosa	Oval	-	-
Grade 1 Mural	*Basal*	*Mid*	*Distal*
Atrialis	Oval=Speckle Round	Speckle Oval=Round	Oval=Spindle
Spongiosa	Filamentous Flat Oval	Round Oval=Speckle=Spindle	Spindle Oval=Spindle
Fibrosa	Round	Sparse	Oval
Grade 2 Mural	*Basal*	*Mid*	*Distal*
Atrialis	Oval	Oval=Speckle	Round
Spongiosa	Filamentous Oval=Flat=Speckle	Flat=Round=Speckle	-
Fibrosa	-	-	-
Grade 3 Mural	*Basal*	*Mid*	*Distal*
Atrialis	Flat Oval	Oval Crystalline	Oval Crystalline
Spongiosa	Filamentous Flat=Crystalline	Oval=Spindle Flat=Round	Oval
Fibrosa	Spindle	Sparse	Spindle
Grade 4 Mural	*Basal*	*Mid*	*Distal*
Atrialis	Oval	Oval=Round	-
Spongiosa	Oval	Oval Spindle	-
Fibrosa	Sparse	-	-

3.3.5 Smooth muscle myosin

Smooth muscle myosin positive cells in mitral valve leaflets from clinically normal dogs were rare and the positive cells were exclusively associated with arteriole walls in the basal zone spongiosa layer (Figure 3.16). In one rare case, a small number of positive cells were located near the atrialis surface in the mid zone of a septal leaflet.

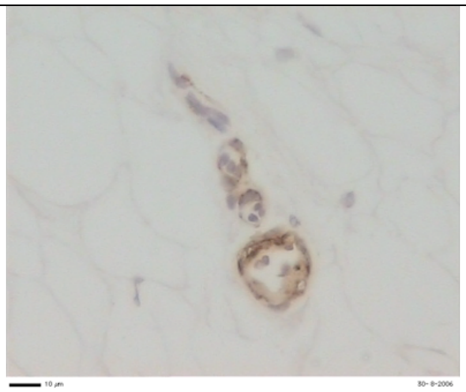

Figure 3.16. Microphotograph showing the arteriole wall stained positive for smooth muscle myosin. Bar = 10 µm.

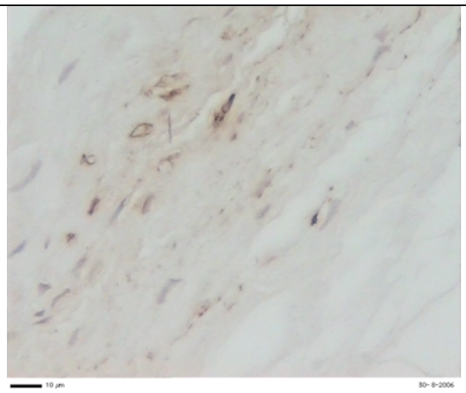

Figure 3.17. Microphotograph showing a vessel wall stained positive for smooth muscle myosin. Bar = 10 µm.

There were no apparent changes in the density of smooth muscle myosin positive cells between normal and varying grades of diseased. In mitral valve leaflets with MMVD, smooth muscle myosin positive cells were closely associated with arteriole walls in the spongiosa layer, mostly situated in the basal zone. On rare occasions, small clusters of myosin positive cells were found possibly involved in angiogenesis (Figure 3.17).

Figure 3.18. Smooth muscle myosin score in septal leaflets. Three different columns represent the three zones and three different colours represent the three layers. Each zone and each layer could have a maximal score of 3, the combined score for a layer or zone could have a maximal score of 9.

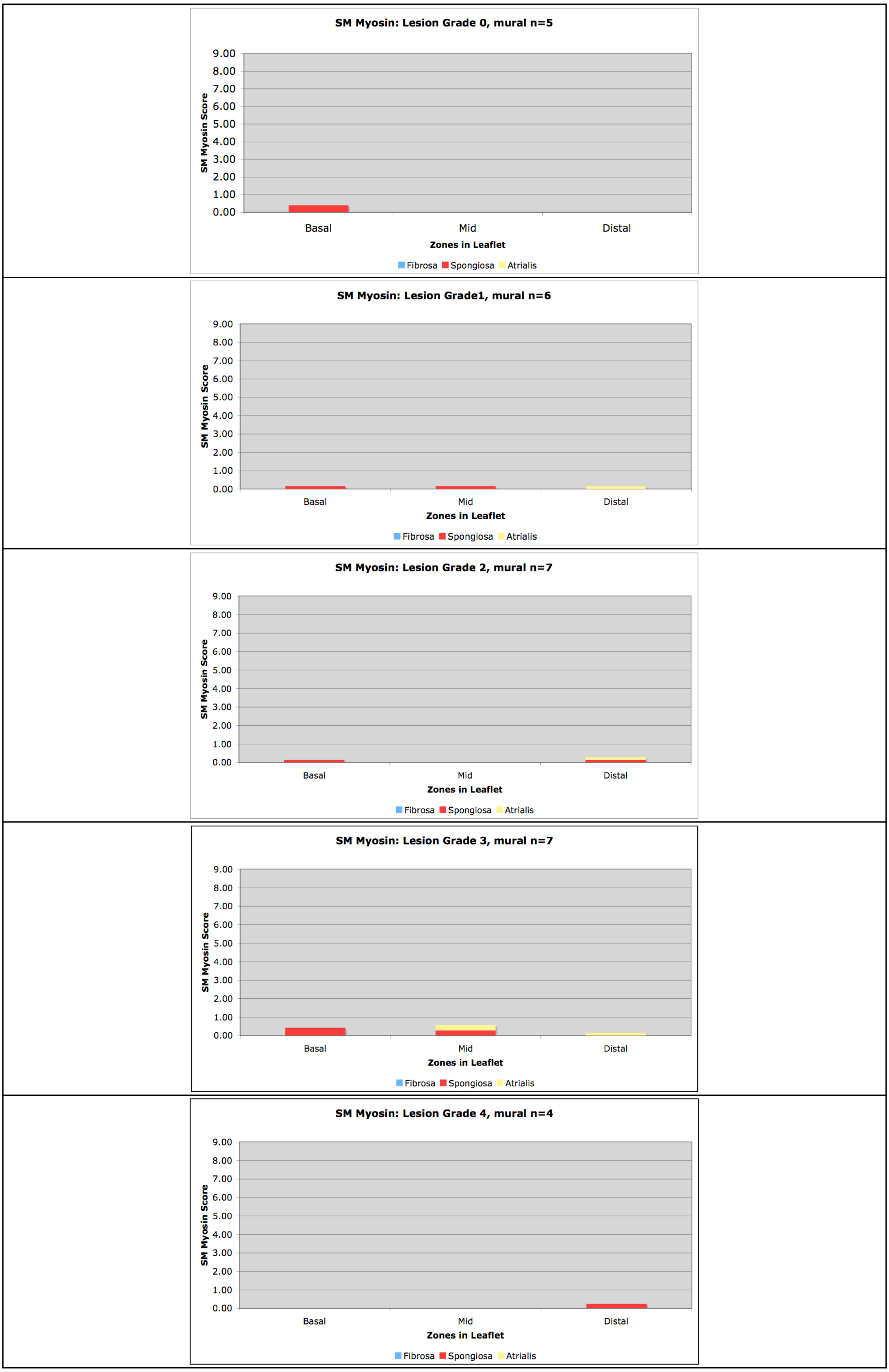

Figure 3.19. Smooth muscle myosin score in mural leaflets. Three different columns represent the three zones and three different colours represent the three layers. Each zone and each layer could have a maximal score of 3, the combined score for a layer or zone could have a maximal score of 9.

3.3.6 Fibrillin

The amount of fibrillin detected in the mitral valve leaflets from clinical normal dogs was limited. In both septal and mural leaflets, immunostaining for fibrillin was predominantly found under the endothelial lining and trace amounts of fribrillin fanning out through the extracellular fibril in the atrialis layer. Occasionally, some cells and their immediate periphery were seen to be fibrillin positive. The fibrillin score in Grade 1 diseased was comparable to the normal, but as the disease progressed, there was a decrease in fibrillin staining (Figure 3.20). In the mitral valve leaflets of dogs with MMVD, weak fibrillin staining was found in the loose connective tissue fibril. Some round shaped endothelial cells were also fibrillin positive.

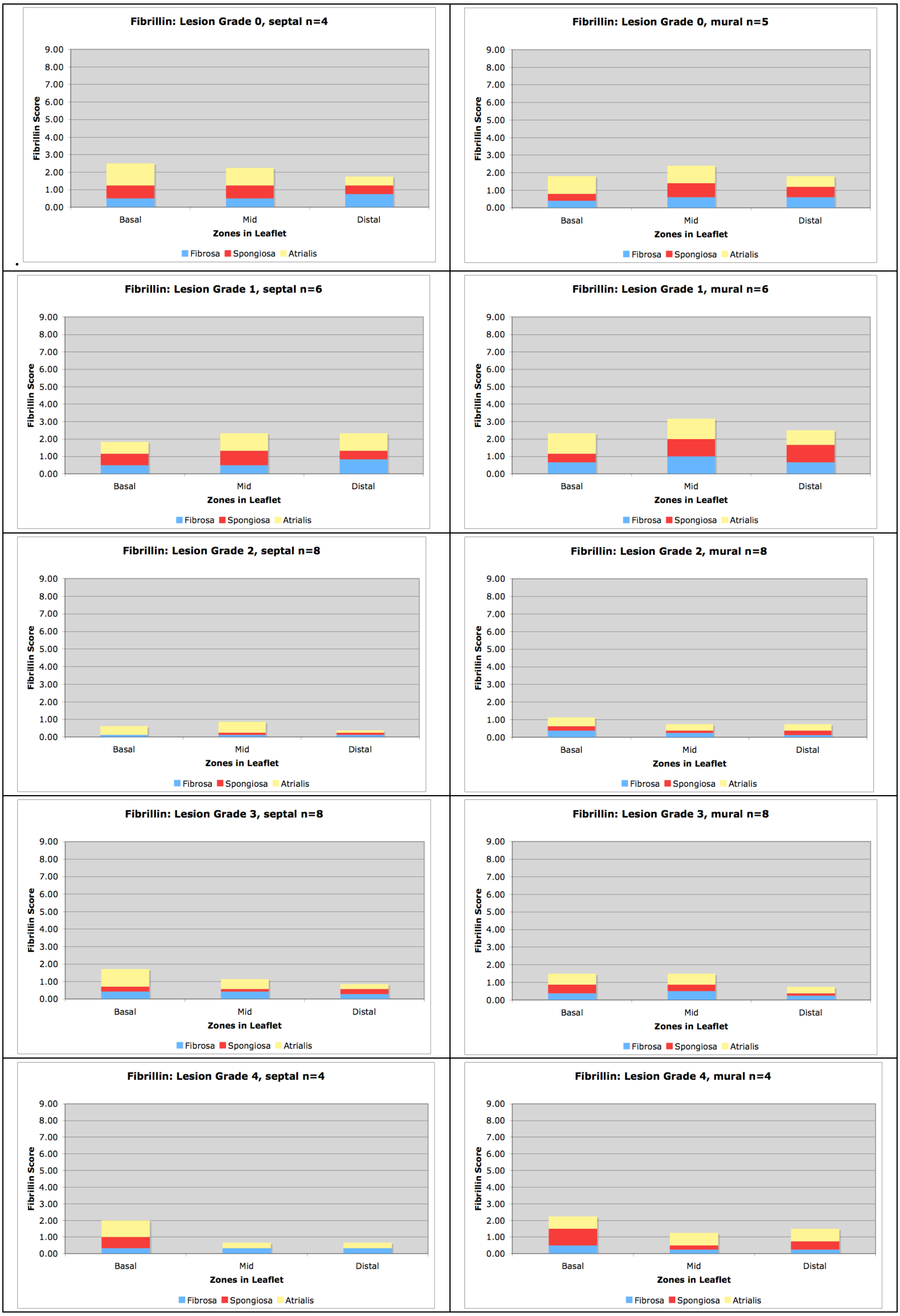

Fibrillin: Lesion Grade 0, septal n=4

Fibrillin: Lesion Grade 0, mural n=5

Fibrillin: Lesion Grade 1, septal n=6

Fibrillin: Lesion Grade 1, mural n=6

Fibrillin: Lesion Grade 2, septal n=8

Fibrillin: Lesion Grade 2, mural n=8

Fibrillin: Lesion Grade 3, septal n=8

Fibrillin: Lesion Grade 3, mural n=8

Fibrillin: Lesion Grade 4, septal n=4

Fibrillin: Lesion Grade 4, mural n=4

Figure 3.20. Fibrillin scores in septal and mural leaflets. Three different columns represent the three zones and three different colours represent the three layers. Each zone and each layer could have a maximal score of 3, the combined score for a layer or zone could have a maximal score of 9.

3.3.7 MMP-2

No staining for MMP-2 was detected in any of the sample slides.

3.3.8 MMP-9

In mitral valve leaflets from Grade 0 clinically normal dogs, trace amount of MMP-9 expression was found restricted to the luminal side of arterioles located near cardiomyocytes at the basal zone. Due to the small number of arterioles found in the valve and the space only occupy in leaflet, the level of MMP-9 staining could be regarded as negligible in most cases. As the disease progressed, MMP-9 was detected in the mid zone of Grade 1 valves. Slight elevation in MMP-9 expression was noted in Grade 2 diseased valves and the staining extended to the distal zone, but was predominantly seen in the spongiosa layer. No further elevation of MMP-9 was found in Grade 3 diseased valves. In Grade 4 diseased, although the MMP-9 level was still low, the expression spread to atrialis and fibrosa layers (Figure 3.23). In the diseased valves, MMP-9 expression was seen as a diffused form in the para-lumenal of vessels. The endothelial cells expressing MMP-9 in the para-lumen were swollen compared to MMP-9 negative cells (Figure 3.21). Occasionally, MMP-9 expression was seen in the tight intercellular space of a series fusiform cells lining up in a row (Figure 3.22). However, at no time was MMP-9 expression associated with myxomatous areas.

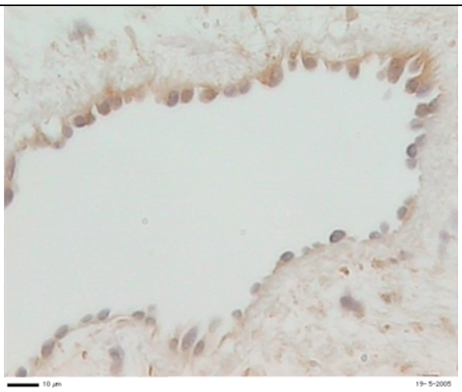

Figure 3.21. Endothelial cells lining the vessel and the para-lumin space are positive for MMP-9. Bar = 10 µm.

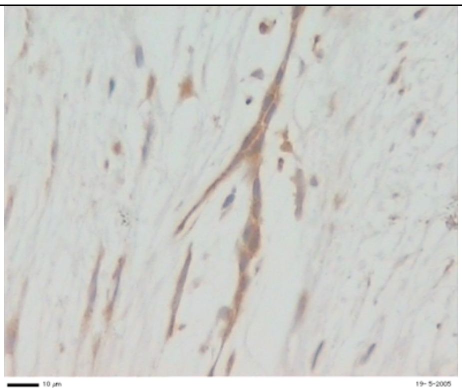

Figure 3.22. The intercellular space near the polar ends of interstitial cells are MMP-9 positive. Bar = 10 µm.

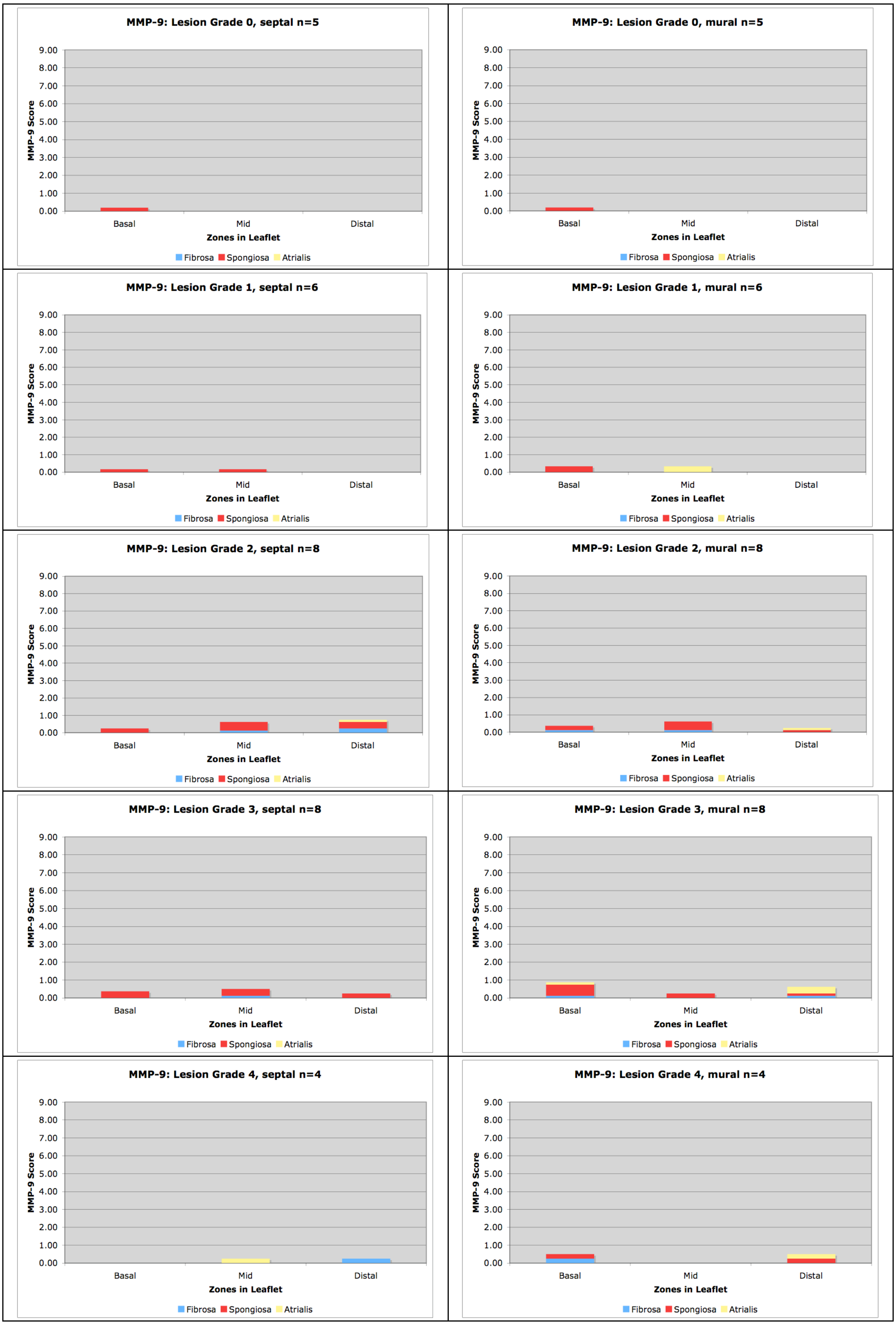

Figure 3.23. MMP-9 scores in septal and mural leaflets. Three different columns represent the three zones and three different colours represent the three layers. Each zone and each layer could have a maximal score of 3, the combined score for a layer or zone could have a maximal score of 9.

3.3.9 MMP-13

The immuno reactivity for MMP-13 was limited in mitral valve leaflets from clinically normal dogs. In both septal and mural leaflets weak immunostaining was confined to certain sub-endothelial space predominantly in the mid zone towards the atrialis surface (Figure 3.24). The MMP-13 positive areas appeared focalised.

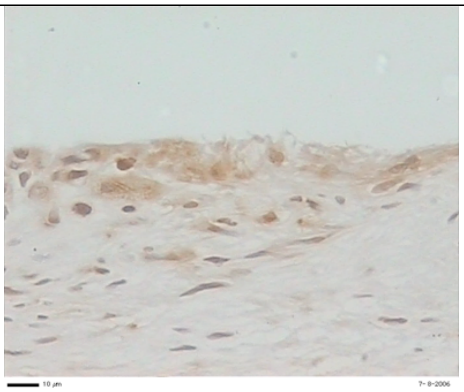

Figure 3.24. MMP-13 positive in sub-endothelial space. Bar = 10 μm.

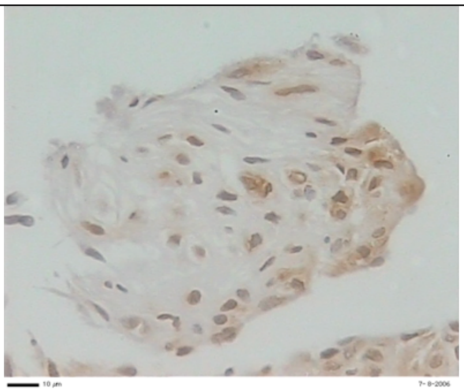

Figure 3.25. MMP-13 positive area associated with a nodule. Bar = 10 μm.

In diseased mitral valve leaflets, MMP-13 reactivity was exclusively associated with the damaged endothelium. More intense immunostaining for MMP-13 was found underneath the endothelial basement membrane (Figure 3.25). As the disease progressed, the MMP-13 expression was slightly increased and extended into the areas of metaplasia beneath the damaged endothelium in distal zone (Figure 3.26). Some of the papillary-like nodule outgrowths on the atrialis surface were MMP-13 positive and staining seemed closely associated with oval or rounded shaped interstitial cells.

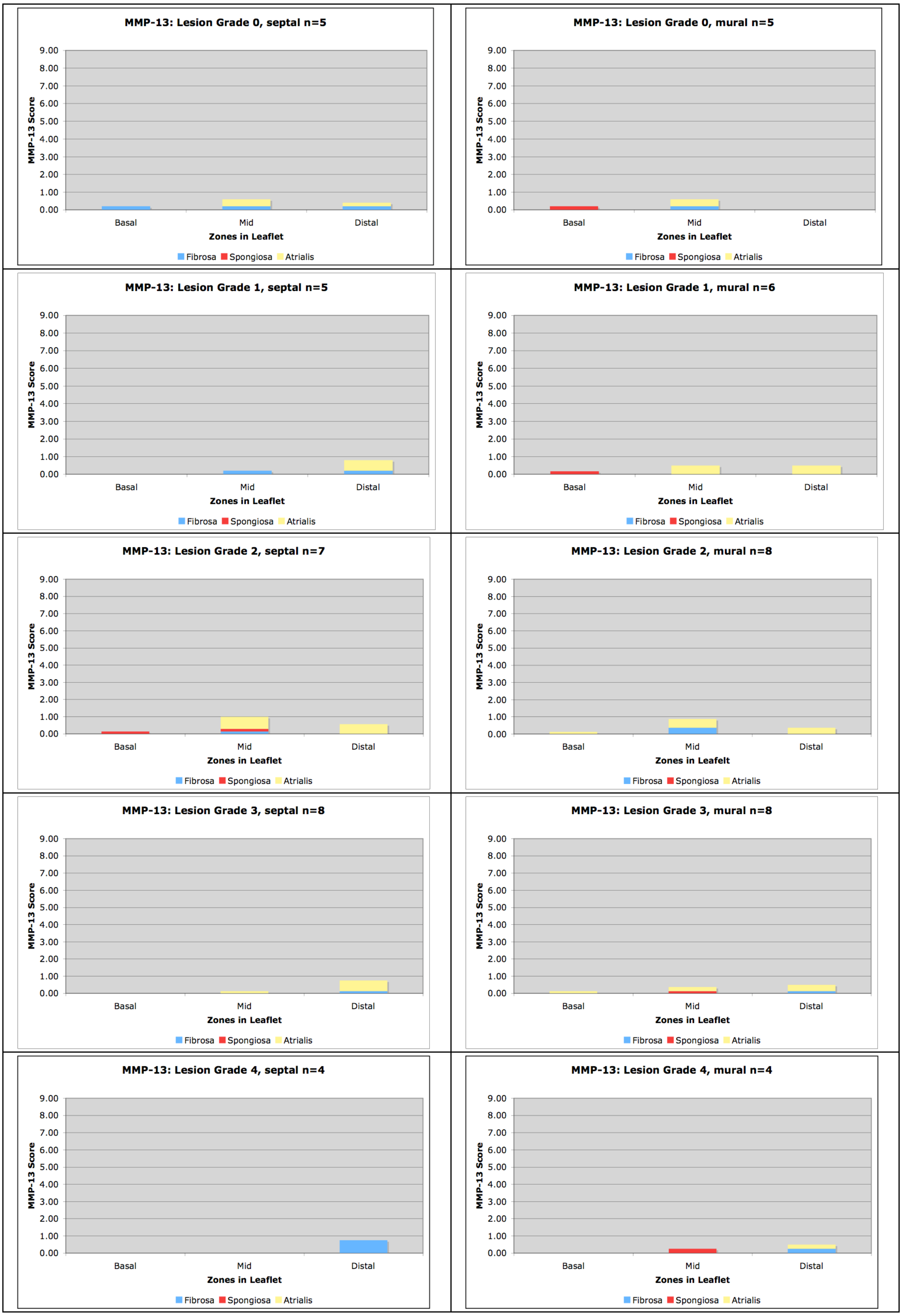

Figure 3.26. MMP-13 scores in septal and mural leaflets. Three different columns represent the three zones and three different colours represent the three layers. Each zone and each layer could have a maximal score of 3, the combined score for a layer or zone could have a maximal score of 9.

3.3.10 Fibronectin

Quantifying the amount of fibronectin in leaflets proved difficult, as fibronectin appeared as a diffuse background stain. Nickel chloride enhanced staining showed the fibronectin as a shade of grey in the background. This meant the scoring system could not be applied to measure fibronectin. However, fibronectin was seen closely associated with structural connective tissue, but in the overtly myxomatous area, there was absence of fibronectin staining. In the areas of metaplasia of the diseased valve, intense staining of fibronectin was often observed in the presence of α-SMA positive cells.

3.3.11 Macrophage

Macrophage (MAC-387 positive cells) numbers in clinically normal dogs were low with only a mean of 6 cells/valve and were predominantly found in the spongiosa layer at the base. An increase in mean macrophage number of 12 cells/valve was found in Grade 1 diseased, but the number fell back to 4 cells/valve in Grade 2. In the more severe forms of disease, the macrophage numbers were markedly increased with a mean of 26 cells/valve in Grade 3 and 27 cells/valve in Grade 4. However, the samples showing obvious increased numbers were widely distributed within the groups of Grade 3 and 4 diseased valves. The distribution of macrophages in later stage disease spread out to the atrialis and fibrosa layers in the mid zone. Although no significant difference (p=0.1719) was found on ANOVA, Wilcoxon ranked test showed the Chi square was significant at 0.0309. The Student t-test also revealed that Grade 2 was statistically different to Grade 3 (Figure 3.29).

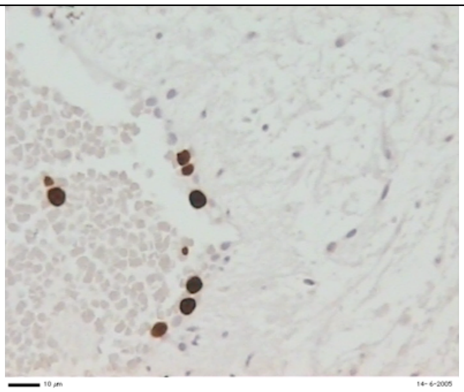 Figure 3.27. MAC-387 positive macrophages associated with luminal side of a vessel. Bar = 10 µm.	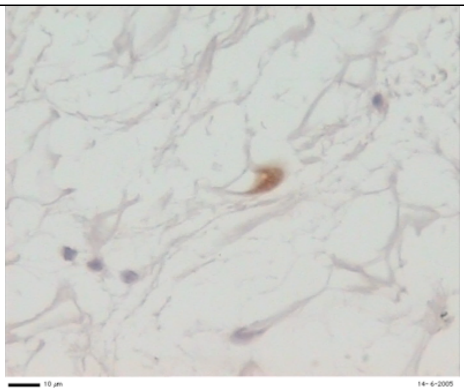 Figure 3.28. MAC-387 positive macrophages associated with tissue. Bar = 10 µm.

Macrophages in the mitral valve could be divided into two groups according to their locality. Macrophages in the first group were associated with the blood vessels, often seen in round shapes sitting in the lumen of the vessels and reacted intensively to the MAC-387 antibody (Figure 3.27). The second group of macrophages were associated with loose connective tissue. They were more lightly stained and more elongated in shape (Figure 3.28). The general impression was that there were more vessel-associated macrophages in the diseased valves.

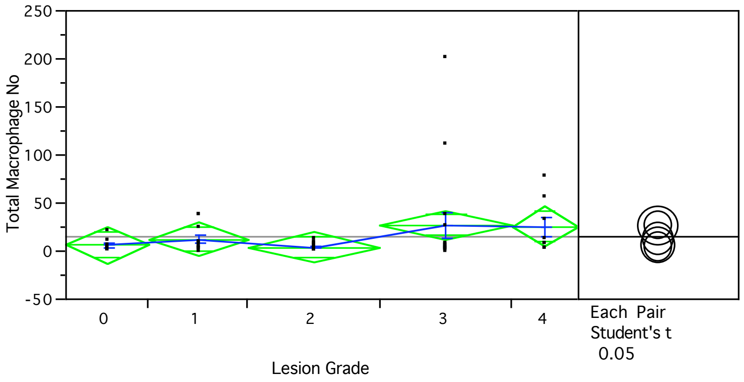

Level			Mean
3	A		27.125000
4	A	B	25.750000
1	A	B	12.166667
0	A	B	6.100000
2		B	4.125000

p=0.1719

ChiSq=0.0309

LSN=92.47

Figure 3.29. Comparison of macrophage number in mitral valve between mitral valve lesion grade. The results from ANOVA, Wilcoxon ranked test, Student's t-test, and LSN are presented.

Even though the ANOVA analysis of macrophage numbers in septal leaflet between grades was not significant (p=0.4104), the Chi square from the Wilcoxon ranked test was significant (ChiSq=0.0246). Macrophage numbers were much higher in septal leaflets of Grade 3 and 4 valves. There were no significant changes in macrophage numbers in the mural leaflet (Figure 3.30).

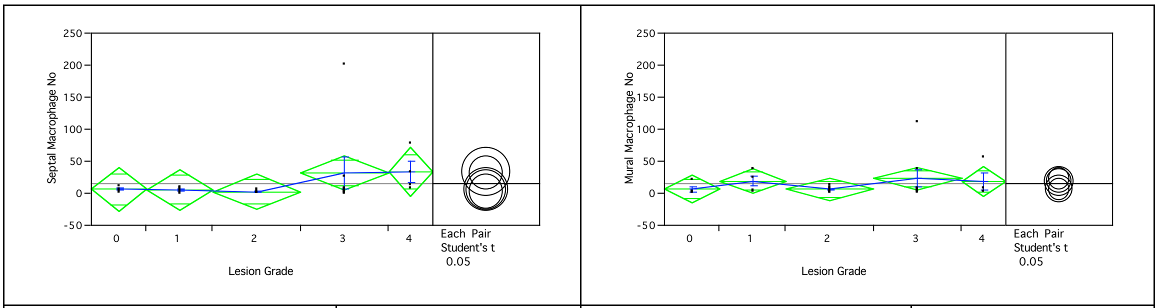

Grade		Mean	
4	A	33.250000	p=0.4104
3	A	31.625000	ChiSq=0.0246
0	A	6.000000	LSN=75.30
1	A	5.333333	
2	A	2.375000	

Grade		Mean	
3	A	22.625000	p=0.5609
1	A	19.000000	ChiSq=0.2994
4	A	18.250000	LSN=100.66
0	A	6.200000	
2	A	5.875000	

Figure 3.30. Comparison of macrophage number in septal leaflet (left) and mural leaflet (right) between mitral valve lesion grade. The results from ANOVA, Wilcoxon ranked test, Student's t-test, and LSN are presented.

When the numbers of macrophages in the valves were normalized to leaflet area (mm^2), the sample distribution within each group was spread out. Outliers in the top tail ends were seen in each sample group. Neither ANOVA nor Wilcoxon test detected any significant differences, but Grade 4 diseased (2,38 cell/mm^2) had the highest number of macrophages per area, the mean was different to Grade 2 (0.50 cell/mm^2) using the Student t-test (Figure 3.31).

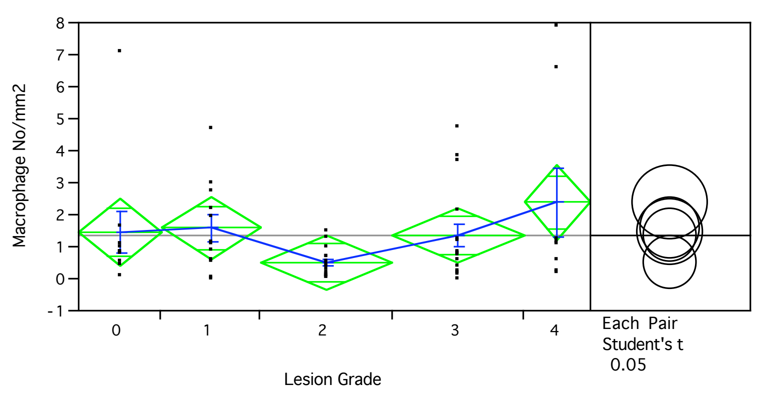

Level			Mean	
4	A		2.3840266	p=0.1299
1	A	B	1.5766032	ChiSq=0.0781
0	A	B	1.4445007	LSN=82.95
3	A	B	1.3566605	
2		B	0.5025476	

Figure 3.31. Comparison of macrophage number per mm^2 area between mitral valve lesion grade. The results from ANOVA, Wilcoxon ranked test, Student's t-test, and LSN are presented.

In septal leaflets alone, the ANOVA of normalized macrophage numbers to area between grades did not achieve a significant statistical difference. The Grade 4 diseased valves attained the highest value (2.38 cell/mm^2) and the mean was significantly different to Grade 2 disease (0.27 cell/mm^2) using Student t-test. In the mural leaflets the normalized macrophage numbers to area between grades did not show a significant difference in either ANOVA or Wilcoxon test. Again, the Grade 4 attained the highest value (2.38 cell/mm^2), but this did not achieve significant difference in comparison to other groups in the series (Figure 3.32).

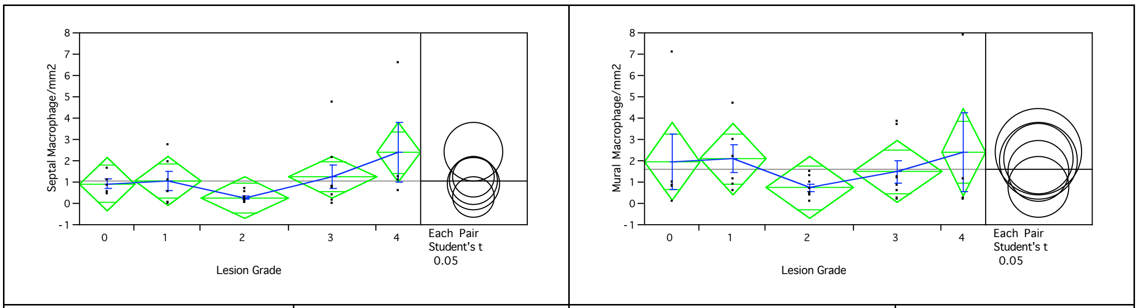

Grade		Mean	p=0.1906
4	A	2.3840878	ChiSq=0.0769
3	A B	1.2306042	
1	A B	1.0619045	LSN=48.44
0	A B	0.9198065	
2	B	0.2738262	

Grade		Mean	p=0.6154
4	A	2.3839654	ChiSq=0.5952
1	A	2.0913019	
0	A	1.9691949	LSN=112.80
3	A	1.4827167	
2	A	0.7312690	

Figure 3.32. Comparison of macrophage number per area in septal leaflet (left) and mural leaflet (right) between mitral valve lesion grade. The results from ANOVA, Wilcoxon ranked test, Student's t-test, and LSN are presented.

The overall distribution of macrophages was variable and no particular pattern was observed. However, the general trend was for a higher distribution in the central spongiosa, spreading out towards the atrialis and fibrosa layers as the disease progresses (Figure 3.33).

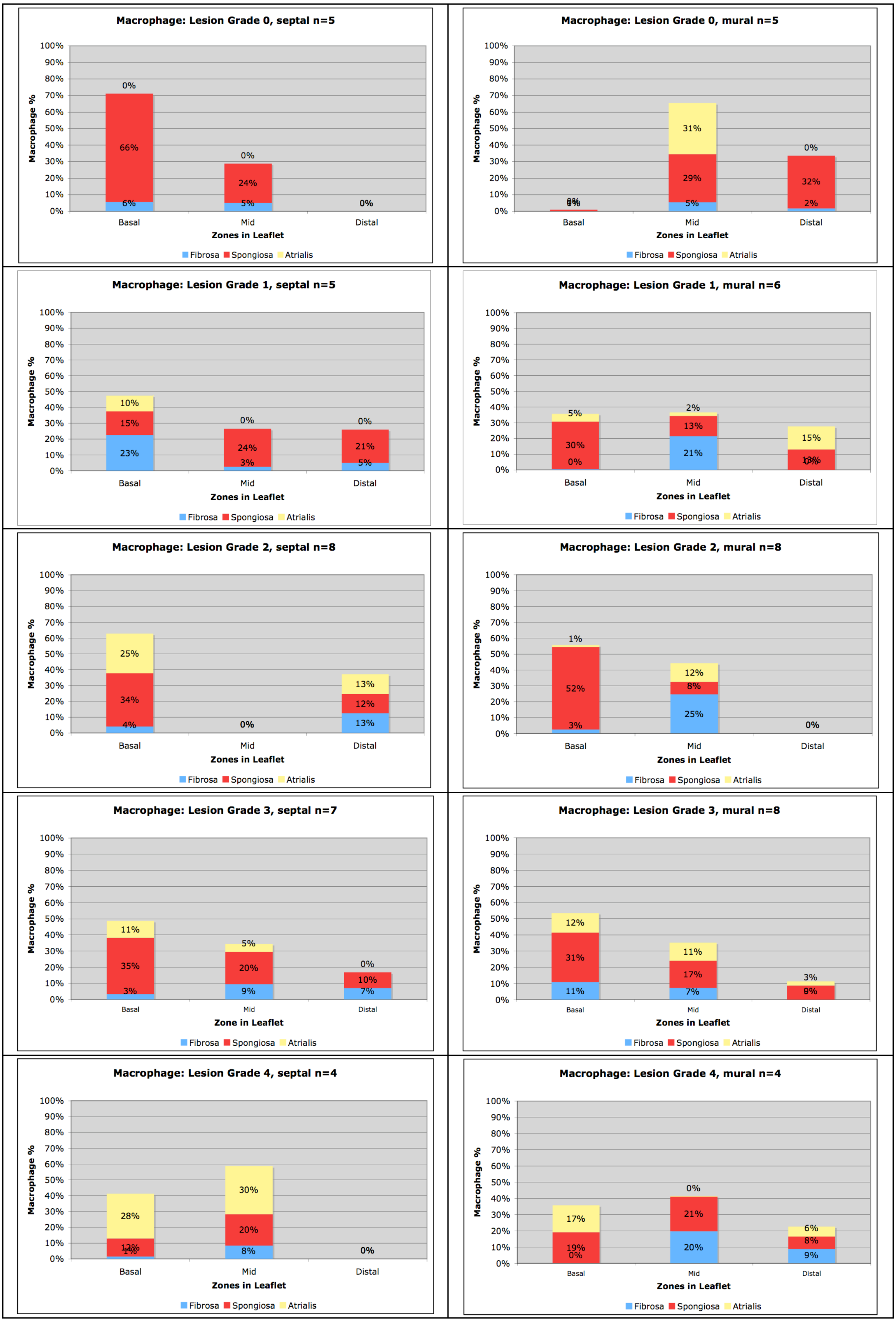

Figure 3.33. Distribution of macrophage as a percentage in septal leaflet (left panel) and mural leaflet (right panel). Three different columns represent the three zones and three different colours represent the three layers.

3.3.12 Mast cells

The mast cell had the appearance of a bright blue colour blob with more polygonal outlines. They were often seen sitting alone in the loose connective tissue, but occasionally in pairs side by side. Some of the mast cells, as demonstrated by the presence of pseudopodia, were in active form. At high magnification, the punctuated dense organelles were visible (Figure 3.34).

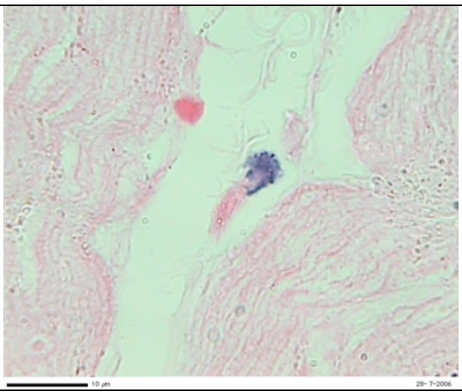

Figure 3.34. Mast cell with punctuated dense organelles by Toluidine Blue stain. Bar = 10 μm.

The number of mast cells in clinically normal valves was low (4.63 cell/valve). The mast cell numbers were similar in Grade 1 (4.67 cell/valve) and Grade 2 (4.81 cell/valve). An increase in mast cell numbers was found in Grade 3 (6.60 cell/valve) with a further increase in Grade 4 (8.00 cell/valve). The samples were widely distributed in each group of the series. No significant differences were found on either ANOVA or Wilcoxon (Figure 3.35).

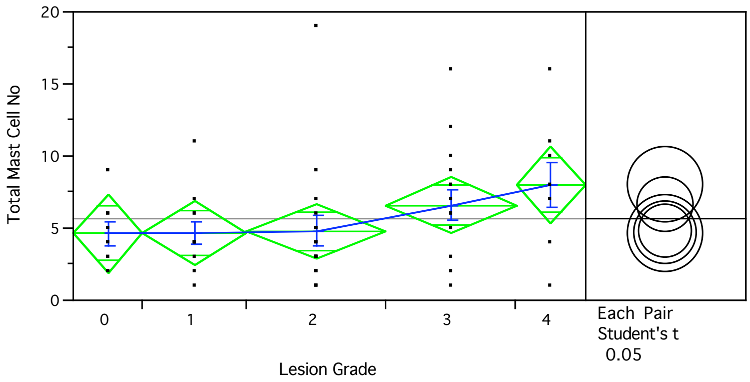

Level		Mean
4	A	8.0000000
3	A	6.6000000
2	A	4.8125000
1	A	4.6666667
0	A	4.6250000

p=0.1998

ChiSq=0.1357

LSN=93.92

Figure 3.35. Comparison of mast cell number in mitral valve between mitral valve lesion grade. The results from ANOVA, Wilcoxon ranked test, Student's t-test, and LSN are presented.

In the septal leaflets, higher mast cell numbers were found in Grade 3 and Grade 4, there was no apparent change in cell number between normal Grade 0 to Grade 2, however, the difference was not significant. In the mural leaflets the highest cell number was found in Grade 4, but again no significant difference was achieved (Figure 3.36).

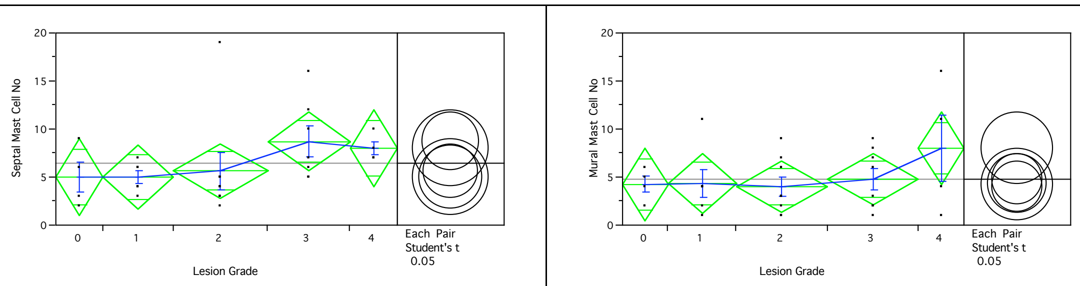

Level		Mean	
3	A	8.7142857	p=0.3413
4	A	8.0000000	ChiSq=0.0478
2	A	5.6250000	LSN=61.85
1	A	5.0000000	
0	A	5.0000000	

Level		Mean	
4	A	8.0000000	p=0.4791
3	A	4.7500000	ChiSq=0.8698
1	A	4.3333333	LSN=83.01
0	A	4.2500000	
2	A	4.0000000	

Figure 3.36. Comparison of mast cell number in septal leaflet (left) and mural leaflet (right) between mitral valve lesion grade. The results from ANOVA, Wilcoxon ranked test, Student's t-test, and LSN are presented.

When the number of mast cells was normalized to area, the normal Grade 0 valve attained the highest cell per area value (1.07 cell/mm^2). Although the ANOVA showed the difference (p=0.0779) was not significant, on the Student's t-test, the Grade 0 was found to be significantly different to Grade 1 and Grade 2. Still, the samples were widely distributed within each group of the series (Figure 3.37).

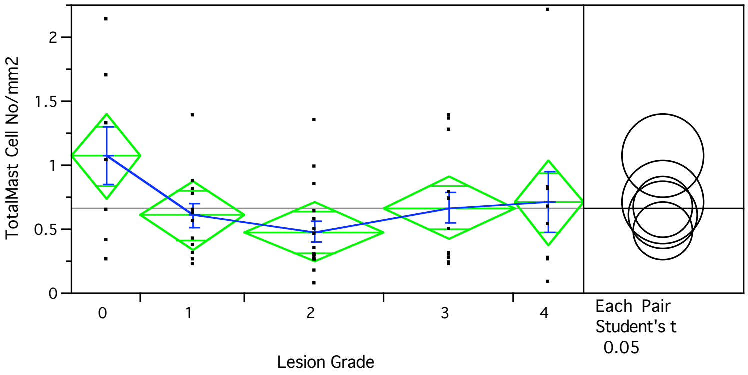

Level			Mean	
0	A		1.0721670	p=0.0779
4	A	B	0.7099065	ChiSq=0.1745
3	A	B	0.6656451	LSN=66.71
1		B	0.6078668	
2		B	0.4782762	

Figure 3.37. Comparison of mast cell number per area between mitral valve lesion grade. The results from ANOVA, Wilcoxon ranked test, Student's t-test, and LSN are presented.

In the septal leaflets, no significant difference was found in the normalized to area mast cell numbers on either ANOVA or Wilcoxon. The Student’s t-test showed that the Grade 3 (0.80 cell/mm^2) was different to Grade 2 (0.38 cell/mm^2). In the mural leaflet, again no significant difference was found in ANOVA or Wilcoxon when mast cell numbers were normalized to area, but the normal Grade 0 (1.38 cell/mm^2) was different to Grade 2 (0.58 cell/mm^2) and Grade 3 (0.55 cell/mm^2) (Figure 3.38).

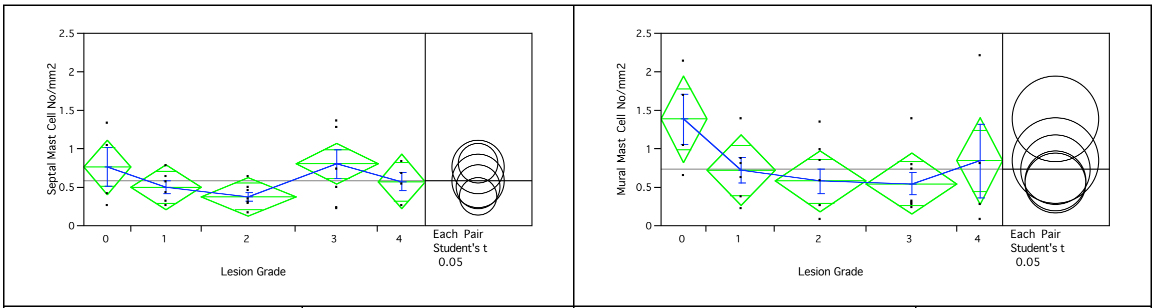

Level		Mean	
3	A	0.80283362	p=0.11608
0	A B	0.76135298	ChiSq=0.4984
4	A B	0.57547913	LSN=42.18
1	A B	0.49896665	
2	B	0.37796837	

Level		Mean	
0	A	1.3829809	p=0.1508
4	A B	0.8443338	ChiSq=0.2662
1	A B	0.7167670	LSN=42.52
2	B	0.5785841	
3	B	0.5456052	

Figure 3.38. Comparison of mast cell number per area in septal leaflet (left) and mural leaflet (right) between mitral valve lesion grade. The results from ANOVA, Wilcoxon ranked test, Student’s t-test, and LSN are presented.

In the normal valve, mast cells were predominantly located in the basal zone and to a lesser extent in the mid zone. The cells in the basal zone were almost entirely associated with the spongiosa layer and this applied to both septal and mural leaflets. The general trend during the disease progression was shifting of mast cells from base towards the distal zone. However, the majority of the cells were still associated with the spongiosa layer (Figure 3.39).

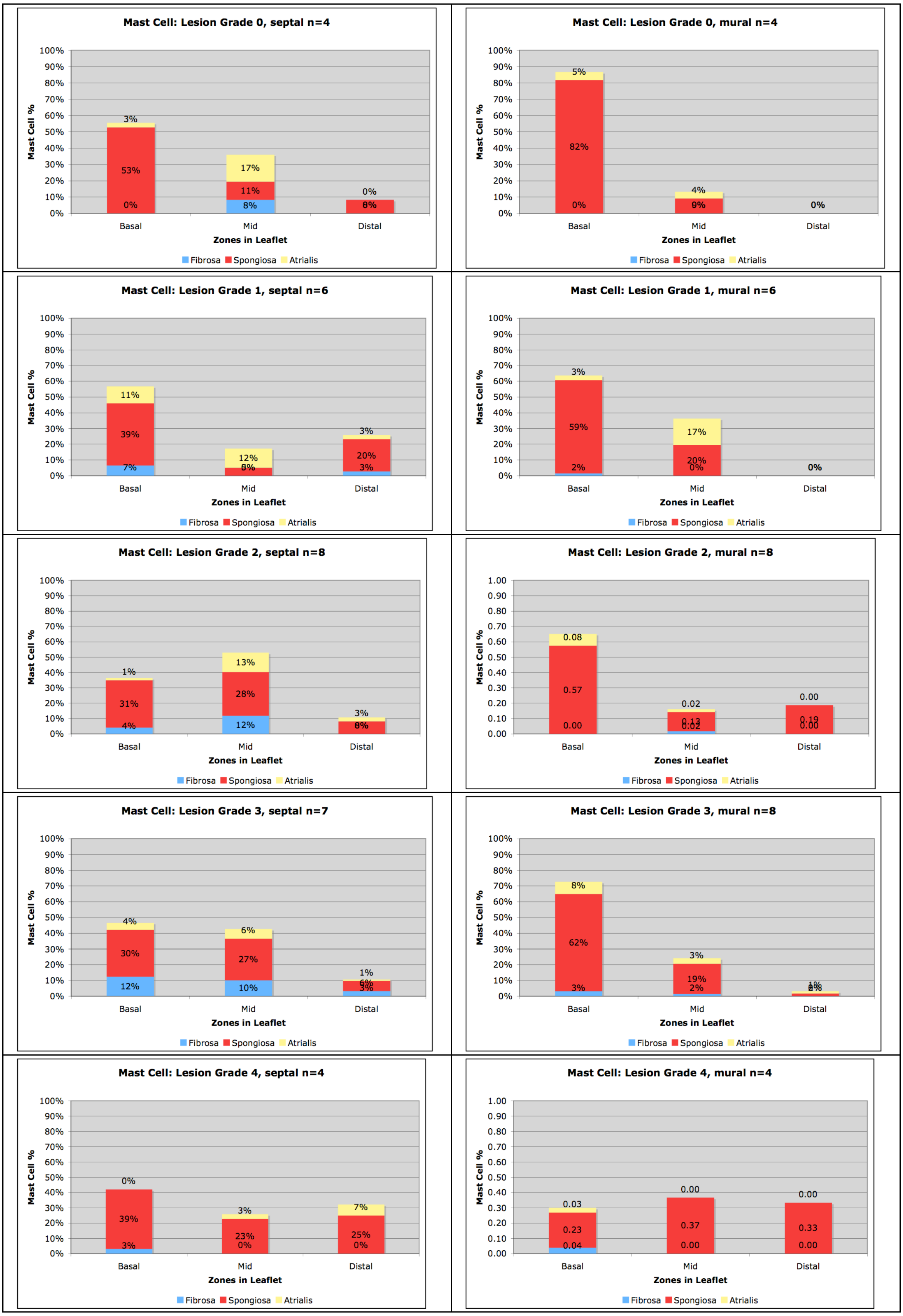

Mast Cell: Lesion Grade 0, septal n=4

Mast Cell: Lesion Grade 0, mural n=4

Mast Cell: Lesion Grade 1, septal n=6

Mast Cell: Lesion Grade 1, mural n=6

Mast Cell: Lesion Grade 2, septal n=8

Mast Cell: Lesion Grade 2, mural n=8

Mast Cell: Lesion Grade 3, septal n=7

Mast Cell: Lesion Grade 3, mural n=8

Mast Cell: Lesion Grade 4, septal n=4

Mast Cell: Lesion Grade 4, mural n=4

Figure 3.39. Distribution of mast cell as a percentage in septal leaflet (left panel) and mural leaflet (right panel). Three different columns represent the three zones and three different colours represent the three layers.

3.3.13 CD34

CD34+ cells were found in only 12 of the 31 mitral valves examined. Even in valves where CD34+ cells were found they were not necessarily in both septal and mural leaflets, and the numbers of positive cells were few. The distribution of CD34+ according to lesion grade is shown in Figure 3.40. In both septal and mural leaflets of normal Grade 0 valve, only 1 out of 5 were CD34+. The majority of the Grade 1 valves were CD34 negative and CD34+ cells were predominately found in Grade 2 and Grade 3 valves. No CD34+ cells were observed in any Grade 4 diseased mitral valves.

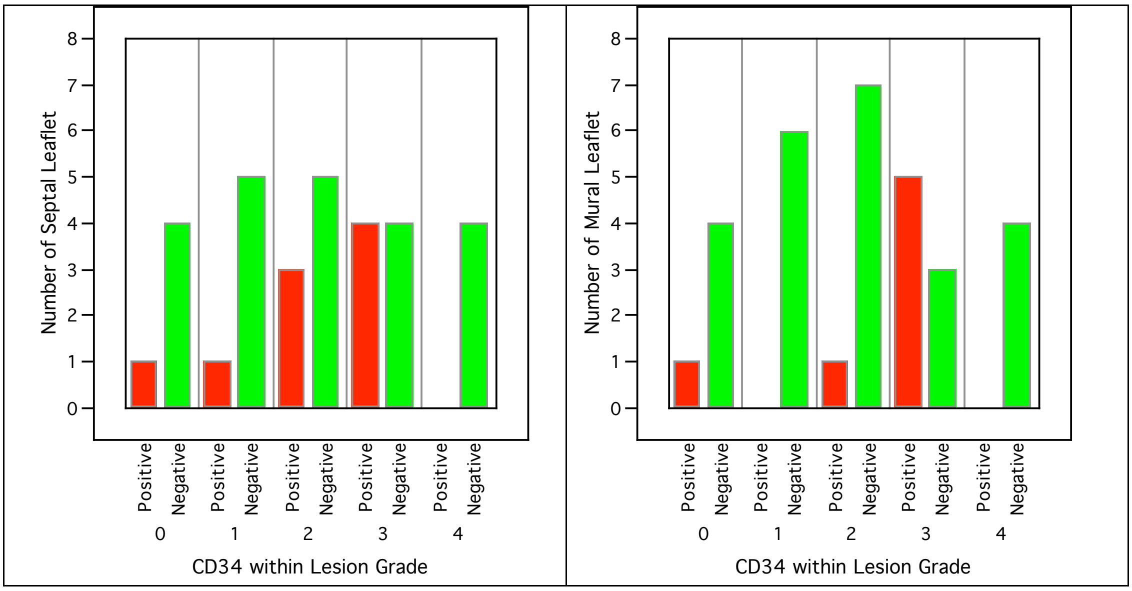

Figure 3.40. Number of septal leaflets (left) and mural leaflets (right) found with and without CD34+ cells.

The localisation of CD34+ cells in the valve was uneven. ANOVA of total CD34+ cells in the valve comparing between grades showed a significant difference (p=0.0240). Grade 3 dogs had the highest number of $CD34^+$ cells and their mean was statistically significantly different to Grade 1, 2 and 4 on the Student's t-test (Figure 3.41).

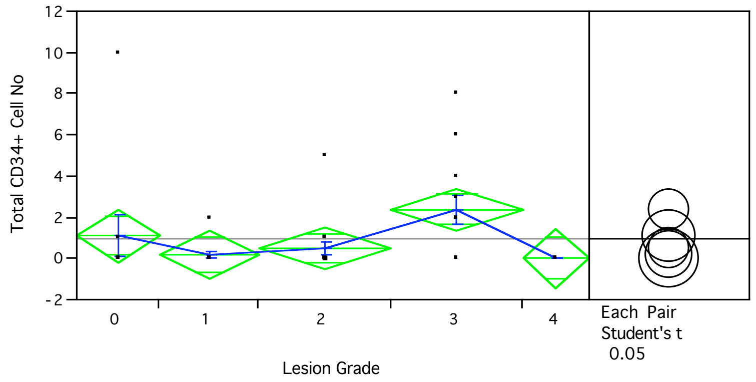

Level			Mean	
3	A		2.3750000	p=0.0240
0	A	B	1.1000000	ChiSq=0.0079
2		B	0.5000000	
1		B	0.1666667	
4		B	0.0000000	

Figure 3.41. Comparison of CD34+ cell number in mitral valve between mitral valve lesion grade. The results from ANOVA, Wilcoxon ranked test, Student's t-test, and LSN are presented.

In the septal leaflets, ANOVA detected no significant difference between grades (p=0.4525) in CD34+ cell numbers, but there was a significant difference in mural leaflets (p=0.0034). On the Student's t-test, the mean of Grade 3 was different to the means for all other grades (Figure 3.42).

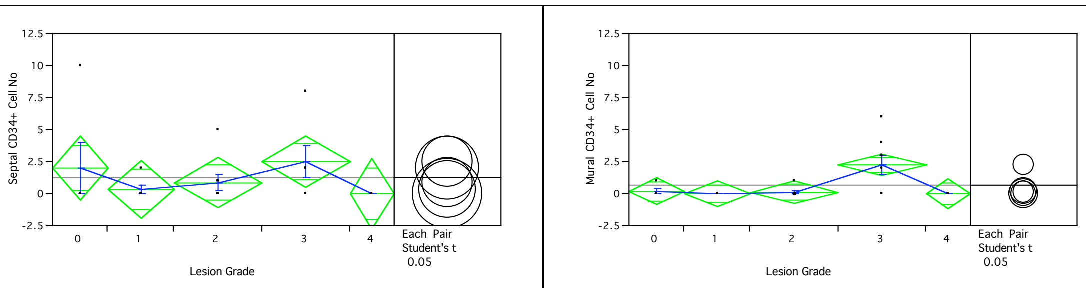

Level		Mean	
3	A	2.5000000	p=0.4525
0	A	2.0000000	ChiSq=0.3952
2	A	0.8750000	LSN=81.51
1	A	0.3333333	
4	A	0.0000000	

Level			Mean	
3	A		2.2500000	p=0.0034
0		B	0.2000000	ChiSq=0.0183
2		B	0.1250000	
1		B	0.0000000	
4		B	0.0000000	

Figure 3.42. Comparison of CD34+ number in septal leaflet (left) and mural leaflet (right) between mitral valve lesion grade. The results from ANOVA, Wilcoxon ranked test, Student's t-test, and LSN are presented.

Although the cells were sparse, the CD34+ cells were mainly found in the spongiosa layer, notably in the mid zone of the leaflets and to a lesser extent in the basal zone. No CD34+ cells were found in the ventricularis layer. Since CD34+ cells were not found in all the valves, normalising cell numbers to valve area could not yield any useful data.

3.3.14 Von Willebrand factor

The immuno-staining for endothelial specific von Willebrand factor proved difficult to assess due to denudation of endothelium. As a result, the semi-quantitative scoring system used for other immunohistochemical studies was not suitable for the complex nature of valve endothelial cell (VEC). The pleomorphic features of VEC along the endothelial lining could be clearly seen in all grades of mitral valves. Morphological features of VEC and endothelial lining consistently observed were listed in Table 3.16.

Table 3.16. Morphological features of VEC and endothelial lining during the disease progression.

Lesion Grade	**Endothelial cell shape**	**Endothelial cell lining**
1	Flat	Attaching
2	Spindle	Detaching
3	Dome	Lifting
4	Round	Separating

It appeared the VECs were showing an injury response involving a series of transformation steps from a flat to spindle then to dome and finally to round shape. However, all the shapes possible for a VEC could be found in one single valve leaflet regardless of the lesion grade of the disease. Local variations between different cell shapes were evident along the endothelium, but there was a greater propensity for round shaped VEC associated with nodules on the atrialis surface of diseased valve. The changes in the endothelial lining were linked to the progression of MMVD. During the advancement of the disease, the endothelium lining detaching from the surface and then lifted, eventually separating from the surface and became free floating after losing the VEC. Two-endothelium damage hotspots were identified, located on either side of the distal zone near the free edge. In the severe cases of MMVD, the endothelial lining at these points were often obliterated and the area of metaplasia could be found underneath. Some of the cells in the dense connective tissue area of metaplasia were found to be immuno-reactive to von Willebrand Factor. Occasionally, papillary projections tissue out growth at the site of endothelium damage was found.

3.4 Discussion

In this study, the cellular profile of the mitral valve in dogs was comprehensively mapped, qualitatively illustrated the changes that occur with MMVD, and semi-quantitatively determine cellular phenotypic changes. Furthermore, this is the first study in which the regional distribution of cell types in the mitral valve leaflet of dogs and how it might relate to disease progression has been examined. To date, studies in dogs and humans with forms of myxomatous degeneration have described cellular changes in localized areas of diseased and have not addressed the issue of spatial organization of this change or change with disease development. Rabkin et al[27] did describe, in a limited fashion, regional distribution of cells in myxomatous valve leaflets of humans, with α-SMA positive cells localized mainly to the base and mid zones of the atrialis layer. The description of the localization of cell types is important in improving understanding of the pathological process of this disease, and was strongly emphasized in this study, as are changes in cell types, density and distribution with disease progression. In addition, this study investigated the roles of certain proteins that have been implicated in matrix remodelling in human mitral valve prolapse, but have not yet been looked into in any animal models.

Initial attempts to quantify the immuno staining with computer-assisted techniques failed, because top range high-resolution slide scanner was not available during the course of this study. The scoring system was developed to assess the immuno staining in a semi-quantitative fashion. The immuno score in a particular zone or layer did not actually reflect the real number of the positive cells, but a relative proportion to the observation area, thus the size variations between samples could be eliminated as a variable in this study. In this way the direction of the phenotypic changes could be accurately measured. Though the scoring system was efficient to assess the immuno staining in most cases, it had limited applications for those antigens where staining was sparse and exclusively associated with blood vessels.

The valvular interstitial cell population is recognized as having phenotypic plasticity[23, 133], in that the cell phenotype can change from a quiescent fibroblast to an activated myofibroblast and eventually to a more smooth muscle like cell phenotype[26, 43, 133, 134]. This cell plasticity seems to be crucial to heart valve development, remodelling and repair and in diseased states, the myofibroblast cell type predominates[27, 134]. Vimentin, an intermediate filament constituent of cells from mesenchymal origin is widely used for the purpose of immunophenotyping interstitial cells[135-137], and it is expressed predominantly in mature cells. In mitral valves of dogs with MMVD, a mixed population of vimentin positive and vimentin negative cells was found, with a gradual reduction in positive cell numbers during the disease progression in all zones and layers. This reduction in vimentin positive cells agrees with previous reports from the human disease[27], but the overall reduction in cell density in myxomatous areas does not. The difficulty in comparing this result with previous reports is knowing the amount of the valve leaflet that was assessed, and either this has not been stated or the amount was small[27, 83]. In the current study, the entire valve length has been assessed for the first time. The nature of MMVD in dogs is that the pathologic change is focal in distribution, and varying grades of pathologic severity of the disease are described[2]. A pathologic grading system is lacking for the human form of the disease, so it is difficult to interpret what level of disease has been described in previous human reports. Nevertheless, the impression in dogs is that cellular changes in visibly pathologic areas of mitral valves are reasonably consistent irrespective of severity, but a variation in change is found across the entire valve length and width. The exact immuno-phenotype of the vimentin negative cells in myxomatous areas was not identified. These cells were also α-SMA negative, suggesting they are not typical activated myofibroblasts seen associated with myxomatous degeneration [27, 138]. They do have an elongated spindle interstitial cell shape that contrasted with the more rounded vimentin negative cells seen in the spongiosa layer of unaffected mitral valves. The overall functional role of vimentin in cells has remained elusive. Vimentin-deficient mouse fibroblasts in culture display a reduced mechanical stiffness, motility, and contractility, but absence of vimentin filament does not impair cellular function needed for growth. Therefore, it was proposed that vimentin deficiency impaired all functions depending upon mechanical stability[139].

The increase in α-SMA positive cells in this study was expected as this has been reported in studies from human patients[27]. α-SMA is a cytoskeletal microfilament and can be used to distinguish smooth muscle cells from fibroblast[140,

[141], but has been mainly used in valve studies to identify activated myofibroblasts since no antibody currently available could definitively distinguish myofibroblast from smooth muscle cells[24]. Consequently, the myofibroblast phenotype was verified by incorporating the results from smooth muscle myosin immuno reactivity[44], as the cells associated with the disease presented an α-SMA positive but myosin negative phenotype. Findings in an electron microscopy study in dogs with MMVD has identified a population of smooth muscle like cells with an increase in these cells in the most severe forms of the disease, but the overall cell numbers are likely to be low[43]. What is interesting about α-SMA positive cells in dogs is the localization to the edge of the valve, with few cells visible in the overtly myxomatous areas. This finding contrasts with reported for human myxomatous degeneration[27]. The consensus is that α-SMA positive cells represent an activated myofibroblast population that are involved in extracellular matrix remodelling, but some disagreement exists as to whether such a phenotypic expression is associated only with disease[24, 26, 27, 92]. It would be reasonable to presume activated myofibroblasts contribute to normal tissue remodelling and also to damage. The data from dogs would suggest a more quiescent vimentin positive fibroblast population predominates in the mitral valve of clinically normal dogs and only in the disease is there an obvious increase in the activated myofibroblast population[44]. This agrees with reports of human disease[26] and animal models[84, 90, 142] of valve damage repair, but it is the distinct localization of the α-SMA positive cells in dogs that is different. However, an ex-vivo study of wound healing in mitral valve has shown an increasing in α-SMA positive cells near the damaged surface[90]. The transition from fibroblast to myofibroblast would appear to be under the control of angiotensin II stimulated transformation growth factor-β (TGF-β) through the MAP kinase-2 pathway[93, 143-145], and in cell culture systems at least, this results in the development of α-SMA with enhanced contractility[84, 146]. Results from a recent study on genomic expression in dogs with MMVD has revealed, among numerous other changes, up regulation of the 5-hydroxytryptamine 2B receptor gene, and the authors speculated that a serotonin-transforming growth factor-β mediated activation of myofibroblasts might be implicated in disease pathogenesis[147]. The serotonin signal could come from platelets adhering to damaged endothelium[148], and endothelial denuding does occur in dogs with MMVD. It can be further speculated that the localization of α-SMA positive

cells to sub-endothelial layers may be in response to such signaling[29, 43]. Indeed, it has long been recognized that in vitro models of valve injury interstitial cells proliferate toward the valve surface, and these cell express α-SMA[84, 142]. Furthermore, in such models, there appears to be a preferential accumulation of α-SMA positive cells on the ventricularis side of the leaflet[142]. The increase in α-SMA positive cells seen in the ventricularis side of the distal zone could be explained by the development of regurgitation during disease progression. In a regurgitating valve, the two leaflets would not coapt properly together and with the distal parts of the leaflets protruding towards the atria, the new contact point between the leaflets might switch from the atrialis side to the ventricularis side. The regurgitation jets exert more force on the ventricular side of the leaflets. The change in distribution of α-SMA positive cells in this study was consistent and related to disease severity, but it was surprising that no increase in α-SMA positive cells were observed in the overtly myxomatous areas. The increase in α-SMA positive cells roughly matched the decrease in vimentin positive cells observed with increased disease severity but not at the same sites. The importance of the initial α-SMA positive cells accumulation adjacent to the atrialis might be to provide additional contractility, as the atrialis surface stretch out more during the opening and closing of the valve. The clustering of cells and their organization close to the valve edge in the distal zone may reflect an attempt to compensate for the reduced mechanical integrity of the valve. Walker et al[92] suggest this augmented contractile myofibroblast response could be a precursor to the alteration in valve matrix seen with myxomatous degeneration, but data from the current dog study and previous electron microscopy data from dogs suggest it might be a later consequence of the disease process[43].

The role of other cell types in the aetiopathogenesis of this disease was considered in this study. The identification of desmin positive chondocyte-like cells was unexpected and the cartilage morphology was also confirmed by the toluidine blue staining. Although their numbers were small in the diseased valves, this might pointed to another route by which valve stromal cells could transform to during the disease progression. Ossification commonly occurs in human aortic valve stenosis but at a low frequency in mitral valves. In the human pathological conditions the myofibroblast in the mitral valve could existed as a combination of vimentin and desmin phenotypes[27]. The adult mesenchymal stromal cells have the potential to differentiate into chondrocytes[149]. The location of ossification corresponded to that seen in human mitral valve studies, namely the ventricular side collagen rich fibrosa layer[150]. The cartilage phenotype seen in myxomatous mitral valves in humans has recently been investigated. Molecular biological studies have shown an up-regulation of low-density lipoprotein receptor related protein 5 (Lrp5) and Sox9, a transcription factor for osteoblast differentiation and it has been hypothesized the osteoblastic differentiation by Lrp5 mediated signalling causes valve thickening[151]. Coincidentally, the VEGF and TGF-β which are implicated in the fibroblast to myofibroblast transformation are also suspected to be involved in fibroblast to osteoblast differentiation[150, 152].

The role of adipocytes in mitral valve has not been discussed in the literature. Presumably the adipocytes were derived from the multi potent mesenchymal stromal cells[149], as the cells were immuno-positive to vimentin. Judging by the location of the adipocytes almost exclusively in the spongiosa layer of the leaflet they could perform an important supporting role by providing resilience to the valve during the dynamic structural change in the cardiac cycle. Although no distinct difference in fat was found between normal and varying grades of diseased, much higher fat content was found in the septal leaflet than the mural leaflet within the same valve. Image analysis study from the previous chapter has revealed the septal leaflet is always longer than the mural and it is probably resonable to assume a higher fat content is related to the mechanical function of the septal leaflet. Adipocytes are soft and compressible in comparison to the rigid neighbouring cardiomyocytes and connective tissue. By wrapping around the cardio myocytes and separating from the connective tissues the fat serves as a cushion to dissipate the mechanical stress generated from the valve opening and the impact of leaflet recoil. In the normal heart, the adipocytes function as an energy storage by providing lipids as fuel to cardiomyocytes for metabolic need[153]. It is possible the adipocytes in mitral valve have a similar energy storage function, judging by their proximaty to the cardiomyocytes in the basal zone of the leaflet. While fat as a risk factor to cardiovascular disease is well established in medicine, what risk, if any, that valve fat has is unknown[154]. Advancement in the understanding of fat cells in cardiovascular system has shown in addition to energy storage they also exert important endocrine control and modulate immune function. Adipocytes express pro-inflammatory products that attract macrophages through the release of adipocytokines. In pathological conditions the pro-atherogenic adipocytokines enhance inflammatory processes and accelerating atherosclerosis[155, 156]. Atherosclerosis in human cardiology has been a major research topic, but the focus is on atherosclerosis in arteries. In a study looking at arteriosclerotic changes in dogs, the intramyocardial arteriosclerosis was found to be more significantly advanced in dogs with MMVD[157]. However, parallel to human medicine, the fat content in dogs is related to the dietary and exercise regimes.

Although a genome expression study has shown the up-regulation of genes for inflammation and immunity in dogs with MMVD[147], There is no concrete evidence exists that MMVD involves an inflammatory process, and this would appear also to be the case in human myxomatous degeneration[158]. Evidence for a possible role of mast cells in the development of MMVD is presented in this study, but the cellular response is small and could be argued to be trivial. The number of mast cells found in mitral valves of humans is also small[150]. However, the cardiac mast cell numbers are known to increase in response to mitral regurgitation in the dog[159]. Mast cells in human heart tissue have previously been found in atrial appendages[160] and calcified valves[150]. Furthermore, since there is an association between mast cells, mast cell chymases, matrix metalloproteinase activity, a role for mast cells in extracellular matrix remodelling of the myocardium is recognized[159, 161-164]. Mast cells can release pro-inflammatory substances, such as tumour necrosis factor-α and prostaglandin D, and the existence of similar mast cell dependent mechanisms in MMVD is worth considering, especially taken into account that the disease is developed during a number of years[165]. The finding of mast cells accumulation in normal and also in diseased valves of variable pathology grades, raises the possibility that local activation of these cell could participate in the disease and valve injury in the dog.

In contrast to the mast cells, no evidence exists of direct involvement of the resident macrophage population in the development of MMVD, at least at the sites where disease develops, and this agrees with findings in human mitral valve disease[158, 166]. The slight increase in the number of macrophage in the spongiosa layer of diseased valves was possibly related to the increased adipocyte numbers. The adipocytokines released by the adipocytes are attractants for macrophages[156].

The damaged endothelium seen with MMVD could facilitate recruitment of macrophages into the valve by providing easy passage for circulating macrophages entering the valve tissue[155]. Once the macrophages entered, they could then become activated and have the potential to take up LDL[158, 167]. Lipid deposition in VIC, proliferation of lamina material and activation of macrophages were induced by hypercholesterolemia in rabbit and hamster[168]. Whether those macrophages subsequently trigger atherosclerosis in mitral valves remain to be proven, but in a co-culture study of macrophages and vascular smooth muscle cells (SMC), the macrophages were found to induce the apoptosis of SMC[169]. This might explain why the macrophages in the valve leaflets were predominantly located in the spongiosa layer towards the base in proximity to the adipocytes, whereas the increase in numbers of myofibroblasts in the diseased valves was found near the two surfaces towards the distal zone.

In a recent report, the predominant cells in both unaffected and affected mitral valves of humans have been identified to be CD34+ fibrocytes. In addition, the expression of α-SMA and CD34 in stromal cells was found to be reciprocal to each other such that most CD34+ cell were α-SMA negative and vice versa. These cells are known to have a functional fibroblast phenotype producing matrix metalloproteinase-9 and collagen I and III. It has therefore been proposed that the CD34+ fibrocytes might play an important role in the aetiopathogenesis of myxomatous mitral valve degeneration[83]. However, using a canine specific antibody, the involvement of CD34+ cells was less obvious in dogs and many samples did not show any immunoreactivity to CD34. Among those that did stain positive for CD34, the numbers found were substantially lower than those reported in human mitral valves. In spite of a slight increase noted in the Grade 3 diseased valves, the disease in dogs does not appear to be associated with changing in numbers of CD34+ cells.

The CD34 antigen is a well recognised marker for multi-potent mesenchymal stem cells[126], but also stains granulated mast cells. Using sequential sections, Veinot et al have found the majority of the CD34+ cells in normal and prolapsed mitral valves were toluidine blue positive but CD117-, indicating they were mast cells. However, a small proportion of cells did exhibit the stem cell marker pattern of tol-/CD34+/ CD117+[165]. This current study is the first to demonstrate the presence of $CD34^+$ cells in both normal and myxomatous canine mitral valves. Comparing with the numbers the of normalized toluidine blue positive mast cells, it is possible that a small number of these cells are valve stem cells and their numbers increased during development of Grade 2 and 3 disease. Their fibroblast-like spindle shaped morphology in the spongiosa layer matched the stem cells morphology seen in human valves. Research on multi potent CD34+ stem cells has created much excitement in the field of regenerative medicine[170], and CD34+ stem cells have shown some promise in the potential treatment of non-valvular heart diseases[105, 171]. The presence of CD34+ stem cells in the canine mitral valve may open new insight into the pathology of this disease and offer new therapeutic options. Whether or not these cells are differentially encountered in varying grades of the disease, and can migrate or differentiate into other cell phenotypes remains to be determined.

The mitral valve ECM is a complex network composed of collage, elastin, proteoglycans and glycosaminoglycans[12, 77]. The matrix secures the cells in space and provides the cells with environmental signals. The interaction between cells and matrix is dynamic and bidirectional. ECM remodelling is mediated by the cells resident in the matrix and MMPs are responsible for breaking down the matrix[39]. MMPs have been suggested to play an important role in myocardial extracellular matrix remodelling in both normal and pathological conditions[172]. Two types of MMPs, the gelatinases (MMP-2 and MMP-9) and the collagenase (MMP-13) were assessed in this study[173].

An altered arrangement of ECM component has been demonstrated in human disease[12, 27, 67, 77]. The expression of MMPs in mitral valves has been the focus in a number of studies, but their exact expression pattern remains to be clarified. This is probably due to the complexity of MMP regulation at various levels, not least their activation from latent forms and their tissue inhibition (TIMPs). Rabkin et al have reported increased expression of MMP-2, MMP-9 and MMP-13 in human myxomatous mitral valves using immunohistochemistry[27]. Soini et al have presented a slightly different view, where they reported MMP-2 was mainly expressed in endocarditis and MMP-9 in inflammed valves, but low levels of expression otherwise[82]. Dreger et al have found no MMP-2 and MMP-9 in any of their normal mitral valves[174]. Togashi et al, using a combination immunohistochemistry and zymographs have demonstrated an increase in both activated MMP-2 and MMP-9 in myxomatous mitral valves[175]. In the only and very recent report from dogs, the

MMP-2 was found to be decreased in diseased mitral valves[176], the authors explained this as a consequence of increased TIMP-1, which has been reported in a separate genomic expression study[147]. However, no visible MMP-2 expression was observed in any of the samples in the current study, irrespective of the grade of disease. These results suggest there is no involvement of MMP-2 in myxomatous valve degeneration[177].

The expression of MMP-9 in the current study was found closely associated with vessel walls and a possible slight increase in MMP-9 staining occurred as the disease progressed. The preferable substrate for MMP-9 is collagen IV which is a constitute of the basement membrane[38]. It could be postulated the endothelial cells lining vessels secrete the MMP-9 and participate in the role of angiogenesis in the diseased valves. Macrophages, often observed near the lumen of the vessels, could also help to raise the MMP-2 level[27], but any other role for MMP-9 in the aetiopathogenesis of MMVD could not be identified.

The MMP-13 (collagenase) cleaves collagen I and collagen III preferentially. The finding of the MMP-13 expression near the damaged endothelium is consistent with in with the TEM morphological study showing endothelial damage. The sub-endothelial space of damaged endothelium is the site of fibroblast migration and transformation from fibroblasts to myofibroblasts. The immediate environment also exhibited a decreased in collagen content. MMP-13 expression by the VICs facilitates the migration of the fibroblasts and participates in matrix remodelling by the newly transformed myofibroblasts in the diseased valves. There is a reasonable amount of evidence to suggest that signalling brought about by endothelial damage and VIC migration towards the damaged endothelium is important in the development of this disease, and the over-expression of MMP-13 would fit this paradigm.

Overall the data presented here are a comprehensive description of the cellular changes in mitral valves of dogs with MMVD, and although changes in cell populations in affected valves have been found, it is the information on temporal and spatial development of these changes that may be most important in the understanding of the disease in both dogs and humans. It is likely that the increase in activated myofibroblast numbers in MMVD is a reaction to the disease process rather than a cause. The variations in the degree of MMP expression in humans with

MMVD, which some patients having no expression of MMP, would support that view.

4 Chapter 4 Proteomics

4.1 Introduction

Despite the high prevalence of MMVD among the adult canine populations, the aetiology and physiochemical features of the disease have not been characterised. Alterations in ECM protein components have been described in human mitral prolapse[12, 67, 77], but very little is known about the abnormalities at the post-translational protein level. Previously, the genome expression pattern of mitral valve from dogs with MMVD was evaluated at transcriptional level[147]. However, the transcriptional profile cannot directly correlate with protein expression due to complex post-transcriptional processing. In order to understand the cellular and molecular mechanisms of this disease, it is paramount to study the gene expression at the protein level. Proteins are responsible for all cellular mechanisms and are functional units within the ECM and their functional activities will be reflected in their proteome. The aim of this study was to compare protein expression profiles of normal and diseased valves and try to identify differentially expressed proteins associated with the diseased valves.

Characterising and identifying of the proteins associated with MMVD could unravel the pathological mechanism at the functional protein level and ultimately provide targets for therapeutic treatments in the future.

In order to investigate alteration in protein expression from dogs with and without MMVD, two strategies were employed: 1D gel SDS-PAGE incorporating liquid chromatography - tandem mass spectrometry (LC-MS/MS) for the qualitative global protein expression profiles, and 2D gel SDS-PAGE combining computer image analysis and matrix-assisted laser desorption / ionisation – time of flight (MALDI-ToF) peptide mass fingerprinting for qualitative and quantitative protein identification.

4.2 Materials and Methods

4.2.1 Protein Extraction

Mitral valve leaflet tissues were collected from normal and affected dogs as described in Chapter 2. The muscle bases of the mitral valve leaflets were trimmed off. The mitral valve tissues were homogenized on dry ice with mortar and pestle. The homogenized tissues were collected, weighed and then transferred to rehydration buffer 8 M urea (Sigma, Dorset, UK), 2% CHAPS (Bio-Rad, Hertfordshire, UK), 0.4% dithiothreitol (DTT, Sigma, Dorset, UK), 0.2% Biolytes 3-10 (Bio-Rad, Hertfordshire, UK). The concentrations (weight to volume ratios) were standardized to 0.20 g tissues per ml of rehydration buffer. To ensure effective solubilization, the homogenized tissues were dissolved in rehydration buffer and gently agitated for 1 h at 21°C, then centrifuged at 12,000 g at 15°C for 15 min. The supernatants were divided into small aliquots and stored in -70°C until required.

4.2.2 1-D SDS-PAGE

Protein samples (150 μl) from three normal (Whitney's type 0)[2] and three severely diseased valves (Whitney's type IV)[2] were mixed with loading buffer and electrophoresed on 10% SDS polyacrylamide separating gels, with a 4% stacking gel on top. Molecular weight standard (SDS-PAGE Broad Range, Bio-Rad, Hertfordshire, UK) were added as size indicators. The gels were run in Bio-Rad Mini PROTEAN cells that contained electrophoresis running buffer 25 mM Tris (Sigma, Dorset, UK); 0.2 M glycine (Fisher, Leicestershire, UK); 0.1% SDS (Fisher, Leicestershire, UK), pH 8.3 at 200 V for about 30 min when the separation distance was 2.5 cm. The separated protein bands were detected with Coomassie Blue R-250 Imperial Protein Stain (Pierce, Northumberland, UK).

4.2.3 2-D SDS-PAGE

Twelve mitral valve protein samples were allocated to three groups according to the severity of the disease as follows: normal healthy n=4; mild (corresponding to Whitney's type I and II) n=4; and severe (correspond to Whitney's[2] type III and IV) n=4. The protein samples (10 μl) were made up to a final volume of 450 μl with rehydration buffer and loaded into separate lanes in the focusing tray. Dry 18 cm immobilized pH gradient strips (Readystrip, pH 3-10, Bio-Rad, Hertfordshire, UK) were first rehydrated in the focusing tray at 50 V for 12 h before the isoelectric focusing step was carried out at 8000 V for 45000 Vhr in a Bio-Rad Protean IEF cell (Bio-Rad, Hertfordshire, UK). After focusing, the strips were equilibrated for 15 min in an equilibration buffer 6 M urea (Sigma, Dorset, UK), 2% SDS (Fisher, Leicestershire, UK), 0.375 M Tris-HCl pH 8.8 (Sigma, Dorset, UK), 20% glycerol (Sigma, Dorset, UK) and 130 mM dithiothreitol (DTT, Sigma, Dorset, UK) to reduce the proteins. A second equilibration step was then performed for 15 min in the same equilibration buffer, but with the DTT replaced by 135 mM iodoacetamide (IAA, Sigma, Dorset, UK) to convert the free cysteine to carboxyamidomethyl cysteine. The strips were placed onto pre-cast 16 × 20 cm 10% SDS polyacylamide gels and sealed with 1% agrose (Ambion, Huntingdon, UK). The second-dimension electrophoresis was carried out on a Bio-Rad Protean-II system that contained electrophoresis running buffer 25 mM Tris (Sigma, Dorset, UK), 0.2 M glycine (Fisher, Leicestershire, UK) and 0.1% SDS (Fisher, Leicestershire, UK) running at 24 mA/gel (16 mA/gel during the initial stacking) for 3 h 50 min[178, 179].

4.2.4 2D Gel Staining

Following 2D SDS-PAGE, analytical gels were stained with a modified silver staining method. The gels were 'fixed' in a fixing solution containing 10% acetic acid (Fisher, Leicestershire, UK) and 40% ethanol (Scientific Laboratory Suppliers, Nottingham, UK) twice for 15 min. This was followed by sensitizing the gels with a solution contained 30% ethanol, 8 mM sodium thiosulphate (Sigma, Dorset, UK) and 0.5 M sodium acetate (Sigma, Dorset, UK) for 30 min. After a brief deionised water wash, the proteins in the gels were allowed to bind with 2.5% silver nitrate (Sigma, Dorset, UK) for 20 min. Excess silver nitrate was rinsed off with deionised water. The gels were then developed in a developing solution 0.24 M sodium carbonate (Fisher, Leicestershire, UK) and 0.04% formaldehyde (Sigma, Dorset, UK) until the desired intensity appeared. The reactions were terminated by the addition of 0.04 M EDTA (Sigma, Dorset, UK) and incubation for 10 min. The gels were finally rinsed in deionised water three times for 5 min.

Gels stained with silver using protocols which include a cross-linking reagent such as formaldehyde proved to be unsuitable for subsequent MALDI-TOF analysis. As a result, higher loading (30 μl) replicating gels running under the same conditions were performed. Gels were stained with Imperial Protein Stain (Pierce, Northumberland, UK) for the detection of abundant proteins. For less abundant proteins, gels were stained with high sensitive mass spec compatible SilverQuest silver staining kit (Invitrogen, Paisley, UK). All staining procedures were carried out according to the manufacturers' recommended instructions. Stained gels were scrutinized and compared on an illumination light box. After spot matching to analytical gels, the protein spots of interest were carefully excised with a clean scalpel blade from the gels. Protein spots derived from SilverQuest stained gels underwent a further de-staining step as recommended by the manufacturer.

4.2.5 Image Analysis

Images of silver stained gels were captured in 16-bit grayscale using a flat bed gel scanner (ImageScanner, Amersham, Buckinghamshire, UK). The spots on the 2-D gel images were detected and analyzed with the Dymension software (Syngene, Cambridge, UK). Background correction was done automatically by the default value. Spot detection and spot matching were checked using default parameters. However, extensive checking with the matched spots was necessary and any mismatches were corrected manually. The detection region of interest (ROI) was carefully defined manually and applied to all analyzing groups uniformly. The spot filtering parameters were adjusted accordingly to show the optimal true spot patterns. Relative spot volumes density were compared between groups using the Student's *t*-test. Whenever a statistically significant value of ($p < 0.05$) was achieved in the comparison, regardless an increase or decrease in spot volumes, the corresponding spots were examined and verified. Significant differences between the two groups in spot density volumes were expressed as fold changes and were also displayed graphically in different colours. The results were presented in a distribution plot using the JMP statistical software (JMP, SAS, NC, USA), where a histogram shows the number of significant protein spot density volumes according to fold changes, and a box and whiskers plot shows the median, two quartiles and the range.

4.2.6 Trypsin Digestion

Each 1-D gel was cut into five horizontal strips of equal thickness (~0.5 cm) before the gel strips were pixilated into approximately the same size as the gel spots excised from the 2-D gel. The gel pieces from 1-D and 2-D gels underwent trypsin digestion. They were washed in 200 mM ammonium bicarbonate (ABC, Sigma, Dorset, UK) in 50% acetonitrile (ACN, Aldrich, Dorset, UK) for 30 min at room temperature three times to remove the SDS. This was followed by incubation in 300 ul 20 mM DTT (Sigma, Dorset, UK), 200 mM ABC in 50% ACN at 32°C for 1 h to reduce the proteins. The DTT was rinsed off with 300 ul 200 mM ABC in 50% ACN, then the gel pieces were incubated in 50 mM IAA (Sigma, Dorset, UK), 200 mM ABC in 50% ACN at room temperature in the dark for 20 min to alkylate sulfhydryl groups of cyteine. The excess IAA was rinsed off with 20mM ABC in 50% ACN, then the gel pieces were spun down at 12,000g for 2 min. The gel pieces were covered in 100% ACN for dehydrate until they turn white. The ACN was removed and the gel pieces were allowed to dry. The gel pieces were then placed in 30 μl of 0.07 μg/μl trypsin (Promega, Southampton, UK) and incubated at 32°C overnight. Peptides from the digested pieces were then run on MALDI-TOF MS and LC-MS/MS mass spectrometers. The trypsin-digested peptides from each strips of 1-D SDS-PAGE were also subjected to MALDI-MS analysis.

4.2.7 MALDI-TOF MS Analysis

0.5 μl tryptic digest was mixed with 0.5 μl a-cyano-4-hydroxy cinnamic acid (CHCA, Sigma, Dorset, UK) matrix on a MALDI target sample plate. The samples were then analyzed on a Voyager DE-STR MALDI-TOF MS (Applied Biosystems) using a mass range between 800 and 3500 Da under 50 laser pulses. The raw data was processed using Data Explorer Software (Applied Biosystems). Processing stages involved baseline correction, noise filter/smooth, deisotoping and calibration against porcine trypsin autolysis peaks formed at 842 and 2211 Da. The processed spectra were converted into a mass list of about 100 masses, searched against the public available SwissProt[180], MSDB and NCBI non-redundant databases using MASCOT (Matrix Science) and Protein Prospector (UCSF). Due to the fact the MSDB and NCBI databases were not curetted and their proteins were not annotated, the search results obtained from these two databases were used as reference. A custom designed database compiled from extracted FTP file of Ensembl canine genome predicted protein sequence (Assembly: CanFam 2.0, May 2006, version 51.2i; Genebuild Dec 2006, last update Sep 2008) was created[181]. MASCOT searches from the genome database were compared with search results obtained from

SwissProt. The MASCOT searching parameters were allowed up to one missed cleavage, while the peptide mass tolerance was ± 100 ppm[182].

The results generated from MASCOT MS searches against mammal database were saved as htm files, only those proteins found to be significant by MASCOT software were carried over for further analysis. The SwissProt Identifier (ID) name, protein name, accession number, theoretical molecular weight, theoretical pI value, Mowse score, number of peptide match and the percent of coverage were recorded. Redundant proteins arising from multi-species comparisons were dealt with on the basis of the unique SwissProt Identifier (ID) name. Should the peptide finger printing identify homology to a protein from more than one species, then the species with the highest significant Mowse score took the precedence. In case the peptide mass fingerprinting identified a homologue from more than one species sharing the same Mowse scores, then the dog (*Canis familiaris*) protein took the precedence if it existed. Otherwise the protein from the species with highest peptide match received priority. Protein isomers and sub-groups were best judged by their peptide matching patterns to the entire protein sequence. Any duplication was discarded.

4.2.8 LC-MS/MS Analysis

The remaining digest solution was then run on a nanoLC-MS system. The nanoLC-MS consisted of a Famos autosampler, Switchos column switching unit and an Ultimate nanoLC (Dionex) and LCQdeca mass spectrometer (ThermoFinnigan). A 60 μl to 80 μl sample of a tryptic digest was loaded onto a PepMap C18 column (3 um particle size, 75 um x 15 cm) at a flow rate of 200 ul/min, monitored at 214 nm. The column was equilibrated with solvent A (aqueous 0.1% (v/v) formic acid, Sigma, Dorset, UK) and eluted with a linear gradient from 10 to 70% solvent B (100% acetonitrile containing 0.09% (v/v) formic acid) over 45 min. The LCQdeca mass spectrometer was fitted with a nanoLC ESI source and interfaced to the MS with a PicoTip (FS-360-20-10-N-20-C12 DOM, New Objective). The HPLC method was controlled by Chromeleon software (Dionex). Data dependent acquisition was controlled by Xcalibur software and database searching was achieved using MASCOT software[182, 183]. The processed spectra were searched against the SwissProt database using MASCOT (Matrix Science). Matched peptide was quoted with its observed mass value (M_r), M_r (expt), M_r (calc), Delta, Miss, Score, Expect, Rank and peptide sequence (data not shown). Further information on each peptide at amino acid level could be scrutinized through hyperlinks. All proteins with at least two significant peptide hits in at least in two samples of the each group were entered into an Excel table. The protein name together with its SwissProt ID, accession number, molecular weight, Mowse score and the number of matched peptide were reported. The location of the protein, whether it is intracellular, extracellular matrix or blood borne were validated.

4.3 Results

4.3.1 1-D SDS-PAGE LS-MS/MS and MALDI-ToF-MS

In both normal and diseased groups, after the proteins were separated in the 1-D SDS-PAGE gels, the Coomassie Blue stained protein gels appeared as gradient smears (Figure 4.1).

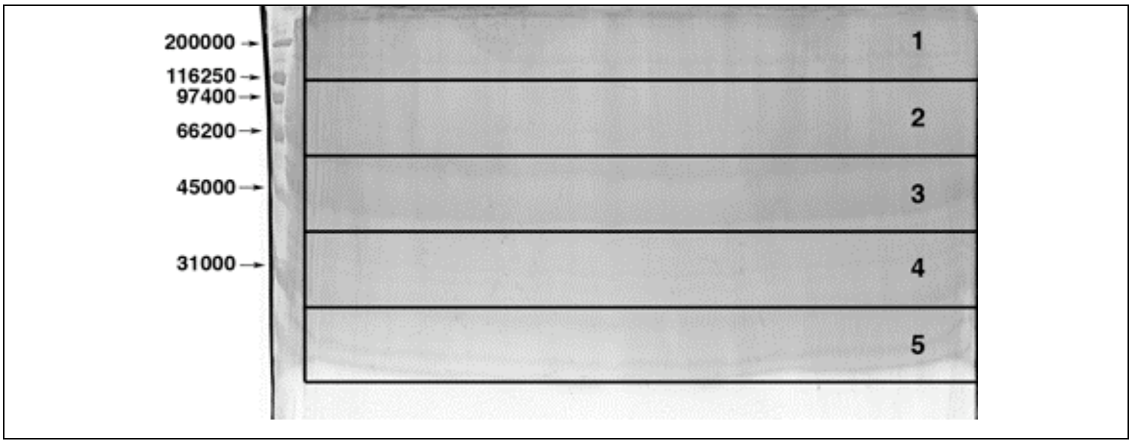

Figure 4.1. Representative 1D SDS-PAGE gel from the normal group which was divided into 5 strips of equal thickness for LC-MS/MS. The molecular weight (MW) markers are indicated on the left.

Each cut out strip from the 1-D gel contained hundreds of trypsin-digested peptides. Mascot MS/MS searches against SwissProt mammal database revealed largely cross-species protein comparisons. The identified protein, together with its M_r, Mowse score and numbers of matched peptide are presented in the list in descending order according to their Mowse scores (Figure 4.2).

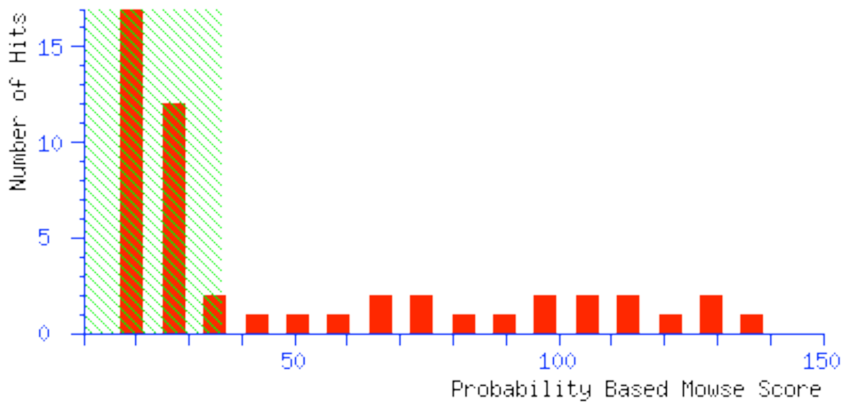

Figure 4.2. Representative Mascot search results showing the probability based Mowse score. The red bars outside the green area indicates the matches were significant.

The peaks generated from MALDI-MS were searched against SwissProt mammalia database via Mascot (Figure 4.3). Proteins found to be significant by MASCOT were compared with the list of proteins identified via LC-MS/MS (Table 4.1).

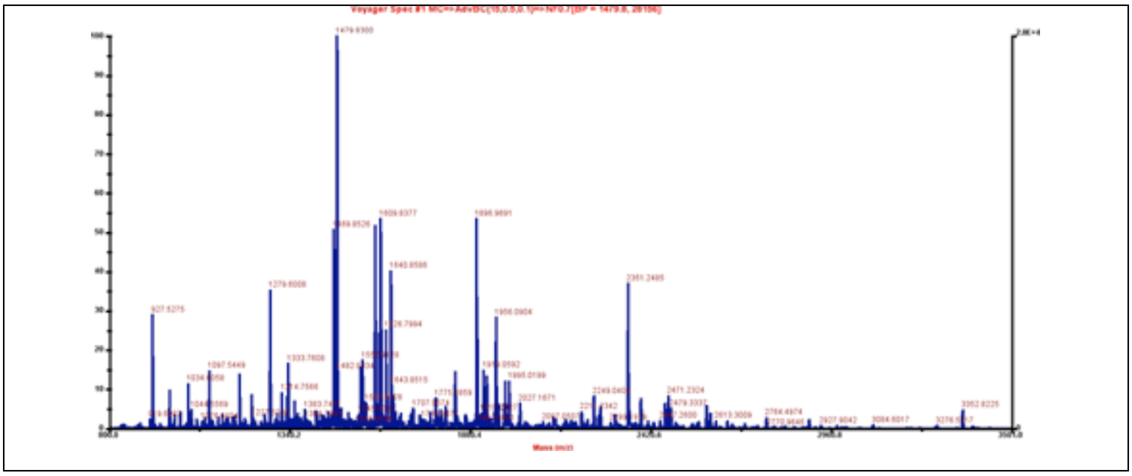

Figure 4.3. Representative of a MALDI-MS peaks chart from a strip of trypsin digested 1D SDS-PAGE.

A total of 64 proteins were detected with significance by MASCOT in both normal and diseased groups. Among them, 40 proteins were found exclusively in the normal groups and 4 proteins were found exclusively in the diseased group; 20 proteins were common in both normal and diseased groups. The name of the protein, SwissProt ID, accession number, mass, Mowse score MS/MS signal and number of matched peptides together with available peptide match and coverage from MALDI-MS are listed in the Table 4.1. One notable finding in the diseased group was the strong signal of serum albumin in almost every single strip of the gel.

Table 4.1. List of significant proteins from 1-D gels identified by LCMS and MALDI-MS through Mascot search against SwissProt.

N D	Location	Protein	SwissPro ID	Acc. No.	Mass	Mowse score	MS/MS Peptides	MALDI Peptide	% Coverage
N	IC	Actin, alpha cardiac (Alpha-cardiac actin)	ACTC_HUMAN	P68032	42334	325	22	14	56
ND	IC	Actin, alpha skeletal muscle (Alpha-actin-1)	ACTS_BOVIN	P68138	42366	113	8	13	50
N	**IC**	Actin, aortic smooth muscle (Alpha-actin-2)	ACTA_BOVIN	P62739	42381	115	7	12	53
ND	IC	Actin, cytoplasmic 1 (Beta-actin)	ACTB_CANFA	O18840	41923	97	8	10	40
ND	IC	Annexin A2 (Annexin II) (Lipocortin II) (Calpactin I heavy chain) (Chromobindin-8) (p36)	ANXA2_BOVIN	P04272	38742	75	3	25	57
ND	BB	Apolipoprotein A-I precursor (Apo-AI) (ApoA-I)	APOA1_CANFA	P02648	30178	283	11	21	66
N	**IC**	ATP synthase beta chain, mitochondrial precursor (EC 3.6.3.14)	ATPB_BOVIN	P00829	56249	86	2	17	45
N	**IC**	ATP synthase gamma chain, mitochondrial precursor (EC 3.6.3.14)	ATPG_BOVIN	P05631	33108	43	1		
ND	EC	Biglycan precursor (Bone/cartilage proteoglycan I) (PG-S1)	PGS1_CANFA	O02678	41939	164	9	19	53
ND	EC	Collagen alpha-1(VI) chain precursor	CO6A1_HUMAN	P12109	109621	73	3	23	23
N	**EC**	Collagen alpha-3(VI) chain precursor	CO6A3_HUMAN	P12111	345051	43	2	58	24
N	**IC**	Creatine kinase M-type (EC 2.7.3.2) (Creatine kinase, M chain) (M-CK)	KCRM_CANFA	P05123	43223	57	3		
N	**IC**	Cysteine and glycine-rich protein 3 (Cysteine-rich protein 3) (CRP3) (LIM domain protein,	CSRP3_HUMAN	P50461	21867	48	1		
ND	EC	Decorin precursor (Bone proteoglycan II) (PG-S2)	PGS2_CANFA	Q29393	40297	147	7	7	27
N	**IC**	Desmin	DESM_CANFA	Q5XFN2	53214	86	2	19	55
D	**IC**	DnaJ homolog subfamily C member 13 (Required for receptor-mediated	DNJCD_HUMAN	O75165	256538	49	3	54	22

		endocytosis 8)							
N	**EC**	Extracellular matrix protein FRAS1 precursor	FRAS1_HUMAN	Q86XX4	453936	38	2		
N	**EC**	Fibromodulin precursor (FM) (Collagen-binding 59 kDa protein) (Keratan sulfate proteoglyca	FMOD_MOUSE	P50608	43427	74	3		
D	**EC**	Fibronectin (FN) (Fragment)	FINC_CANFA	Q28275	58235	40	2		
N	**IC**	Glyceraldehyde-3-phosphate dehydrogenase (EC 1.2.1.12) (GAPDH)	G3P_CANFA	Q28259	35935	248	9	13	50
ND	BB	Haptoglobin [Contains: Haptoglobin alpha chain; Haptoglobin beta chain]	HPT_CANFA	P19006	36890	38	3	23	48
N	**IC**	Heat-shock protein beta-1 (HspB1) (Heat shock 27 kDa protein) (HSP 27)	HSPB1_CANFA	P42929	22925	53	1		
N	**BB**	Hemoglobin alpha subunit (Hemoglobin alpha chain) (Alpha-globin)	HBA_CANFA	P60529	15322	184	7	3	41
N	**BB**	Hemoglobin beta subunit (Hemoglobin beta chain) (Beta-globin)	HBB_CANFA	P60524	16100	278	13	11	82
N	**IC**	Hermansky-Pudlak syndrome 3 protein homolog (Cocoa protein)	HPS3_MOUSE	Q91VB4	115074	46	2		
ND	IC	Histone H2A type 1-B	H2A1B_HUMAN	P04908	14033	109	3		
ND	IC	Histone H2A type 2-A (H2A.2)	H2A2A_HUMAN	Q6FI13	13956	119	5		
N	**IC**	Histone H2B F (H2B 291A)	H2B1_MOUSE	P10853	13797	128	4		
N	**IC**	Histone H2B.f (H2B/f) (H2B.1)	H2BF_HUMAN	P33778	13811	125	7		
ND	BB	Ig heavy chain V region GOM	HV01_CANFA	P01784		46	1		
ND	BB	Ig heavy chain V region MOO	HV02_CANFA	P01785	12809	46	1		
ND	EC	Keratin, type I cytoskeletal 10 (Cytokeratin-10) (CK-10) (Keratin-10) (K10)	K1C10_HUMAN	P13645	59711	62	3	25	39
ND	EC	Keratin, type II cytoskeletal 1 (Cytokeratin-1) (CK-1) (Keratin-1) (K1) (67 kDa cytokerati	K2C1_HUMAN	P04264	66018	92	3	23	41

N	**IC**	Lactotransferrin precursor (EC 3.4.21.-) (Lactoferrin) (Fragment)	TRFL_HORSE	O77811	77938	39	1		
ND	EC	Lumican (Keratan sulfate proteoglycan lumican) (KSPG lumican) (Fragment)	LUM_PIG	Q9TTB4	16676	49	4		
N	**IC**	Malate dehydrogenase, mitochondrial precursor (EC 1.1.1.37)	MDHM_MOUSE	P08249	36030	63	2	11	46
N	**EC**	Microfibril-associated glycoprotein 4 precursor	MFAP4_MOUSE	Q9D1H9	29261	55	3		
ND	EC	Mimecan precursor (Osteoglycin) [Contains: Corneal keratan sulfate proteoglycan 25 core pr	MIME_BOVIN	P19879	34530	259	7		
N	**IC**	Myoglobin	MYG_CANFA	P63113	17195	78	3		
N	**IC**	Myosin heavy chain, cardiac muscle alpha isoform (MyHC-alpha)	MYH6_HUMAN	P13533	224349	128	5	62	36
N	**IC**	Myosin heavy chain, cardiac muscle beta isoform (MyHC-beta)	MYH7_RAT	P02564	223743	122	5	67	35
N	**IC**	Myosin light polypeptide 4 (Myosin light chain 1, atrial isoform)	MYL4_RAT	P17209	21252	196	7	10	55
N	**IC**	Neuropeptide S receptor (G-protein coupled receptor 154)	GP154_RAT	P0C0L6		43	2		
ND	IC	Oxygen-regulated protein 1 (Retinitis pigmentosa RP1 protein) (Retinitis pigmentosa 1 protein)	RP1_HUMAN	P56715	243362	39	5		
ND	EC	Periostin precursor (PN) (Osteoblast-specific factor 2) (OSF-2)	POSTN_HUMAN	Q15063	93883	99	6	16	27
N	**IC**	Peripherin	PERI_HUMAN	P41219	53960	48	2		
N	**IC**	Peroxiredoxin-1 (EC 1.11.1.15) (Thioredoxin peroxidase 2) (Thioredoxin-dependent peroxide	PRDX1_HUMAN	Q06830	22324	48	1		
N	**EC**	Prolargin precursor (Proline-arginine-rich end leucine-rich repeat protein)	PRELP_HUMAN	P51888	44181	51	2		
D	**IC**	Ribosome-binding protein 1 (Ribosome	RRBP1_HUMAN	Q9P2E9	152780	37	1		

		receptor protein) (180 kDa ribosome receptor homolog)							
N	**EC**	Sacsin	SACS_MOUSE	Q9JLC8	441437	46	3	71	20
N	**IC**	Serine/threonine-protein kinase TAO3 (EC 2.7.11.1) (Thousand and one amino acid protein 3)	TAOK3_HUMAN	Q9H2K8	105796	43	1		
N	**BB**	Serotransferrin (Transferrin) (Siderophilin) (Beta-1 metal-binding globulin)	TRFE_PIG	P09571	78971	49	2		
ND	BB	Serum albumin precursor (Allergen Can f 3)	ALBU_CANFA	P49822	70556	682	40	31	54
N	**IC**	Superoxide dismutase [Cu-Zn] (EC 1.15.1.1)	SODC_CALJA	Q8HXP8	15920	38	1		
D	**IC**	Transformation/transcription domain-associated protein (350/400 kDa PCAF-associated factor	TRRAP_HUMAN	Q9Y4A5	441752	51	4	91	27
N	**IC/EC**	Transforming growth factor-beta-induced protein ig-h3 precursor (Beta ig-h3) (Kerato-epith	BGH3_PIG	O11780	75042	49	2		
N	**IC**	Triosephosphate isomerase (EC 5.3.1.1) (TIM) (Triose-phosphate isomerase)	TPIS_CANFA	P54714	26852	85	3		
N	**IC**	Tropomyosin 1 alpha chain (Alpha-tropomyosin)	TPM1_HUMAN	P09493	32746	195	8		
N	**IC**	Tropomyosin beta chain (Tropomyosin 2) (Beta-tropomyosin)	TPM2_HUMAN	P07951	32945	121	4		
N	**IC**	Troponin I, cardiac muscle (Cardiac troponin I)	TNNI3_CANFA	Q8MKD5	23938	41	1		
N	**IC**	Tubulin alpha-ubiquitous chain (Alpha-tubulin ubiquitous) (Tubulin K-alpha-1)	TBAK_HUMAN	P68363	50804	42	2		
N	**IC**	Tubulin beta chain	TBB_PIG	P02554	50285	48	3	15	46
N	**IC**	Ubiquitin	UBIQ_BOVIN	P62990	8560	38	1		
ND	IC	Vimentin	VIME_BOVIN	P48616	53570	528	26	15	39

N: Normal, D: Diseased; IC: Intracellular, EC: Extracellular, BB: Blood Borne.

4.3.2 2-D SDS-PAGE and MALDI-MS

In all groups, the majority of the protein spots resolved on 2-D gel separation were scattered across the entire molecular weight range in between pH 4-8. The consistency in spot resolution and reproducibility between gels within each group was very good. However, when comparing between groups, the two horizontal bands (at approx 55 and 25 kDa), normally associated with IgG heavy and light chains, became more prominent and extended towards the basic end of the gel during the disease progression.

Spot detection and matching functions of the Dymension software identified a total of 1880 protein spots from the normal group, 1705 protein spots from the moderate group and 1687 protein spots from the severe group on their 2-D gel patterns.

When comparing the protein spots between groups based on spot density volume, after manual corrections, expression in 25 protein spots were found different at a significant level ($p<0.05$) from normal group to moderate group, including 10 up-regulated and 15 down-regulation proteins (Figure 4.4).

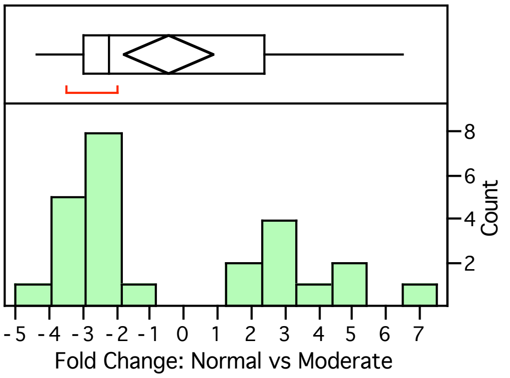

Figure 4.4. The distribution of protein spots found to be significantly different between normal and moderate groups. The plot shows the fold change of protein spots from normal group to moderate group. The x-axis is the fold change in density volume and y-axis is the number of counts (n=25).

Another 25 protein spots were found to be significantly different from moderate to severe group, including 8 up-regulated in diseased and 17 down-regulated proteins in diseased (Figure 4.5).

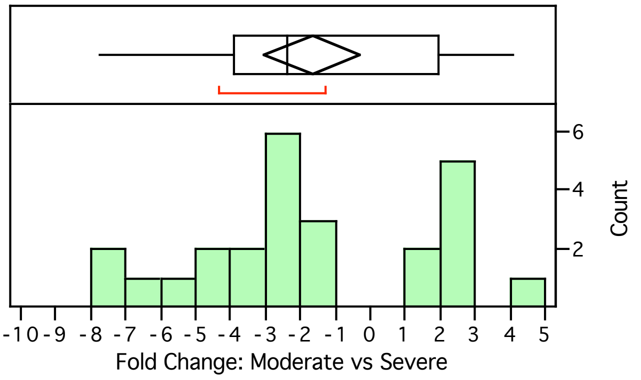

Figure 4.5. The distribution of protein spots found to be significantly different between moderate and severe groups. The plot shows the fold change of protein spots from moderate to severe group. The x-axis is the fold change in density volume and y-axis is the number of counts (n=25).

A significant difference in expression was found in 37 spots between normal and severe groups, including 9 up-regulated in diseased and 28 down-regulated proteins in diseased in comparison with normal (Figure 4.6).

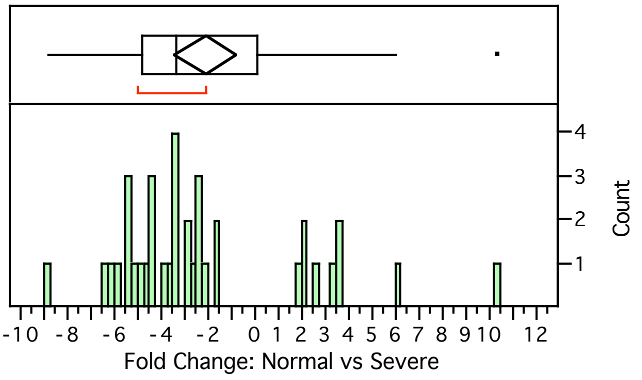

Figure 4.6. The distribution of protein spots found to be significantly different between normal and severe groups. The plot shows the fold change of protein spots from normal to severe group. The x-axis is the fold change in density volume and y-axis is the number of counts (n=37).

Initially, abundant protein spots were chosen for tryptic peptide mapping to generate a reference map for canine mitral valve. Additional protein spots observed to change during the disease states were also selected. Together, the proteins identified via peptide mass fingerprinting were used as landmarks to establish the protein-profiling mapping. A total of 60 protein spots at different positions were analyzed by tryptic peptide mapping. 22 spots that were positively identified and conspicuous on the normal group gels are shown in Figure 4.7.

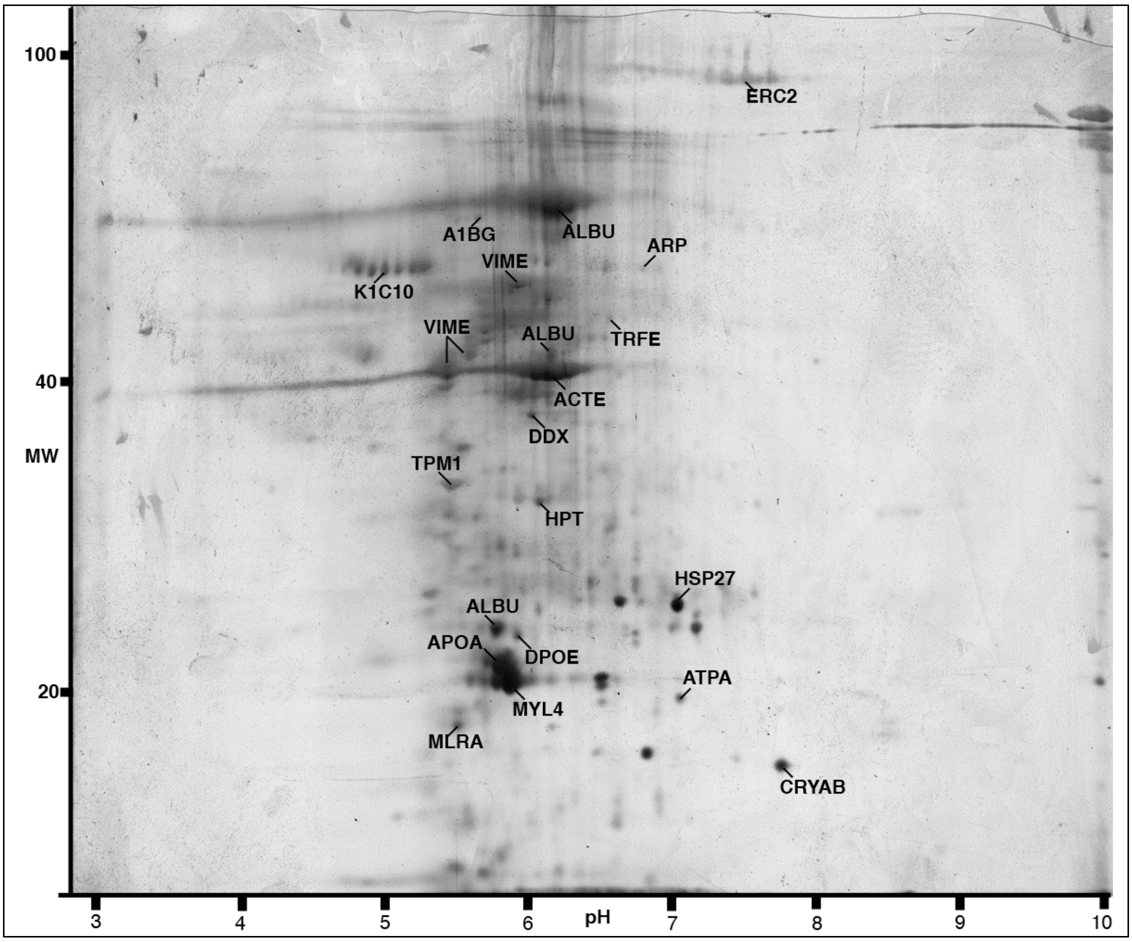

Figure 4.7. Two-dimensional electrophoretic map for normal canine mitral valve. First-dimensional separation with immobilized pH gradient strips (18 cm, pH range: 3–10); second dimension was by SDS-PAGE (10% acrylamide; 16 × 20 cm gels); proteins were visualized by silver staining. Protein spots were identified by tryptic peptide mapping from matched Coomassie blue-stained and SilverQuest stained gels. Identified proteins are labeled in with the corresponding SwissProt gene name: see Table 4.2 below for key.

The spots are indicated by their SwissProt gene names on a representative gel from the normal group (Table 4.2). Only the peptide mass fingerprint search shown the highest homology above the significant level was taken to formulate the Table.

Table 4.2. Protein identification for normal canine mitral valve.

SwissProt	Protein	Acc No.	MW	pI	Score	Peptide match	% Cover
A1BG_CANFA	Alpha 1B glycoprotein	73947277	56264	5.38	126	12	35
ACTE_STRPU	Actin cytoskeleton	P53474	41877	5.32	70	14	51
ALBU_CANFA	Albumin	3319897	67857	5.36	92	12	21
ALBU_CANFA	Albumin	55742764	70556	5.52	296	34	59
ALBU_CANFA	Serum albumin	7397495	70558	5.51	111	13	23
APOA_CANFA	Apolipoprotein A-I	73955106	30163	5.28	162	18	58
APOH_CANFA	Apolipoprotein	54792721	38378	8.51	165	8	30
APR11_BOVIN	Actinrelated protein 3 beta	76675550	47997	5.62	58	7	10
ATPA1_BOVIN	ATP synthase alpha heart isoform	P19483	59797	9,21	87	18	29
DDX3S_HUMAN	DEAD box ATP-dependent RNA helicase	O00571	73597	6.73	71	20	37
ERC2_CANFA	Cytimetrix protein p100	73985242	99732	6.41	48	15	11
HPT_CANFA	Haptoglobin heavy chain	258499	27269	5.80	136	13	40
HSP27_CANFA	Heat shock 27kDa protein	50979116	22925	6.23	65	7	29
K1C10_CANFA	Keratin 1	Q6EIZ0	57847	5.09	48	13	23
MLRI_HUMAN	Myosin regulatory LC-2 atrial	Q01449	19607	4.83	62	11	67
MYL4_CANFA	Myosin light polypeptide 4	57091013	21159	4.97	106	10	54
TBPA_CANFA	Transthyretin Precursor	57089193	15972	6.42	34	3	34
TPM1_CANFA	Tropomyosin 1 alpha	74000377	32748	4.69	222	22	57
TRFE_CANFA	Serotransferrin precursor isoform 4	73990148	80444	7.56	67	13	16
VIME_CANFA	Vimentin isoform 10	73948974	53210	5.01	163	19	43
VIME_CANFA	Vimentin isoform 12	73948978	53622	5.06	305	37	66
VIME_CANFA	Vimentin isoform 7	73948968	49854	5.13	76	11	30

The 2-D separation pattern from the moderate diseased group showed a high degree of similarity to the normal group. The positions of landmark protein spots closely matched the corresponding spots in the normal group. However, one striking feature was the emerging of the two horizontal bands of spots across pH 5.5 to 9.0, one at approximately Mr 50- to 60 kDal; another at approximately Mr 20- to 30 kDal. The intensities of the tropomyosin, apolipoprotein and myosin light chain 4 spots were reduced in comparison with normal. The different isoforms of vimentin spots were no longer apparent (Figure 4.8).

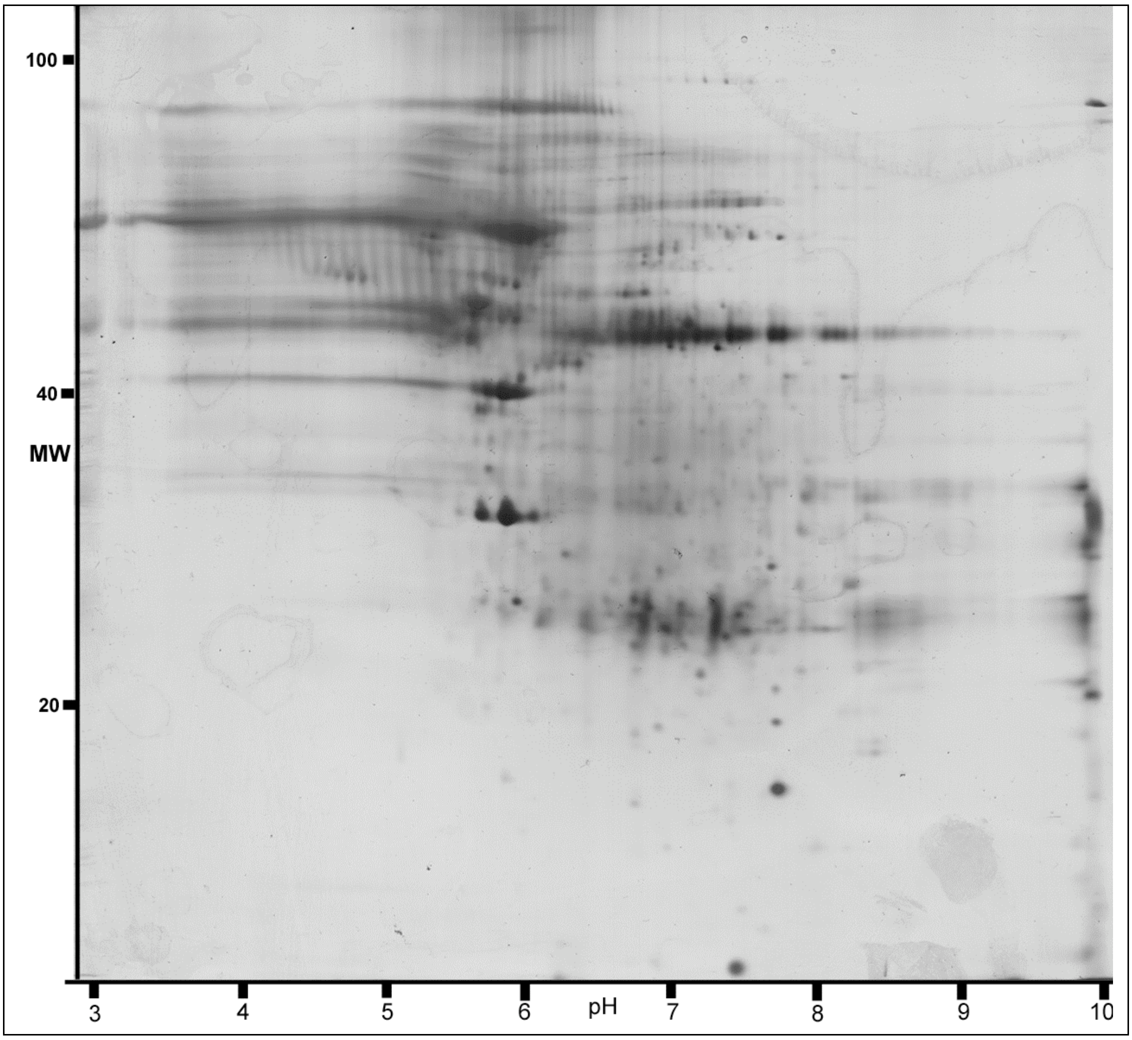

Figure 4.8. Two-dimensional electrophoretic map for moderately diseased mitral valve. First-dimensional separation with immobilized pH gradient strips (18 cm, pH range: 3–10); second dimension was by SDS-PAGE (10% acrylamide; 16 × 20 cm gels); proteins were visualized by silver staining.

The 2-D separation pattern from the severely diseased groups resembled the moderately disease to a certain degree, and was clearly different from the normal. The two horizontal bands of spots clusters became more pronounced. Many landmark protein spots were identifiable. In particular, the spots corresponding to α-actin, albumin and haptoglobin were more intense than the normal and moderately diseased (Figure 4.9). Mascot search against a customer-created database made from Ensembl dog genome predicted peptides, has further identified six significant tentative protein spots (Table 4.3) in the severely diseased valves. These six identified protein spots were not visible in the normal group. Although two of the spots, namely FILIP and FANK were shown weakly stained with silver staining, but they were highly distinguishable on the corresponding SilverQuest stained gels.

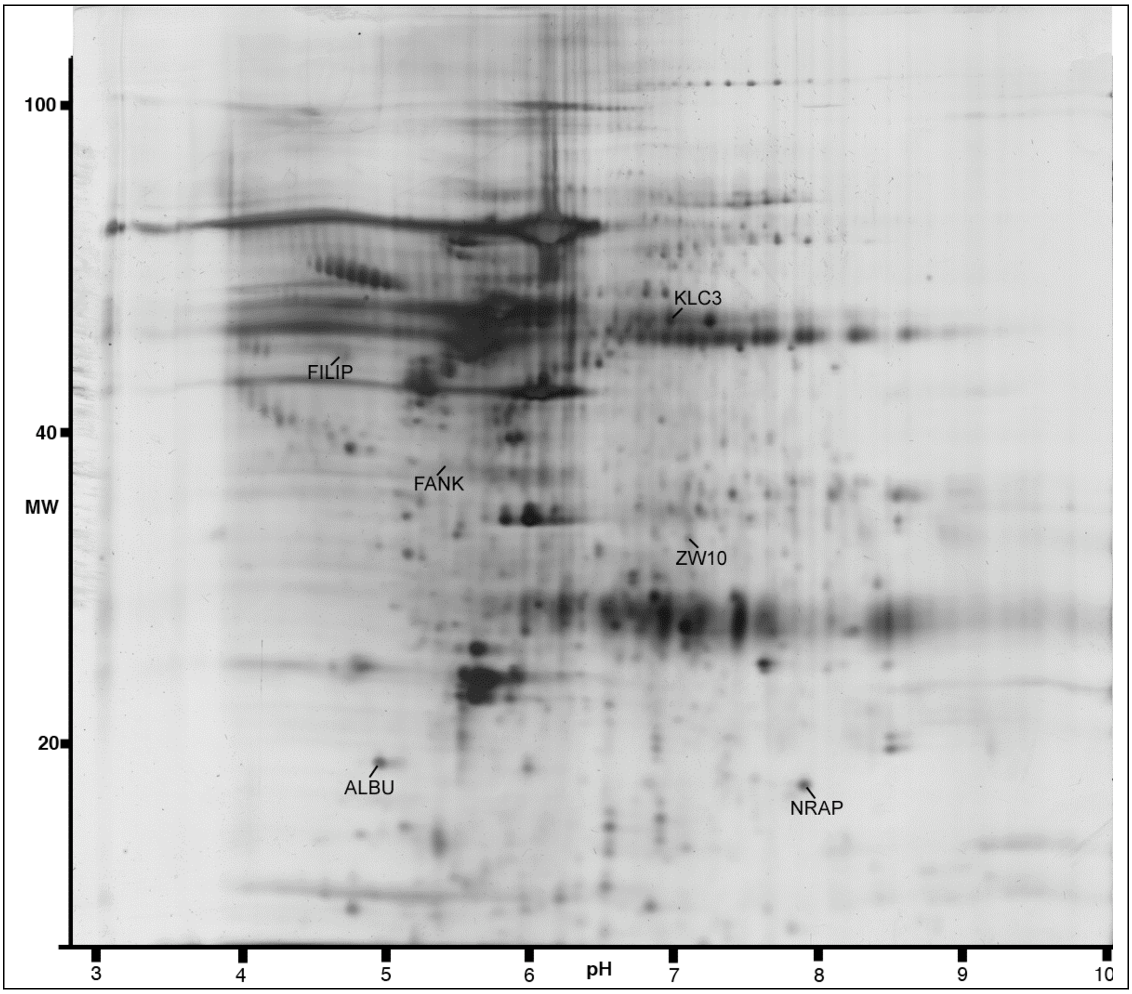

Figure 4.9. Two-dimensional electrophoretic map for severely diseased mitral valve. First-dimensional separation with immobilized pH gradient strips (18 cm, pH range: 3–10); second dimension was by SDS-PAGE (10% acrylamide; 16 × 20 cm gels); proteins were visualized by silver staining. Protein spots were identified by tryptic peptide mapping from matched SilverQuest stained gels. Identified proteins from canine genome sequence are labeled in with the corresponding SwissProt gene name: see Table below for key.

Table 4.3. Proteins identified via searching against Ensembl canine genome predicted protein sequence.

SwissProt	**Protein**	**Score**	**Peptide Match**
ALBU	Albumin	54	11
FANK	Fibronectin Type 3/Ankyrin repeat domain	56	11
FILIP	Filamin A interacting protein	52	23
KLC3	Kinesin light chain 3	62	13
NRAP	Nubulin related anchoring protein	60	27
ZW10	Centromere/kinetochore protein	62	20

Superimposing the warped average gel image from each group using Dymension software, the spots in common or differential could be represented in contrast colours (Figure 4.10). Two areas of interest were further scrutinized. Two protein spots were found differently expressed in the normal, but absent in the severely diseased.

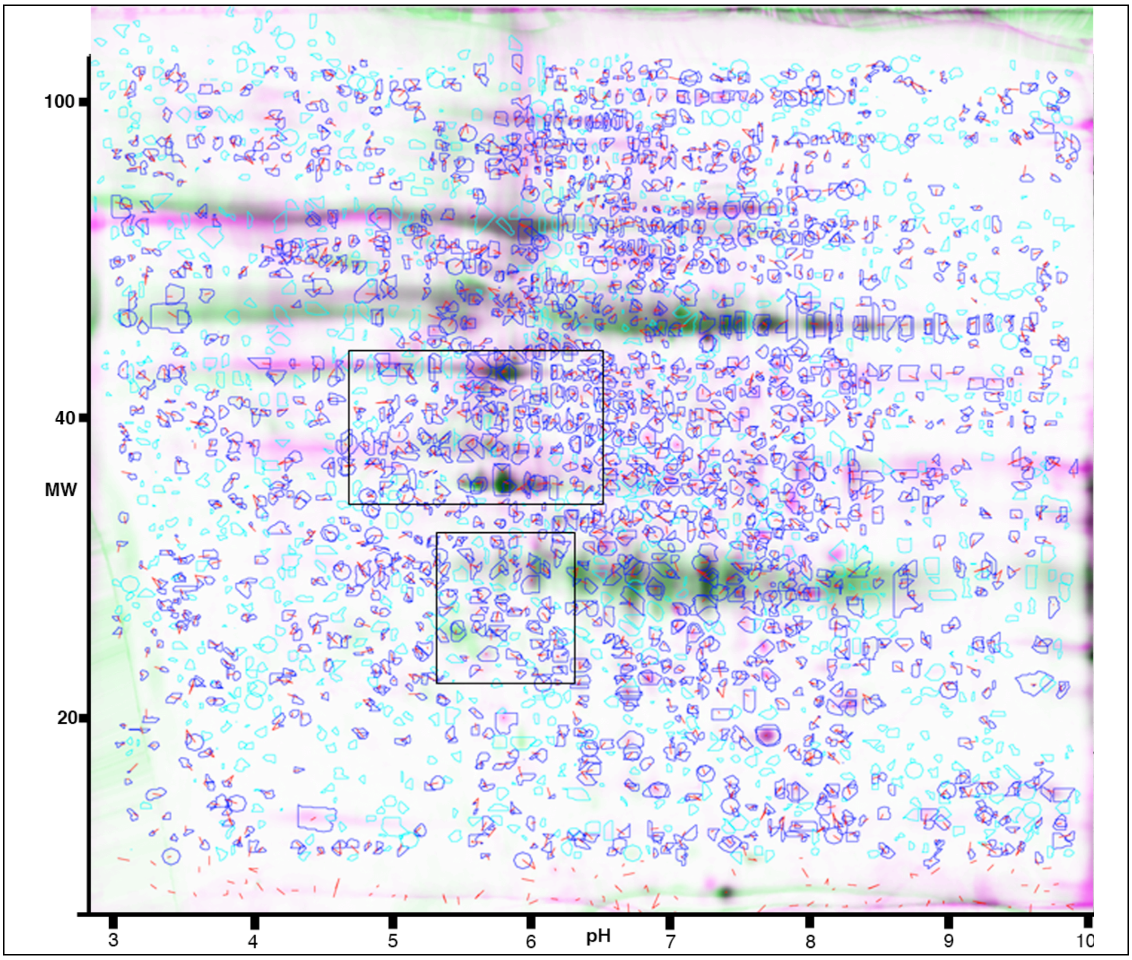

Figure 4.10. Dymension software generated 2-D protein spot pattern from superimposed average spots in normal and severely diseased groups. The green colour shows the spots increased in intensity, the red colour shows the spots in decreased in intensity, and the black represents unchanged spots.

In an area around 40kDa, the spot for tropomyosin was present in the normal valves, but down regulated in the moderately diseased valves, and the spot was not visible in the severely diseased valves (Figure 4.11).

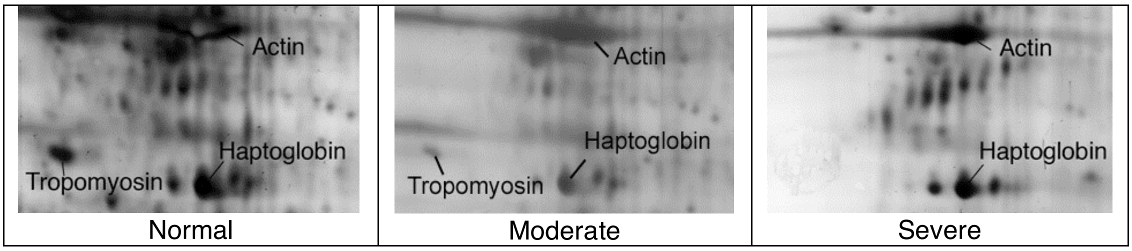

Normal Moderate Severe

Figure 4.11. Panel showing how the tropomysin spot was present in the normal, down regulated in the moderate and absent in the severely diseased.

In another area around 20kDa, the spot for myosin regulatory light chain 2 was detected in the normal valves, but drastically down regulated in the moderately diseased valves and disappeared in the severely diseased valves (Figure 4.12).

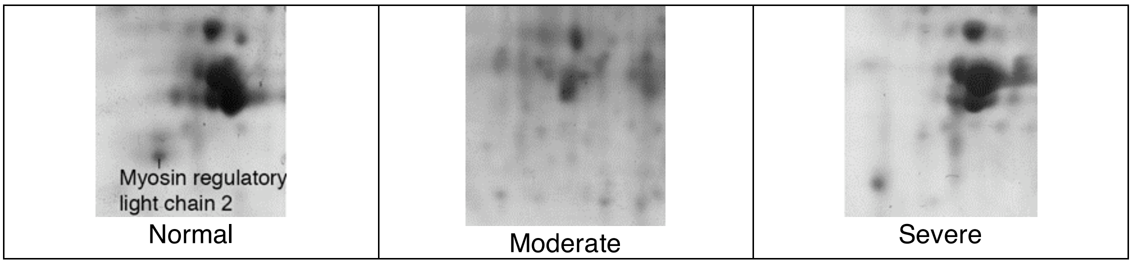

Normal Moderate Severe

Figure 4.12. Panel showing how the myosin regulatory light chain 2 spot was present in the normal, down regulated in the moderate and absent in the severely diseased.

4.4 Discussion

This study was undertaken to establish the protein expression profiling in the canine mitral valve and to identify proteins that are associated with MMVD. Altogether, sixty-four (64) proteins of significance were detected from 1-D gels and twenty-two (22) protein spots were positively identified on 2-D gels. Two contractile regulatory proteins, namely tropomyosin and myosin regulatory light chain-2 were found to be expressed in the normal valves, but down regulated in the moderately diseased valves and absent in the diseased. In additional six tentative proteins were identified only on the 2-D gels of the diseased valves.

Recently, the genome expression patterns of the mitral valve from dogs with MMVD was reported[147]. In that study, the transcriptional activities of 23,851 canine genes were examined by using oligonucleotide microarray; 229 transcripts (0.96%) were found differentially expressed in diseased valves. However, as the levels of mRNA do not necessarily correlate with protein synthesis[184], the functional significance of any gene expression can not be accurately evaluated[185]. The proteomics commodity of gel electrophoresis has the capacity to physically separate the proteins found in the mitral valve[186]. Combining this with mass spectrometry, the total protein complement can be characterized[182]. In this way gene expression at the protein level can best represent the pathophysiological mechanisms involved in MMVD. As there is likely to be a inherited component in this disease, and a polygenic mode of inheritance is suspected in dogs[63], finding only a small proportion of proteins with significant levels of fold difference in expression between each of the two groups (normal and diseased) is highly informative. For example, only 44 proteins from the qualitative 1-D LC-MS/MS and 37 proteins from quantitative 2-D MALDI were found significantly differentially expressed between the normal and severely diseased group. These results have brought into perspective those genes associate with MMVD that could lead to novel targets for drug development.

The global approach of proteomics presents an advantage in viewing the interrelationship between proteins in any particular tissue. However, in the dog its proteins (proteome) are not well characterized at present. Previously attempts to identify the dog heart proteins on 2-D gel using peptide mass fingerprinting have encountered the same problem[187]. Due to lack of entries for dog gene products in the current protein databases, protein identification in the current study relied heavily on the cross-species comparison of protein sequences. To illustrate this problem, only 18 out of the 64 (28%) proteins identified from 1-D gel LC-MS/MS were identified from the dog databases. While peptide mass fingerprinting can be applied successfully for cross-species identification of protein, even a single variation in one amino acid residue could affect that protein function, for example alteration of enzyme cleavage sites and influence the results.

As the quantity of protein loaded onto each of the 2-D gels were adjusted to weight, any variations in spot intensity between gels would suggest that there was proportionally more insoluble material in the gels with apparently lower intensity. However, since the spots were quantified relative to the total spot volume, this provides a correction for loading effects.

The repository type of database such as the Mass Spectrometry Protein Sequence Database (MSDB) are a rich source for peptide mass fingerprinting analysis[188]. However, as a non-curated database, search results often generated high redundancy with little information to the sequence. The National Centre of Biotechnology Information non-redundant (NCBInr) database is a comprehensive but similarly non-curated protein database. Searched results from NCBInr sometimes included protein mixtures, making protein identification difficult. Furthermore, high noise signal for the protein keratin was experienced in the data obtained from NCBInr. Swiss-Prot is a curated protein sequence database with minimal level of redundancy. The protein sequences in Swiss-Prot are manually annotated and constantly reviewed[180]. Nevertheless, interpreting the protein identification and associated annotation was sometimes problematic due to synonym usage and multi-isoforms of the proteins. To achieve the most accurate protein identification work in the current study, the Swiss-Prot database was taken as standard. Only the proteins identified in Swiss-Prot above the significant level were chosen. Having said that, the search results obtained from all three databases did correspond to each other resonably well, with a protein identified in Swiss-Prot likewise being found in MSDB and NCBInr. The main obstacle to protein comparison from different databases was the fact that the identifier, such as the accession number, from one database could not be reconciled with the identifier from another database. Hopefully, with the ongoing expansion of Swiss-Prot the establishment of UniProt and the integration of predicted protein sequences form the dog genome project this problem could be addressed.

In view of the inadequacy of the current databases, a custom designed database compiled from extracted files of ENSEMBL canine genome predicted protein sequence was created and was housed in the Institute of Molecular Biology, University of Edinburgh server. However, searching against this database was not as straightforward as hoped. Results form Mascot peptide mass fingerprint search revealed only the ENSEMBL gene transcript code and the gene name was not revealed. To obtain the gene name required a further search in ENSEMBL. The gene product was confirmed by an additional blast search using gene sequence against the coding sequence. Nonetheless, six protein spots were identified on the 2-D gels of severely diseased group using the dog genome database.

Based on the results of the current study, the protein expression profile found in the canine mitral valve could be categorised into intracellular (n=41), extracellular (n=15) and blood borne (n=8). The following discussion will comment on each of the proteins of most interest in turn. The intracellular class could be sub-divided into proteins responsible for cytoskeleton formation and organisation and contractility, and proteins involved in transcription, cell signalling and energy production. An obstacle to applying proteomics analysis was the heterogeneous cellular composition of the mitral valve. It is likely that the fibroblast, SMC, VEC, macrophage, mast cells and fat cells all contributed to the intracellular protein category[80]. Therefore, proteomics was neither suitable in identifying the cell type in mitral valve tissue that expresses the proteins, nor in confirming the protein of interest is altered in a particular cell type. However, the changes in protein levels may reflect changes in the populations of cells according to the states of the disease.

Similar to human mitral valve prolapse, myxomatous degeneration of the mitral valve in dogs is associated with cell phenotypic alteration, changing from an interstitial cell predominantly of fibroblast to a myofibroblast phenotype[27, 44, 80, 93]. The increase in density and size of the actin spot and diminishing of vimentin isomer spots associated with disease progression were appreciated on 2-D gels. This supports the phenotypic changes represented by the increasing expression of actin in myofibroblast[44, 80]. In may be possible that the over expression of actin filament in diseased valve could provide contractile strength in response to mechanical valve failure[33, 189]. Actins in myofibroblasts also play a role in mediating the formation of focal adhesion in ECM[146]. The actin associated cell–matrix adhesion transmits the intracellular contractile force to the substrate and detects the level of stress in the matrix[190]. External signals are relayed into the cell and the myofibroblast responds by expressing specific ECM components that then participate in tissue modeling[191-193]. α-SMA is transiently expressed in vascular wound healing[194]. When tissue is being reconstituted in normal healing wound, myofibroblasts disappear through an apoptotic process. If this process as in fibrocontractive disease is missing, the persistence of contractile activity leads to continuous matrix remodeling and retraction. The focal adhesion maturation during myofibroblast differentiation requires reciprocal proportions of two actin isomers, cytoplasmic actin and α-SMA[190]. Four different isotypes of actin were identified from 1-D LC/MS. Two of the isotypes, β-1 cytoplasmic and α-actin 1 were common in both normal and diseased valves, whereas the α-cardiac and α-2 aortic were found in the normal valves only. It is not known which isotypes or what proportion of each isotype is optimal for normal mitral valve function, and so how this differential expression might contribute to valve disease cannot be stated. Further studies are required to confirm these apparent changes in actin isotype expression.

The intermediate filament vimentin is one major protein found in all mesenchymal cells. Previous studies using 2D electrophoresis have shown vascular smooth muscle vimentin appears as two isoelectric variants[140]. Vimentin is highly associated with α-actin in vascular tissue[195]. Three vimentin spots were positively identified on 2-D gels in this study, but the significance of this finding cannot be stated. It has been proposed that the vimentin and actin composition reflects a differential pathway and may be related to special function and pathological disorders[140]. Further sequence study could explore the functionality of the different isoforms and their roles in MMVD.

Two different tropomyosin (TPM) isoforms, namely 1-α and β were positively identified in the normal valve, were partially absent from the moderately affected valves, but neither were detected in the severely diseased. On the 2-D gels, the down regulation of TPM 1-α in the disease process was readily visible. TPM is an actin binding protein[196]. It is widely distributed in skeletal muscle, smooth muscle and non-muscle cells. In mammals, there are at least 20 TPM isoforms[197]. The isoforms are generated from four genes through alternative promoter and alternative splice at transcription[198, 199]. The different isoforms exhibit distinct biochemical properties that appear to be performing cell type specific functions[200-202]. The role of TPM is well understood in skeletal muscle, where it regulates actin-myosin interaction during contraction[203]. However, its corresponding role in non-muscle cells remains obscure. Investigation from in-vitro and in-vivo experiments suggested the multiple isoforms of TPM in non-muscle cells are required for actin filament stability, intracellular granule movement, cell shape determination and cytokinesis[204, 205]. As there is clear evidence of a contribution of cellular phenotypic alteration in the pathogenesis of MMVD, it is this role that is worth considering in the context of MMVD. Since the muscle at the base of the leaflet was dissected away, TPM from cardiomyocytes was not expected to contribute to the TPM pool. Previously, the TPM α and β isoforms from dog's carotid have been identified as two separate spots on 2-D gel electrophoresis[196]. The carotid arteries contain predominantly a smooth muscle cell (SMC) type. The high homology of non-muscle TPM to skeletal TPM, and its interaction with actin in the presence of ATP and Ca^{2+} has suggested a role in cell contractility[206]. In the absence of actin, experimental work has shown a direct interaction between tropomyosin and myosin in smooth muscle cells, thus further supporting its role in modifying contractile properties in smooth muscle[207]. The loss of TPM in the latter stages of the disease might compromise the contractile function of VICs and any contribution they might make to mechanical stability.

Myosin light chain 2 (MLC2) is a contractile regulatory protein and was identified in the normal but lacking in the severely diseased. The gene expression of MLC2 along with other contractile related proteins have been discovered in the of interstitial cell cultures from human mitral valve[208]. Mutation of MLC2 is associated with various type of cardiomyopathy[209, 210], and it is believed MLC2 is an integral part of the myofilaments, loss of which abolishes myofilament assembly resulting in embryonic lethality in zebrafish[211]. The phosphorylation of this protein is essential in maintain normal cardiac function during development. Mutation in the phosphorylation site leads to dilation and severe tricuspid valve insufficiency[212]. Of possible more relevance to MMVD are studies on vascular SMCs in wound repair where it has been shown low-density lipoprotein (LDL) infiltrates the vessel wall and becomes aggregated in the ECM proteoglycan. The aggregated LDL induces a differential phenotypic pattern of MLC as revealed in the proteome. Lower levels of phosphorylated MLC are found in LDL exposed SMC[213]. By analogy, it is likely during the MMVD process that damaged endothelium no longer modulates the infiltration of LDL. Increasing in LDL receptor expression has been linked to MMVD[151]. This idea is supported by the evidence of increasing level of LDL carrier apolipoprotein in the disease. Once inside the tissue, the LDL has the potential to alter the MLC2 expression and hinder the MLC2 phosphorylation mechanism.

Heat shock protein 27 (HSP27) was positively identified on 2-D gels in all groups on 2-D gels, although less obvious, in the diseased groups. HSP27 is a stress inducible cytosolic protein that is present in many normal cells. The synthesis of HSP27 is induced by environmental and pathophysiological stresses. Besides its putative role in thermo-resistance, HSP27 may be involved in the survival and recovery of cells when exposed to stressful conditions[214]. HSP27 is also associated with the contractile proteins actin, myosin and TPM in SMCs[215], and it is in this role its differential expression may contribute to MMVD changes. Phosphorylation of HSP27 enhances its association with actin and TPM[216]. The phosphorylated HSP27 modulates the dissociation of caldesmon from TPM leading to contraction in SMC[217]. Interestingly in dogs with mitral regurgitation, survival signaling stimulates the activation of HSP27 to counter apoptosis in the left ventriclar myocardium. β-adrenergic blockade prevents this activation of HSP27[218].

The contribution of changes to the contractile proteins and their modifiers in the MMVD proteome is worth considering. Human floppy mitral valve is a complication of mitral valve prolapse in part caused by myxomatous degeneration, and often leads to severe mitral regurgitation and left ventricular dysfunction[109, 219, 220]. Myxomatous mitral valve leaflets have been shown to be more extensible than normal[13, 221]. Although the mitral valve mechanics in dog was not investigated in the current study, mitral valve mechanical dynamics in other animal models have shown the leaflets experience large anisotropic strains and high strain rate during systole. The leaflet functionally behaves as an anisotropic quasi-elastic material[222, 223], and undergoes deformation until the stretching reaches a plateau. It has been suggested this plateau phase is a result of full stretching of leaflet upon closure[74, 224]. During the MMVD process, the VICs changes from a relatively quiescent synthetic fibroblast phenotype to a more activated contractile myofibroblast phenotype. Each phenotype is characterized by expression of a unique set of structural and contractile proteins, and of different isoforms that correlate to different gene expression patterns[225]. TGF-β is usually considered the inducer of the differentiation of fibroblasts into myofibroblasts[94, 144, 226], while α-SMA is a prominent phenotypic feature of and contributor to the contractile properties of myofibroblasts. TGF-β, furthermore, can induce actin-associated proteins that may contribute to the contractile properties of the myofibroblast, while TPM and HSP27 also can contibute to cellular contractile function[227]. From this we can see a role for each individual differentially expressed protein, and the potential for close interaction between such changes, in MMVD, but their possible contribution to aetiopathogenesis cannot be stated.

Another consideration is the potential role for cysteine and glycine-rich proteins found in the normal valve in mechanical stretch sensing[228]. Proteins involved in contractility (actin, TPM, MLC2 and HSP27) together with proteins responsible for energy production (ATP synthases and creatine kinase) suggest the contractile properties are important in normal functionality of the mitral valve during the cardiac cycle. Contraction of VICs could regulate the return of the mitral valve to its original configuration after systole[229]. In diseased valve, while contractile myofibroblasts participate in mitral valve repair and remodeling, down regulation of the contractile regulatory proteins TPM and MLC2 in diseased valves could hamper the contractile mechanism and further promote MMVD.

In the previous chapter, using an antibody against smooth muscle myosin for immunophenotyping, small number of myosin positive cells was found exclusively associated with vessel walls, regardless the grade of disease. However, in the proteomics study MLC2 was found to be expressed in the normal, but down regulated in the diseased valves. It is necessary to explain this disparity. Myosin is composed of 6 subunits; 2 myosin heavy chains, 2 essential light chains and 2 regulatory light chains (MLC2)[210]. The antibody employed specifically targeted the only smooth muscle myosin heavy chains (SM-1 and SM-2). It did not cross-react with skeletal, cardiac or non-muscle myosin. Myosin heavy chains were identified from LC/MS in the normal valve, but at non-significant low level in the diseased. The exact modes of the contractile apparatus in smooth muscle are not clear. It is known that the smooth muscle does not have troponin, but instead calponin is expressed at the late stage of cell development[230, 231].

A putative filamin A interacting protein (FILIP) was found in the severely diseased mitral valves. The functional characteristic of FILIP has recently been reported. Over expression of FILIP in vitro results in inhibition of cell proliferation and migration[232, 233]. FILIP as its name literately suggests is a filamin (FLN) associated protein. FLN is a cytoplasmic protein cross-linking actin into a 3-D network structure[234]. Unfortunately identification of FLN was not found altered by mass spec, probably due to its large size. FLN has been shown to be in competitive binding with tropomyosin[235, 236] and is required for cell migration[237] and mutation in the gene coding for FLN has been found in human MMVD[238]. Whether or not defective FLN and over expression of FILIP contribute to myxomatous areas in valve leaflets requires further investigation.

VICs manifest their phenotypic plasticity in response to change in environment and functional requirement, acquiring different structure and morphologies[239]. Proteins governing gene transcription such as histones could bring about these changes, and there was reduced expression of histones in the diseased mitral valves. Histones are DNA interacting proteins responsible for the chromatin structure[240]. The fundamental unit of chromatin is nucleosome, an octamer consisting two molecules of each of the histones H2A, H2B, H2 and H4[241]. Histone proteins and their modification play a vital role in the regulation and expression of genes. The cellular level of H2B histone is linked to the control of the cell cycle and the onset of differentiation[242]. Gene activation and repression is regulated by acetylation and deacetylation for the histone modifications[243]. Transformation transcription domain associated protein (TRRAP) is a cofactor for histone acetyltransferase. TRRAP appears to be responsible for the recruitment of the histone acetyltransferase to chromatin during transcription, replication and DNA repair. The ability of TRRAP to coordinate distinct chromatin based processes suggests its deregulation may contribute to disease[244]. The presence of these H2B histone variants in the normal valve but not diseased and TRRAP in the diseased valve but absent in normal might suggest a higher level of control at gene transcription.

Other proteins that were positively identified in the normal valves possess a “protective” function. The serine threonine protein kinase has a role in cell survival and under stress conditions[245]. Peroxiredoxin is involved in redox regulation of the cell, eliminating harmful peroxides generated during metabolism[246]. Superoxide dismutase catalyzes destruction of free radicals superoxide produced within the cell. The superoxide is a common radical which is toxic to cells. Superoxide dismutase acts as an anti-oxidant in the body[247], and is known to protect against endothelial dysfunction in the heart[248]. To what extent changes in these proteins affect the diseased valve is not known, but can be speculated to have adverse effects on cell function.

The functional mechanical dynamics of the mitral valve are intricately linked to the composition of its ECM[249]. Alterations in ECM contents have been found in the equivalent human disease[118]. The histological changes in MMVD are disruption of the fibrosa layer with fragmentation of collagen bundles and an associated myxomatous degeneration[17]. Normal mitral valves contain mainly collagen I, III and V. However, the results from collagen composition analysis in human MMVD are contradictory and so difficult to interpret[77, 78, 115]. X-ray diffraction has shown the loss of collagen in visibly diseased areas of valves, changes in fibril alignment and total tissue volume in canine MMVD[35]. In addition, visibly normal areas, often co-exist in close proximity to diseased areas in diseased valves suggesting the collagen change is patchy even at the histological level. Collagen abnormality is suspected to contribute to the pathological processes that occur in diseased leaflets for two reasons. Firstly, collagen is the major component of the ECM bearing stress and strain[250]. Secondly, mitral valve prolapse is a complication to some inherited connective tissue disorders such as in Marfan syndrome and Ehlers-Danlos syndrome[67, 69, 251]. Despite this, while linkage analysis using human pedigrees for mitral valve prolapse has traced a marker mapping to chromosome 16p[252], and another genotypic linkage study has mapped a locus for mitral valve prolapse on chromosome 13[253], the genes encoding collagen in valve tissue have not been linked to mitral valve prolapse[254] and furthermore, mutations in the collagen I, III and V genes were found not to be responsible for mitral valve prolapse. However, more recent understanding of single nucleotide polymorphism has questioned these findings and a collagen III polymorphism has been linked to mitral valve prolapse in people[255].

Allied with the collagens and the organisation of the ECM are fibronectin and members of the small leucine rich proteoglycans family (SLRP), and these ECM components with collagen binding domains were identified in canine mitral valve proteome. The proteomics work presents a picture of an intricate mitral valve ECM that requires all the components to be present in the correct proportions to permit normal mechanical functions. It is the relationships and interactions between different ECM components that are critical to the structural and functional of the mitral valve. The current understanding of the normal mitral valve is that there is a differential localisation and distribution of the ECM components resulting directly from VIC regional synthetic heterogeneity[34, 111, 124, 239, 256], and this is affected by mitral valve leaflet response to loading and accommodation of physical stresses that occur throughout the cardiac cycle[223, 257, 258].

Fibronectin (FN) is a high molecular weight multi-domain ECM glycoprotein, that binds to cell surface receptor integrins and to other structural elements, including collagen, glycosaminoglycan and fibrin[259]. Expression of FN by both mitral valve interstitial cells and endothelial cells has been demonstrated in vitro[260, 261]. FN also plays a role in wound healing by providing suitable substrate for cell migration[262, 263]. FN is known to interact with TGF-β by regulating matrix assembly of latent TGF-β binding protein[264] and FN along with laminin have a role in sequestering and presenting TGF-β so controlling VIC differentiation to myofibroblasts[144, 265, 266]. FN also has been shown to stimulate VIC adhesion and expression of α-SMA[144, 267]. Once differentiated, myofibroblasts exert tension on the ECM resulting in realignment of FN fibrils[92]. Up regulation of FN in diseased valves could promote VIC migration towards injured sites and induce fibroblast to myofibroblast differentiation. In a previous chapter using immunohistochemistry, FN was found densely accumulated near the surfaces in the distal zone of the leaflet, but decreased in myxomatous areas. This corresponds with observations in morphological studies where increasing α-SMA cell numbers are found near the surfaces in diseased valves, but there is a decrease in cell numbers in the myxomatous areas in the spongiosa layer.

The small leucine rich proteoglycans (SLRP) are a family of proteins that share a common repeats of leucine rich structural motif. They are present in the ECM and linked to members of the GAG family. The four SLRPs (biglycan, decorin, fibromodulin and lumincan) identified in the mitral valve in this study fall into two classes. Class I comprises of biglycan and decorin, and Class II includes fibromodulin and lumincan[268]. Fibromodulin was the only one found to be absent in the diseased valves. SLRPs interact with different types of collagen in ECM[269]. In vitro, they were shown to regulate collagen fibrillogenesis, an important process in development and tissue repair. SLRP deficient mice developed a wide array of connective tissue disorders, resulting primarily from the abnormal collagen fibrillogenesis[270]. Biglycan and decorin can bind to collagen VI in a competitive manner and it was interesting to note collagen VI was absent in the diseased valves. While collagen VI is not a major contributor to the total collagen content of the valve, it is a major component of the microfibril network and interacts with cell membrane integrin[271]. Collagen VI with fibronectin may act as anchor point linking the basement membrane of interstitial cells[272]. It is thought these proteoglycans play a regulatory role in the process of microfibril assembly[273]. Moreover, collagen phagocytosis by fibroblast is regulated by decorin[274]. Over expression of mRNA for decorin has been detected in MMVD and it has been suggested over production of decorin accounts for the defective organization of collagen and contributes to fragility of the diseased tissue[125]. Fibromodulin is known to interact with type I and type II collagen[275]. Fibromodulin and its close relative lumincan bind to the same region on collagen type I fibril, suggesting they have a function related to the regulation of collagen organization[276]. Decorin, biglycan and fibromodulin all interact with TGF-β, with fibromodulin showing the highest affinity. They may regulate TGF-β activities by sequestering TGF-β within the ECM from cells[277]. In this study, absence of the strong TGF-β binding fibromodulin in the diseased valves corresponds with the presumed TGF-β induced transformation of fibroblasts to myofibroblasts. Interestingly, TGF-β was also identified in the normal valve proteome, and it may be that TGF-β is bound to fibromodulin in the ECM reservoir, and so limiting its availability for fibroblast in transformation.

Currently, there is no strong evidence suggesting that MMVD involves an inflammatory process, and this would appear also to be the case in human myxomatous mitral valve degeneration[150, 158]. Genetic polymorphism in the interleukin gene has not been linked to human mitral valve prolapse[278]. However, a recent genomic expression study has shown the up-regulation of genes for inflammation and immunity in dogs with MMVD[147]. In the early part of this thesis, mast cells and macrophages were identified in mitral valve of dogs with and without MMVD[80]. The significance of the increase in IgG found during the disease process is not known. Presumably, the IgG derived from circulating IgG entered through damaged endothelium. Their exact functions require further study.

This proteomics study has revealed the following were associated with MMVD: the intracellular proteins involved in contractile regulatory, gene activation, stress relief, anti-oxidant and motility; down regulation of collagen type VI and fibromodulin, but up-regulation in fibronectin in the ECM; possibly blood borne LDL attached to apolipoprotein. These proteins could potentially yield novel biomarkers reflecting MMVD, establishing detection strategies and response to therapeutic treatments[279]. While this has been a limited discussion on the function of the individual differentially expressed proteins found in this proteomic study, it can be appreciated that reasonable conclusions can be made as to how proteome changes fit into our understanding of this disease. The combined morphological, cellular and proteomic data support a dyscollagenesis explanation for what is happening in diseased valves but does not point directly to causality.

Lastly, this proteomic study reiterates the potential application of the canine disease as a model of disease in human and veterinary medicine. The dog model has been used widely in early research studying cardiovascular physiology pertinent to human. Dog models have made the greatest contribution to medical advance in cardiology, from development of heart lung machine, heart valve repair and heart transplant. In 2004, the dog was the fifth mammal to have its entire genome sequenced and the dog genome places itself closer to humans in the evolutionary tree than mouse or rat[181]. Canine MMVD has a strong resemblance in human mitral valve prolapse. The parallel of these two diseases in different aspects were astonishing and has been discussed in detail[71]. In proteomics, cardiac tissue from human and dog co-migrate on 2-D gels and a higher success rate in being identified compared to the rat and mouse[280]. Overall, the dog would appear to represent a good model for study of the phenotypic to genotypic relationships of this disease in human[281].

5 Chapter 5 Polymerase chain reaction

5.1 Introduction

The reverse transcription polymerase chain reaction (RT-PCR) is a common method used to compare expression of the mRNA of a specific gene. In previous chapters using antibodies against specific phenotypic markers and protein electrophoresis incorporating mass spectrometry, many proteins potentially associated with MMVD were identified. In order to validate the findings of the immunohistochemistry and proteomics generated data, gene expression for eight selected proteins of interest (vimentin, α-SMA, tropomyosin, myosin light polypeptide 4, MMP-13, biglycan and fibrillin) were examined using RT-PCR. To quantify gene expression, a housekeeping gene that is constitutively expressed was used as an internal control. The control gene is essential to correct the sampling difference. By referring to the control gene, the mRNA level is normalized thus making comparisons between groups possible. In this study, three commonly used housekeeping genes glyceraldehyde 3-phosphate dehydrogenase (GAPDH), ribosomal protein L19 (RPL19) and 18S rRNA were analyzed as references for gene expression in canine MMVD. All the primers used in PCR amplification were purpose designed canine specific oligonucleotide primers.

5.2 Materials and Methods

5.2.1 Total RNA isolation

A total of eighteen dog mitral valve tissue samples were allocated to three groups according to the severity of the disease as follows: six healthy normal (Whitney's type 0), six moderately diseased (corresponding to Whitney's type I and II) and six severely diseased (corresponding to Whitney's type III and IV). The mitral valve tissue samples stored in RNAlater (Ambion, Huntington, UK) were removed from -20° C storage and thawed at room temperature. Any excessive muscle and/or chordae tendinae were quickly trimmed off. The remaining tissues were diced into small pieces using a sterile scalpel blade. About 30 mg of the tissue was transferred into a 2.0 ml tube containing 1.4 mm ceramic spheres (Lysing Matrix D, QBioGene, Cambridge, UK). The remaining RNA isolation was carried out using an RNeasy Fibrous Tissue Mini kit (Qiagen, West Sussex, UK) with slight modifications. Complete cell disruption was carried out in 900 μl Buffer RLT on a FastPrep FP120 mixer mill, (Thermo Electron Corporation, Berkshire, UK). The lysate was loaded onto a QIAshredder column (Qiagen, West Sussex, UK) placed in a 2 ml collection tube and centrifuged for 2 min at 10,000 g. The collected homogenate was mixed with 10 μl of proteinase K (Qiagen, West Sussex, UK) solution and placed in 55° C water bath for 10 min to remove the proteins. After the proteinase K digestion, the homogenate was centrifuged for 3 min at 10,000 g. The supernatant was transferred into a new 2 ml microcentrifuge tube and mixed with half volume of ethanol. Up to 700 μl of the sample was loaded into the RNeasy Mini Spin Column in a 2 ml collection tube before centrifuging at 10,000 g for 1 min. The flow through was discarded. This step was repeated for the remaining sample and the flow through were discarded. 350 μl of Buffer RW1 was pipetted into the RNeasy Spin Column and centrifuged at 10,000 g for 1 min to wash the column. 10 μl of DNase 1 stock solution was mixed with 70 μl Buffer RDD (Qiagen, West Sussex, UK), the DNase mixture was pipetted directly onto the RNA sitting on the silica gel in the RNeasy Spin Column. The DNase digestion was incubated at room temperature for 15 min. 350 μl of Buffer RW1 was pipetted into the RNeasy Spin Column, the column was washed by centrifuge at 10,000 g for 1 min. The flow through was discarded. The RNeasy Spin Column was further washed by loading two successions of 500 μl Buffer RPE into the column and centrifuging at 10,000 g for 1 min. To ensure no ethanol was carried over, the RNeasy Spin Column was place in a new 2 ml collection tube and centrifuged at 10,000. Finally, the RNeasy Spin Column was placed in a new 1.5 ml collection tube. 100 μl of RNase-free water was added in the RNeasy Spin Column and centrifuged at 10,000 g for 1 min to elute the RNA.

5.2.2 RNA quantification

RNA was accurately quantified by measuring its absorbance in a NanoDrop ND-1000 UV-Vis spectrophotometer (NanoDrop Techologies, Labtech, East Sussex, UK). The optical density (OD) of RNA was measured at its peak absorbance wavelength of 260 nm. The concentrations of RNA samples were calculated automatically in ng/μl. The RNA samples were stored at -70°C until further reaction.

5.2.3 Reverse transcription of RNA

Approximately 100 ng of RNA samples were reverse transcribed to complementary DNA (cDNA) in a final reaction volume of 20 μl containing 5 mM $MgCl_2$, 1X Reverse Transcription Buffer (10 mM Tris-HCl pH 9.0 at 25°C, 50 mM KCl, 0.1% Triton® X-100), 1 mM each dNTP, 1 unit/μl Recombinant RNasin® Ribonuclease Inhibitor, 15 unit/μl AMV Reverse Transcriptase, and 0.5 μg $Oligo(dT)_{15}$ primers (Reverse Transcription System, Promega, Southampton, UK) and incubated for 1 hr at 42°C and then for 5 min at 99°C to terminate the reaction on a thermo cycler (TechGene, Techne, Staffordshire, UK). The cDNA solutions were then diluted to 50 μl with RNase free water (Promega, Southampton, UK). The cDNA preparations were stored at -20°C.

5.2.4 Primer design

Canine specific oligonucleotide primers to amplify the genes of interest were designed from searching the published genes sequences using Ensembl[282] and/or EntrezGene (National Centre for Biotechnology Information, National Institute of Health). The primer sequences were determined in the coding regions of the target mRNAs with the online Primer3 primer design software[283] with settings (size opt 20; T_m 60°C; PCR product size ranges 250 to 500 base pairs) to maximise specificity and priming efficiency at the optimal temperature, whilst avoiding secondary structure formation and self annealing. The primer sequences were screened against other known sequences to eliminate unwanted cross reactivity via BLAST (National Centre for Biotechnology Information). The oligonucleotide primers syntheses were performed by Operon Biotechnologies (Cologne, Germany). The oligonucleotide primers were first reconstituted to 100 μM according to the manufacturer's instructions before being diluted to 2 μM in DNase-free water. The oligonucleotide primers were stored in -20°C until used.

Oligonucleotide primers for polymerase chain reactions

Gene	**Accession number**	**Primer sequence**		**Product size (bp)**
RPL19	403682 EntrezGene	Left Right	CCTCCAGTGTCCTCCGCTGT GCGGGCCTCCTTGGTCTTAG	479
18S rRNA	DQ287955 EntrezGene	Left Right	TTTGGTCGCTCGCTCCTCTC GGTAGGCACGGCCACTACCA	273
GAPDH	403755 EntrezGene	Left Right	AATGGGGTGATGCTGGTGCT TACATTGGGGGTGGGGACAC	464
Vimentin (VIME)	607206 EntrezGene	Left Right	ACAAGGTGCGCTTCCTGGAG TTGGCAGCCACGCTTTCATA	490
Smooth Muscle α-Actin (ACT)	477587 EntrezGene	Left Right	CTGCTACGTGGCCCTGGACT CGGCCTCGTCGTACTCCTGT	449
Tropomyosin (TPM)	478332 EntrezGene	Left Right	AGGCGGAGGCCGATAAGAAG CAGCCTCCTCCAGCTTCTGC	279
Myosin light polypeptide 4 (MYL-4)	480490 EntrezGene	Left Right	ACCGGACACCGACTGGAGAG AGGCACCCTGGACGAGTCTG	426
MMP-13	403763 EntrezGene	Left Right	TCAGTGGCTGACAGGCTTCG AGGAGTGGCCGAACTCATGG	496
Biglycan (PGS)	403905 EntrezGene	Left Right	CACCTGCGGGTTGTTCAGTG CAGGGTCTCGGGGAGGTCTT	486
Fibronectin (FN)	481269 EntrezGene	Left Right	CCAGCAAATGGCCAGAATCC GGGGACGAGGGACCACTTCT	307
Fibrillin (FBN)	478293 EntrezGene	Left Right	GGACAGCTCAGCGGGATTGT GCCCCCATCACAGATTCCAG	318

5.2.5 Polymerase chain reaction (PCR)

PCR amplifications were carried out in 50 μl volumes containing 5 μl of cDNA template, 0.4 μM of each of left and right primers, 1.25 U Taq polymerase (Roche, East Sussex, UK), 0.2 mM of each deoxyribonuceotide triphosphates (dNTPs) in 1X PCR reaction buffer composed of 10 mM Tris-Hcl and 1.5 mM Mg_2Cl_2 (Roche, East Sussex, UK). The PCR conditions were chosen to maximize the reaction rate. The PCR reaction conditions consisted of the initial denaturing at 94°C for 2 min, then in cycles of denaturing at 94°C for 40 sec, primer annealing at 60°C for 40 sec and elongation at 72°C for 2 min, before a final elongation at 72°C for 7 min; at the end of the reactions the temperature was brought down to 10°C (GeneAmp PCR System 2400, Perkin Elmer, Buckinghamshire, UK). Negative controls without cDNA templates were included in every reaction.

5.2.6 PCR analysis by electrophoresis

10 μl of each PCR reaction product was mixed with 2 μl of the gel loading dye and eletrophoresed through a 1.2% w/v agarose gel (Invitrogen, Paisley, UK) in Tris-acetate-EDTA (TAE) buffer containing 0.5 μg ethidium bromide (Sigma, Dorset, UK) running for 45 min at 100 V using a Horizon 11-14 Gel Electrophoresis System (Whatman, Kent, UK). 1kb DNA ladder was included in each gel for molecular size indication. The eletrophoresed gels were placed in the imaging chamber of a Kodak Digital Image Station 440CF (Kodak, Rochester, NY, USA). The gels were exposed under ultra-violet light at 580 nm for 3 cycles of 20 s, the images were captured using the Kodak 1D 3.6 software (Kodak, Rochester, NY, USA).

5.2.7 Semi-quantitative PCR by densitometry

The optimal numbers of PCR cycles for each primer set were estimated empirically, by running the PCR for varying cycle numbers and plotting the results to determine cycle number corresponding to the linear amplification phase. This rendered comparison of amplified DNA between samples possible. All images were analyzed with ImageJ (National Institute of Health, USA) to determine integrated pixel density as a measure of the amount of PCR amplification product formed.

5.2.8 Statistical analysis

The statistical method used is similar to the statistical method described in Chapter 2. The densitometric data are expressed as means ± standard error of the means. Inferential statistical analysis involved one-way analysis of variance ANOVA testing, a *p*-value less than 0.05 was considered as being statistically significant. Means comparisons between groups were subjected to each pair student's t-test. Due to the number of samples in this study, the non-parametric Wilcoxon ranked score was applied to validate the significance level and Chi^2 were reported along side the *p*-value. In the case that ANOVA of group means yielded no statistical difference, that is when $p>0.05$, then the least significant number of power were calculated. Statistical analysis was performed using JMP software (JMP version 5.0.1, SAS, NC, USA).

5.3 Results

5.3.1 RNA quantification

RNA quantification has shown five samples, three in the normal group, one in each of the moderately diseased and severely diseased groups had very low total RNA concentration below 10 ng/μl. Due to their low RNA concentrations, they were excluded for further analysis.

5.3.2 Glyceraldehyde 3-phosphate dehydrogenase (GAPDH)

The gene expression level for the housekeeping gene GAPDH was inconsistent between samples. The RT-PCR amplification produced a segment of GAPDH that is 464 bp in length. The variable expression of GAPDH was obvious by visual inspection. One of the samples in the severely diseased group had no visible band on the gel (Figure 5.1). Triplicates of RT-PCR amplifications for GAPDH yielded identical results proving the GAPDH expression was indeed variable between samples. This inconsistency in mRNA expression renders GAPDH unsuitable to be use as a reference gene. No further analysis was justifiable.

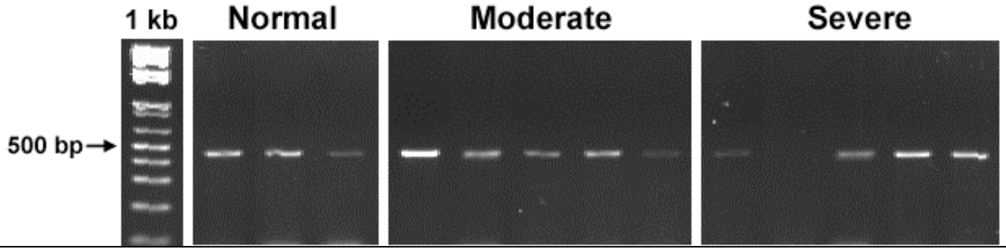

Figure 5.1. The gel electrophoresis picture shows the RT-PCR products for the housekeeping gene GAPDH (464 bp) after 29 cycles. The variable expression of GAPDH between samples was visible; one sample in the severe group has virtually no visible mRNA.

5.3.3 Ribosomal protein L19

The RT-PCR for the housekeeping gene RPL19 produced a fragment 479 bp in length. The level of RPL19 expression was much more consistent across all samples than GAPDH (Figure 5.2).

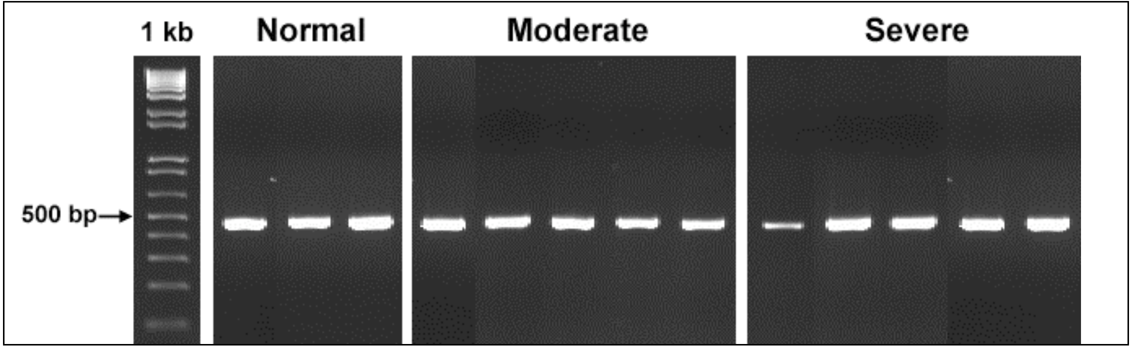

Figure 5.2. The gel electrophoresis picture shows the RT-PCR products for the housekeeping gene RPL19 (479 bp) after 32 cycles. The bands on the gel show a consistent RPL19 expression across all samples.

Semi-quantitative analyses using densitometry showed the expressions of RPL19 in all three groups were closely matched. Although the expression in the normal group was slightly higher, there was no significant difference (p=0.6998) in ANOVA and the t-test found no difference in group comparisons (Figure 5.3).

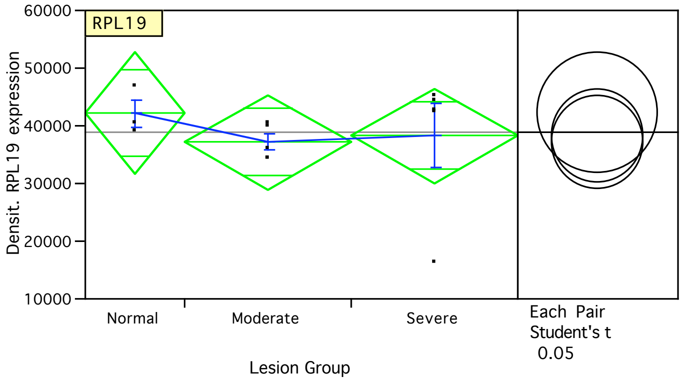

frGroup		Mean	
Normal	A	42208.333	p=0.6998
Severe	A	38298.800	ChiSq=0.1635
Moderate	A	37148.600	LSN=108.30

Figure 5.3. Densitometric analysis of the RPL19 gene expression. The results from ANOVA, t-test, Wilcoxon ranked test and LSN are presented.

5.3.4 18S ribosomal RNA

The RT-PCR for the housekeeping gene 18S rRNA produced a fragment of 273 bp in length (Figure 5.4). The amplified 18S rRNA products appeared as distinct bands uniformly aligned on the gel after 22 cycles. That was fewer amplification cycles than were required for GAPDH (29 cycles) and RPL19 (32 cycles). Therefore, the 18S rRNA expression level was much higher compared to GAPDH and RPL19.

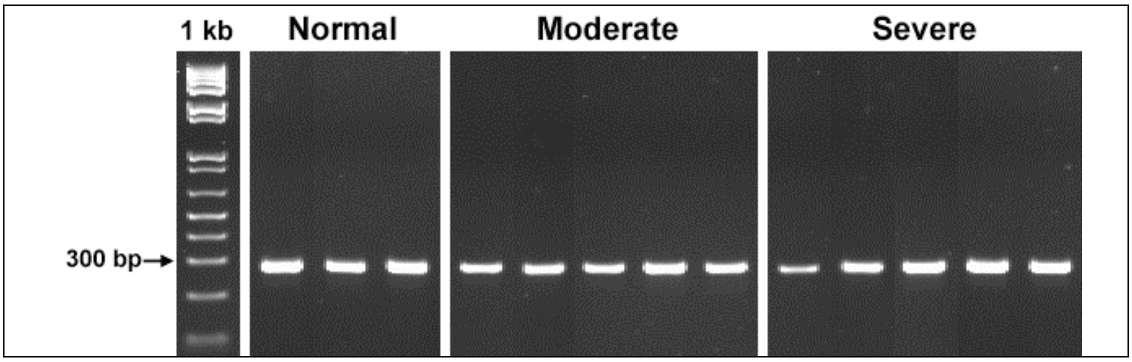

Figure 5.4. The gel electrophoresis picture shows the RT-PCR products for the housekeeping gene 18S rRNA (273 bp) after 22 cycles. The bands on the gel show a consistent 18S rRNA expression across all samples.

The densitometric analysis of 18S rRNA expression has shown the mRNA concentrations were evenly matched in all groups, as indicated by the high p-value (0.8867) and larger LSN (322.91) (Figure 5.5). The constant transcription of 18S rRNA in canine mitral valve with or without MMVD has made 18S rRNA a suitable reference gene. Therefore, the expression levels of other genes were normalized against 18S rRNA transcription level.

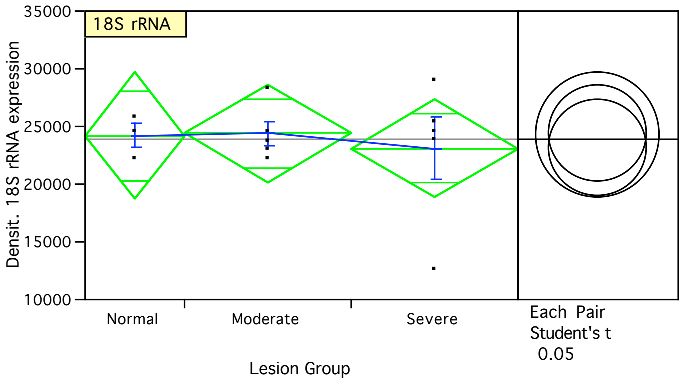

Group		Mean
Moderate	A	24384.600
Normal	A	24188.333
Severe	A	23122.600

p=0.8867
ChiSq=0.8881
LSN=322.91

Figure 5.5. Densitometric analysis of the 18S rRNA gene expression. The results from ANOVA, t-test, Wilcoxon ranked test and LSN are presented.

5.3.5 Vimentin

The RT-PCR for vimentin produced a fragment of 490 bp. Variations in band intensities between samples were recognized (Figure 5.6).

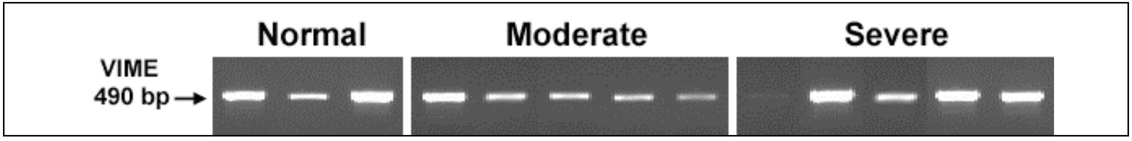

Figure 5.6. The gel electrophoresis picture shows the RT-PCR products for the vimentin gene (490 bp) after 28 cycles.

Analysis of the normalized densitometry values, normalised against 18S rRNA showed the vimentin expression was slightly higher in the normal group, followed by the severely diseased group, and the moderately diseased group had the lowest expression level. However, no significant difference was achieved using ANOVA (p=0.3949) and no difference was found in between group comparison using the t-test (Figure 5.7).

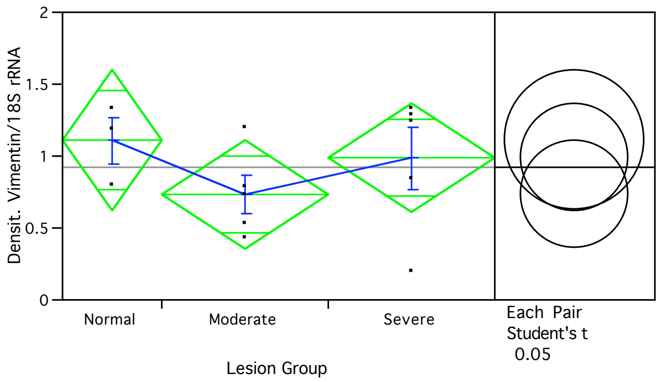

Group		Mean	
Normal	A	1.1078917	p=0.3949
Severe	A	0.9843864	ChiSq=0.2055
Moderate	A	0.7378030	LSN=41.29

Figure 5.7. Densitometric analysis of the normalized vimentin gene expression. The results from ANOVA, t-test, Wilcoxon ranked test and LSN are presented.

5.3.6 Smooth muscle α-actin (α-SMA)

The RT-PCR for (α-SMA) produced a 449 bp fragment in all samples (Figure 5.8).

Figure 5.8. The gel electrophoresis picture shows the RT-PCR products for the α-SMA gene (449 bp) after 28 cycles.

Analysis of the normalized densitometry showed the α-SMA expression level in the normal group was the highest, followed by the severely diseased group whereas the moderately diseased group showed the lowest level of expression. The sample distribution in the moderately diseased groups covered a wide range. Both ANOVA and t-test found no significant differences (Figure 5.9).

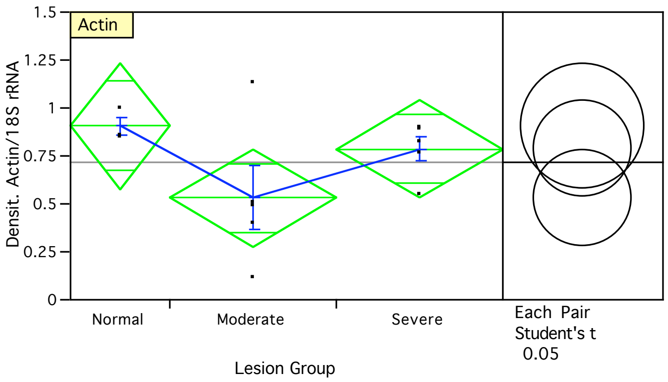

Group		Mean	p=0.1486
Normal	A	0.90588275	ChiSq=0.1723
Severe	A	0.78651207	LSN=20.09
Moderate	A	0.53171198	

Figure 5.9. Densitometric analysis of the normalized smooth muscle α-actin gene expression. The results from ANOVA, t-test, Wilcoxon ranked test and LSN are presented.

5.3.7 Tropomyosin (TPM)

RT-PCR for TPM amplified a 279 bp fragment. Weaker bands were visible on the gel from the moderately diseased groups (Figure 5.10).

Figure 5.10. The gel electrophoresis picture shows the RT-PCR products for the tropomyosin gene (279 bp) after 30 cycles.

Analysis of the normalized densitometry values revealed the expression level of TMP in severely diseased group was the highest followed by the normal group. The moderately diseased group had the lowest expression level. No difference was found in the ANOVA or on the t-test (Figure 5.11).

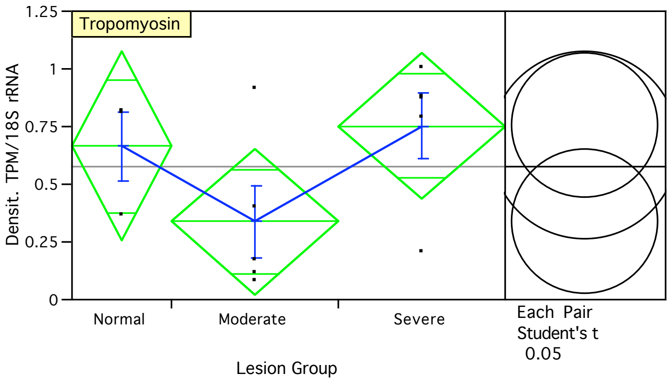

Group		Mean	p=0.1503
Severe	A	0.75284532	ChiSq=0.2304
Normal	A	0.66555601	LSN=20.22
Moderate	A	0.33785257	

Figure 5.11. Densitometric analysis of the normalized tropomyosin gene expression. The results from ANOVA, t-test, Wilcoxon ranked test and LSN are presented.

5.3.8 Myosin light polypeptide 4 (MYL-4)

RT-PCR for MYL-4 produced a 426 bp fragment. The intensity of PCR product bands was considerably weaker in the moderately diseased group (Figure 5.12).

Figure 5.12. The gel electrophoresis picture shows the RT-PCR products for the myosin light polypeptide 4 gene (426 bp) after 28 cycles.

Analysis of normalized densitometry values has showed the MYL-4 expression was highest in the severely disease group, followed by the normal group and was lowest in the moderately disease groups. Although the p=0.0829 from ANOVA is quite low, it did not reach a significant different level. Between group comparisons using the t-test has found the severely diseased group was significantly different to moderately diseased (Figure 5.13).

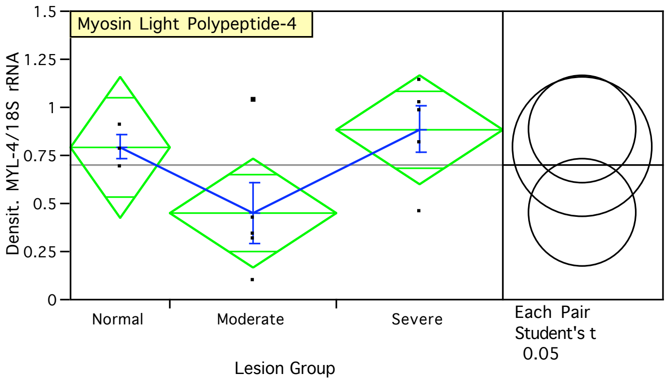

Group			Mean
Severe	A		0.88630832
Normal	A	B	0.79435731
Moderate		B	0.44635097

p=0.0829
ChiSq=0.1256
LSN=15.49

Figure 5.13. Densitometric analysis of the normalized myosin light polypeptide-4 gene expression. The results from ANOVA, t-test, Wilcoxon ranked test and LSN are presented.

5.3.9 Biglycan

RT-PCR for biglycan produced a fragment of 486 bp in length. Variation in band intensities between samples was evident. The bands in the moderately diseased group appeared faint (Figure 5.14).

Figure 5.14. The gel electrophoresis picture shows the RT-PCR products for the biglycan gene (486 bp) after 31 cycles.

Analysis of normalized densitometry showed the biglycan expression level in the normal groups was slightly higher than the severely diseased. The expression level in the moderately diseased was at the lowest. No significant difference was found in ANOVA or t-test (Figure 5.15).

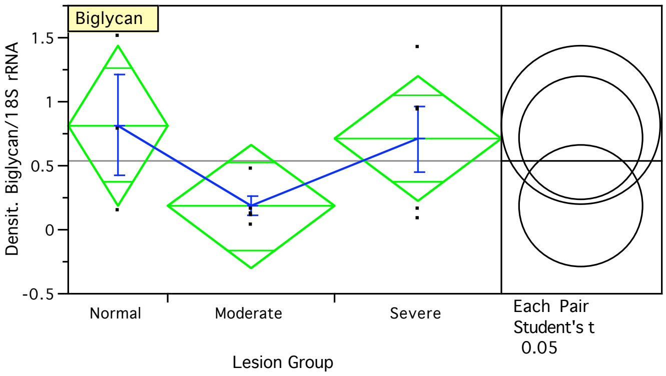

Group		Mean	p=0.1664
Normal	A	0.81687501	ChiSq=0.1599
Severe	A	0.71221670	LSN=21.35
Moderate	A	0.18317035	

Figure 5.15. Densitometric analysis of the normalized biglycan gene expression. The results from ANOVA, t-test, Wilcoxon ranked test and LSN are presented.

5.3.10 Fibronectin (FN)

RT-PCR for FN produced a 307 bp fragment. Variation in band intensity between samples was evident (Figure 5.16).

Figure 5.16. The gel electrophoresis picture shows the RT-PCR products for the fibronectin gene (307 bp) after 28 cycles.

Analysis of normalized densitometry has shown the highest FN expression level was in the severely diseased, then the normal and lastly the moderately diseased group. However, no significant difference was achieved in ANOVA or t-test (Figure 5.17).

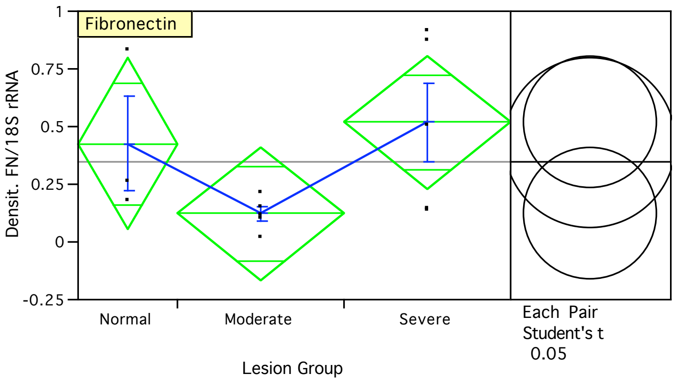

Group		Mean
Severe	A	0.51737561
Normal	A	0.42558810
Moderate	A	0.12303393

p=0.1353
ChiSq=0.0895
LSN=19.17

Figure 5.17. Densitometric analysis of the normalized fibronectin gene expression. The results from ANOVA, t-test, Wilcoxon ranked test and LSN are presented.

5.3.11 Fibrillin (FBN)

RT-PCR for FBN produced a fragment of 318 bp in length. The variation in band intensity between samples was recognized (Figure 5.18).

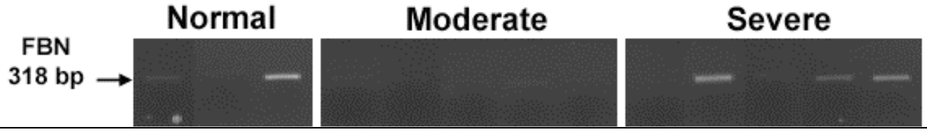

Figure 5.18. The gel electrophoresis picture shows the RT-PCR products for the fibrillin gene (318 bp) after 31 cycles.

Analysis of densitometry has shown the highest FBN expression in the normal, markedly attenuated in the severely diseased and low in the moderately diseased. No significant difference was achieved in ANOVA or t-test (Figure 5.19).

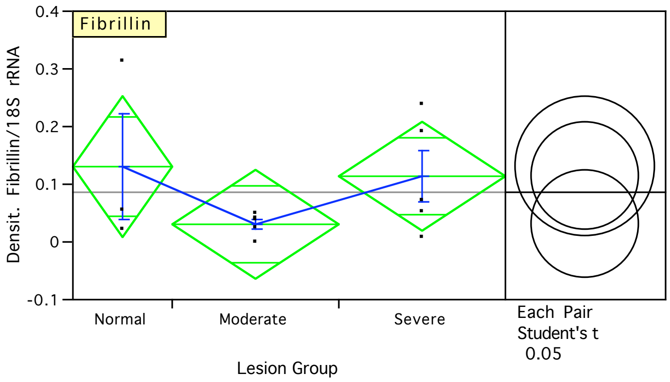

Level		Mean	p=0.2985
Normal	A	0.13061076	ChiSq=0.2128
Severe	A	0.11327050	LSN=31.67
Moderate	A	0.03102787	

Figure 5.19. Densitometric analysis of the normalized fibrillin gene expression. The results from ANOVA, t-test, Wilcoxon ranked test and LSN are presented.

5.3.12 MMP-13

The RT-PCR for MMP-13 produced no visible bands on the gel after 35 cycles. After 55 cycles of amplification, two bands appeared in the normal group, and apart from the expected 496 bp fragment there was an additional band measured about 310 bp. The moderately disease group did not produce the expected 496 bp fragment, but produced a 310 bp fragment instead. Neither the 496 bp nor 310 bp fragment were found in the severely diseased, instead it produced a unique fragment about 600 bp in length (Figure 5.20). The erratic expression patterns and low expression level in MMP-13 rendered further analysis impossible.

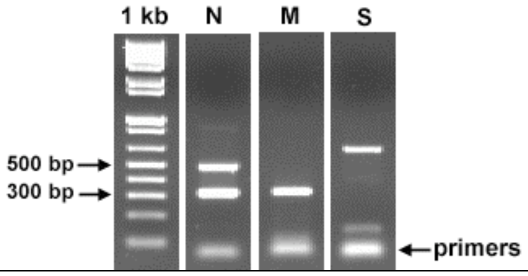

Figure 5.20. The gel electrophoresis picture shows the RT-PCR products for the MMP-13 gene after 55 cycles. The normal (N) contains two bands, the expected 496 bp and a fragment about 310 bp. The moderately diseased lacking the expected 496 bp fragment but produced a 310 bp fragment instead. The severely disease also lacking the expected 496 bp fragment but it produced a unique fragment about 600 bp.

5.4 Discussion

Previous Chapters in this thesis have identified changes in the expression of proteins potentially associated with MMVD. This study forms a pilot experiment to investigate the gene expression in the mitral valve associated with MMVD. The primary aim of this study is to validate the results obtained from the immunophenotypic and proteomics studies. Eight genes of interest were selected and their expression levels in normal and diseased states were investigated. Confirmation of expression of these genes also served another purpose since positive gene expression would clear concern arising due to technical limitations in other studies. For example, in the immunohistochemistry study, almost all the commercially available antibodies were designed against human or mouse antigens and seldom against the canine antigens. Although before purchase, a specific antibody was scrutinized, evaluated and compared to other similar antibodies on the market, often the decision on one antibody, but not another was based on personal opinion rather than experience, even in the case where an antibody had been reported to cross react with dogs. The financial implications of checking multiple antibodies against the same antigen also had to be considered. In the proteomics study, many proteins were identified through cross species comparison of protein sequences. Using canine specific oligonucleotides primers to amplify transcriptional mRNAs in this study the expression of a particular protein in the dog could be ascertained.

Unfortunately, five samples with low levels of RNA concentrations had to be excluded in this study. Losing these samples, especially three in the normal group has affected the statistical powers in the samples groups. It is known that the temperature and time-course after tissue removal are factors influencing RNA degradation[284, 285]. It is possible the time-course between the tissue collection and tissue preservation in RNA stabilization reagent was not tolerated in these samples, so the RNA had degraded.

Since a suitable reference gene for the canine mitral valve system was not known, the first task was to find a suitable endogenous reference gene as control[286, 287]. A variable expressed gene would end up with misleading results[288]. Previous study had shown the β-actin cannot be used as a control gene in ovine VICs[289]. Three common housekeeping genes GAPDH, RPL-19 and 18S rRNA were evaluated for expression in normal, moderately diseased and severely diseased states. It could be shown that the 18S rRNA gene expression appeared almost constant throughout all stages of MMVD. The expression of RPL-19 was reasonably consistent. In contrast, the expression of GAPDH was too variable and deemed unsuitable to be considered as a reference gene for canine MMVD work. It is known that the RNA for 18S rRNA is more tolerant to degradation than the RNA for GAPDH[290], and this may explain the difference found.

The gene expression for vimentin, α-SMA, TPM, MYL-4, biglycan, FN, FBN MMP-13 were demonstrated in canine mitral valve using RT-PCR. Their functions and possible roles related to MMVD were discussed in previous Chapters. Unfortunately, ANOVA analyses did not detected statistical differences in any of the gene expressions as the disease progressed (normal to moderate to severe). The least significant numbers (LSN) indicated an inadequate number in the sampling pool. If there were an increase by just two samples in each group or six or seven samples in the total pool, the statistical analyses might give a different outcome. Limitations of time and the problem of clinical tissue availability prevented large number of samples being examined.

While expression of some genes was in agreement with the results already reported in the early Chapters of this thesis (increased FN [section 3.3.10] in severely diseased valves for example), others results contradicted the earlier work (decreased actin [section 3.3.3] and increased in TPM [section 4.3.2] expressions). However, to presume functionality of a protein based on its transcriptional level is an incorrect way of looking at a complex biological system, since once an mRNA has been transcribed, it undergoes a series of downstream splicings and modifications which might not necessary result in protein expression[291]. Moreover, isoforms with high sequence homology add to the complication. However, gene expression can provide much valuable information on the level of gene activity in MMVD valves[184]. Since the MMVD has a heritable component, understanding at gene expression would provide useful information prior to closer inspection of the genome[292]. Even though the RT-PCR products in this study were not sequenced, with the canine genome fully sequenced and some of the single nucleotide polymorphisms (SNPS) are now known[293], genetic approaches using genetic markers or candidate gene methodologies can now be used to understand MMVD at molecular level[294].

6 Conclusion

Prior to undertaking this study there was limited information on various aspects of the pathobiology of canine MMVD. This study has expanded our understanding of MMVD and has provided data on morphological changes, cellular alteration and functional protein expression. Together such data allows a more complete understanding of what happens to the valve with this disease, how these changes occur over time and inform possible explanations for the cause of MMVD in the dog and humans.

1. This study once again highlighted the prevalence of myxomatous mitral valve disease in older dogs. Although categorising the dogs according to grade of disease was in line with previously published data, dogs entering the study were generally older and often diseased. In fact, no aged dog was found to be disease free and we seldom encountered healthy dogs without any evidence of valvular disease. Therefore, it is difficult to say if the frequency of the disease grades reflects the wider spectrum of the entire population. Additionally the opportunity to age-match groups was not a feasible option considering the close age-association of the disease.
2. The destruction of the ordered fibrosa tissue and fibro-elastic proliferation accompanied by glycosylaminoglycan accumulation in the diseased leaflets was clearly demonstrated and can be easily understood to compromise mitral valve function. The thickening of the leaflets near the free edge (zone of apposition of the leaflets) was confirmed, and it is suspected that repeated trauma at time of valve closure is implicated in this finding, and in itself could be the initiating cause of MMVD. The progressive nature of the disease was manifested in the gradual expansion of the spongiosa at the distal zone as disease severity increased with age. Similar to human mitral valve prolapse, the posterior leaflets were found to be more severely affected than anterior. The posterior leaflet in dogs would appear to degenerate at a more accelerated rate than the anterior leaflet.
3. We had hypothesised that interstitial cells would play an important role in this disease, since these cells determine the nature of the extracellular matrix. In contrast to human mitral valve disease, where increased interstitial cell numbers were found[27], in dogs the cell numbers in the myxomatous areas were not

significantly different irrespective of the severity of the disease. However, the fibrosa tissues adjacent to myxomatous areas in the distal zone were found to have increased cell numbers or at least patchy accumulations of cells. These areas were close to the site of valve closure and might reflect a response to friction or stress injury. It was apparent that cells accumulate close to the valve edge and these cells have an activated myofibroblast phenotype (α-SMA +/Vim-), while the number of quiescent fibroblasts (Vim-) decreases. This was clear evidence of interstitial cell phenotypic alteration, possibly coupled with cell migration and translocation to the valve edge, and this could also be identified on TEM. Fat cell numbers were also found to increase in diseased valves and might be an additional source of fibroblasts. Lastly there was a small increase in mast cells, macrophages and desmin-positive chondrocyte-like cells, but their exact role in MMVD cannot be stated with certainty. The desmin-positive cells may be further evidence for interstitial cell capacity to switch phenotypic.

4. Endothelial cell abnormalities, including detachment, denuding and apoptosis, were clearly seen in diseased valves, with additional areas of basement membrane damage and loss and ECM extrusion. Interestingly such changes, although to a more minor degree, could be seen in normal valves, suggesting endothelial damage and repair is an ongoing process. Interstitial cells could also be seen in close proximity to the damaged endothelium, with cells even touching and occasionally incorporating into the endothelium itself.
5. Stromal damage could be readily appreciated on histological sections, with a quantifiable loss of connective tissue in myxomatous regions, and on TEM and SEM, with a likely concomitant increase in glycosaminoglycan content. On SEM the disorganisation of collagen could be clearly seen and at high power TEM abnormal collagen bundle formation, and extrusion of pro-collagen that failed to be organise into collagen fibrils could be identified, all suggesting a dyscollagenesis abnormality.
6. Several proteins and classes of protein were found to be differentially expressed when comparing diseased and normal valves. Not unexpectedly, several were constituent parts of, or important in the formation, laying down and organisation of the extra-cellular matrix. However, which proteins might have been altered could not have been deduced intuitively. The SLRPs were particularly interesting considering their crucial role in matrix production, but also the necessity for

close interaction with each other to allow this process to function properly. This means that reduced expression of one SLRP alone could have adverse effects on the function of other SLRPs and other connective tissue constituents (collagen, elastin and other proteoglycans). An additional interesting group of altered proteins were those involved in contractility and cell architecture. These proteins also have pivotal roles in cell function. The main effect of loss of these proteins would be on interstitial cell function, migration, cell division and differentiation.

The underlying cause of MMVD in dogs and humans is unknown. There is evidence to show it may be due to over-expression of certain catabolic enzymes by activated contractile and secretory myofibroblasts, but the initiating cause is not understood. Using the combined data of this study and data form other studies, the following paradigm can be proposed:

Under normal circumstances of valve growth and development, a stage is reached where there is a low level of remodelling and repair of the leaflet and this extends during early and mature adult life. At this stage VICs are relatively quiescent, but processes manage the replacement of valve matrix and can repair endothelial damage when needed. With progression to adulthood the continual trauma to the valve edge caused by valve closure results in endothelial damage that cannot be readily repaired. The damaged endothelium signals to the valve stromal cells, which alter their phenotype to a more secretory and contractile form (activated myofibroblasts), and the cells migrate toward the damaged valve surface. Extra-cellular matrix production is compromised by a combination of excess production of catalytic enzymes (MMPs) and the failure to produce enough collagen to meet turnover demand, and organise the collagen which is produced into collagen fibrils and collagen bundles. Eventually, there is expansion of the lose connective tissue component of the valve and an overall loss of valve mechanical integrity. The resulting shear stress cause by regurgitating blood flow damages the endothelium further and the process continues unchecked.

Suggested Future Work

1. In a clinical study of this nature there is invariably a problem the collection of a sufficient number of samples to ensure adequate statistical power of

analysis and the first stage in any further work should be to increase the number of samples and confirm the observations made.

2. A key element of the hypothesis outlined earlier is the role of endothelial cell trauma as the trigger for phenotypic alteration of valve stromal cells. The nature of this interaction and in particular signal transduction between endothelial cells and VICs could be investigated in normal and diseased valves using molecular techniques.
3. Another possible consequence of endothelial cell trauma is the genesis of an inflammatory response and the potential role of inflammatory disease in MMVD needs to be investigated further using a combination of immunohistochemistry and Western blots.
4. This work has confirmed the occurrence of changes in the protein matrix as a result of remodelling, repair and replacement and the proteomics studies could be expanded using shorter-range pH gradient strips in 2-D gels to produce more detailed studies of the expression of important matrix proteins.
5. In addition morphogenesis of the cytosolic structure of interstitial cells could be studied at the ultrastructural level using TEM at higher magnifications.
6. Finally, subtractive hybridization techniques could be employed to identify the differentially expressed genes associated with MMVD and the genome examined for these genes.

7 References

1. Buchanan JW. Chronic valvular disease (endocardiosis) in dogs. *Adv Vet Sci Comp Med.* 1977;21:75-106.
2. Whitney JC. Observations on the effect of age on the severity of heart valve lesions in the dog. *J Small Anim Pract.* Aug 1974;15(8):511-522.
3. Cheng TO. Mitral valve prolapse--some historical facts. *International journal of cardiology.* Sep 20 2006;112(2):264.
4. Pomerance A, Whitney JC. Heart valve changes common to man and dog: a comparative study. *Cardiovasc Res.* Jan 1970;4(1):61-66.
5. Pedersen HD. *Mitral valve prolapse in the dog: Pathogenesis, pathophysiology, diagnosis and comparative aspects of early myxomatous mitral valve disease*. Copenhagen: Department of Anatomy and Physiology, The Royal Veterinary and agricultural University; 2000.
6. Anderson RH, Wilcox BR. The anatomy of the mitral valve. In: Wells FC, Shapiro LM, eds. *Mitral Valve Disease*: Butterworth-Heinemann; 1996:4-27.
7. Ho SY. Anatomy of the mitral valve. *Heart (British Cardiac Society).* Nov 2002;88 Suppl 4:iv5-10.
8. Kanani M, Anderson RH. The anatomy of the mitral valve: a retrospective analysis of yesterday's future. *J Heart Valve Dis.* Sep 2003;12(5):543-547.
9. Fenoglio JJ, Jr., Tuan Duc P, Wit AL, Bassett AL, Wagner BM. Canine mitral complex. Ultrastructure and electromechanical properties. *Circulation research.* Sep 1972;31(3):417-430.
10. Lam JH, Ranganathan N, Wigle ED, Silver MD. Morphology of the human mitral valve. I. Chordae tendineae: a new classification. *Circulation.* Mar 1970;41(3):449-458.
11. Ranganathan N, Lam JH, Wigle ED, Silver MD. Morphology of the human mitral valve. II. The value leaflets. *Circulation.* Mar 1970;41(3):459-467.
12. Akhtar S, Meek KM, James V. Immunolocalization of elastin, collagen type I and type III, fibronectin, and vitronectin in extracellular matrix components of normal and myxomatous mitral heart valve chordae tendineae. *Cardiovasc Pathol.* Jul-Aug 1999;8(4):203-211.
13. Barber JE, Kasper FK, Ratliff NB, Cosgrove DM, Griffin BP, Vesely I. Mechanical properties of myxomatous mitral valves. *J Thorac Cardiovasc Surg.* Nov 2001;122(5):955-962.
14. van der Bel-Kahn J, Becker AE. The surgical pathology of rheumatic and floppy mitral valves. Distinctive morphologic features upon gross examination. *Am J Surg Pathol.* Apr 1986;10(4):282-292.
15. Detweiler DK, Patterson DF. The prevalence and types of cardiovascular disease in dogs. *Ann N Y Acad Sci.* Sep 8 1965;127(1):481-516.
16. Ernst E, Schneider P, Trautwein G. [Etiology and pathogenesis of the endocardiosis and endocarditis in dogs. II. Anatomicopathological findings]. *Dtsch Tierarztl Wochenschr.* Jul 15 1973;80(14):322-328.
17. Kogure K. Pathology of chronic mitral valvular disease in the dog. *Nippon Juigaku Zasshi.* Jun 1980;42(3):323-335.
18. Machida N, Hoshi K, Kobayashi M, Katsuda S, Yamane Y. Cardiac myxoma of the tricuspid valve in a dog. *J Comp Pathol.* Nov 2003;129(4):320-324.
19. Haggstrom J, Kvart C, Hansson K. Heart sounds and murmurs: changes related to severity of chronic valvular disease in the Cavalier King Charles

spaniel. *Journal of veterinary internal medicine / American College of Veterinary Internal Medicine.* Mar-Apr 1995;9(2):75-85.

20. Pedersen HD, Haggstrom J, Falk T, Mow T, Olsen LH, Iversen L, Jensen AL. Auscultation in mild mitral regurgitation in dogs: observer variation, effects of physical maneuvers, and agreement with color Doppler echocardiography and phonocardiography. *Journal of veterinary internal medicine / American College of Veterinary Internal Medicine.* Jan-Feb 1999;13(1):56-64.

21. Olsen LH, Martinussen T, Pedersen HD. Early echocardiographic predictors of myxomatous mitral valve disease in dachshunds. *The Veterinary record.* Mar 8 2003;152(10):293-297.

22. Pedersen HD, Kristensen B, Norby B, Lorentzen KA. Echocardiographic study of mitral valve prolapse in dachshunds. *Zentralblatt fur Veterinarmedizin.* Apr 1996;43(2):103-110.

23. Filip DA, Radu A, Simionescu M. Interstitial cells of the heart valves possess characteristics similar to smooth muscle cells. *Circulation research.* Sep 1986;59(3):310-320.

24. Taylor PM, Batten P, Brand NJ, Thomas PS, Yacoub MH. The cardiac valve interstitial cell. *Int J Biochem Cell Biol.* Feb 2003;35(2):113-118.

25. Mulholland DL, Gotlieb AI. Cell biology of valvular interstitial cells. *Can J Cardiol.* Mar 1996;12(3):231-236.

26. Rabkin-Aikawa E, Farber M, Aikawa M, Schoen FJ. Dynamic and reversible changes of interstitial cell phenotype during remodeling of cardiac valves. *J Heart Valve Dis.* Sep 2004;13(5):841-847.

27. Rabkin E, Aikawa M, Stone JR, Fukumoto Y, Libby P, Schoen FJ. Activated interstitial myofibroblasts express catabolic enzymes and mediate matrix remodeling in myxomatous heart valves. *Circulation.* Nov 20 2001;104(21):2525-2532.

28. Peine CJ, Low FN. Scanning electron microscopy of cardiac endothelium of the dog. *Am J Anat.* Feb 1975;142(2):137-157.

29. Corcoran BM, Black A, Anderson H, McEwan JD, French A, Smith P, Devine C. Identification of surface morphologic changes in the mitral valve leaflets and chordae tendineae of dogs with myxomatous degeneration. *Am J Vet Res.* Feb 2004;65(2):198-206.

30. Stein PD, Wang CH, Riddle JM, Sabbah HN, Magilligan DJ, Jr., Hawkins ET. Scanning electron microscopy of operatively excised severely regurgitant floppy mitral valves. *The American journal of cardiology.* Aug 1 1989;64(5):392-394.

31. Mow T, Pedersen HD. Increased endothelin-receptor density in myxomatous canine mitral valve leaflets. *J Cardiovasc Pharmacol.* Aug 1999;34(2):254-260.

32. Olsen LH, Mortensen K, Martinussen T, Larsson LI, Baandrup U, Pedersen HD. Increased NADPH-diaphorase activity in canine myxomatous mitral valve leaflets. *J Comp Pathol.* Aug-Oct 2003;129(2-3):120-130.

33. Durbin AD, Gotlieb AI. Advances towards understanding heart valve response to injury. *Cardiovasc Pathol.* Mar-Apr 2002;11(2):69-77.

34. Kunzelman KS, Cochran RP, Murphree SS, Ring WS, Verrier ED, Eberhart RC. Differential collagen distribution in the mitral valve and its influence on biomechanical behaviour. *J Heart Valve Dis.* Mar 1993;2(2):236-244.

35. Hadian M, Corcoran BM, Han RI, Grossmann JG, Bradshaw JP. Collagen organization in canine myxomatous mitral valve disease: an x-ray diffraction study. *Biophysical journal.* Oct 1 2007;93(7):2472-2476.

36. Fujiki M, Misumi K, Sakamoto H. Evaluation of collagenase-induced mitral valve regurgitation in dogs. *Am J Vet Res.* Dec 2000;61(12):1593-1598.

37. Kimura N, Shukunami C, Hakuno D, Yoshioka M, Miura S, Docheva D, Kimura T, Okada Y, Matsumura G, Shin'oka T, Yozu R, Kobayashi J, Ishibashi-Ueda H, Hiraki Y, Fukuda K. Local tenomodulin absence, angiogenesis, and matrix metalloproteinase activation are associated with the rupture of the chordae tendineae cordis. *Circulation.* Oct 21 2008;118(17):1737-1747.

38. Matrisian LM. Metalloproteinases and their inhibitors in matrix remodeling. *Trends Genet.* Apr 1990;6(4):121-125.

39. Dollery CM, McEwan JR, Henney AM. Matrix metalloproteinases and cardiovascular disease. *Circulation research.* Nov 1995;77(5):863-868.

40. Birkedal-Hansen H. Proteolytic remodeling of extracellular matrix. *Current opinion in cell biology.* Oct 1995;7(5):728-735.

41. Hibbetts K, Hines B, Williams D. An overview of proteinase inhibitors. *Journal of veterinary internal medicine / American College of Veterinary Internal Medicine.* Jul-Aug 1999;13(4):302-308.

42. Barlow JB, Pocock WA. Billowing, floppy, prolapsed or flail mitral valves? *The American journal of cardiology.* Feb 1 1985;55(4):501-502.

43. Black A, French AT, Dukes-McEwan J, Corcoran BM. Ultrastructural morphologic evaluation of the phenotype of valvular interstitial cells in dogs with myxomatous degeneration of the mitral valve. *Am J Vet Res.* Aug 2005;66(8):1408-1414.

44. Disatian S, Ehrhart EJ, 3rd, Zimmerman S, Orton EC. Interstitial cells from dogs with naturally occurring myxomatous mitral valve disease undergo phenotype transformation. *J Heart Valve Dis.* Jul 2008;17(4):402-411; discussion 412.

45. Ruifrok AC, Johnston DA. Quantification of histochemical staining by color deconvolution. *Analytical and quantitative cytology and histology / the International Academy of Cytology [and] American Society of Cytology.* Aug 2001;23(4):291-299.

46. Ruifrok AC, Katz RL, Johnston DA. Comparison of quantification of histochemical staining by hue-saturation-intensity (HSI) transformation and color-deconvolution. *Appl Immunohistochem Mol Morphol.* Mar 2003;11(1):85-91.

47. Sall J, Lehman A, Creighton L, SAS Institute. *JMP start statistics : a guide to statistics and data analysis using JMP and JMP IN software.* 3rd ed. Pacific Grove, CA: Duxbury; 2005.

48. Ernst E, Drommer W, Schneider P, Trautwein G. [Electron microscopy studies on the normal structure of atrioventricular valves of the dog]. *Anat Anz.* 1973;134(4):309-326.

49. Ernst E, Schneider P, Trautwein G. [Electron microscopic studies on amyloidosis of the atrioventricular valves of the dog (author's transl)]. *Beitr Pathol.* Sep 1974;152(4):361-382.

50. Rossi MA, Abreu MA, Santoro LB. Images in cardiovascular medicine. Connective tissue skeleton of the human heart: a demonstration by cell-maceration scanning electron microscope method. *Circulation.* Mar 10 1998;97(9):934-935.

51. Impoco G, Carrato S, Caccamo M, Tuminello L, Licitra G. Quantitative analysis of cheese microstructure using SEM imagery. *SIMAI 2006 Minisymposium: Image Analysis for Industrial Application*. Baia Samuele, Italy; 2006.

52. Guglielmini C. Cardiovascular diseases in the ageing dog: diagnostic and therapeutic problems. *Veterinary research communications.* Sep 2003;27 Suppl 1:555-560.

53. Beardow AW, Buchanan JW. Chronic mitral valve disease in cavalier King Charles spaniels: 95 cases (1987-1991). *J Am Vet Med Assoc.* Oct 1 1993;203(7):1023-1029.

54. Pedersen HD, Lorentzen KA, Kristensen BO. Echocardiographic mitral valve prolapse in cavalier King Charles spaniels: epidemiology and prognostic significance for regurgitation. *The Veterinary record.* Mar 20 1999;144(12):315-320.

55. Fornes P, Heudes D, Fuzellier JF, Tixier D, Bruneval P, Carpentier A. Correlation between clinical and histologic patterns of degenerative mitral valve insufficiency: a histomorphometric study of 130 excised segments. *Cardiovasc Pathol.* Mar-Apr 1999;8(2):81-92.

56. Davies MJ, Moore BP, Braimbridge MV. The floppy mitral valve. Study of incidence, pathology, and complications in surgical, necropsy, and forensic material. *British heart journal.* May 1978;40(5):468-481.

57. Rahimtoola SH. The year in valvular heart disease. *J Am Coll Cardiol.* Feb 4 2004;43(3):491-504.

58. Levy D, Savage D. Prevalence and clinical features of mitral valve prolapse. *Am Heart J.* May 1987;113(5):1281-1290.

59. Hickey AJ, Wilcken DE. Age and the clinical profile of idiopathic mitral valve prolapse. *British heart journal.* Jun 1986;55(6):582-586.

60. Singh JP, Evans JC, Levy D, Larson MG, Freed LA, Fuller DL, Lehman B, Benjamin EJ. Prevalence and clinical determinants of mitral, tricuspid, and aortic regurgitation (the Framingham Heart Study). *The American journal of cardiology.* Mar 15 1999;83(6):897-902.

61. Freed LA, Levy D, Levine RA, Larson MG, Evans JC, Fuller DL, Lehman B, Benjamin EJ. Prevalence and clinical outcome of mitral-valve prolapse. *N Engl J Med.* Jul 1 1999;341(1):1-7.

62. Nishimura RA, McGoon MD. Perspectives on Mitral-Valve Prolapse. *N Engl J Med.* July 1, 1999 1999;341(1):48-a-50.

63. Olsen LH, Fredholm M, Pedersen HD. Epidemiology and inheritance of mitral valve prolapse in Dachshunds. *Journal of veterinary internal medicine / American College of Veterinary Internal Medicine.* Sep-Oct 1999;13(5):448-456.

64. Olsen LH, Kristensen AT, Haggstrom J, Jensen AL, Klitgaard B, Hansson H, Pedersen HD. Increased platelet aggregation response in Cavalier King Charles Spaniels with mitral valve prolapse. *Journal of veterinary internal medicine / American College of Veterinary Internal Medicine.* May-Jun 2001;15(3):209-216.

65. Cowan SM, Bartges JW, Gompf RE, Hayes JR, Moyers TD, Snider CC, Gerard DA, Craft RM, Muenchen RA, Carroll RC. Giant platelet disorder in the Cavalier King Charles Spaniel. *Exp Hematol.* Apr 2004;32(4):344-350.

66. Tarnow I, Kristensen AT, Olsen LH, Pedersen HD. Assessment of changes in hemostatic markers in Cavalier King Charles Spaniels with myxomatous mitral valve disease. *Am J Vet Res.* Dec 2004;65(12):1644-1652.

67. Nasuti JF, Zhang PJ, Feldman MD, Pasha T, Khurana JS, Gorman JH, 3rd, Gorman RC, Narula J, Narula N. Fibrillin and other matrix proteins in mitral valve prolapse syndrome. *Ann Thorac Surg.* Feb 2004;77(2):532-536.

68. Chou HT, Shi YR, Hsu Y, Tsai FJ. Association between fibrillin-1 gene exon 15 and 27 polymorphisms and risk of mitral valve prolapse. *J Heart Valve Dis.* Jul 2003;12(4):475-481.

69. Weyman AE, Scherrer-Crosbie M. Marfan syndrome and mitral valve prolapse. *J Clin Invest.* Dec 2004;114(11):1543-1546.

70. Thrusfield MV, Aitken CGG, Darke PGG. Observations on breed and sex in relation to canine heart valve incompetence. *J Small Anim Pract.* 1985;26:709-717.

71. Pedersen HD, Haggstrom J. Mitral valve prolapse in the dog: a model of mitral valve prolapse in man. *Cardiovasc Res.* Aug 2000;47(2):234-243.

72. Whitney JC. Cardiovascular pathology. *J Small Anim Pract.* Aug 1967;8(8):459-465.

73. Pomerance A. Ballooning deformity (mucoid degeneration) of atrioventricular valves. *British heart journal.* May 1969;31(3):343-351.

74. Sacks MS, He Z, Baijens L, Wanant S, Shah P, Sugimoto H, Yoganathan AP. Surface strains in the anterior leaflet of the functioning mitral valve. *Annals of biomedical engineering.* Nov-Dec 2002;30(10):1281-1290.

75. Hayek E, Gring CN, Griffin BP. Mitral valve prolapse. *Lancet.* Feb 5-11 2005;365(9458):507-518.

76. Murata K. Acidic glycosaminoglycans in human heart valves. *Journal of molecular and cellular cardiology.* Mar 1981;13(3):281-292.

77. Cole WG, Chan D, Hickey AJ, Wilcken DE. Collagen composition of normal and myxomatous human mitral heart valves. *The Biochemical journal.* Apr 15 1984;219(2):451-460.

78. Lis Y, Burleigh MC, Parker DJ, Child AH, Hogg J, Davies MJ. Biochemical characterization of individual normal, floppy and rheumatic human mitral valves. *The Biochemical journal.* Jun 15 1987;244(3):597-603.

79. McDonald PC, Wilson JE, McNeill S, Gao M, Spinelli JJ, Rosenberg F, Wiebe H, McManus BM. The challenge of defining normality for human mitral and aortic valves: geometrical and compositional analysis. *Cardiovasc Pathol.* Jul-Aug 2002;11(4):193-209.

80. Han RI, Black A, Culshaw GJ, French AT, Else RW, Corcoran BM. Distribution of myofibroblasts, smooth muscle-like cells, macrophages, and mast cells in mitral valve leaflets of dogs with myxomatous mitral valve disease. *Am J Vet Res.* Jun 2008;69(6):763-769.

81. Darke PG. Valvular incompetence in cavalier King Charles spaniels. *The Veterinary record.* Apr 11 1987;120(15):365-366.

82. Soini Y, Satta J, Maatta M, Autio-Harmainen H. Expression of MMP2, MMP9, MT1-MMP, TIMP1, and TIMP2 mRNA in valvular lesions of the heart. *J Pathol.* Jun 2001;194(2):225-231.

83. Barth PJ, Koster H, Moosdorf R. CD34+ fibrocytes in normal mitral valves and myxomatous mitral valve degeneration. *Pathol Res Pract.* 2005;201(4):301-304.

84. Lester WM, Damji AA, Tanaka M, Gedeon I. Bovine mitral valve organ culture: role of interstitial cells in repair of valvular injury. *J Mol Cell Cardiol.* Jan 1992;24(1):43-53.

85. Mirzaie M, Meyer T, Schwarz P, Lotfi S, Rastan A, Schondube F. Ultrastructural alterations in acquired aortic and mitral valve disease as revealed by scanning and transmission electron microscopical investigations. *Ann Thorac Cardiovasc Surg.* Feb 2002;8(1):24-30.

86. Sarphie TG. Pleomorphic surface features of mammalian endocardium: fine structure of canine bicuspid valves. *Journal of molecular and cellular cardiology.* Mar 1980;12(3):241-255.

87. Butcher JT, Penrod AM, Garcia AJ, Nerem RM. Unique morphology and focal adhesion development of valvular endothelial cells in static and fluid flow environments. *Arteriosclerosis, thrombosis, and vascular biology.* Aug 2004;24(8):1429-1434.

88. Butcher JT, Tressel S, Johnson T, Turner D, Sorescu G, Jo H, Nerem RM. Transcriptional profiles of valvular and vascular endothelial cells reveal phenotypic differences: influence of shear stress. *Arteriosclerosis, thrombosis, and vascular biology.* Jan 2006;26(1):69-77.

89. Butcher JT, Nerem RM. Valvular endothelial cells regulate the phenotype of interstitial cells in co-culture: effects of steady shear stress. *Tissue Eng.* Apr 2006;12(4):905-915.

90. Tamura K, Jones M, Yamada I, Ferrans VJ. Wound healing in the mitral valve. *J Heart Valve Dis.* Jan 2000;9(1):53-63.

91. Gotlieb AI, Rosenthal A, Kazemian P. Fibroblast growth factor 2 regulation of mitral valve interstitial cell repair in vitro. *J Thorac Cardiovasc Surg.* Sep 2002;124(3):591-597.

92. Walker GA, Masters KS, Shah DN, Anseth KS, Leinwand LA. Valvular myofibroblast activation by transforming growth factor-beta: implications for pathological extracellular matrix remodeling in heart valve disease. *Circulation research.* Aug 6 2004;95(3):253-260.

93. Aupperle H, Marz I, Thielebein J, Schoon HA. Expression of Transforming Growth Factor-beta1, -beta2 and -beta3 in Normal and Diseased Canine Mitral Valves. *J Comp Pathol.* Aug-Oct 2008;139(2-3):97-107.

94. Liu AC, Gotlieb AI. Transforming Growth Factor-{beta} Regulates in Vitro Heart Valve Repair by Activated Valve Interstitial Cells. *Am J Pathol.* November 1, 2008 2008;173(5):1275-1285.

95. Eisenberg LM, Markwald RR. Molecular regulation of atrioventricular valvuloseptal morphogenesis. *Circulation research.* Jul 1995;77(1):1-6.

96. Armstrong EJ, Bischoff J. Heart valve development: endothelial cell signaling and differentiation. *Circulation research.* Sep 3 2004;95(5):459-470.

97. de Lange FJ, Moorman AF, Anderson RH, Manner J, Soufan AT, de Gier-de Vries C, Schneider MD, Webb S, van den Hoff MJ, Christoffels VM. Lineage and morphogenetic analysis of the cardiac valves. *Circulation research.* Sep 17 2004;95(6):645-654.

98. Paranya G, Vineberg S, Dvorin E, Kaushal S, Roth SJ, Rabkin E, Schoen FJ, Bischoff J. Aortic valve endothelial cells undergo transforming growth factor-beta-mediated and non-transforming growth factor-beta-mediated transdifferentiation in vitro. *Am J Pathol.* Oct 2001;159(4):1335-1343.

99. Armulik A, Abramsson A, Betsholtz C. Endothelial/pericyte interactions. *Circulation research.* Sep 16 2005;97(6):512-523.

100. Liu AC, Joag VR, Gotlieb AI. The Emerging Role of Valve Interstitial Cell Phenotypes in Regulating Heart Valve Pathobiology. *Am J Pathol.* November 1, 2007 2007;171(5):1407-1418.

101. Klinkner DB, Densmore JC, Kaul S, Noll L, Lim HJ, Weihrauch D, Pritchard KA, Jr., Oldham KT, Sander TL. Endothelium-derived microparticles inhibit human cardiac valve endothelial cell function. *Shock (Augusta, Ga.* Jun 2006;25(6):575-580.

102. Fiedler LR, Schonherr E, Waddington R, Niland S, Seidler DG, Aeschlimann D, Eble JA. Decorin regulates endothelial cell motility on collagen I through activation of insulin-like growth factor I receptor and modulation of alpha2beta1 integrin activity. *The Journal of biological chemistry.* Jun 20 2008;283(25):17406-17415.

103. Ishihara T, Ferrans VJ, Jones M, Boyce SW, Roberts WC. Occurrence and significance of endothelial cells in implanted porcine bioprosthetic valves. *The American journal of cardiology.* Sep 1981;48(3):443-454.

104. Davis GE, Senger DR. Endothelial extracellular matrix: biosynthesis, remodeling, and functions during vascular morphogenesis and neovessel stabilization. *Circulation research.* Nov 25 2005;97(11):1093-1107.

105. Silva GV, Litovsky S, Assad JA, Sousa AL, Martin BJ, Vela D, Coulter SC, Lin J, Ober J, Vaughn WK, Branco RV, Oliveira EM, He R, Geng YJ, Willerson JT, Perin EC. Mesenchymal stem cells differentiate into an endothelial phenotype, enhance vascular density, and improve heart function in a canine chronic ischemia model. *Circulation.* Jan 18 2005;111(2):150-156.

106. Kunzelman KS, Cochran RP, Verrier ED, Eberhart RC. Anatomic basis for mitral valve modelling. *J Heart Valve Dis.* Sep 1994;3(5):491-496.

107. Mautner SL, Klues HG, Mautner GC, Proschan MA, Roberts WC, Maron BJ. Comparison of mitral valve dimensions in adults with valvular aortic stenosis, pure aortic regurgitation and hypertrophic cardiomyopathy. *The American journal of cardiology.* Apr 15 1993;71(11):949-953.

108. Waller BF, Morrow AG, Maron BJ, Del Negro AA, Kent KM, McGrath FJ, Wallace RB, McIntosh CL, Roberts WC. Etiology of clinically isolated, severe, chronic, pure mitral regurgitation: analysis of 97 patients over 30 years of age having mitral valve replacement. *Am Heart J.* Aug 1982;104(2 Pt 1):276-288.

109. Wooley CF, Baker PB, Kolibash AJ, Kilman JW, Sparks EA, Boudoulas H. The floppy, myxomatous mitral valve, mitral valve prolapse, and mitral regurgitation. *Prog Cardiovasc Dis.* May-Jun 1991;33(6):397-433.

110. Rusted IE, Scheifley CH, Edwards JE. Studies of the mitral valve. I. Anatomic features of the normal mitral valve and associated structures. *Circulation.* Dec 1952;6(6):825-831.

111. Grande-Allen KJ, Borowski AG, Troughton RW, Houghtaling PL, Dipaola NR, Moravec CS, Vesely I, Griffin BP. Apparently normal mitral valves in patients with heart failure demonstrate biochemical and structural derangements: an extracellular matrix and echocardiographic study. *J Am Coll Cardiol.* Jan 4 2005;45(1):54-61.

112. Timek TA, Lai DT, Dagum P, Liang D, Daughters GT, Ingels NB, Jr., Miller DC. Mitral Leaflet Remodeling in Dilated Cardiomyopathy. *Circulation.* July 4, 2006 2006;114(1_suppl):I-518-523.

113. Gillinov AM, Cosgrove DM. Mitral valve repair for degenerative disease. *J Heart Valve Dis.* Jan 2002;11 Suppl 1:S15-20.

114. Barlow JB, Pocock WA. Mitral valve billowing and prolapse: perspective at 25 years. *Herz.* Aug 1988;13(4):227-234.

115. Hammer D, Leier CV, Baba N, Vasko JS, Wooley CF, Pinnell SR. Altered collagen composition in a prolapsing mitral valve with ruptured chordae tendineae. *The American journal of medicine.* Nov 1979;67(5):863-866.

116. Whittaker P, Boughner DR, Perkins DG, Canham PB. Quantitative structural analysis of collagen in chordae tendineae and its relation to floppy mitral valves and proteoglycan infiltration. *British heart journal.* Mar 1987;57(3):264-269.

117. Tamura K, Fukuda Y, Ishizaki M, Masuda Y, Yamanaka N, Ferrans VJ. Abnormalities in elastic fibers and other connective-tissue components of floppy mitral valve. *Am Heart J.* Jun 1995;129(6):1149-1158.

118. Grande-Allen KJ, Griffin BP, Ratliff NB, Cosgrove DM, Vesely I. Glycosaminoglycan profiles of myxomatous mitral leaflets and chordae parallel the severity of mechanical alterations. *J Am Coll Cardiol.* Jul 16 2003;42(2):271-277.

119. Akhtar S, Meek KM, James V. Ultrastructure abnormalities in proteoglycans, collagen fibrils, and elastic fibers in normal and myxomatous mitral valve chordae tendineae. *Cardiovasc Pathol.* Jul-Aug 1999;8(4):191-201.

120. Eyre DR, Paz MA, Gallop PM. Cross-linking in collagen and elastin. *Annual review of biochemistry.* 1984;53:717-748.

121. Stephens EH, Grande-Allen KJ. Age-related changes in collagen synthesis and turnover in porcine heart valves. *J Heart Valve Dis.* Nov 2007;16(6):672-682.

122. Henney AM, Tsipouras P, Schwartz RC, Child AH, Devereux RB, Leech GJ. Genetic evidence that mutations in the COL1A1, COL1A2, COL3A1, or COL5A2 collagen genes are not responsible for mitral valve prolapse. *British heart journal.* Mar 1989;61(3):292-299.

123. Grunkemeier GL, Li HH, Starr A. Heart valve replacement: a statistical review of 35 years' results. *J Heart Valve Dis.* Sep 1999;8(5):466-470; discussion 470-461.

124. Latif N, Sarathchandra P, Taylor PM, Antoniw J, Yacoub MH. Localization and pattern of expression of extracellular matrix components in human heart valves. *J Heart Valve Dis.* Mar 2005;14(2):218-227.

125. Radermecker MA, Limet R, Lapiere CM, Nusgens B. Increased mRNA expression of decorin in the prolapsing posterior leaflet of the mitral valve. *Interactive cardiovascular and thoracic surgery.* Sep 2003;2(3):389-394.

126. McSweeney PA, Rouleau KA, Wallace PM, Bruno B, Andrews RG, Krizanac-Bengez L, Sandmaier BM, Storb R, Wayner E, Nash RA. Characterization of monoclonal antibodies that recognize canine CD34. *Blood.* Mar 15 1998;91(6):1977-1986.

127. Tsuchiya Y, Endo Y, Sato H, Okada Y, Mai M, Sasaki T, Seiki M. Expression of type-IV collagenases in human tumor cell lines that can form liver colonies in chick embryos. *International journal of cancer.* Jan 2 1994;56(1):46-51.

128. Nakagawa T, Kubota T, Kabuto M, Sato K, Kawano H, Hayakawa T, Okada Y. Production of matrix metalloproteinases and tissue inhibitor of metalloproteinases-1 by human brain tumors. *Journal of neurosurgery.* Jul 1994;81(1):69-77.

129. Christgau M, Caffesse RG, Newland JR, Schmalz G, D'Souza RN. Characterization of immunocompetent cells in the diseased canine periodontium. *J Histochem Cytochem.* Dec 1998;46(12):1443-1454.

130. Shi SR, Key ME, Kalra KL. Antigen retrieval in formalin-fixed, paraffin-embedded tissues: an enhancement method for immunohistochemical staining based on microwave oven heating of tissue sections. *J Histochem Cytochem.* Jun 1991;39(6):741-748.

131. Shi SR, Cote RJ, Taylor CR. Antigen retrieval immunohistochemistry: past, present, and future. *J Histochem Cytochem.* Mar 1997;45(3):327-343.

132. Emoto K, Yamashita S, Okada Y. Mechanisms of heat-induced antigen retrieval: does pH or ionic strength of the solution play a role for refolding antigens? *J Histochem Cytochem.* Nov 2005;53(11):1311-1321.

133. Zacks S, Rosenthal A, Granton B, Havenith M, Opas M, Gotlieb AI. Characterization of Cobblestone mitral valve interstitial cells. *Arch Pathol Lab Med.* Aug 1991;115(8):774-779.

134. Merryman WD, Youn I, Lukoff HD, Krueger PM, Guilak F, Hopkins RA, Sacks MS. Correlation between heart valve interstitial cell stiffness and transvalvular pressure: implications for collagen biosynthesis. *Am J Physiol Heart Circ Physiol.* Jan 2006;290(1):H224-231.

135. Yperman J, De Visscher G, Holvoet P, Flameng W. Molecular and functional characterization of ovine cardiac valve-derived interstitial cells in primary isolates and cultures. *Tissue Eng.* Sep-Oct 2004;10(9-10):1368-1375.

136. Flanagan TC, Black A, O'Brien M, Smith TJ, Pandit AS. Reference models for mitral valve tissue engineering based on valve cell phenotype and extracellular matrix analysis. *Cells Tissues Organs.* 2006;183(1):12-23.

137. Schenke-Layland K, Riemann I, Opitz F, Konig K, Halbhuber KJ, Stock UA. Comparative study of cellular and extracellular matrix composition of native and tissue engineered heart valves. *Matrix Biol.* May 2004;23(2):113-125.

138. Rabkin-Aikawa E, Aikawa M, Farber M, Kratz JR, Garcia-Cardena G, Kouchoukos NT, Mitchell MB, Jonas RA, Schoen FJ. Clinical pulmonary autograft valves: pathologic evidence of adaptive remodeling in the aortic site. *J Thorac Cardiovasc Surg.* Oct 2004;128(4):552-561.

139. Eckes B, Dogic D, Colucci-Guyon E, Wang N, Maniotis A, Ingber D, Merckling A, Langa F, Aumailley M, Delouvee A, Koteliansky V, Babinet C, Krieg T. Impaired mechanical stability, migration and contractile capacity in vimentin-deficient fibroblasts. *Journal of cell science.* Jul 1998;111 (Pt 13):1897-1907.

140. Gabbiani G, Schmid E, Winter S, Chaponnier C, de Ckhastonay C, Vandekerckhove J, Weber K, Franke WW. Vascular smooth muscle cells differ from other smooth muscle cells: predominance of vimentin filaments and a specific alpha-type actin. *Proc Natl Acad Sci U S A.* Jan 1981;78(1):298-302.

141. Yoshida T, Owens GK. Molecular determinants of vascular smooth muscle cell diversity. *Circulation research.* Feb 18 2005;96(3):280-291.

142. Lester WM, Damji AA, Gedeon I, Tanaka M. Interstitial cells from the atrial and ventricular sides of the bovine mitral valve respond differently to denuding endocardial injury. *In Vitro Cell Dev Biol.* Jan 1993;29A(1):41-50.

143. Campbell SE, Katwa LC. Angiotensin II stimulated expression of transforming growth factor-beta1 in cardiac fibroblasts and myofibroblasts. *Journal of molecular and cellular cardiology.* Jul 1997;29(7):1947-1958.

144. Cushing MC, Liao JT, Anseth KS. Activation of valvular interstitial cells is mediated by transforming growth factor-beta1 interactions with matrix molecules. *Matrix Biol.* Sep 2005;24(6):428-437.

145. Sousa AM, Liu T, Guevara O, Stevens J, Fanburg BL, Gaestel M, Toksoz D, Kayyali US. Smooth muscle alpha-actin expression and myofibroblast differentiation by TGFbeta are dependent upon MK2. *Journal of cellular biochemistry.* Apr 15 2007;100(6):1581-1592.

146. Hinz B, Dugina V, Ballestrem C, Wehrle-Haller B, Chaponnier C. Alpha-smooth muscle actin is crucial for focal adhesion maturation in myofibroblasts. *Molecular biology of the cell.* Jun 2003;14(6):2508-2519.

147. Oyama MA, Chittur SV. Genomic expression patterns of mitral valve tissues from dogs with degenerative mitral valve disease. *Am J Vet Res.* Aug 2006;67(8):1307-1318.

148. Roy A, Brand NJ, Yacoub MH. Expression of 5-hydroxytryptamine receptor subtype messenger RNA in interstitial cells from human heart valves. *J Heart Valve Dis.* Mar 2000;9(2):256-260; discussion 260-251.

149. Valtieri M, Sorrentino A. The mesenchymal stromal cell contribution to homeostasis. *Journal of cellular physiology.* Nov 2008;217(2):296-300.

150. Mohler ER, 3rd, Gannon F, Reynolds C, Zimmerman R, Keane MG, Kaplan FS. Bone formation and inflammation in cardiac valves. *Circulation.* Mar 20 2001;103(11):1522-1528.

151. Caira FC, Stock SR, Gleason TG, McGee EC, Huang J, Bonow RO, Spelsberg TC, McCarthy PM, Rahimtoola SH, Rajamannan NM. Human degenerative valve disease is associated with up-regulation of low-density lipoprotein receptor-related protein 5 receptor-mediated bone formation. *J Am Coll Cardiol.* Apr 18 2006;47(8):1707-1712.

152. Narine K, Wever OD, Valckenborgh DV, Francois K, Bracke M, Desmet S, Mareel M, Nooten GV. Growth Factor Modulation of Fibroblast Proliferation, Differentiation, and Invasion: Implications for Tissue Valve Engineering. *Tissue Eng.* Sep 1 2006.

153. Sacks HS, Fain JN. Human epicardial adipose tissue: a review. *Am Heart J.* Jun 2007;153(6):907-917.

154. Rosito GA, Massaro JM, Hoffmann U, Ruberg FL, Mahabadi AA, Vasan RS, O'Donnell CJ, Fox CS. Pericardial fat, visceral abdominal fat, cardiovascular disease risk factors, and vascular calcification in a community-based sample: the Framingham Heart Study. *Circulation.* Feb 5 2008;117(5):605-613.

155. Sengenes C, Miranville A, Lolmede K, Curat CA, Bouloumie A. The role of endothelial cells in inflamed adipose tissue. *Journal of internal medicine.* Oct 2007;262(4):415-421.

156. Guzik TJ, Mangalat D, Korbut R. Adipocytokines - novel link between inflammation and vascular function? *J Physiol Pharmacol.* Dec 2006;57(4):505-528.

157. Falk T, Jonsson L, Olsen LH, Pedersen HD. Arteriosclerotic changes in the myocardium, lung, and kidney in dogs with chronic congestive heart failure and myxomatous mitral valve disease. *Cardiovasc Pathol.* Jul-Aug 2006;15(4):185-193.

158. Wallby L, Steffensen T, Broqvist M. Role of inflammation in nonrheumatic, regurgitant heart valve disease. A comparative, descriptive study regarding apolipoproteins and inflammatory cells in nonrheumatic heart valve disease. *Cardiovasc Pathol.* May-Jun 2007;16(3):171-178.

159. Stewart JA, Jr., Wei CC, Brower GL, Rynders PE, Hankes GH, Dillon AR, Lucchesi PA, Janicki JS, Dell'Italia LJ. Cardiac mast cell- and chymase-mediated matrix metalloproteinase activity and left ventricular remodeling in mitral regurgitation in the dog. *Journal of molecular and cellular cardiology.* Mar 2003;35(3):311-319.

160. Szombathy T, Janoskuti L, Szalai C, Csaszar A, Miklosi M, Meszaros Z, Kempler P, Laszlo Z, Fenyvesi T, Romics L. Angiotensin II type 1 receptor gene polymorphism and mitral valve prolapse syndrome. *Am Heart J.* Jan 2000;139(1 Pt 1):101-105.

161. Janicki JS, Brower GL, Gardner JD, Forman MF, Stewart JA, Jr., Murray DB, Chancey AL. Cardiac mast cell regulation of matrix metalloproteinase-related ventricular remodeling in chronic pressure or volume overload. *Cardiovasc Res.* Feb 15 2006;69(3):657-665.

162. Brower GL, Chancey AL, Thanigaraj S, Matsubara BB, Janicki JS. Cause and effect relationship between myocardial mast cell number and matrix metalloproteinase activity. *Am J Physiol Heart Circ Physiol.* Aug 2002;283(2):H518-525.

163. Brower GL, Janicki JS. Pharmacologic inhibition of mast cell degranulation prevents left ventricular remodeling induced by chronic volume overload in rats. *Journal of cardiac failure.* Sep 2005;11(7):548-556.

164. Forman MF, Brower GL, Janicki JS. Rat cardiac mast cell maturation and differentiation following acute ventricular volume overload. *Inflamm Res.* Oct 2006;55(10):408-415.

165. Veinot JP, Prichett-Pejic W, Song J, Waghray G, Parks W, Mesana TG, Ruel M. CD117-positive cells and mast cells in adult human cardiac valves--observations and implications for the creation of bioengineered grafts. *Cardiovasc Pathol.* Jan-Feb 2006;15(1):36-40.

166. Mohler ER, 3rd, Chawla MK, Chang AW, Vyavahare N, Levy RJ, Graham L, Gannon FH. Identification and characterization of calcifying valve cells from human and canine aortic valves. *J Heart Valve Dis.* May 1999;8(3):254-260.

167. Llorente-Cortes V, Royo T, Juan-Babot O, Badimon L. Adipocyte differentiation-related protein is induced by LRP1-mediated aggregated LDL internalization in human vascular smooth muscle cells and macrophages. *Journal of lipid research.* Oct 2007;48(10):2133-2140.

168. Filip DA, Nistor A, Bulla A, Radu A, Lupu F, Simionescu M. Cellular events in the development of valvular atherosclerotic lesions induced by experimental hypercholesterolemia. *Atherosclerosis.* Oct 1987;67(2-3):199-214.

169. Seshiah PN, Kereiakes DJ, Vasudevan SS, Lopes N, Su BY, Flavahan NA, Goldschmidt-Clermont PJ. Activated monocytes induce smooth muscle cell death: role of macrophage colony-stimulating factor and cell contact. *Circulation.* Jan 15 2002;105(2):174-180.

170. Seta N, Kuwana M. Human circulating monocytes as multipotential progenitors. *The Keio journal of medicine.* Jun 2007;56(2):41-47.

171. Theiss HD, David R, Engelmann MG, Barth A, Schotten K, Naebauer M, Reichart B, Steinbeck G, Franz WM. Circulation of CD34+ progenitor cell populations in patients with idiopathic dilated and ischaemic cardiomyopathy (DCM and ICM). *European heart journal.* May 2007;28(10):1258-1264.

172. Mann DL, Spinale FG. Activation of matrix metalloproteinases in the failing human heart: breaking the tie that binds. *Circulation.* Oct 27 1998;98(17):1699-1702.

173. Visse R, Nagase H. Matrix Metalloproteinases and Tissue Inhibitors of Metalloproteinases: Structure, Function, and Biochemistry. *Circulation research.* May 2, 2003 2003;92(8):827-839.

174. Dreger SA, Taylor PM, Allen SP, Yacoub MH. Profile and localization of matrix metalloproteinases (MMPs) and their tissue inhibitors (TIMPs) in human heart valves. *J Heart Valve Dis.* Nov 2002;11(6):875-880; discussion 880.

175. Togashi M, Tamura K, Nitta T, Ishizaki M, Sugisaki Y, Fukuda Y. Role of matrix metalloproteinases and their tissue inhibitor of metalloproteinases in myxomatous change of cardiac floppy valves. *Pathology international.* May 2007;57(5):251-259.

176. Aupperle H, Thielebein J, Kiefer B, Marz I, Dinges G, Schoon HA. An immunohistochemical study of the role of matrix metalloproteinases and their tissue inhibitors in chronic mitral valvular disease (valvular endocardiosis) in dogs. *Vet J.* Feb 21 2008.

177. Mahimkar R, Nguyen A, Mann M, Yeh CC, Zhu BQ, Karliner JS, Lovett DH. Cardiac transgenic matrix metalloproteinase-2 expression induces myxomatous valve degeneration: a potential model of mitral valve prolapse disease. *Cardiovasc Pathol.* Sep 30 2008.

178. Pemberton AD, Knight PA, Wright SH, Miller HR. Proteomic analysis of mouse jejunal epithelium and its response to infection with the intestinal nematode, Trichinella spiralis. *Proteomics.* Apr 2004;4(4):1101-1108.

179. Gorg A, Weiss W, Dunn MJ. Current two-dimensional electrophoresis technology for proteomics. *Proteomics.* Dec 2004;4(12):3665-3685.

180. Boeckmann B, Blatter MC, Famiglietti L, Hinz U, Lane L, Roechert B, Bairoch A. Protein variety and functional diversity: Swiss-Prot annotation in its biological context. *Comptes rendus biologies.* Oct-Nov 2005;328(10-11):882-899.

181. Lindblad-Toh K, Wade CM, Mikkelsen TS, Karlsson EK, Jaffe DB, Kamal M, Clamp M, Chang JL, Kulbokas EJ, 3rd, Zody MC, Mauceli E, Xie X, Breen M, Wayne RK, Ostrander EA, Ponting CP, Galibert F, Smith DR, DeJong PJ, Kirkness E, Alvarez P, Biagi T, Brockman W, Butler J, Chin CW, Cook A, Cuff J, Daly MJ, DeCaprio D, Gnerre S, Grabherr M, Kellis M, Kleber M, Bardeleben C, Goodstadt L, Heger A, Hitte C, Kim L, Koepfli KP, Parker HG, Pollinger JP, Searle SM, Sutter NB, Thomas R, Webber C, Baldwin J, Abebe A, Abouelleil A, Aftuck L, Ait-Zahra M, Aldredge T, Allen N, An P, Anderson S, Antoine C, Arachchi H, Aslam A, Ayotte L, Bachantsang P, Barry A, Bayul T, Benamara M, Berlin A, Bessette D, Blitshteyn B, Bloom T, Blye J, Boguslavskiy L, Bonnet C, Boukhgalter B, Brown A, Cahill P, Calixte N, Camarata J, Cheshatsang Y, Chu J, Citroen M, Collymore A, Cooke P, Dawoe T, Daza R, Decktor K, DeGray S, Dhargay N, Dooley K, Dooley K, Dorje P, Dorjee K, Dorris L, Duffey N, Dupes A, Egbiremolen O, Elong R, Falk J, Farina A, Faro S, Ferguson D, Ferreira P, Fisher S, FitzGerald M, Foley K, Foley C, Franke A, Friedrich D, Gage D, Garber M, Gearin G, Giannoukos G, Goode T, Goyette A, Graham J, Grandbois E, Gyaltsen K, Hafez N, Hagopian D, Hagos B, Hall J, Healy C, Hegarty R, Honan T, Horn A, Houde N, Hughes L, Hunnicutt L, Husby M, Jester B, Jones C, Kamat A, Kanga B, Kells C, Khazanovich D, Kieu AC, Kisner P, Kumar M, Lance K, Landers T, Lara M, Lee W, Leger JP, Lennon N, Leuper L, LeVine S, Liu J, Liu X, Lokyitsang Y, Lokyitsang T, Lui A, Macdonald J, Major J, Marabella R, Maru K, Matthews C, McDonough S, Mehta T, Meldrim J, Melnikov A, Meneus L, Mihalev A, Mihova T, Miller K, Mittelman R, Mlenga V, Mulrain L, Munson G, Navidi A, Naylor J, Nguyen T, Nguyen N, Nguyen C, Nguyen T, Nicol R, Norbu N, Norbu C, Novod N, Nyima T, Olandt P, O'Neill B, O'Neill K, Osman S, Oyono L, Patti C, Perrin D, Phunkhang P, Pierre F, Priest M, Rachupka A, Raghuraman S, Rameau R, Ray V, Raymond C, Rege F, Rise C, Rogers J, Rogov P, Sahalie J, Settipalli S, Sharpe T, Shea T, Sheehan M, Sherpa N, Shi J, Shih D, Sloan J, Smith C, Sparrow T, Stalker J, Stange-Thomann N, Stavropoulos S, Stone C, Stone S, Sykes S, Tchuinga P, Tenzing P, Tesfaye S, Thoulutsang D, Thoulutsang Y, Topham K, Topping I, Tsamla T, Vassiliev H, Venkataraman V, Vo A, Wangchuk T, Wangdi T, Weiand M, Wilkinson J, Wilson A, Yadav S, Yang S, Yang X, Young G, Yu Q, Zainoun J, Zembek L, Zimmer A, Lander ES. Genome sequence, comparative analysis and haplotype structure of the domestic dog. *Nature.* Dec 8 2005;438(7069):803-819.

182. Perkins DN, Pappin DJ, Creasy DM, Cottrell JS. Probability-based protein identification by searching sequence databases using mass spectrometry data. *Electrophoresis.* Dec 1999;20(18):3551-3567.

183. Palagi PM, Hernandez P, Walther D, Appel RD. Proteome informatics I: bioinformatics tools for processing experimental data. *Proteomics.* Oct 2006;6(20):5435-5444.

184. Henriksen PA, Kotelevtsev Y. Application of gene expression profiling to cardiovascular disease. *Cardiovasc Res.* Apr 2002;54(1):16-24.

185. Mayr M, Mayr U, Chung YL, Yin X, Griffiths JR, Xu Q. Vascular proteomics: linking proteomic and metabolomic changes. *Proteomics.* Dec 2004;4(12):3751-3761.

186. Jiang L, Tsubakihara M, Heinke MY, Yao M, Dunn MJ, Phillips W, dos Remedios CG, Nosworthy NJ. Heart failure and apoptosis: electrophoretic methods support data from micro- and macro-arrays. A critical review of genomics and proteomics. *Proteomics.* Dec 2001;1(12):1481-1488.

187. Dunn MJ, Corbett JM, Wheeler CH. HSC-2DPAGE and the two-dimensional gel electrophoresis database of dog heart proteins. *Electrophoresis.* Dec 1997;18(15):2795-2802.

188. Apweiler R, Bairoch A, Wu CH. Protein sequence databases. *Current Opinion in Chemical Biology.* 2004;8(1):76-80.

189. Hinz B, Gabbiani G. Mechanisms of force generation and transmission by myofibroblasts. *Current opinion in biotechnology.* Oct 2003;14(5):538-546.

190. Hinz B, Gabbiani G. Cell-matrix and cell-cell contacts of myofibroblasts: role in connective tissue remodeling. *Thrombosis and haemostasis.* Dec 2003;90(6):993-1002.

191. Grinnell F. Fibroblast biology in three-dimensional collagen matrices. *Trends in cell biology.* May 2003;13(5):264-269.

192. Weber KT, Sun Y, Katwa LC. Local regulation of extracellular matrix structure. *Herz.* Apr 1995;20(2):81-88.

193. Leslie KO, Taatjes DJ, Schwarz J, vonTurkovich M, Low RB. Cardiac myofibroblasts express alpha smooth muscle actin during right ventricular pressure overload in the rabbit. *Am J Pathol.* Jul 1991;139(1):207-216.

194. Darby I, Skalli O, Gabbiani G. Alpha-smooth muscle actin is transiently expressed by myofibroblasts during experimental wound healing. *Laboratory investigation; a journal of technical methods and pathology.* Jul 1990;63(1):21-29.

195. Skalli O, Schurch W, Seemayer T, Lagace R, Montandon D, Pittet B, Gabbiani G. Myofibroblasts from diverse pathologic settings are heterogeneous in their content of actin isoforms and intermediate filament proteins. *Laboratory investigation; a journal of technical methods and pathology.* Feb 1989;60(2):275-285.

196. Fatigati V, Murphy RA. Actin and tropomyosin variants in smooth muscles. Dependence on tissue type. *The Journal of biological chemistry.* Dec 10 1984;259(23):14383-14388.

197. Gunning P, Weinberger R, Jeffrey P. Actin and tropomyosin isoforms in morphogenesis. *Anatomy and embryology.* Apr 1997;195(4):311-315.

198. Lin JJ, Warren KS, Wamboldt DD, Wang T, Lin JL. Tropomyosin isoforms in nonmuscle cells. *International review of cytology.* 1997;170:1-38.

199. Helfman DM, Cheley S, Kuismanen E, Finn LA, Yamawaki-Kataoka Y. Nonmuscle and muscle tropomyosin isoforms are expressed from a single gene by alternative RNA splicing and polyadenylation. *Molecular and cellular biology.* Nov 1986;6(11):3582-3595.

200. Pittenger MF, Kazzaz JA, Helfman DM. Functional properties of non-muscle tropomyosin isoforms. *Current opinion in cell biology.* Feb 1994;6(1):96-104.

201. Schevzov G, Vrhovski B, Bryce NS, Elmir S, Qiu MR, O'Neill G M, Yang N, Verrills NM, Kavallaris M, Gunning PW. Tissue-specific tropomyosin isoform composition. *J Histochem Cytochem.* May 2005;53(5):557-570.

202. Bryce NS, Schevzov G, Ferguson V, Percival JM, Lin JJ, Matsumura F, Bamburg JR, Jeffrey PL, Hardeman EC, Gunning P, Weinberger RP. Specification of actin filament function and molecular composition by tropomyosin isoforms. *Molecular biology of the cell.* Mar 2003;14(3):1002-1016.

203. Perry SV. Vertebrate tropomyosin: distribution, properties and function. *Journal of muscle research and cell motility.* 2001;22(1):5-49.

204. Warren KS, Lin JL, McDermott JP, Lin JJ. Forced expression of chimeric human fibroblast tropomyosin mutants affects cytokinesis. *J. Cell Biol.* May 1, 1995 1995;129(3):697-708.

205. Gunning PW, Schevzov G, Kee AJ, Hardeman EC. Tropomyosin isoforms: divining rods for actin cytoskeleton function. *Trends in cell biology.* Jun 2005;15(6):333-341.

206. Bacchiocchi C, Graceffa P, Lehrer SS. Myosin-induced movement of alphaalpha, alphabeta, and betabeta smooth muscle tropomyosin on actin observed by multisite FRET. *Biophysical journal.* Apr 2004;86(4):2295-2307.

207. Merkel L, Ikebe M, Hartshorne DJ. Interaction of smooth muscle tropomyosin and smooth muscle myosin. Effect on the properties of myosin. *Biochemistry.* Mar 7 1989;28(5):2215-2220.

208. Roy A, Brand NJ, Yacoub MH. Molecular characterization of interstitial cells isolated from human heart valves. *J Heart Valve Dis.* May 2000;9(3):459-464; discussion 464-455.

209. Poetter K, Jiang H, Hassanzadeh S, Master SR, Chang A, Dalakas MC, Rayment I, Sellers JR, Fananapazir L, Epstein ND. Mutations in either the essential or regulatory light chains of myosin are associated with a rare myopathy in human heart and skeletal muscle. *Nat Genet.* May 1996;13(1):63-69.

210. Moss RL, Fitzsimons DP. Myosin light chain 2 into the mainstream of cardiac development and contractility. *Circulation research.* Aug 4 2006;99(3):225-227.

211. Rottbauer W, Wessels G, Dahme T, Just S, Trano N, Hassel D, Burns CG, Katus HA, Fishman MC. Cardiac Myosin Light Chain-2: A Novel Essential Component of Thick-Myofilament Assembly and Contractility of the Heart. *Circulation research.* August 4, 2006 2006;99(3):323-331.

212. Sanbe A, Fewell JG, Gulick J, Osinska H, Lorenz J, Hall DG, Murray LA, Kimball TR, Witt SA, Robbins J. Abnormal Cardiac Structure and Function in Mice Expressing Nonphosphorylatable Cardiac Regulatory Myosin Light Chain 2. *J. Biol. Chem.* July 23, 1999 1999;274(30):21085-21094.

213. Padro T, Pena E, Garcia-Arguinzonis M, Llorente-Cortes V, Badimon L. Low-density lipoproteins impair migration of human coronary vascular smooth muscle cells and induce changes in the proteomic profile of myosin light chain. *Cardiovasc Res.* Jan 2008;77(1):211-220.

214. Ferns G, Shams S, Shafi S. Heat shock protein 27: its potential role in vascular disease. *Int J Exp Pathol.* Aug 2006;87(4):253-274.

215. Ibitayo AI, Sladick J, Tuteja S, Louis-Jacques O, Yamada H, Groblewski G, Welsh M, Bitar KN. HSP27 in signal transduction and association with contractile proteins in smooth muscle cells. *Am J Physiol.* Aug 1999;277(2 Pt 1):G445-454.

216. Bitar KN. HSP27 phosphorylation and interaction with actin-myosin in smooth muscle contraction. *American journal of physiology.* May 2002;282(5):G894-903.

217. Somara S, Bitar KN. Tropomyosin interacts with phosphorylated HSP27 in agonist-induced contraction of smooth muscle. *Am J Physiol Cell Physiol.* Jun 2004;286(6):C1290-1301.

218. Sabri A, Rafiq K, Seqqat R, Kolpakov MA, Dillon R, Dell'italia LJ. Sympathetic activation causes focal adhesion signaling alteration in early compensated volume overload attributable to isolated mitral regurgitation in the dog. *Circulation research.* May 9 2008;102(9):1127-1136.

219. Olsen EG, Al-Rufaie HK. The floppy mitral valve. Study on pathogenesis. *British heart journal.* Dec 1980;44(6):674-683.

220. Lucas RV, Jr., Edwards JE. The floppy mitral valve. *Curr Probl Cardiol.* Jul 1982;7(4):1-48.

221. Mills WR, Barber JE, Ratliff NB, Cosgrove DM, 3rd, Vesely I, Griffin BP. Biomechanical and echocardiographic characterization of flail mitral leaflet due to myxomatous disease: further evidence for early surgical intervention. *Am Heart J.* Jul 2004;148(1):144-150.

222. Grashow JS, Sacks MS, Liao J, Yoganathan AP. Planar biaxial creep and stress relaxation of the mitral valve anterior leaflet. *Annals of biomedical engineering.* Oct 2006;34(10):1509-1518.

223. Grashow JS, Yoganathan AP, Sacks MS. Biaixal stress-stretch behavior of the mitral valve anterior leaflet at physiologic strain rates. *Annals of biomedical engineering.* Feb 2006;34(2):315-325.

224. Sacks MS, Enomoto Y, Graybill JR, Merryman WD, Zeeshan A, Yoganathan AP, Levy RJ, Gorman RC, Gorman JH, 3rd. In-vivo dynamic deformation of the mitral valve anterior leaflet. *Ann Thorac Surg.* Oct 2006;82(4):1369-1377.

225. Halayko AJ, Solway J. Plasticity in Skeletal, Cardiac, and Smooth Muscle: Invited Review: Molecular mechanisms of phenotypic plasticity in smooth muscle cells. *J Appl Physiol.* January 1, 2001 2001;90(1):358-368.

226. Ng CM, Cheng A, Myers LA, Martinez-Murillo F, Jie C, Bedja D, Gabrielson KL, Hausladen JM, Mecham RP, Judge DP, Dietz HC. TGF-beta-dependent pathogenesis of mitral valve prolapse in a mouse model of Marfan syndrome. *J Clin Invest.* Dec 2004;114(11):1586-1592.

227. Malmstrom J, Lindberg H, Lindberg C, Bratt C, Wieslander E, Delander EL, Sarnstrand B, Burns JS, Mose-Larsen P, Fey S, Marko-Varga G. Transforming growth factor-beta 1 specifically induce proteins involved in the myofibroblast contractile apparatus. *Mol Cell Proteomics.* May 2004;3(5):466-477.

228. Knoll R, Hoshijima M, Hoffman HM, Person V, Lorenzen-Schmidt I, Bang ML, Hayashi T, Shiga N, Yasukawa H, Schaper W, McKenna W, Yokoyama M, Schork NJ, Omens JH, McCulloch AD, Kimura A, Gregorio CC, Poller W, Schaper J, Schultheiss HP, Chien KR. The cardiac mechanical stretch sensor machinery involves a Z disc complex that is defective in a subset of human dilated cardiomyopathy. *Cell.* Dec 27 2002;111(7):943-955.

229. Mulholland DL, Gotlieb AI. Cardiac Valve Interstitial Cells: Regulator of Valve Structure and Function. *Cardiovascular Pathology.* 1997/5/6 1997;6(3):167-174.

230. Frid MG, Shekhonin BV, Koteliansky VE, Glukhova MA. Phenotypic changes of human smooth muscle cells during development: late expression of heavy caldesmon and calponin. *Developmental biology.* Oct 1992;153(2):185-193.

231. Pucovsky V, Harhun MI, Povstyan OV, Gordienko DV, Moss RF, Bolton TB. Close relation of arterial ICC-like cells to the contractile phenotype of vascular smooth muscle cell. *Journal of cellular and molecular medicine.* Jul-Aug 2007;11(4):764-775.

232. Kwon M, Hanna E, Lorang D, He M, Quick JS, Adem A, Stevenson C, Chung J-Y, Hewitt SM, Zudaire E, Esposito D, Cuttitta F, Libutti SK. Functional Characterization of Filamin A Interacting Protein 1-Like, a Novel Candidate for Antivascular Cancer Therapy. *Cancer Res.* September 15, 2008 2008;68(18):7332-7341.

233. Nagano T, Yoneda T, Hatanaka Y, Kubota C, Murakami F, Sato M. Filamin A-interacting protein (FILIP) regulates cortical cell migration out of the ventricular zone. *Nat Cell Biol.* Jul 2002;4(7):495-501.

234. Feng Y, Walsh CA. The many faces of filamin: A versatile molecular scaffold for cell motility and signalling. *Nat Cell Biol.* 2004;6(11):1034-1038.

235. van der Flier A, Sonnenberg A. Structural and functional aspects of filamins. *Biochimica et Biophysica Acta (BBA) - Molecular Cell Research.* 2001;1538(2-3):99-117.

236. Zhou X, Borén J, Akyürek LM. Filamins in Cardiovascular Development. *Trends in cardiovascular medicine.* 2007;17(7):222-229.

237. Yu N, Erb L, Shivaji R, Weisman GA, Seye CI. Binding of the P2Y2 Nucleotide Receptor to Filamin A Regulates Migration of Vascular Smooth Muscle Cells. *Circulation research.* March 14, 2008 2008;102(5):581-588.

238. Kyndt F, Gueffet JP, Probst V, Jaafar P, Legendre A, Le Bouffant F, Toquet C, Roy E, McGregor L, Lynch SA, Newbury-Ecob R, Tran V, Young I, Trochu JN, Le Marec H, Schott JJ. Mutations in the gene encoding filamin A as a cause for familial cardiac valvular dystrophy. *Circulation.* Jan 2 2007;115(1):40-49.

239. Blevins TL, Peterson SB, Lee EL, Bailey AM, Frederick JD, Huynh TN, Gupta V, Grande-Allen KJ. Mitral valvular interstitial cells demonstrate regional, adhesional, and synthetic heterogeneity. *Cells Tissues Organs.* 2008;187(2):113-122.

240. Kornberg RD. Chromatin structure: a repeating unit of histones and DNA. *Science (New York, N.Y.* May 24 1974;184(139):868-871.

241. Bonenfant D, Coulot M, Towbin H, Schindler P, van Oostrum J. Characterization of histone H2A and H2B variants and their post-translational modifications by mass spectrometry. *Mol Cell Proteomics.* Mar 2006;5(3):541-552.

242. Collart D, Ramsey-Ewing A, Bortell R, Lian J, Stein J, Stein G. Isolation and characterization of a cDNA from a human histone H2B gene which is reciprocally expressed in relation to replication-dependent H2B histone genes during HL60 cell differentiation. *Biochemistry.* Feb 12 1991;30(6):1610-1617.

243. Henry KW, Wyce A, Lo WS, Duggan LJ, Emre NC, Kao CF, Pillus L, Shilatifard A, Osley MA, Berger SL. Transcriptional activation via sequential histone H2B ubiquitylation and deubiquitylation, mediated by SAGA-associated Ubp8. *Genes & development.* Nov 1 2003;17(21):2648-2663.

244. Murr R, Vaissiere T, Sawan C, Shukla V, Herceg Z. Orchestration of chromatin-based processes: mind the TRRAP. *Oncogene.* Aug 13 2007;26(37):5358-5372.

245. Guerra S, Lopez-Fernandez LA, Garcia MA, Zaballos A, Esteban M. Human gene profiling in response to the active protein kinase, interferon-induced serine/threonine protein kinase (PKR), in infected cells. Involvement of the transcription factor ATF-3 IN PKR-induced apoptosis. *The Journal of biological chemistry.* Jul 7 2006;281(27):18734-18745.

246. Kang SW, Baines IC, Rhee SG. Characterization of a mammalian peroxiredoxin that contains one conserved cysteine. *The Journal of biological chemistry.* Mar 13 1998;273(11):6303-6311.

247. Muller FL, Song W, Liu Y, Chaudhuri A, Pieke-Dahl S, Strong R, Huang TT, Epstein CJ, Roberts LJ, 2nd, Csete M, Faulkner JA, Van Remmen H. Absence of CuZn superoxide dismutase leads to elevated oxidative stress and acceleration of age-dependent skeletal muscle atrophy. *Free radical biology & medicine.* Jun 1 2006;40(11):1993-2004.

248. Beresewicz A, Czarnowska E, Maczewski M. Ischemic preconditioning and superoxide dismutase protect against endothelial dysfunction and endothelium glycocalyx disruption in the postischemic guinea-pig hearts. *Molecular and cellular biochemistry.* Sep 1998;186(1-2):87-97.

249. Grande-Allen KJ, Calabro A, Gupta V, Wight TN, Hascall VC, Vesely I. Glycosaminoglycans and proteoglycans in normal mitral valve leaflets and chordae: association with regions of tensile and compressive loading. *Glycobiology.* Jul 2004;14(7):621-633.

250. Liao J, Yang L, Grashow J, Sacks MS. The relation between collagen fibril kinematics and mechanical properties in the mitral valve anterior leaflet. *J Biomech Eng.* Feb 2007;129(1):78-87.

251. Jaffe AS, Geltman EM, Rodey GE, Uitto J. Mitral valve prolapse: a consistent manifestation of type IV Ehlers-Danlos syndrome. The pathogenetic role of the abnormal production of type III collagen. *Circulation.* Jul 1981;64(1):121-125.

252. Disse S, Abergel E, Berrebi A, Houot AM, Le Heuzey JY, Diebold B, Guize L, Carpentier A, Corvol P, Jeunemaitre X. Mapping of a first locus for autosomal dominant myxomatous mitral-valve prolapse to chromosome 16p11.2-p12.1. *Am J Hum Genet.* Nov 1999;65(5):1242-1251.

253. Nesta F, Leyne M, Yosefy C, Simpson C, Dai D, Marshall JE, Hung J, Slaugenhaupt SA, Levine RA. New locus for autosomal dominant mitral valve prolapse on chromosome 13: clinical insights from genetic studies. *Circulation.* Sep 27 2005;112(13):2022-2030.

254. Wordsworth P, Ogilvie D, Akhras F, Jackson G, Sykes B. Genetic segregation analysis of familial mitral valve prolapse shows no linkage to fibrillar collagen genes. *British heart journal.* Mar 1989;61(3):300-306.

255. Chou HT, Hung JS, Chen YT, Wu JY, Tsai FJ. Association between COL3A1 collagen gene exon 31 polymorphism and risk of floppy mitral valve/mitral valve prolapse. *International journal of cardiology.* Jun 2004;95(2-3):299-305.

256. Gupta V, Werdenberg JA, Blevins TL, Grande-Allen KJ. Synthesis of Glycosaminoglycans in Differently Loaded Regions of Collagen Gels Seeded with Valvular Interstitial Cells. *Tissue Eng.* Nov 1 2006.

257. Weinberg EJ, Kaazempur Mofrad MR. A finite shell element for heart mitral valve leaflet mechanics, with large deformations and 3D constitutive material model. *J Biomech.* 2007;40(3):705-711.

258. He Z, Ritchie J, Grashow JS, Sacks MS, Yoganathan AP. In vitro dynamic strain behavior of the mitral valve posterior leaflet. *J Biomech Eng.* Jun 2005;127(3):504-511.

259. Pankov R, Yamada KM. Fibronectin at a glance. *Journal of cell science.* Oct 15 2002;115(Pt 20):3861-3863.

260. Fayet C, Bendeck MP, Gotlieb AI. Cardiac valve interstitial cells secrete fibronectin and form fibrillar adhesions in response to injury. *Cardiovascular Pathology.* 2007;16(4):203-211.

261. Johnson CM, Helgeson SC. Fibronectin biosynthesis and cell-surface expression by cardiac and non-cardiac endothelial cells. *Am J Pathol.* May 1993;142(5):1401-1408.

262. Kitten GT, Markwald RR, Bolender DL. Distribution of basement membrane antigens in cryopreserved early embryonic hearts. *Anat Rec.* Apr 1987;217(4):379-390.

263. Armstrong PB, Armstrong MT. Intercellular invasion and the organizational stability of tissues: a role for fibronectin. *Biochimica et biophysica acta.* Mar 27 2000;1470(2):O9-20.

264. Dallas SL, Sivakumar P, Jones CJ, Chen Q, Peters DM, Mosher DF, Humphries MJ, Kielty CM. Fibronectin regulates latent transforming growth factor-beta (TGF beta) by controlling matrix assembly of latent TGF beta-binding protein-1. *The Journal of biological chemistry.* May 13 2005;280(19):18871-18880.

265. Hedin U, Bottger BA, Forsberg E, Johansson S, Thyberg J. Diverse effects of fibronectin and laminin on phenotypic properties of cultured arterial smooth muscle cells. *The Journal of cell biology.* Jul 1988;107(1):307-319.

266. Hedin U, Bottger BA, Forsberg E, Johansson S, Thyberg J. Diverse effects of fibronectin and laminin on phenotypic properties of cultured arterial smooth muscle cells. *J. Cell Biol. %R 10.1083/jcb.107.1.307.* July 1, 1988 1988;107(1):307-319.

267. Masters KS, Shah DN, Walker G, Leinwand LA, Anseth KS. Designing scaffolds for valvular interstitial cells: cell adhesion and function on naturally derived materials. *J Biomed Mater Res A.* Oct 1 2004;71(1):172-180.

268. Hocking AM, Shinomura T, McQuillan DJ. Leucine-rich repeat glycoproteins of the extracellular matrix. *Matrix Biol.* Apr 1998;17(1):1-19.

269. Iozzo RV. The biology of the small leucine-rich proteoglycans. Functional network of interactive proteins. *The Journal of biological chemistry.* Jul 2 1999;274(27):18843-18846.

270. Ameye L, Young MF. Mice deficient in small leucine-rich proteoglycans: novel in vivo models for osteoporosis, osteoarthritis, Ehlers-Danlos syndrome, muscular dystrophy, and corneal diseases. *Glycobiology.* Sep 2002;12(9):107R-116R.

271. Loeser RF. Growth factor regulation of chondrocyte integrins. Differential effects of insulin-like growth factor 1 and transforming growth factor beta on alpha 1 beta 1 integrin expression and chondrocyte adhesion to type VI collagen. *Arthritis and rheumatism.* Feb 1997;40(2):270-276.

272. Bashey RI, Martinez-Hernandez A, Jimenez SA. Isolation, characterization, and localization of cardiac collagen type VI. Associations with other extracellular matrix components. *Circulation research.* May 1992;70(5):1006-1017.

273. Wiberg C, Hedbom E, Khairullina A, Lamande SR, Oldberg A, Timpl R, Morgelin M, Heinegard D. Biglycan and Decorin Bind Close to the N-terminal Region of the Collagen VI Triple Helix. *J. Biol. Chem.* May 25, 2001 2001;276(22):18947-18952.

274. Bhide VM, Laschinger CA, Arora PD, Lee W, Hakkinen L, Larjava H, Sodek J, McCulloch CA. Collagen Phagocytosis by Fibroblasts Is Regulated by Decorin. *J. Biol. Chem.* June 17, 2005 2005;280(24):23103-23113.

275. Hedbom E, Heinegard D. Interaction of a 59-kDa connective tissue matrix protein with collagen I and collagen II. *The Journal of biological chemistry.* Apr 25 1989;264(12):6898-6905.

276. Svensson L, Narlid I, Oldberg A. Fibromodulin and lumican bind to the same region on collagen type I fibrils. *FEBS letters.* Mar 24 2000;470(2):178-182.

277. Hildebrand A, Romaris M, Rasmussen LM, Heinegard D, Twardzik DR, Border WA, Ruoslahti E. Interaction of the small interstitial proteoglycans biglycan, decorin and fibromodulin with transforming growth factor beta. *The Biochemical journal.* Sep 1 1994;302 (Pt 2):527-534.

278. Chou HT, Shi YR, Hsu Y, Tsai FJ. Lack of association of genetic polymorphisms in the interleukin-1beta, interleukin-1 receptor antagonist, interleukin-4 and interleukin-10 genes with mitral valve prolapse in Taiwan Chinese. *J Heart Valve Dis.* Jan 2003;12(1):38-44.

279. Arab S, Gramolini AO, Ping P, Kislinger T, Stanley B, van Eyk J, Ouzounian M, MacLennan DH, Emili A, Liu PP. Cardiovascular proteomics: tools to develop novel biomarkers and potential applications. *J Am Coll Cardiol.* Nov 7 2006;48(9):1733-1741.

280. Corbett JM, Wheeler CH, Dunn MJ. Coelectrophoresis of cardiac tissue from human, dog, rat and mouse: towards the establishment of an integrated two-dimensional protein database. *Electrophoresis.* Aug 1995;16(8):1524-1529.

281. Galibert F, André C. The dog: A powerful model for studying genotype-phenotype relationships. *Comparative Biochemistry and Physiology Part D: Genomics and Proteomics.* 2008;3(1):67-77.

282. Hubbard TJ, Aken BL, Beal K, Ballester B, Caccamo M, Chen Y, Clarke L, Coates G, Cunningham F, Cutts T, Down T, Dyer SC, Fitzgerald S, Fernandez-Banet J, Graf S, Haider S, Hammond M, Herrero J, Holland R, Howe K, Howe K, Johnson N, Kahari A, Keefe D, Kokocinski F, Kulesha E, Lawson D, Longden I, Melsopp C, Megy K, Meidl P, Ouverdin B, Parker A, Prlic A, Rice S, Rios D, Schuster M, Sealy I, Severin J, Slater G, Smedley D, Spudich G, Trevanion S, Vilella A, Vogel J, White S, Wood M, Cox T, Curwen V, Durbin R, Fernandez-Suarez XM, Flicek P, Kasprzyk A, Proctor G, Searle S, Smith J, Ureta-Vidal A, Birney E. Ensembl 2007. *Nucleic acids research.* Jan 2007;35(Database issue):D610-617.

283. Rozen S, Skaletsky H. Primer3 on the WWW for general users and for biologist programmers. *Methods in molecular biology (Clifton, N.J.* 2000;132:365-386.

284. Ohashi Y, Creek KE, Pirisi L, Kalus R, Young SR. RNA degradation in human breast tissue after surgical removal: a time-course study. *Experimental and molecular pathology.* Oct 2004;77(2):98-103.

285. Huang J, Qi R, Quackenbush J, Dauway E, Lazaridis E, Yeatman T. Effects of ischemia on gene expression. *The Journal of surgical research.* Aug 2001;99(2):222-227.

286. Peters IR, Peeters D, Helps CR, Day MJ. Development and application of multiple internal reference (housekeeper) gene assays for accurate normalisation of canine gene expression studies. *Veterinary immunology and immunopathology.* May 15 2007;117(1-2):55-66.

287. Etschmann B, Wilcken B, Stoevesand K, von der Schulenburg A, Sterner-Kock A. Selection of reference genes for quantitative real-time PCR analysis in canine mammary tumors using the GeNorm algorithm. *Veterinary pathology.* Nov 2006;43(6):934-942.

288. Huggett J, Dheda K, Bustin S, Zumla A. Real-time RT-PCR normalisation; strategies and considerations. *Genes and immunity.* Jun 2005;6(4):279-284.

289. Yperman J, De Visscher G, Holvoet P, Flameng W. Beta-actin cannot be used as a control for gene expression in ovine interstitial cells derived from heart valves. *J Heart Valve Dis.* Sep 2004;13(5):848-853.

290. Port M, Schmelz HU, Stassen T, Mueller K, Stockinger M, Obermair R, Abend M. Correcting false gene expression measurements from degraded RNA using RTQ-PCR. *Diagn Mol Pathol.* Mar 2007;16(1):38-49.

291. Farhadian F, Contard F, Corbier A, Barrieux A, Rappaport L, Samuel JL. Fibronectin expression during physiological and pathological cardiac growth. *Journal of molecular and cellular cardiology.* Apr 1995;27(4):981-990.

292. Going JJ, Gusterson BA. Molecular pathology and future developments. *Eur J Cancer.* Dec 1999;35(14):1895-1904.

293. Mellersh C. Give a dog a genome. *Vet J.* Oct 2008;178(1):46-52.

294. Tsai KL, Clark LA, Murphy KE. Understanding hereditary diseases using the dog and human as companion model systems. *Mamm Genome.* Jul 2007;18(6-7):444-451.

8 Appendix

8.1 Publications

8.1.1 Journal Articles

This PhD project has so far generated two journal articles. It is with great intention to publish other part of this thesis. Publication plans have already been formulated for TEM, SEM and proteomics studies.

Han RI, Black A, Culshaw GJ, French AT, Corcoran BM. Structural and cellular changes in canine myxomatous mitral valve disease: an image analysis study.
J Heart Valve Dis. (accepted Jun 2009)

Han RI, Black A, Culshaw GJ, French AT, Else RW, Corcoran BM. Distribution of myofibroblasts, smooth muscle-like cells, macrophages, and mast cells in mitral valve leaflets of dogs with myxomatous mitral valve disease. *Am J Vet Res.* Jun 2008;69(6):763-769.

8.1.2 Proceedings

Han RI, Black A, Else RW, Corcoran BM. Structural and Cellular Changes in Canine Myxomatous Mitral Valve Disease: An Image Analysis Study. 3rd Biennial Heart Valve Biology and Tissue Engineering. 2008

Gow D, Han RI, French AT, Culshaw GJ, Martinez Y, Argyle SA, Corcoran BM. Expression of CD34+ cells in canine myxomatous mitral valve leaflets. European College of Veterinary Internal Medicine. 2007

Corcoran BM, Han RI, French AT, Pemberton AD. Parallel quantitative protein expression profiles of mitral valve tissues of dogs with and without myxomatous mitral valve disease. British Small Animal Veterinary Association Congress. 2007

O'Connell P, Han RI, Black A, French AT, Else RW, Corcoran BM. Distribution of macrophages and mast cells in the valve leaflets of dogs with myxomatous mitral valve disease. European College of Veterinary Internal Medicine. 2006

Han RI, Black A, French AT, Else RW, Corcoran BM. Expression of mesemchymal cell markers (vimentin, desmin, smooth muscle actin, smooth muscle myosin) in the valve leaflets of dogs with myxomatous mitral valve disease. European College of Veterinary Internal Medicine. 2006

Han RI, Black A, French AT, Corcoran BM. Interstitial cells in myxomatous areas of canine mitral valves. Image Analysis for Microscopy. 2006

Sheehan EM, Han RI, Devine C, French AT, Black A, Dukes-McEwan J, Corcoran BM. Interstitial cell density in myxomatous areas of canine mitral

valves does not vary with disease severity. Clinical Research Abstract. British Small Animal Veterinary Association Congress 2005